AUTOGENOUS SHRINKAGE OF CARDIFRC®

A thesis submitted for the degree of
Doctor of Philosophy

by

Antonios Kanellopoulos

School of Engineering
Cardiff University
United Kingdom

September 2004

ProQuest LLC
789 East Eisenhower Parkway
P.O. Box 1346
Ann Arbor, MI 48106-1346

"I have not failed 700 times. I have not failed once. I have succeeded in proving that those 700 ways will not work. When I have eliminated the ways that will not work, I will find the way that will work."

Thomas Edison

DECLARATION

This is to certify that neither this thesis, nor any part of it, has been presented or is being concurrently submitted in candidature for any degree at any university.

Candidate.....

Date.....30/11/04.....

STATEMENT 1

This thesis is the result of my own investigations, except where otherwise stated. Other sources are acknowledged by given references. A bibliography is appended.

Candidate.....

Date.....30/11/04.....

STATEMENT 2

I hereby give consent for my thesis, if accepted, to be made available for photocopying and inter-library loan, for the title and summary to be made available to outside organisations.

Candidate.....

Date.....30/11/04.....

To my beloved family

ACKNOWLEDGEMENT

First of all, I would like to express my sincere appreciation to my supervisor, Professor Bhushan Karihaloo, for his continuous advice, encouragement, support and guidance throughout, without which, this work would not have been completed.

I would like to thank the civil engineering laboratory staff, in particular Des Sanford, Brian Hooper, Carl Wadsworth, Andrew Sweeney, whose assistance was invaluable. Special thanks to my colleagues and friends Demetris Nicolaides and Farhat Farhat for their valuable support and continuous encouragement. Their friendship and loyalty have been fantastic.

I am also grateful to my sister Marianthi who has been very tolerant with me all these three years and helped me a lot all these sad and difficult moments.

Last but not least, I would like to pay a special tribute to my parents, without the love, understanding, encouragement and support of whom I could not have sustained all these years of study and to whom I owe everything.

SYNOPSIS

Durability requirements have become a major issue in the design of concrete structures today. The hardening process plays a key role in the quality of the concrete. Autogenous shrinkage is considered to be a factor that may cause damage to the concrete structure during hardening. The concept of autogenous shrinkage is relatively new and in the case of conventional concrete with fairly high water to cement ratios these self-induced volume changes are found to be relatively small and therefore are neglected. Self-desiccation and autogenous shrinkage are pronounced phenomena in the case of low water to cement ratio concretes.

The current study deals with the development of autogenous shrinkage strains in a new class of High Performance Fibre Reinforced Cementitious Composites (HPFRCCs) designated CARDIFRC® that has been recently developed at Cardiff University. The scope of the study was to investigate how the self-induced shrinkage strains develop in CARDIFRC® matrix without fibres and what was the effect of the inclusion of a large amount of fibre on the autogenous shrinkage. Both experimental and theoretical studies were undertaken as a part of this investigation.

Autogenous shrinkage strains were measured on large and small prisms of CARDIFRC® under isothermal conditions. The experiments revealed a relatively large scatter in the measured values for the case of large beams with fibres, whereas the beams of same size but without any fibres gave consistent results. This large scatter has been confirmed to be a result of the uneven distribution of fibres in the large prisms. Small prisms with and without fibres gave very consistent results, with autogenous shrinkage taking place up to 75 days. The autogenous shrinkage strains have been modelled using a thermodynamic approach which follows the continuous change in the moisture content, pore volume and stiffness of the mix with degree of hydration. The predictions of the model are in good agreement with the measured strains in all specimens with and without fibres.

Table of Contents

List of Figures

List of Tables

Chapter 1: Introduction

1.1 Introduction

In the design of structures, durability aspects are gaining more and more interest from the engineers. The desired lifetime of a structure as well as the quality of the materials used in its construction play a key role in this. In case of concrete structures, durability is strongly connected with the microstructure of the material and the chemical and mechanical processes taking place in it.

New types of concrete have been developed in order to meet the increasing demands for materials with improved mechanical properties and durability. These new types of concrete are widely known as high strength (HSC), high performance (HPC) and ultra high performance concretes (UHPC). The material properties of such concretes show a substantial improvement over the conventional concrete. However, the improved microstructure of these new types of concrete not only lead to improved properties but also introduce significant volume changes which occur during the hardening of the material. Generally, such self-induced volume change is termed *autogenous shrinkage*.

A very early description of the self-induced volume changes dates back to the start of the 20th century. Le Chatelier was one of the pioneers of cement research and the first who addressed the problem of self-desiccation. Apparently, in one of his early papers, Le Chatelier states that in order to understand the ongoing volume changes in cement paste it is very important to distinguish the volume changes induced by chemical and autogenous shrinkage. He believed that these two types of shrinkage are two different, but interconnected phenomena (Jensen and Hansen, 2001).

The term *autogenous shrinkage* was first defined almost three decades after the first observations by Le Chatelier. Experimental results at that time revealed small values for the autogenous shrinkage strains. Moreover, the self-induced deformations compared to thermal and drying deformations were found to be very small and

therefore could be neglected. In fact, that is the reason for the little attention given to autogenous shrinkage for many years in both concrete practice and research.

It is the last two decades the importance of autogenous shrinkage has gained prominence, when the production of HSC, HPC and UHPC became feasible with the help of chemical admixtures and microfillers. The addition of superplasticisers made possible dramatic reductions in water to cement ratios, whereas the incorporation of silica fume resulted in a very dense homogeneous microstructure, as well as in a significantly refined pore structure.

In terms of self-induced volume changes, these new types of concrete are considerably different to conventional concrete. The pozzolanic reaction of silica fume results in a densely packed microstructure and moreover leads to a large amount of chemical shrinkage. These factors promote self-desiccation and therefore autogenous shrinkage. Extensive research in the field confirmed that the governing physio-chemical phenomenon that connects self-desiccation and autogenous shrinkage are the capillary stresses in the pore water (Hua *et al.*, 1995).

The significance of the subject of autogenous shrinkage and self-desiccation has been established both in terms of scientific research and engineering practice. Autogenous shrinkage has been related to many factors such as the water to cement ratio, the cement composition, the cement fineness, the silica fume content, the silica fume fineness, the volume of aggregate used and the exposure temperature. However, there is a lack of agreement between the researchers on the extent of influence of the different factors, as well as the actual microstructural processes leading to autogenous volume changes (Koenders, 1997; Tazawa, 1999; Tazawa *et al.*, 1995;Wittmann, 2001).

A lot of effort has also gone into the modelling of the self-induced shrinkage strains. It was known from the case of conventional concrete that the modelling of microstructural processes is a very complicated procedure. The problem is further complicated in the case of concretes with denser microstructures. The introduction of pozzolans into the mix not only leads to a better packing of particles in the

microstructure but is also followed by a number of chemical reactions. Such chemical reactions proved to be very difficult to model and therefore the majority of the models, dealing with the phenomenon of self-desiccation and autogenous shrinkage reported in the literature, offer only a very good approximation of the ongoing processes during hardening. Another pitfall that some of the available models have is the fact that they proved to be insufficient to deal with very dense microstructures and very low water to cement ratios.

1.2 Objectives of the thesis

The main objective of the current work is to give a thorough description of the mechanisms responsible for the phenomena of self-desiccation and autogenous shrinkage in the high performance fibre-reinforced cement-based material, CARDIFRC®. Moreover, a model has to be developed in order to predict the self-induced shrinkage strains in this material. The work is summarised in the following steps:

- Thorough review and discussion of the literature regarding the development of High Performance Fibre Reinforced Cementitious Composites, the microstructural modelling of their mechanical properties, the aspects of hydration of cement-based materials and the associated volume changes in cement-based materials.

- Identification of the microstructural parameters responsible for the development of autogenous shrinkage strains and the methods to model them.

- Design of the appropriate experimental procedures in order to measure the autogenous shrinkage strains in CARDIFRC® cured at ambient temperature.

- Development of an appropriate model to simulate the evolution of the self-induced shrinkage strains in CARDIFRC®.

1.3 Outline of the thesis

The contents of the thesis are organised as follows:

Chapter 2 gives a thorough description of the development of High Performance Fibre Reinforced Cementitious Composites (HPFRCCs), as well as of a new class of HPFRCC materials that has been recently developed at Cardiff University designated CARDIFRC®. The mechanical behaviour of these materials is also examined.

Chapter 3 deals with the microstructural modelling of volume changes in cement-based materials. A distinction is made between the existing empirical models and the recently developed mathematical models. Models like Bazant-Panula model, Parrott's model, NIST model and the HYMOSTRUC model are discussed.

Cement, in the general sense of the word, can be described as a material with adhesive and cohesive properties which make it capable of bonding mineral fragments into a compact whole. A large variety of cementing materials are embraced in this definition. On contact with water Portland cement particles start to dissolve and react with water leading to the formation of hydration products. Hydration products form a complex gel. In Chapter 4 the chemistry of cement is briefly examined, as well as some of the mechanisms associated with the cement hydration. This will be the basis of further analysis towards the understanding of the volume changes that the cementitious materials undergo.

Chapter 5 describes how the induced stresses from autogenous shrinkage can be modelled. The analysis will be focused on the mechanisms behind the autogenous shrinkage. Analysis of the moisture state in the constantly changing pore system is the primary scope of this Chapter.

The experimental program consists of control tests in order to obtain the mechanical properties of the material, as well as tests for the autogenous shrinkage measurement. The results of the experimental work are presented and analysed in Chapter 6.

The experimental results are compared with the model predictions in Chapter 7. The feasibility of using empirical formulae for the evaluation of autogenous shrinkage in strains in CARDIFRC® is also explored.

Chapter 8 is devoted to the major conclusions of the thesis, as well as to some recommendations for future work in the area of self-desiccation and autogenous shrinkage of HPFRCCs.

In order not to interrupt the flow of text, detailed experimental results and other secondary material are relegated to Appendices.

Chapter 2: HPFRCCs and CARDIFRC®

2.1 Introduction

High Performance Fibre Reinforced Cementitious Composites (HPFRCCs) represent a class of cement composites whose stress strain response in tension exhibits strain hardening behaviour accompanied by multiple cracking, leading to a high failure strain capacity. HPFRCCs result from advances in manufacturing processes that permit the inclusion of a large amount of fibres in the cement based matrix without affecting the workability of the mix. These advances are based on the use of silica fume and surfactants which reduce water demand and densify the matrix, thereby improving the fibre-matrix interfacial bond (Morin *et al.*, 2001; Bache, 1981).

A new class of HPFRCC materials has been recently developed at Cardiff University designated CARDIFRC®. It is characterised by high tensile/flexural strength and high-energy absorption capacity (Karihaloo *et al.*, 2002). This chapter will focus on the behaviour of this class of material, as well as other HPFRCCs that have been presented to the industry so far.

2.2 HPFRCCs

Fibre reinforced cementitious composites (FRCs) can be classified into three groups. FRC employing low fibre volume fractions (< 1%) utilize the fibre for reducing shrinkage cracking (Balaguru and Shah, 1992). FRC with moderate fibre volume fractions (between 1% and 2%) exhibit improved mechanical properties including improved modulus of rupture (MOR), fracture toughness, and impact resistance. In the last decade, a third class of FRCs, generally labelled as high performance FRC, or simply HPFRCC, has been introduced. HPFRCC exhibits apparent strain-hardening behaviour by employing high fibre contents.

FRCs can be categorised into two classes according to their tensile response: conventional FRC and high performance FRC (HPFRCC). Conventional FRC exhibits an increase in ductility over that of plain concrete, whereas HPFRCCs exhibit a substantial strain-hardening response, leading to a large improvement in both strength and toughness compared with the plain concrete (Shah *et al.*, 1999).

HPFRCCs include materials such as SIFCON (Slurry Infiltrated Fibre Concrete), MDF (Macro Defect Free), ECC (Engineered Cementitious Composites), Fibre Reinforced DSP (Densified Small Particle Systems), CRC (Compact Reinforced Composite), RPC (Reactive Powder Concrete) and CARDIFRC®. These materials have been shown to develop outstanding combinations of strength and ductility, as well as long-term durability (Reinhardt, 1991; Karihaloo et al., 2001).

HPFRCCs can be designed systematically, based on the knowledge of how crack-like defects in the composite grow and on the influence of fibre bridging on the mode of composite failure. Fracture mechanics plays a significant role in the development of composite design strategy (Li, 1993).

2.2.1 The effect of high temperature curing conditions

Curing conditions and curing temperature influence the properties of hardened concrete. Neville (1995) reported that a rise in the curing temperature speeds up the chemical reactions of hydration and thus affects beneficially the early strength of concrete. Typically, the remarkable strength properties observed in HPFRCCs are obtained by curing at 90° C. For example, compressive strength of CARDIFRC® reaches up to 200 MPa when the specimens are cured at high temperature up to 90°C for only 7 days. At this temperature the microstructure of such materials changes leading to:

- A homogeneous and cohesive interface between CSH paste and the sand.
- A dense CSH matrix.
- A fibril CSH nanostructure.

Zanni *et al.* (1996) investigated the effect of heat treatment on the hydration of RPC. The investigations showed that silica fume consumption was highly dependent on heat treatment temperature and duration. Moreover, crushed quartz reactivity was also proved to be dependent on heat treatment and duration.

Heat treatment accelerates the hydration process, activates the pozzolanic reaction of silica fume and reduces the curing time of concrete. Karihaloo and de Vriese (1999)

showed that the curing time of RPC specimens could be reduced from 28 to 16 days when the specimens are cured under the following regime:

7 days	at	ambient temperature
3 days	at	90°C
7 days	at	ambient temperature

The curing time can be reduced further to seven days. Sullivan (1999) confirmed this by exposing RPC specimens to high temperature curing for the entire seven days at 90° C immediately after the moulds are stripped. Similarly, the strengths attained for CARDIFRC® specimens cured at 90° C for seven days have been found to be the equivalent of standard 28-day water curing at 20° C (Alaee, 2002).

2.2.2 The effect of silica fume

Silica fume is an extremely fine powder whose particles are about 100 times smaller than cement. The particles of such material pack tightly against the surface of the aggregate and fit in-between the cement particles, thus greatly improving packing. Neville (1995) reported that because the extremely fine particles of silica fume reduce the size and volume of voids near the surface of the aggregate, the so-called interface zone has improved properties with respect to microcracking and permeability. The bond between the aggregate and the cement paste is improved, allowing the aggregate to participate better in stress transfer.

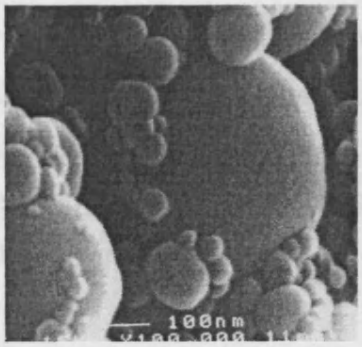

Figure 2.1: Microsilica Particles (concrete.elkem.com).

The main functions of silica fume in HPFRCCs as reported by Richard and Cheyrezy (1995) are:

- Filling the voids between the next larger size particles (cement).
- Enhancement of rheological characteristics by the lubrication effect resulting from the perfect spherical shape of the basic particles.

- Production of secondary hydrates by pozzolanic reaction with the lime resulting from primary hydration.

One of the main advantages of using silica fume particles (particle size 0.1-0.2 μm) with cement (particle size 5-10 μm) is to fill the spaces between the cement particles and thus to achieve a very dense packing system. Bache (1981) attributed these to the following: a) the silica particles are smaller than even the finest cement we can produce by grinding and are therefore more conducive to dense packing into the spaces between the cement particles, b) the silica particles, being formed by condensation from gas phase, are spherical in shape (unlike crushed cement particles, which are angular) and this makes the silica particles even more suitable for dense packing than very fine cement, and finally c) the particles are chemically less reactive than cement, which eliminates the problem of too rapid hardening encountered with very fine cement; in addition, the silica is likely to ensure the formation of a coherent structural skeleton between the cement particles, resulting in a fine dense microstructure.

The use of microsilica in HPFRCCs can improve the bond by increasing the contact area between the fibre and the surrounding matrix. The introduction of fine microsilica particles will increase the density of the matrix, filling any pore spaces around the fibre. The increase in the surface contact area increases the fibre pull-out force (Bache, 1981).

Another important property of microsilica is its pozzolanic behaviour. The material is extremely reactive, and hence can react with the surplus of calcium hydroxide, which in ordinary cement paste it will crystallize out as a separate and relatively weak phase. The reaction of microsilica with the remaining calcium hydroxide, from the primary cement water reaction, results in the production of an extra C-S-H. The chemical representation of this process is shown below:

Primary reaction: Cement + Water

$$2C_3S + 6H \rightarrow C_3S_2H_3 + 3Ca(OH)_2$$

$$(C\text{-}S\text{-}H) + [CH] \quad (2.1)$$

Secondary Reaction: Silica + Calcium Hydroxide + Water

$$S + CH + H \rightarrow C\text{-}S\text{-}H \quad (2.2)$$

The extra production of C-S-H results in a microstructure, which is very dense in the freshly mixed state and gets even denser during the succeeding hydration process. The effect of microsilica on the cement paste is shown in Figure 2.2.

(a) Cement paste (b) DSP paste

Figure 2.2: (a) Flocculated particles in ordinary cement paste. (b) Densely packed cement grains and microsilica in DSP paste.

2.2.3 The effect of dispersing agent (superplasticiser)

As mentioned earlier, the silica fume (SF) is a ground material and as such, generally increases the water demand for a given degree of workability at low water/cement ratio. Thus, a high range water-reducing admixture is often introduced to promote the workability. Neville (1995) reported that, superplasticisers are long and heavy molecules, which wrap themselves around the cement particles and give them a highly negative electrical charge so that they repel each other. This results in deflocculation and dispersion of the cement particles (Figure 2.3) and therefore, in high workability.

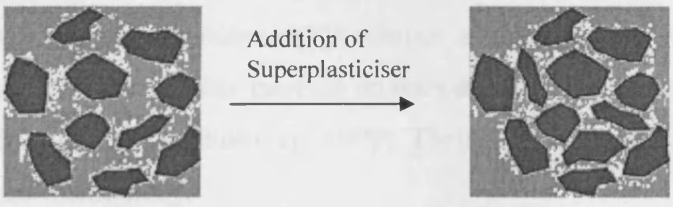

(a) Cement paste (b) Deflocculated cement paste

Figure 2.3: (a) Flocculated particles in cement paste. (b) Superplasticised cement particles.

Superplasticisers are added to the CARDIFRC® matrix in order to obtain a very workable mix at low water/cement ratio, thus achieving dense packing which results in high strength and durable concrete. One of the main difficulties of achieving such a system, as described by Bache (1987) is the presence of surface forces. These forces interlock neighbouring particles, consequently counteracting mutual particle movement during mixing and shaping. However, effective dispersing agents such as superplasticizers eliminate the locking effect of surface forces and it becomes possible to pack fine particle systems densely on the basis of purely geometrical principle.

The combination of superplasticisers with silica fume in the concrete mix results in high strength and/or high durability. Dugat et al. (1996) reported that by using superplasticisers with silica fume it was possible to reduce the water/cement ratio to less than 0.15. This helps reduce the total pore volume of the cement paste and the average diameter of the pores, hence improving durability. Moreover, experience with RPC, DSP and CARDIFRC® showed remarkable strength properties when superplasticisers and silica fume are incorporated in the original mix.

The amount of superplasticiser used in CARDIFRC® mixes is somewhat higher than that of the original RPC and DSP mixes. This improves the workability of the mixes.

2.2.4 The effect of steel fibres

The incorporation of fibres in the CARDIFRC® matrix increases the tensile load-carrying capacity and turns an otherwise brittle material into a very ductile one. Brass-coated steel fibres (diameter 0.16 mm, 6 mm or 13 mm long) are used to prevent corrosion. The use of long and short fibres was found necessary to improve the material properties whilst minimising loss of workability. The short fibres prevent microcrack growth and coalescence (Tjiptobroto and Hansen, 1993) and provide a high tensile strength. Long fibres provide increased ductility, greater pullout strength and will bridge longer cracks (Sullivan, 1999). Their disadvantage is that they have an adverse effect on workability.

2.2.4.1 Volume fraction of fibres

The volume fraction of fibres in concrete affects both the fresh and hardened state. Hoy and Bartos (1999) reported that when higher volumes of steel fibre are added to concrete, there is a more significant loss of workability and greater chance that fibres will interlock. For these reasons, there is an optimum fibre content for any given fibre-matrix combination. Higher fibre contents will produce mixes which lack homogeneity and have poor workability, while lower fibre contents will result in less efficient reinforcement. By a careful selection of mix proportions, the optimum fibre content can be increased with a resulting performance improvement.

Basically, as the volume fraction of fibre increases and as the fibres are more uniformly dispersed, the growth of microcracks is hindered, and the localisation of deformation is delayed with a consequent substantial increase in the tensile strength and strain capacities of the composite (Balaguru and Shah, 1992). Mobasher et al. (1990) carried out an experimental programme on the effect of fibre content on the fracture properties of concrete. They concluded that as the volume fraction of fibres increases the growth of microcracks was hindered through an arrest mechanism and the matrix fracture toughness was increased. The higher the volume fraction of fibres, the higher the peak load, and the higher the matrix contribution and the higher the acoustic emission (AE) rate. The higher AE event count means that there is a greater number of microcracks.

Karihaloo and de Vriese (1999) studied the effect of volume fraction of fibres on RPC mix. They found that increasing the volume fraction of steel fibres V_f led to major improvements in the properties of RPC, namely, specific fracture energy and indirect tensile strength. Furthermore, Shannag and Hansen (2000) showed that incorporating large volume fractions of short steel fibres (more than 2% by volume) in DSP composites results in a dramatic increase in matrix tensile strength (up to 100%).

2.2.4.2 Aspect ratio of fibre (*l/d*)

The physical shape of steel fibres is described by their aspect ratio (length/diameter). As a general rule, higher aspect ratio fibres perform better than lower aspect ones. Gopalaratnam and Shah (1986) found a monotonic increase in compressive strength

and ductility when the aspect ratio increased from 47 to 100. Sullivan (1999) also found that long fibres increased both the tensile strength and ductility of concrete. Karihaloo and de Vriese (1999) reported that an increase in fibre length – and consequently of aspect ratio -- seems to be more effective than an increment only in the volume fraction of fibres. The incorporation of long fibres (13 mm) in CARDIFRC® mixes was primarily for enhancing the ductility.

2.2.4.3 Bridging action of the fibres

Extensive research has shown that the most fundamental property of a fibre reinforced cementitious material is the fibre bridging across a matrix crack (Li, 1992b; Li *et al.*, 1991).

Incorporation of fibres in HPFRCCs is a vital factor for increasing the tensile strength of the composite and for improving its ductility (turns a brittle material into a very ductile one). When the composite is first loaded, the load-displacement response is approximately linear and the fibres act as a crack arrester, thus increasing the required energy for crack propagation. The response starts to become non-linear just before the matrix first crack. The region after the initiation of first crack is called the multiple cracking region in which the stress-strain curve deviates from linearity. The first crack strength depends primarily on the matrix properties and is only minimally dependent on the fibre parameters. As the load is further increased, some microcracks will emerge. These microcracks will be bridged by fibres. Very high shear stresses are developed between the fibres and the matrix where the fibres emerge from the crack face. The shear stress values attained depend on the difference on the elastic modulus between the fibres and the matrix and on the fibre volume fraction. This shear stress helps transfer some of the load to the fibres. According to Balaguru and Shah (1992) when the matrix cracks, the fibre transmits the load across the crack.

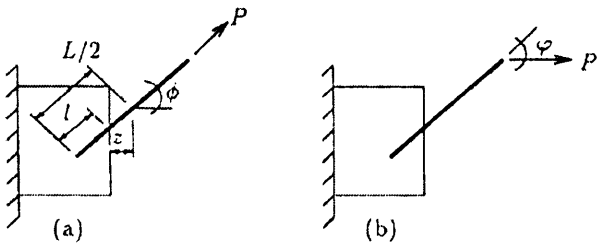

Figure 2.4: (a) A single fibre pull-out without snubbing ($\phi = 0$) and (b) with snubbing ($\phi \neq 0, \phi = \varphi$) (After Karihaloo and Wang, 2000).

Since fibres are randomly dispersed throughout the matrix, their orientations relative to the direction of the applied load are an important factor. In a matrix containing randomly distributed fibres, few fibres align in the direction of applied load; instead almost all fibres are oriented at different angles to the load direction (Figure 2.4). When a fibre is pulled out from the cementitious matrix, the snubbing friction at the fibre exit point can increase the pull-out resistance, and contribute to the overall composite action. Experimental observations showed that inclined fibres can sustain a greater load as they bend. This is known as dowel action. Naaman and Shah (1976) reported that after matrix cracking, the load and energy required to pull a steel fibre out from the matrix can be higher for fibres inclined to the load direction.

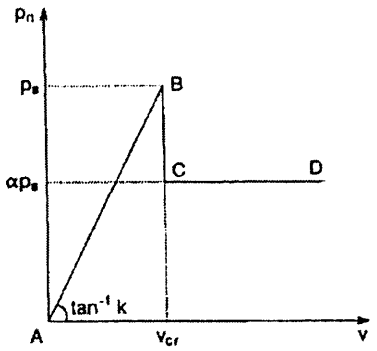

Figure 2.5: A linearised bridging law describing the relation between the bridging force and the crack opening displacement (After Karihaloo *et al.*, 1996).

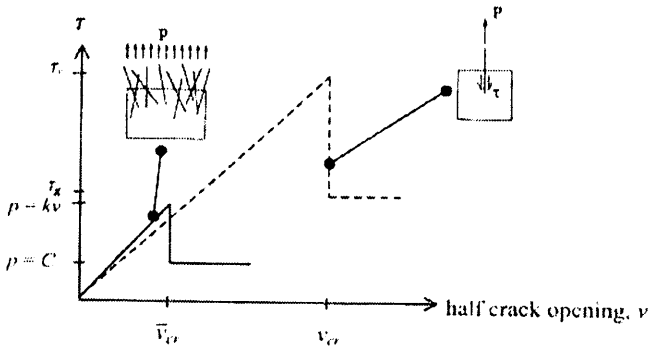

Figure 2.6: Idealised interfacial matrix-fibre shear stress (τ) vs. half crack mouth opening for single fibre (dashed line) and multiple fibre (solid line) pull-out (After Lange-Kornbak, 1997).

It is assumed that when the crack opening displacement reaches a critical value v_{cr} , some of the fibres bridging the crack will debond from the matrix, resulting in a sudden drop in the bridging force (BC), whereafter these fibres will exert a reduced closure force by frictional pull-out (CD) (Figure 2.5). This is based on single pull-out tests. From this single fibre relationship, the average closure force on crack faces bridged by many fibres is obtained through an approximation to the fibre distribution function (Figure 2.6). The slope of the elastic part of this averaged pullout diagram gives directly the parameter k in equation (2.4) below.

When the crack opening exceeds the critical value $\bar{v}_{cr}$, the bridging stress $p(v)=kv$ drops to the constant frictional pull-out value, the parameter C in equation (2.5) below.

The bridging stress for multiple fibre bridging is expressed in terms of single fibre properties $\tau_{v,}$ the adhesive bond strength of the fibre and the matrix, and τ_g the frictional pull-out strength of fibre. This is achieved by introducing the ratio:

$$\zeta = \frac{\bar{v}_{cr}}{v_{cr}} \tag{2.3}$$

where $\bar{v}_{cr}$ follows from the multiple crack model, since it is assumed that slip is initiated immediately after reaching the ultimate tensile load, whereby the corresponding maximum half opening of the crack equals $\bar{v}_{cr}$ (Lange-Kornback and Karihaloo, 1997).

The fibre bridging forces are:

$$p(v) \approx 2V_f \frac{\tau_v}{\tau_g} E_f \frac{h}{L} v \equiv kv \qquad v < \bar{v}_{cr} \tag{2.4}$$

$$p(v) \approx \frac{1}{2} V_f \tau_g \frac{L}{d} h \frac{\bar{v}_{cr}}{v_{cr}} \equiv C \qquad v \geq \bar{v}_{cr} \tag{2.5}$$

where V_f is the volume friction of fibre, L the length of the fibre, d the diameter of the fibre, k is the bridging stiffness and h is the snubbing factor, defined by Karihaloo and Wang (2000)

$$h = \frac{2}{(4+f^2)}(e^{f\pi/2} + 1) \tag{2.6}$$

where f is the snubbing friction coefficient between the fibre and matrix.

2.2.5 Constitutive model

A constitutive model describes the stress-strain behaviour of short fibre-reinforced cementitious composite in tension/flexure. The similarities and differences in the constitutive behaviour of two types of FRC (conventional FRC and high-performance FRC), as described by Karihaloo and Wang (2000), follow.

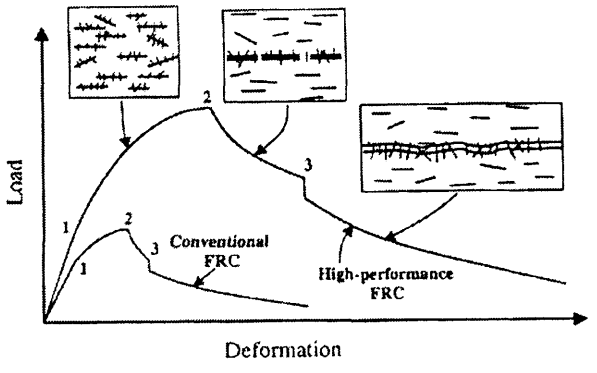

Figure 2.7: Complete pre- and post-peak tensile response of two short fibre-reinforced cementitious composites (After Karihaloo and Wang, 2000).

Figure 2.7 illustrates the load-deformation response of conventional and high performance FRC to tensile/flexural loading. As can be seen, the total tensile strain and load carrying capacity of HPFRCC are higher than for the conventional FRC, and

the amount of stored energy represented by the area under the curve in HPFRCC is much higher than that of conventional FRC. The deformation is generally expressed in terms of strain up to the peak load (point 2) and through crack opening displacement thereafter.

Both materials exhibit the following responses:

- Linear elastic behaviour up to 1.
- Strain hardening behaviour between 1 and 2.
- Tension softening due to localisation of damage in the form of unconnected macrocracks 2 and 3.
- Continued tension softening due to localisation of damage in the form of a through crack until complete rupture.

The complete constitutive relation will be briefly outlined next.

2.2.5.1 Linear elastic behaviour

As can be seen in Figure 2.7 both materials exhibit linear elastic behaviour up to point 1 at which the transition from linear elastic to strain hardening behaviour takes place. This transition point is only governed by the tensile strength of the matrix and is mostly unaffected by the fibre parameters (i.e. fibre aspect ratio, volume fraction and bond strength). Due to the fact that the HPFRCC contains no coarse aggregate it is extremely brittle, therefore the stress at transition point 1, is uniquely related to the fracture toughness of this brittle matrix:

$$K_{IC,m} = f(w/c, g, V_a) \tag{2.7}$$

where $K_{IC,m}$ is the fracture toughness of the matrix (where I denotes Mode I cracking), w/c is the water to cement ratio, g is the maximum size of aggregate and V_a is the volume fraction of fine aggregate. For the calculation of Young's modulus of fibre reinforced concrete Karihaloo and Lange-Kornbak (2001) used the following equation for a two-phase system based on the work of Nielsen (1992)

$$E = E_m \frac{n + \Theta + V\Theta(n-1)}{n + \Theta - V(n-1)} \tag{2.8}$$

where V is the volume fraction of discrete phase, Θ is the geometry function accounting for the configuration (aspect ratio) of the discrete phase and n is the ratio of the modulus of elasticity of the discrete phase to that of continuous phase E_m (i.e. of matrix). The Young modulus for HPFRCC mix can be obtained by applying equation (2.8) twice (Benson, 2003). First, to a two-phase system in which the continuous phase is the cement-silica binder paste and the discrete phase is the fine aggregate, and then to a system in which the cement-silica-fine aggregate mortar is the continuous phase and the fibres the discrete phase. The values of n, V, E_m and Θ are different in the two steps. A similar procedure will be used in Chapter 5 to follow the development of the Young modulus of CARDIFRC® with hydration.

2.2.5.2 Strain-hardening behaviour

As can be seen in Figure 2.7, the strain hardening region is located between points 1 and 2. This is known to be a result of the bridging action of fibres on microcracks which prevents their growth and coalescence. This region, which is inelastic strain region due to micro-cracking (also called multiple cracking region), is a unique property of HPFRCCs (Tjiptobroto and Hansen, 1993). Multiple cracking occurs in the bulk material, and no strain localisation occurs. The density of microcracks increases with increasing tensile/flexural loading until it reaches a saturation level (point 2). The extent of strain hardening is determined by the microstructure of the cementitious matrix, the volume fraction of fibres and the bond strength of the fibres.

The occurrence of multiple cracking was explained in an analytical approach developed by Tjiptobroto and Hansen (1993) assuming that the first crack is also the failure crack (observed from failure tests). If the energy needed to form new microcracks is smaller than the energy needed to open the first microcrack (i.e. the onset of failure) then multiple cracking takes place. The model predicts that the existence of a multiple cracking process depends on the fibre properties (fibre length and fibre diameter), interface and matrix properties (debonding energy, interface frictional stress, matrix strength, and water-cement ratio). Moreover, their analysis predicts that the major energy term determining the behaviour of multiple cracking is the fibre debonding energy.

Bridging of the multiple cracks by short fibres is a significant mechanism for increasing the strength and toughness of the composite and for preventing a sudden loss of the overall stiffness when the microcracks coalesce into large bands (Wang and Karihaloo, 2000). The role of fibres in the composite matrix was explained by Balaguru and Shah (1992) and Karihaloo et al. (1996).

When the matrix is loaded, part of the load is transferred to the fibres along its surface. As mentioned earlier due to the difference in stiffness of fibre and matrix, shear stresses develop along the surface of the fibre. This shear stress helps transfer some of the load to the fibre. When the matrix cracks, the fibre transmits the load across the crack. Fibres added to concrete arrest cracks and distribute imposed deformation into many microcracks.

These microcracks are arbitrarily oriented. Because of this, modelling of the constitutive behaviour of a material with microcracks is a difficult and complicated problem. One simplified way to model a microcracked solid from a fracture mechanics point of view is to assume that the cracks are arranged in a regular pattern, among which the simplest form is the doubly periodically arranged array (Karihaloo et al., 1996). Karihaloo et al. (1996) solved the problem of doubly periodic arrays of cracks when the cracks are free of traction and when they are subjected to a closure pressure by the fibres (equations (2.4) and (2.5)). They showed that the stiffness decreases in the strain hardening region between 1 and 2 according to the following formula:

$$\frac{E_y}{E} = \left[1 - \eta \frac{\omega}{\pi \Omega^2} \ln\left(\cos\frac{\pi}{2}\Omega\right)\right]^{-1} \tag{2.9}$$

where (Ey/E) is the normalised instantaneous modulus in the direction of loading, $\omega = a^2/(WH)$ is the crack density and $\Omega = 2a/W$. W and H are the horizontal and vertical crack spacings, respectively (Figure 2.8). The coefficient

$$\eta = \frac{1}{1 + \alpha + \beta} \tag{2.10}$$

and

$$\alpha = 4\sin^2\frac{\pi a}{W}e^{-2\frac{H}{W}\pi}\left[\frac{1}{1-e^{-2\frac{H}{W}\pi}}+\frac{2\frac{H}{W}\pi}{\left(1-e^{-2\frac{H}{W}\pi}\right)^2}\right] \tag{2.11}$$

$$\beta = -\frac{kW^2}{\pi aE}\ln\left(\cos\frac{\pi a}{W}\right) \tag{2.12}$$

Note that k is the bridging stiffness (equation 2.4) and for unbridged cracks $\beta = 0$.

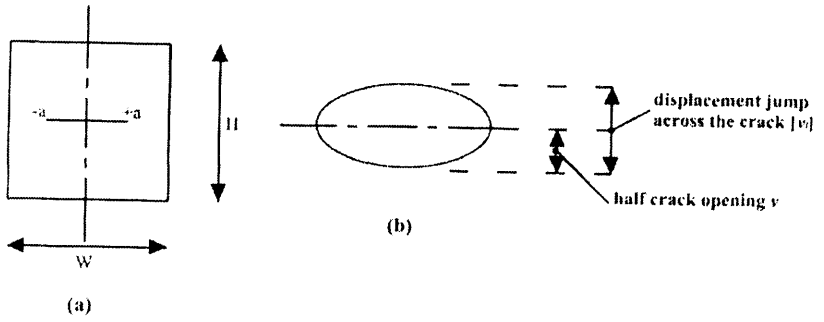

Figure 2.8: (a) Representative unit volume of the matrix containing one microcrack of length $2a$ (note that the volume V of this unit = $W*H*1$ and the surface area of the crack $S = 2a*1$); (b) an enlarged view of the crack opening (After Benson, 2003).

2.2.5.3 Tensile strength (f_t')

The uniaxial tensile strength of the composite f_t' is the effective stress at the onset of localisation of deformation along the eventual failure plane (i.e. point 2 in Figure 2.7). At this stage, the cracks in the localisation zone are still unconnected, so that the force is transmitted across the localisation zone partly by fibres (P_f) and partly by the unbroken matrix ligaments (P_b) (Karihaloo and Lange-Kornbak, 2001)

$$f_t' = \frac{P_b + P_f}{W^2} \tag{2.13}$$

where W is the centre-to-centre distance between the unconnected crack segments (Figure 2.8). The contribution of the unbroken matrix ligaments (P_b/W^2) and the

contribution P_f / W^2 to f_t' can be evaluated. Lange-Kornbak and Karihaloo (1997) have shown that the rigorous estimate of f_t' given by this method is very close to that given by the rule of mixtures.

$$f_t' = \beta_1 \frac{\eta K_{Ic,m}}{\sqrt{\pi a_0}}(1 - V_f) + \beta_2 \tau_v V_f \frac{L}{d} \tag{2.14}$$

where $\beta_1 \approx 1, \beta_2 \approx 0.5$, τ_v is the average bond stress at the fibre-matrix interface at the attainment of f_t'. L and d are the length and diameter of fibres, respectively, $K_{Ic,m}$ is the fracture toughness of the matrix (cement-microsilica binder), α_0 is the half-length of each crack segment in the array at peak load and $\eta(>1)$ is a factor that depends on the volume fraction and shape of the fine aggregate V_a.

2.2.5.4 Tension softening behaviour

The tension softening behaviour is due to localisation of damage in the form of unconnected crack fragments between points 2 and 3 (Figure 2.7). When the strain hardening capacity has been exhausted (i.e. the tensile/flexural strength of the composite has been reached), some of the fibres begin to debond from the matrix, resulting in the localisation of deformation along the eventual failure plane. The localisation manifests itself in the opening of cracks along this plane, but without their actual coalescence. The strain level away from this localised zone usually decreases first and then remains almost unchanged. The increased deformation is due to the progressive debonding of the fibre under decreased applied loading which results in the opening of fragmented cracks and their growth (region between 2 and 3).

The fraction of fibres that remains elastically bonded to the matrix progressively decreases from 2 to 3 until at 3 (Figure 2.7) all the fibres debond, resulting in an instantaneous drop in the residual load carrying capacity and in the coalescence of crack fragments to form a through crack. Thereafter, the residual tensile carrying capacity is determined entirely by the frictional contact between the fibres and the matrix until the fibres are completely pulled out of the matrix, and failure occurs.

The tension softening response of short-fibre-reinforced cementitious composites (SFRCC) which exhibit extensive matrix cracking was modelled by Karihaloo et al. (1996) and Li *et al.* (1991). Karihaloo et al. (1996) model is suitable to describe the initial softening behaviour (prior to coalescence of the cracks). It is akin to that used by Horii et al. (1989) and Ortiz (1988) for the tension-softening of un-reinforced quasi-brittle materials. However, it differs from that used by Li et al. (1991) who assumed that the localized damage has resulted in a through crack. Thus, this model is more appropriate for describing the extensive tail region of this response when the crack fragments have coalesced and their faces are held together by frictional forces only (Karihaloo *et al.*, 1996). The fragmented crack model of Karihaloo et al. (1996) (see below) and the through crack model of Li *et al.* (1991) were combined to yield the complete tension softening behaviour of fibre reinforced composites (Lange-Kornbak and Karihaloo, 1997).

Karihaloo *et al.* (1996) modelled the tension softening response of SFRCC using a collinear array (row) of cracks subjected to bilinear bridging forces. They proposed that the initial tension softening curve (i.e. point 2 to 3 in Figure 2.7) was the result of the growth of discontinuous crack fragments in the localisation zone into the unbroken material (Figure 2.9a). The fibres in this zone are progressively pulled out beginning from the centre of each crack where the opening is largest, so that the crack can grow towards its neighbours. Eventually, when the neighbouring cracks have linked up, a through crack forms which is under the action of the residual frictional fibre bridging force (Figure 2.9b). Finally, at point 3 in Figure 2.7 only a few fibres remain elastically bonded to the matrix, hence a sudden drop in the stress is anticipated when the crack fragments link up to form a through crack (Lang-Kornbak and Karihaloo, 1997).

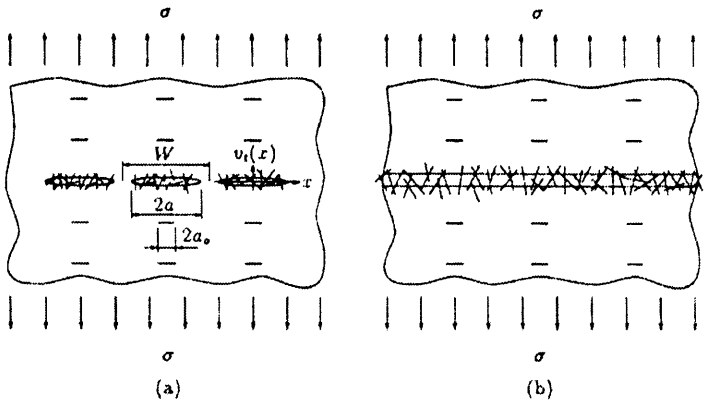

Figure 2.9: (a) Crack configuration prior to coalescence of cracks (b) after coalescence of cracks during tension softening of fibre-reinforced quasi-brittle materials (After Karihaloo and Wang, 2000).

2.2.6 Types of HPFRCC

2.2.6.1 Macro-Defect-Free cement (MDF)

The MDF cementitious materials (also called new inorganic materials, NIMs or chemically bonded ceramics, CBCs) are composites combining Portland or high-alumina cement with a water–soluble polymer of high molecular mass (e.g. polyvinyl alcohol, PVA, hydroxy-propyl methyl cellulose, HPMC). The latter acts as a rheological aid, reduces the inter-particle friction coefficient and reacts with the hydration products. It prevents flocculation of cement particles, increases the viscosity of the mix at low water to solids ratio, thus permitting the use of intensive-high shear mixing processes without inducing cavitation (Shah and Young, 1990).

The MDF pastes have very high tensile strength (150 MPa or more) particularly when mixed with alumina cement. They are prepared under high shear, by mixing inorganic cement with a water-soluble polymer in the presence of limited amounts of water. The final product has very high bend strength, greater than 200 MPa, together with a high modulus of elasticity and relatively high fracture energy. However, the material may display some drawbacks like a high sensitivity to water (Lewis and Kriven, 1993). Moreover, the use of fibres in MDF cements is restricted (only long fibres may be used).

2.2.6.2 Slurry Infiltrated Fibre Concrete (SIFCON)

It is a high performance fibre reinforced concrete with very high fibre content, up to 20 percent by volume depending on the type of fibres used and manufacturing method (Lankard and Newell, 1984).

The matrix of this material has no coarse aggregate but a high cementitious content; however, it may contain fine sand and additives such as fly ash, microsilica, and latex emulsion (Naaman, 1991). Furthermore, steel fibres are primary candidates for this type of material. Balaguru and Kendzulak (1986) have shown that in SIFCON the fibres are pre-placed in a mould to its full capacity and the corresponding fibre network is then infiltrated by cement-based slurry. The presence of fibres in SIFCON leads to an enhancement of ductility, as well as a reduction in crack width. The use of a SIFCON matrix in over-reinforced concrete beams can lead to ductility factors three to five times larger than control beams made from a plain concrete matrix (Naaman *et al.*, 1990). They also observed that the use of such materials helps reduce crack widths in the tensile zone at least by one order of magnitude, and contributes to the spread of the zone of plasticity in the compression zone prior to failure.

2.2.6.3 Engineered Cementitious Composites (ECC)

Engineered Cementitious Composites are high performance fibre-reinforced cement based composite materials designed with micromechanical principles. Micromechanical parameters associated with fibre, matrix and interface are combined to satisfy a pair of criteria, the first crack stress criterion and steady state cracking criterion to achieve the strain hardening behaviour (Li, 1993). ECC has a tensile strain capacity of up to 6% and exhibits pseudo-strain hardening behaviour accompanied by multiple cracking. It also has high ultimate tensile strength (5-10 MPa), modulus of rupture (8-25 MPa), fracture toughness (25-30 kJ/m^2) and compressive strength (up to 80 MPa) and strain (0.6%). Due to its superior properties, the ECC can be used as a durable repair material.

2.2.6.4 Reactive Powder Concrete (RPC)

Reactive Powder Concrete RPC has been developed by the Scientific Division of Bouygues, SA, an international construction company with headquarters at St Quentin

en Yvelines in France. The material is characterised by high silica fume content and very low water to cement ratio. It exhibits very high mechanical and durability properties (Richard and Cheyrezy 1994). Compared to conventional concrete, the ductility estimated in terms of fracture energy is increased by one to two orders of magnitude, while the compressive strength values are in the range of 200 to 800 MPa. As reported by Richard and Cheyrezy (1995) the development of RPC was based on the following principles:

- Elimination of coarse aggregate significantly improves the homogeneity of the mix
- Optimisation of the granular mixture. Microsilica improves the compacted density of the mix thereby reducing voids and defects.
- Incorporation of steel fibres results in a ductile material.
- Reduction of the water to cement ratio and inclusion of superplasticiser ensures a workable mix.

2.2.6.5 DSP cementitious materials

Densified cement ultra fine particle based materials DSP was developed by the Danish cement producer, Aalborg Portland-Cement. Production of this material is made possible by superplasticizers and silica fume to systems that can be densely packed in a low stress field and with very low water content (Bache, 1981). DSP belongs to a new class of materials formed from:

- Densely packed particles of a size ranging from 0.5 to 100μm,
- Homogeneously arranged ultra fine particles ranging in size from about 50Å to 0.5 μm and arranged in the spaces between the larger particles.

Dense packing of the particles (sand, cement and ultra-fine silica) together with fibres is essential for achieving the desired mechanical properties. It is also the prime feature of HPFRCCs materials. Materials such as DSP combine very densely packed cement particles (5-10μm) and ultra fine silica fume (0.1-0.2μm) filled the spaces between the

cement particles and, normally densely arranged fibres, Figure 2.1 (Bache, 1981; Bache, 1987).

Furthermore, the DSP matrix is a very strong and brittle material with a compressive strength of 150 MPa – 270 MPa. Due to its brittleness, it is difficult to utilize this material effectively without the incorporation of fine, strong and stiff fibres. The fibres improve the tensile properties of DSP based matrix, such as Densit®.

2.3 CARDIFRC®

Researchers at CARDIFF University (Karihaloo and de Vriese, 1999; Sullivan, 1998; Karihaloo *et al.*, 2000) have attempted to reproduce RPC and Densit® with materials widely used by the UK concrete industry. The mechanical properties were found to be inferior to those reported in the literature (Richard and Cheyrezy, 1995; Bache, 1981), and the workability of some mixes was poor. These attempts however provided valuable clues on how to improve the mixing and processing techniques in order to produce HPFRCCs similar to RPC and Densit® but whose mechanical performance even exceeds that of the original mixes. Another type of mix, a HPFRCC with 6 mm coarse aggregate, was also investigated (Benson, 1999). The workability of this mix was satisfactory but the mechanical properties were inferior to those achieved with mixes containing no coarse aggregate (i.e. Densit® and RPC) (Benson, 2003).

Further rheological studies were continued at Cardiff to optimise the HPFRCC. The aim was to achieve good workable mixes with a very low water/binder ratio and a high volume fraction of steel fibre, in order that the resulting concrete, in its hardened state, was very ductile with a relatively high tensile strength. This was achieved by using large amounts (up to 8 % by volume) of short steel fibres (6-13 mm long, 0.16 mm diameter) in a cementitious matrix densified by the use of silica fume. The matrix contains only very fine quartz sands (up to 2mm), instead of ordinary river sand and coarse aggregates. By optimising the grading of fine sands, the water demand is considerably reduced without affecting the workability of the mix.

As a result of many trial mixes and testing, the mixes shown in Table 2.1 are the optimised ones. Two different mixes (designated CARDIFRC®, Mix I and Mix II) of high-performance concrete differing mainly by the maximum size of quartz sand used in the mix have been developed using novel mixing procedures. These procedures are described in patent application GB 0109686.6.

CARDIFRC® differs in several respects from RPC and DSP mixes. First of all, are the two different types of fibres used in combination with the high volume fraction adopted. This rather innovative technique was found to be quite beneficial to the load deflection response of the matrix in terms of both strength and ductility. Investigations showed that the use of two grades of fine quartz sand (Table 2.1) substantially improved the performance of Mix I. Similarly, in Mix II in order to maximize the dry density of the mix three grades of fine quartz were used. This optimisation of grading of quartz sands used led to considerable reduction in the water demand without any loss in workability.

As claimed by Karihaloo et al. (2001) the produced material (CARDIFRC®) in its hardened state is characterised by very high compressive strength (in excess of 200 MPa), tensile/flexural strength (up to 30 MPa), high energy-absorption capacity (up to 20,000 J/m^2). Table 2.2 shows the material properties of CARDIFRC®.

Table 2.1: Mix proportions for optimised CARDIFRC® Mix I and Mix II (per m^3) (After Karihaloo *et al.*, 2001).

Constituents (kg)	**Mix I**	**Mix II**
Cement	855	744
Microsilica	214	178
Quartz sand:		
9-300μm	470	166
250-600μm	470	-
212-1000μm	-	335
1-2mm	-	672
Water	188	149
Superplasticiser	28	55
Fibres: - 6mm	390	351
- 13mm	78	117
Water/cement	0.22	0.20
Water/binder	0.18	0.16

Table 2.2: Typical material properties of CARDIFRC® Mix I and Mix II.

Material Properties	**Mix I**	**Mix II**
Indirect tensile strength (MPa)	28.6	21.4
Size Independent Specific Fracture Energy (J/m^2)	22,909	17,875
Compressive Strength (MPa)	207.0	185.0

2.3.1 Constitutive description of CARDIFRC®

As mentioned previously (Karihaloo *et al.*, 1996; Wang and Karihaloo, 2000; Karihaloo and Wang, 2000) the strain hardening of HPFRCC is due to the nucleation of microcracks under increased tensile/flexural stress. In the literature, assumptions have been made on their evolution but no experimental evidence is available to

validate them. An experimental programme was implemented on CARDIFRC® specimens to quantify the increase in the crack density ω (equation 2.9) as a function of applied tensile stress σ and fibre parameters (Benson, 2003). The results show that the fracture process zone is not due to one dominant crack but is due to many cracks. In support of this, parallel cracks, crack branching, cracks linking-up and multiple cracking were all observed and recorded. Moreover, as the active crack opens, evidence of fibre bridging was confirmed. It was also noted that not all cracks continued to propagate; some cracks became dormant since the failure plane will occur along the path of least resistance.

Numerical expressions have been fitted to the test data to describe the behaviour of CARDIFRC® in uniaxial tension. Figure 2.10 shows the three regions predicted by the equations. Laboratory test work shows clear evidence that the linear elastic region is larger than theoretically predicted (Karihaloo and Wang, 2000), a smaller strain hardening region with a distinct plateau at the peak load followed by a gradual decrease in the stress after the peak load.

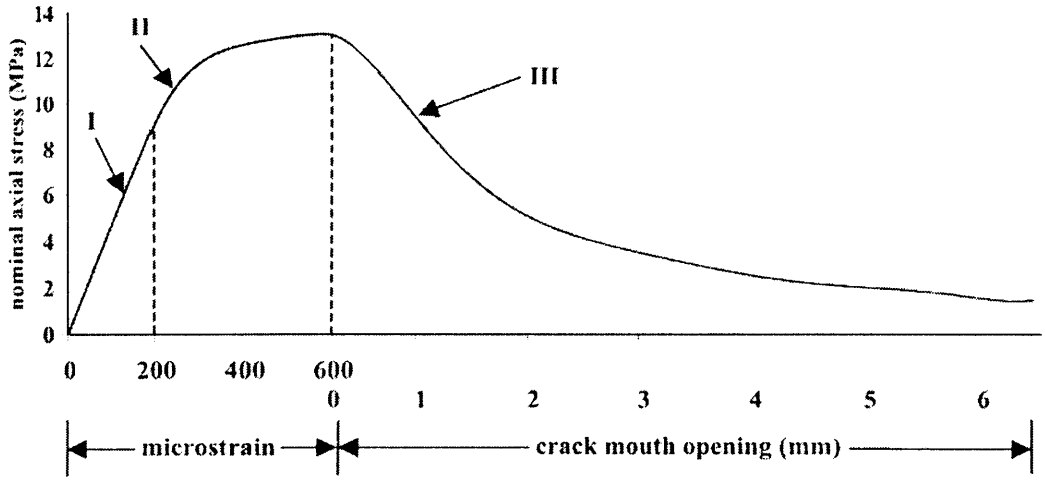

Figure 2.10: Complete pre- and post peak tensile curve for CARDIFRC®.

Stage I- Linear-elastic region

Applicable from 0 to 200 microstrain

$$\sigma_1 = 0.046\varepsilon \qquad (2.15)$$

Stage II- Strain hardening region

Applicable from 200 to 600 microstrain

$$\sigma = -4.34*10^{-10}\varepsilon^4 + 8.32*10^{-7}\varepsilon^3 - 6.03*10^{-4}\varepsilon^2 - 0.199\,\varepsilon - 12.62 \quad (2.16)$$

Stage III- Tension hardening region

Applicable from 0 to 6.5 mm

$$\sigma = 3.07*10^{-3}w^7 - 0.08\,w^6 + 0.82\,w^5 - 4.42\,w^4 + 12.80\,w^3 - 18.10\,w^2 + 5.73\,w + 12.89 \quad (2.17)$$

2.4 Conclusions

From the foregoing literature review, it is clear that HPFRCC materials have superior characteristics in terms of material properties. Their mechanical and fracture properties have been enhanced very substantially compared to other types of concrete. In fact, the brittleness of concrete is reduced by incorporating fibres. The influence of small amount of fibres is mostly apparent in the post-cracking response. However, improvements in other properties such as first cracking strength, tensile strain capacity, and peak load are insignificant. With the advent of special processing methods (novel mixing procedures) and the use of high volume fraction of steel fibre, concretes of high compressive, tensile strength as well as high energy absorption have been reported. The produced material (CARDIFRC®) is characterized by strain hardening (multiple-cracking) and followed by tension softening due to localization of cracks.

CARDIFRC® is a new kind of high performance fibre reinforced cementitious composite (HPFRCC). It is an exciting durable material with great potential. It has many potential applications. This material can be used for retrofitting (Alaee, 2002; Karihaloo *et al.*, 2002), for durable and reliable joining of pre-cast concrete elements, for the construction of structures for the containment and retention of hazardous materials and for the protection of valuable civilian and military assets, offshore and marine structures, overlays on ordinary concrete subjected to chemical attack, water and sewage pipes, etc.

Chapter 3: Microstructural Shrinkage Models

3.1 Introduction

By the term model we mean a mathematical description of a system without the need of any experimentation. Models in general can be divided into two main categories. The constitutive models and the simulation models. A constitutive model deals only with observed patterns. Mathematical equations can be derived to describe accurately these observed phenomena. The basis or the triggering mechanism behind the observed patterns cannot be identified directly. Therefore, in order to proceed with the modelling, a theoretical mechanism is considered. This assumed mechanism is the theoretical link between the *cause* and the *effect*. On the other hand, a simulation model incorporates two or more (existing and not theoretical) mechanisms together. In the case of cement-based materials the mechanism that connects the starting materials with the properties of the final product is the microstructure. Two very important parameters of the microstructure for shrinkage modelling are the pore volume and the surface tension.

Cement is one of many materials that depend on chemical reactions and associated changes in the microstructure for their effective use. The microstructure of cement involves a complexity of influencing factors including interparticle forces, kinetics of reactions, volume distributions of various phases and connectivity between these phases. The microstructure has a direct effect on cement properties such as rheology at early ages, permeability, strength, creep and shrinkage.

Ordinary Portland cement (OPC) is based on mineral oxides that undergo hydration when mixed with water. The initial product is a fluid which hardens with time to a solid material. The latter is known as cement paste and is a very porous multiphase material, having a relatively complex microstructure. The hydration product is termed calcium silicate hydrate (CSH). Defining the porosity of CSH as well as the size of the capillary pores has been a subject of great controversy since modelling began.

CSH is used as the matrix in the so-called cement-based materials. In other words having as basis the CSH and by adding various ingredients new materials are formed

Cement Paste + Sand ➔ Mortar
Mortar + Aggregate ➔ Concrete

All the added ingredients, such as sand, aggregate, microsilica, superplasticisers, fibres etc, modify the microstructure of cement-based materials and make the modelling a very complex and challenging task.

The ultimate goal of the microstructural modelling is to be able to predict the behaviour of a cement-based material throughout its service life. Moreover, models can be a useful design tool towards the optimisation of microstructure in order to minimise defects and to control properties affected by environmental conditions such as humidity.

3.2 Modelling microstructure and hydration

Concretes with low water to cement (*w/c*) ratios behave differently from ordinary concretes. These differences are mainly the result of different mix proportions and constituents used in such low *w/c* materials. The very low water to cement ratio results in a very dense microstructure, which develops relatively quickly. The addition of microfillers such as microsilica to the cement-based materials, leads to the development of a very fine pore system. This will provoke the self-desiccation of such a system and eventually will cause a pronounced volume reduction. This volume reduction originates not only from the change in the pore system itself, but also from the state of water in this pore system. Any changes in the state of the water will affect the vapour pressure and in turn the surface tension of the system (Koenders, 1997).

In the case of cement paste it is generally assumed that the pore diameters exhibit a continuous size distribution. The degree of hydration, the water to cement ratio, the temperature, the cement composition and the maximum particle size used are the factors that affect the pore volume and hence the porosity of cement paste. The term

pore volume is defined by the subtraction of the volume of the solid material from the initial paste volume. Porosity is, simply, the ratio between the pore volume and the initial paste volume. As the hydration proceeds, the pore structure of the system undergoes changes and so does the state of water in the pore system. At the point from which the microstructure will start to gain some strength, the volume reduction of the reaction products, compared to the initial constituents (cement, water) will cause a gradual emptying of the larger pores of the pore system. Vapour will fill the newly formed empty pores, whereas water will be adsorbed on the wall surface area of such pores. This process of the gradual emptying of the pores is defined as self-desiccation.

Self-desiccation of the system is strongly associated with the relative humidity, the degree of hydration and the changes in the effective surface energy followed by changes in the adsorption layer (Koenders, 1997). A relationship between the degree of hydration, the relative humidity, the pore structure and the changes in the effective surface energy, can be obtained from the thermodynamic equilibrium of the pore system. This will be further explained in Chapter 4.

3.3 Existing shrinkage models

3.3.1 Empirical models

The realistic prediction of volume changes is of crucial importance if the durability and long-time serviceability of concrete structures are to be achieved. Several prediction models have been shown to give good agreement with the bulk of the test data available in the literature. The vast majority of these models have been developed to predict volume changes under certain environmental conditions and under no mechanical loading. The accuracy of the models varies. Some models are based on the direct evaluation of experimental results, whereas some others are more sophisticated and try to take into account the mechanisms arising due to drying and wetting. Oldest models are based on the exponential curve to describe the phenomena associated with the volume changes. On the other hand, later models adopted the hyperbolic curve to approach the problem.

Engineers often want to represent test data using an empirical model based on simple mathematical expressions. With the correct model and calculus, one can determine important characteristics of the data, such as the rate of change anywhere on the curve (first derivative), the local minimum and maximum points of the function (zeros of the first derivative), and the area under the curve (integral). The goal of this empirical curve fitting is to find the parameter values that most closely match the test data. The models to which data are fitted depend on adjustable parameters.

To perform curve fitting, a function is defined, which depends on the parameters that measure the closeness between the test data and the assumed model. This function is then minimized to the smallest possible value with respect to the parameters. The parameter values that minimize the function are the best-fit values. In some cases, the parameters are the coefficients of the terms of the model, for example, if the model is a polynomial or a Gaussian function. In the simplest case, known as linear regression, a straight line is fitted to the data. In most engineering models, however, the function depends on the parameters in a nonlinear way.

Take the formula $Y = e^X$, in which X is the independent variable and Y is the dependent variable. In an experiment, one typically measures variable Y at a discrete set of values of variable X. In such a formula when the independent variable reaches infinity the dependent variable reaches infinity, as well. Such a curve is also known as an exponential growth curve (Figure 3.1a). There are also some variations of the above-mentioned formula, such as $Y= e^{-X}$, which is known as an exponential decay curve (Figure 3.1b).

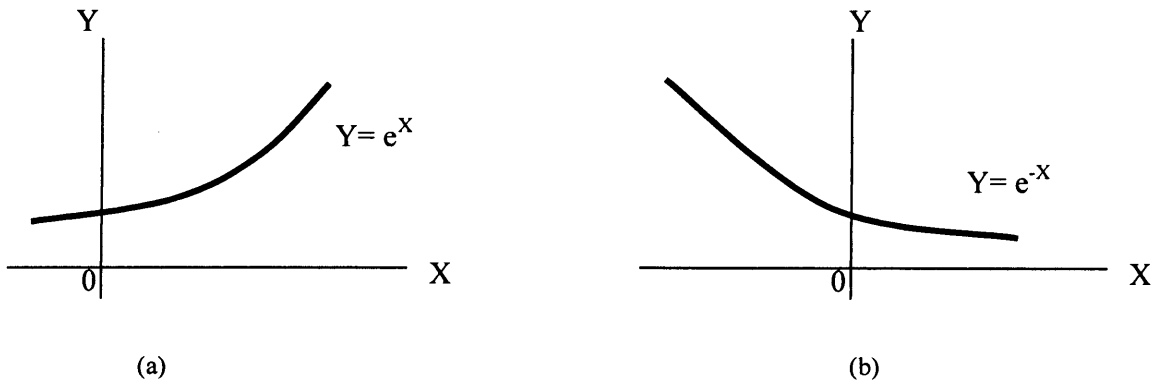

Figure 3.1: Exponential curves. (a) Growth curve, (b) Decay curve (Stroud and Booth, 2001).

Combination of the above mentioned exponential curves gives the hyperbolic curves of $Y = \cosh X = \frac{e^X + e^{-X}}{2}$ and $Y = \sinh X = \frac{e^X - e^{-X}}{2}$. Such an approach has been adopted in some recent empirical models, since it was considered to be more accurate.

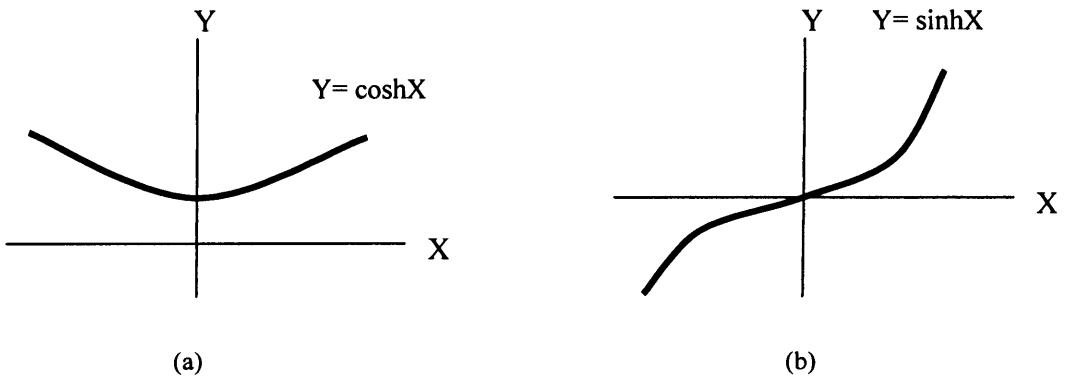

Figure 3.2: Hyperbolic curves. (a) coshX, (b) sinhX (Stroud and Booth, 2001).

Some of the most important existing empirical models are presented next.

3.3.1.1 Bazant – Panula Model (BP)

The basic form of the BP model presents some empirical equations which help towards the prediction of shrinkage strains in concrete. According to the developers of the model, shrinkage can be estimated from the composition of concrete, its strength, conditions of the environment, size and shape of the specimen (Bazant and Wittmann, 1982). The BP-model equations are:

$$\varepsilon_{sh}(t,t_0) = \varepsilon_{sh\infty} K_h S(t') \tag{3.1}$$

$$S(t') = \sqrt{\frac{t'}{t' + \tau_{sh}}} \tag{3.2}$$

$$K_h = 1\text{-}h^3 \quad \text{(For } h \leq 0.98\text{)} \tag{3.3}$$

$$K_h = -0.2 \qquad \text{(For h=1.0)} \tag{3.4}$$

$$\tau_{sh} = 600\left(\frac{k_s}{150}D\right)^2 \frac{10}{C_1(t_0)} \tag{3.5}$$

where ε_{sh} represents the shrinkage strain, t is time (in days) representing the age of concrete, t_0 is the age when drying starts, t′ ($t'=t-t_0$) is the duration of drying, $\varepsilon_{sh\infty}$ represents the ultimate shrinkage strain, K_h is a factor depending on the relative humidity, h represents the relative humidity, τ_{sh} is a factor depending on the effective thickness of the cross section D, k_s is a shape factor (ranging between 1.0 and 1.55), $C_1(t_0)$ is the drying diffusivity when the drying starts at t_0.

There were some further developments on the original BP model, which was proposed in 1978. The later models have been designated as BP-Model II (1980), in which there were slight changes in some functions including τ_{sh}, BP-New Model (1982), which was the same as BP-Model II but included some modifications for the shape factors k_s, BP-KX Model (1991), which was an update of all the previous BP models. The update was possible due to collection of more experimental data and at the same time the improvement in the knowledge of physical concepts and mechanisms behind the time-dependent deformations. The final version of the BP model is the Simplified BP-KX Model (1992), which is conceptually exactly the same as the previous update, but the equations used are given in a much simpler form.

3.3.1.2 CEB-FIP Model

The model for shrinkage that is given by CEB-FIP: 1990 is used to predict the mean behaviour of a concrete cross-section. Unless special provisions are given, the model is valid for ordinary structural concrete, subjected to a compressive stress not exceeding $0.4\ f_{cm}(t_0)$ at an age of loading t_o, mean relative humidity in the range of 40 to 100%, and mean temperature between 5°C and 30°C. It is considered that the scope of the model also extends to concrete in tension (CEB – FIP, Model Code '90, 1990).

The total shrinkage or swelling strains may be calculated from:

$$\varepsilon_{cs}(t, t_s) = \varepsilon_{cso} \cdot \beta_s(t - t_s) \quad (3.6)$$

where ε_{cso} represents the notional shrinkage coefficient, β_s is a coefficient to describe the development of shrinkage with time, t represents the age of concrete (days), t_s is the age of concrete (days) at the beginning of shrinkage or swelling. Equation (3.6) is similar to the one suggested by the BP Model (equation 3.1).

3.3.1.3 B3 Model

The prediction of the material parameters of the present model is restricted to Portland cement concretes. Formulae predicting model parameters from the composition of concrete have not been developed for special concretes containing admixtures, pozzolans, microsilica and fibres. However, if the model parameters are not predicted from concrete composition and strength but are calibrated by experimental data, the model can also be applied, for example, to high strength concretes, fibre-reinforced concretes and mortars. The present prediction model is restricted to the service stress range for which creep is assumed to be linearly dependent on stress. Generalisation to a multi-axial stress state can be based on the principle of superposition (RILEM TC 107, 1995).

The model suggests that the parameters of shrinkage – as well as those for creep - must be considered as statistical variables. Thus to take into account statistical uncertainties, the model suggests uncertainty factors for creep and shrinkage. At present the only way to reduce the uncertainty in the prediction of shrinkage of concrete is to conduct short-time tests and use them to update the values of the material parameters used in the model. This approach is particularly effective for creep but is more difficult for shrinkage. Although more intensive studies are needed, the authors of the model suggest five levels of sensitivity, based on general experience (RILEM TC 107, 1995).

According to B3 model the average shrinkage due to drying can be calculated using the following formulae:

$$\varepsilon_{sh}(t,t_0) = -k_h \varepsilon_{sh\infty} \tanh[\frac{(t-t_0)}{\tau_{sh}}]^{1/2} \quad (3.7)$$

where $$\tau_{sh} = k_t (k_s D)^2 \quad (3.8)$$

where k_h is the humidity factor, $\varepsilon_{sh\infty}$ is the ultimate shrinkage strain, k_s is the shape factor, considered 1 for simplified analysis sometimes, D is the effective cross section thickness and k_t is the correction factor. An objection often raised with regards to the adoption of Model B3 is that the evaluation by hand is a very tedious, time consuming process.

3.3.1.4 ACI Model

According to ACI 209R-82 the development of shrinkage with the time can be predicted by the following equation (Neville, 1995):

$$\varepsilon_{sh}(t) = \frac{t}{35+t} \varepsilon_{sh\infty} \quad (3.9)$$

where $\varepsilon_{sh}(t)$ represents the shrinkage strain after t days since the start of drying, $\varepsilon_{sh\infty}$ represents the ultimate shrinkage strain and t is the time in days since the start of drying. Prediction of the development of shrinkage by the above formula is subject to considerable variability, however the equation can be used to estimate the ultimate shrinkage strain of a wide range of moist-cured concretes. From equation (3.9) it can be seen that one half of the ultimate shrinkage is expected to occur after 35 days of drying. In the case of steam-cured concretes, the value of 35 in the denominator is replaced by 55 and time t starts from the end of steam curing (Neville, 1999).

The value of the ultimate shrinkage can be obtained by experiments for any particular concrete or alternatively can be taken from the ACI recommendation tables ($\varepsilon_{sh\infty}$= -780x10^{-6}). For any non-standard conditions, the ultimate shrinkage strain can be evaluated by the following equation:

$$\varepsilon_{sh\infty} = -780 \times 10^{-6} K_{cp} K_h K_s K_f K_c K_A K_H \quad (3.10)$$

where K_{cp}, K_h, K_s, K_f, K_c, K_A and K_H are correction factors for curing period, member size in terms of volume/surface, slump value, fine aggregate/total aggregate ratio, cement content, air content and ambient relative humidity, respectively.

3.3.1.5 Gardner & Zhao Model (GZ)

Based upon a survey of published experimental data, equations were developed to calculate the modulus of elasticity, shrinkage, and creep coefficient in terms of concrete strength. Most design codes use the concept of an ultimate shrinkage or ultimate creep coefficient. The GZ Model does not use the concept of an ultimate value of shrinkage, but accepts that the latter increases indefinitely with time (Gardner and Zhao, 1993).

The following equation was developed to calculate the shrinkage at time t, from the concrete shrinkage at 40 percent relative humidity.

$$\varepsilon_{sh} = \varepsilon_{shu}\,\beta(h)\,\beta(t) \tag{3.11}$$

In the above equation each of the variables ε_{shu}, $\beta(h)$ and $\beta(t)$ are given by separate formulae

$$\varepsilon_{sh} = 900 \times K \times \left(\frac{f'_{cm28}}{f'_{cmtc}}\right)^{1/2} \times \left(\frac{25}{f'_{cm28}}\right)^{1/2} \times 10^{-6} \tag{3.12}$$

$$\beta(t) = \left[\frac{7.27 + \ln(t - t_c)}{17.18}\right] * \left(\frac{t - t_c}{t - t_c + 0.0125 \times (V/S)^2}\right) \tag{3.13}$$

and $\beta(h) = (1-h^4)$ for $h<0.99$ (3.14)

$\beta(h) = -0.20$ for $h = 1.00$ (3.15)

where t is the age of concrete in days, t_c represents the age at which drying commenced in days, h represents the relative humidity expressed as a decimal number, f'_{cm28} represents the concrete mean compressive strength at 28 days (MPa), f'_{cmtc} is the concrete mean compressive strength when drying commenced (MPa), V/S represents

the volume to surface ratio of the member and K is a factor dependent on the cement type used in the mix.

The concrete mean compressive strength when drying commenced was calculated according to the formula suggested by Zhao (Gardner and Zhao, 1993) and is similar to that recommended by ACI 209-82:

$$f'_{cmt} = f'_{cm28}\,[t^{3/4}/(4 + 0.85t^{3/4})] \qquad (3.16)$$

3.3.1.6 BS 5400: Part 4: 1990

The treatment of creep and shrinkage in BS 5400: Part 4: 1990 is identical to that recommended by CEB-FIP: 1970, for the design and construction of concrete structures. The creep and shrinkage data are valid only for Portland cement concretes of normal quality, and BS5400 recommends that such data should form a working basis for assessing the effects of shrinkage on structural concrete. The effect of shrinkage depends on the inherent shrinkage of the concrete, on the size of the members, and on the amount and distribution of reinforcement (BS 5400: Part 4: 1990).

The shrinkage deformation, $\Delta\Delta_{cs}$, at any instant may be determined as the product of four partial coefficients:

$$\Delta\,\Delta_{cs} = k_L . k_C . k_e . k_j \qquad (3.17)$$

where k_L is a factor depending on the environment, k_C, depends on the composition of concrete, k_e, depends on the effective thickness of the member and, k_j defines the development of shrinkage as a function of time. The average values of the coefficients k_L, k_C, k_e, and k_j as functions of the parameters that define them, may be taken from diagrams, which are valid only for concretes that have been protected from excessive losses of moisture in their early days (BS 5400: Part 4: 1990).

3.3.1.7 Powers Model

The microstructure of cement-based materials was first represented and described by the Powers model. Besides being one of the few coherent models based on the physical properties of cement paste, it is also used to obtain the volumetric composition of hardened cement paste. The model yields estimates in good agreement with experimentally determined values of capillary and gel porosity in cement pastes, as reported in literature (Jennings *et al.*, 1996). Powers model assumes that the cement paste is comprised of three phases namely, the unreacted cement, the hydration product and the capillary pores. Powers defined two types of pores; the capillary and the gel pores. Gel pores are the pores within CSH whereas capillary pores are the pores that remain as the product expands into the original water-filled space. This distinction of pores has proven to be important and useful.

The volume of pores in the matrix has been associated with the degree of hydration (α) and the original water to cement ratio (w_0/c) (Table 3.1) and the whole process of the Powers model is summarised in the flowchart shown in Figure 3.3. However, there are some limitations of the Powers model. Individual solid products such as CSH and CH are not considered. The model does not account for the composition of the starting cement, which influences the type of products formed. Furthermore, it is believed that the model is not valid for pastes cured at high temperatures or when certain admixtures are used.

Table 3.1: Formulae for the calculation of the fractional pore volumes as given by Powers model (Jennings *et al.*, 1996).

Fractional Volume	Formula
Cement Gel	$\frac{0.68\alpha}{(w_0/c)+0.32}$
Gel Pores	$\frac{0.19\alpha}{(w_0/c)+0.32}$
Capillary Pores	$\frac{(w_0/c)-0.36\alpha}{(w_0/c)+0.32}$
Unhydrated Cement	$\frac{0.32(1-\alpha)}{(w_0/c)+0.32}$
Total Pores	$\frac{(w_0/c)-0.17\alpha}{(w_0/c)+0.32}$
Empty Capillary Pores	$\frac{0.0575\alpha}{(w_0/c)+0.32}$

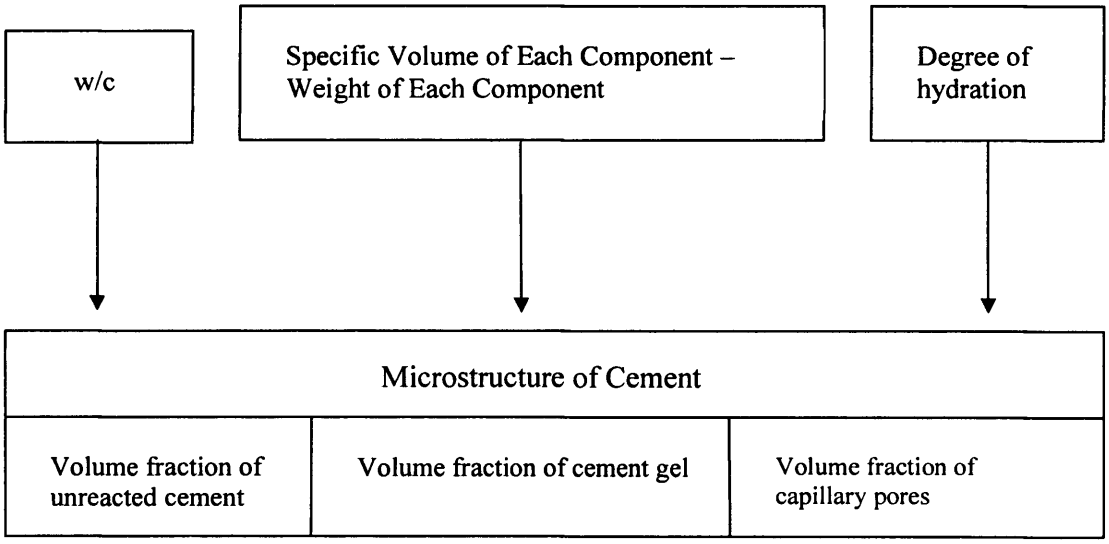

Figure 3.3: Flowchart describing the processes in the Powers model (Jennings *et al.*, 1996).

3.3.1.8 Parrott's Model

Parrott's model is a mathematical model of cement microstructure. Parrott was one of the first to develop a true computer model as a basis for predicting the engineering properties of cement in association with hydration reactions and reaction products.

This model is not a fundamental model, since there is no direct representation of microstructure at the cement particle level, and moreover properties are not exactly calculated from a numerical representation of microstructure (Garboczi and Bentz, 1992).

The progress of hydration is estimated through an iterative series of calculations, each of which evaluates the rate of hydration of one compound. Using the obtained rates, the outputs of the model are generated which include the degree of hydration of cement, the bound water content as a function of relative humidity and the heat evolved (Jennings *et al.*, 1996). Once the degree of hydration is determined, the calculation of volumes of phases is achieved using the stoichiometry of the reactions. One of the key aspects of the Parrott model is the relatively detailed relationship between microstructure and engineering properties. Properties are predicted, mainly as a function of porosity, using empirical relations that summarise experimental knowledge, and not by direct calculation. Porosity is perhaps the most important feature of the microstructure, playing a dominant role in controlling properties such as the compressive strength, elasticity, shrinkage and permeability. Total porosity is obtained by subtracting the solid volume of the anhydrous and hydrated phases from the original volume. The volume of CSH is used to estimate the corresponding volumes of small diameter pores. The large diameter porosity is then the difference between the total porosity and the small diameter porosity. Despite the fact that many properties are dependent on the distribution of pores, the model uses many variables and bases most of its predictions on volumes (Jennings *et al.*, 1996). Regardless of some drawbacks, Parrotts's model has proved to be a very powerful model which not only predicts the engineering properties but also includes the cost in the output values.

3.3.1.9 Tazawa and Miyazawa Model

Prediction of autogenous shrinkage strains with the help of empirical equations is not very common in literature, unlike the prediction of drying shrinkage strains. Autogenous shrinkage is affected by a number of factors such as water to cement ratio, type and content of admixtures and type of cement. A very small number of empirical equations have been developed taking all of these factors into account. Tazawa and

Miyazawa (Tazawa, 1999) proposed an empirical equation for the calculation of the autogenous shrinkage strains. The equation (equation 3.18) consists of the rate and ultimate value of autogenous shrinkage strain as a function of water to binder ratio and a coefficient to express the effects of different types of cement and mineral admixtures.

$$\varepsilon_c(t) = \gamma \cdot \varepsilon_\infty \left[1 - \exp\left\{-a(t - t_s)^b\right\}\right] \tag{3.18}$$

$$\varepsilon_\infty = 3070 \exp[-7.2(w/b)] \tag{3.19}$$

where $\varepsilon_c(t)$ is the autogenous shrinkage strain of concrete, γ is a coefficient representing the influence of the cement and admixtures type, ε_∞ is the final value of the autogenous shrinkage strain, t_0 is the initial setting time in days, t is the age in days, a and b are constants, w/b represents the water to binder ratio. Table 3.2 shows the different values of γ according to the cement type and admixture used.

Table 3.2: Variation of coefficient γ for different admixtures (OP: ordinary Portland cement; BS: blast-furnace slag; SF: silica fume; BC: belite-rich cement) (Tazawa, 1999).

Type of binder	w/b	Coefficient γ
OP + BS	0.25	0.53
OP		0.39
OP + SF		0.54
BC	0.30	0.41

3.3.2 Image based and digital models

The introduction of "single particle" models had been considered as a "boost" for the development of the several types of numerical models to simulate hardening process of cement-based materials. The "single particle" model as proposed by Jander describes the hydration of one single cement particle. Hydration products will be formed at the surface of the hydrating cement particle (Koenders, 1997).

In the category of "single particle" models, the model as proposed by Pommersheim appears to be the most advanced. The model is derived for the hydration of the tri-calcium silicate (C_3S) (Koenders, 1997).

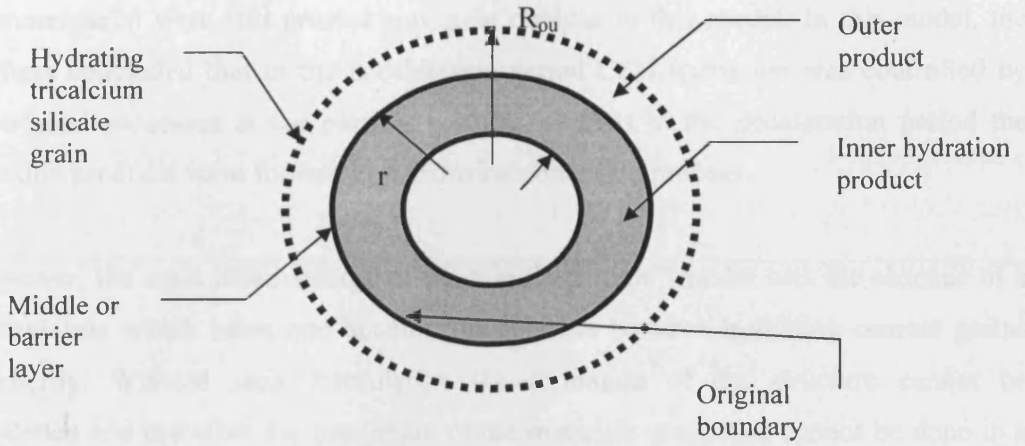

Figure 3.4: Model for hydration of tricalcium silicate according to Pommersheim.

In this model, distinction is made between different types of hydration products. The so called "outer product" is assumed to grow from the original surface of the cement grain in outward direction. The "inner product" is considered to grow from the original cement grain surface towards the centre of the particle. With the term "middle layer" is designated the layer that separates the inner and the outer product layers. The middle layer is assumed to dissolve gradually during hydration. The inner and outer products are characterised by different densities and therefore different diffusion properties.

The rate of hydration process can be determined with various numerical techniques and is considered to be independent of the position of individual particles in the system. Pommersheim concluded at first that before the formation of any middle layer has occurred, the combined effects of the chemical reactions at the particle surface and diffusion in the initially thin inner hydrate dominated the rate of hydration (Breugel, 1991). During the induction period and the beginning of the acceleration period the resistance of the middle layer becomes predominant. In later stages the

dominant resistance turns into diffusion through the outer hydrate layer as mentioned earlier.

Further research by Pommersheim and Brown (Brown *et al.*, 1985) has led to a more detailed model for C_3S hydration. The key aspects of the earlier model developed by Pommersheim were still present and quite obvious in this model. In this model, the authors concluded that in the acceleration period CSH formation was controlled by interfacial processes at the particle surface, whereas in the deceleration period the reaction products were formed in a diffusion controlled process.

However, the main disadvantage of the "single particle" model was the absence of a formulation which takes into account the contacts between hydrating cement grains explicitly. Without such formulation the formation of the structure cannot be modelled and therefore the prediction of the materials properties cannot be done in a reliable way. It was Jennings, as we are going to see in a following section, who proposed a model to quantify the interparticle contacts between hydrating cement grains. More models that include the formation of a microstructure have also been developed.

3.3.2.1 NIST Model

The most advanced model of the hydration of cement based materials is a digital image model developed by the National Institute of Standardisation and Technology (NIST) in Washington, USA (Bentz and Garboczi, 1991). The model is an early attempt to simulate the process of hydration of C_3S and associated development of microstructure. This process is simulated using a computer algorithm that cyclically "reacts" small volumes of C_3S and forms the appropriate volumes of CSH and CH. The result is a schematic microstructure containing information about the volume fractions and positions of each phase, namely the C_3S, water, CH and CSH. In order for this analysis to take place, the model develops a digital image of the cement paste. This image is subdivided into elements which are represented by pixels.

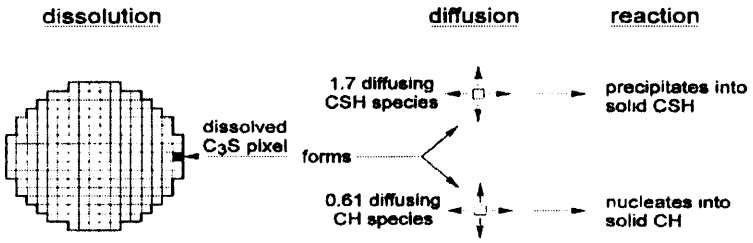

Figure 3.5: The main layout of the NIST model (Bentz and Garboczi, 1991).

Each pixel is assumed to have a volume of $1\mu m^3$ and considered to store information about the position in the system as well as the chemical composition each time. Pixels situated at the borders of the cement grain are considered to come into solution and therefore are able to react chemically with other hydration products. The reaction products, which are formed, will precipitate on a cement grain surface. This process is driven randomly. The process begins by placing spheres with a predetermined size distribution in a specified volume of water. The water to cement ratio chosen by the user determines the number of spheres and the volume. As long as all spheres have been placed without any overlap, hydration starts. The first step in the hydration process is the reduction of the diameter of the smallest sphere by a very small increment. The corresponding volumes of products, determined by the stoichiometric equations, and densities are then added. Some CSH is placed in the space created by the removal of C_3S. The rest of the products expand around the particle. This sequence is repeated on each sphere, consequently completing one hydration cycle. The data obtained for the volume fractions of each phase are stored in a data file and then another cycle begins. This cyclic hydration process will stop either when a certain number of cycles have been reached or until a desired degree of hydration is attained. The collected data on the locations and the amounts of various phases is compiled in numeric and schematic forms. Numeric output includes diagrams and summarised tables whereas graphic output shows a slice through the volume with different symbols and colours representing the phases (Figure 3.6).

The main advantage of this form of modelling is that a unique microstructure is created for each set of variables entered by the user. This kind of simulation for the hydration is a rough reproduction of how actual hydration is believed to occur.

Moreover, the NIST model proved to be a relatively good model since the parameters involved in the hydration of cement can be investigated with high accuracy; besides, it can provide the user with valuable information about the volume fractions and the distributions of various phases. Furthermore, it gives a clear idea of the development of the pore structure within the continuously hardening microstructure. The developers of the model (Bentz and Garboczi) have created an algorithm that consists of four major subroutines. These subroutines are defined as the initiation, the dissolution, the diffusion and the nucleation (Jennings *et al.*, 1996). The flowchart of the NIST model is shown in Figure 3.7.

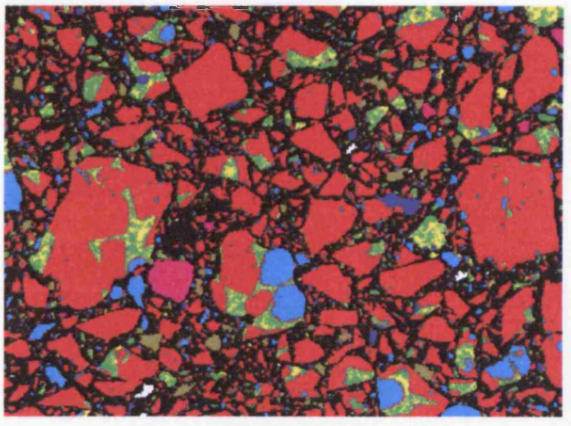

Figure 3.6: Two-dimensional graphic image of a Type I Portland Cement as reproduced by NIST model. Colour assignments are: red- C_3S, aqua- C_2S, green- C_3A, yellow- C_4AF, pale green- gypsum, white- free lime (CaO), purple- K_2SO_4, light magenta- periclase (magnesium containing phase), black- porosity (Bentz, 2000).

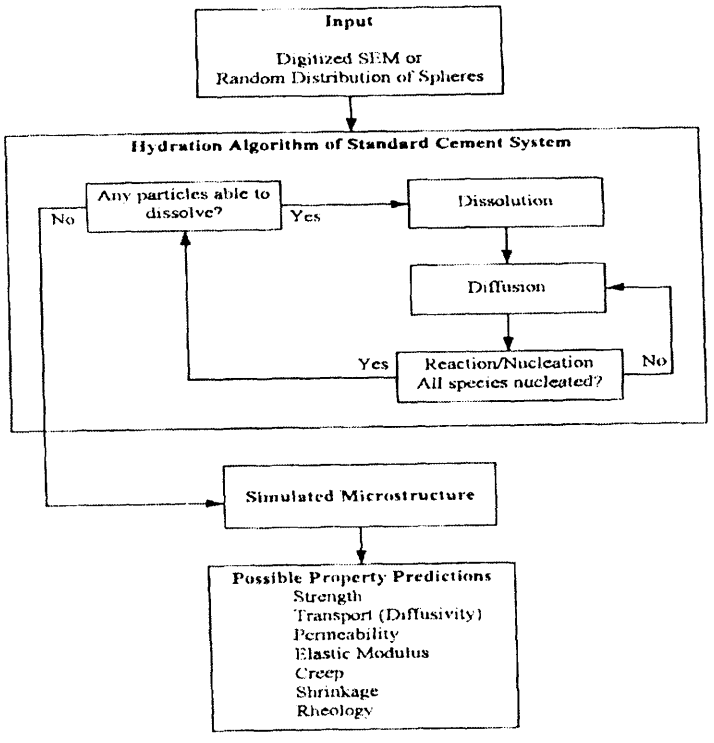

Figure 3.7: Flowchart of the NIST pixel model (Jennings *et al.*, 1996).

The concept of such a powerful model is impressive, however the actual implementation is more complicated. The microstructure created by this model is based on spheres of anhydrous material that remain spherical after hydration. Actual C_3S particles are not spherical and their surfaces do not necessarily react uniformly. The model may predict some properties with high accuracy because these properties are independent of such details as particle shape. The main problem is that defining the spatial distribution of all relevant phases is difficult to manage mathematical problem and only the simplest microstructures can be simulated. Furthermore, it has been observed that the NIST model is valid up to certain values of water to cement ratios. For cements with very low water content ($w/c<0.25$) it was proved to give invalid results regarding the formation of the hydrating microstructure and the corresponding properties. Another defect of this model is that in order to have a reliable result a large number of pixels is required. The large number of pixels is associated with an enormous consumption of Central Processing Unit (CPU)-time needed for a single calculation. This in turn simply means that a very large storage

memory is needed. However, the NIST model is considered to be a very useful tool towards the modelling of the hydration of cement based materials.

3.3.2.2 Jennings and Johnson Model

This mathematical model was developed by Jennings and Johnson (Jennings *et al.*, 1996) (Garboczi and Bentz, 1992) in order to simulate the hydration process and the development of microstructure in the cement based materials. The model simulates the development of microstructure during the hydration of cement (C_3S). The initial state of the model is formed by randomly distributed cement particles. These cement particles are represented as expanding spheres while hydration takes place (Figure 3.8). At the contact zone where two hydrating cement grains meet, the overlapping volume of hydration products is smeared out around the outer shells of two touching cement particles. The formation of these types of interparticle contacts represents the development of the microstructure. This process is simulated by using a computer algorithm that cyclically deals with small volumes of cement and produces the corresponding volumes of calcium silicate hydrate (CSH) and calcium hyrdoxide (CH) (Koenders, 1997).

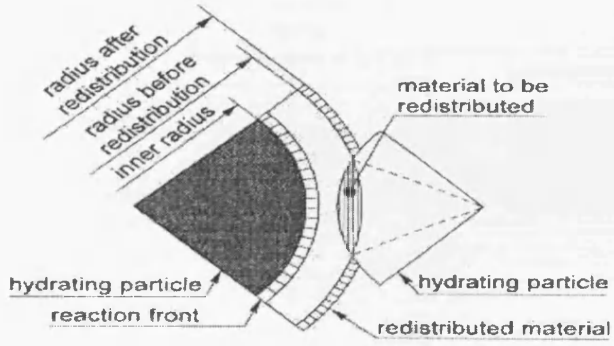

Figure 3.8: Schematical representation of the Jennings and Johnson model (Koenders, 1997).

The result of the model is a schematic microstructure containing information about the volume fractions and the position of each phase in the system. Mathematical operations can be done upon the formed microstructure in order to simulate some processes such as shrinkage. The main advantage of this model is that a unique

microstructure is created using different set of variables each time. Furthermore, the model has the potential to predict the development of the microstructure and the bulk properties for a wide range of hardening conditions.

On the other hand, the main disadvantage of the Jennings and Johnson model is that the mathematical representation of each phase (C_3S, CSH, CH, water) at each time step is very difficult since very complex processes take place. The microstructure created by this model is based on spheres of anhydrous material. The anhydrous particles remain spherical after hydration. Actual C_3S particles are not spherical and their surfaces do not necessarily react uniformly. The model may predict some properties quite accurately because these properties do not depend on such details as particle shape. Other properties for instance may be integrally connected to the shapes and locations of the particles. As a result the definition of the spatial distribution of all relevant phases becomes a very difficult mathematical problem. Therefore, only the simplest microstructures can be simulated. Figure 3.9 shows the flowchart of the Jennings and Johnson model.

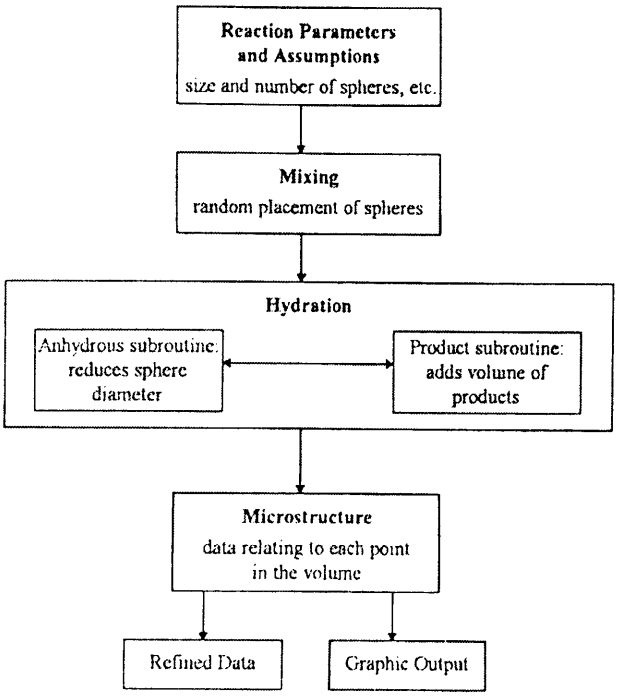

Figure 3.9: Flowchart for the Jennings and Johnson Model (Jennings *et al.*, 1996).

3.3.2.3 HYMOSTRUC Model

Incorporation of reaction kinetics is something that has been mostly neglected by microstructurally based models. This has been partly due to uncertainty in the mechanisms of the hydration process itself. The numerical model HYMOSTRUC (Breugel, 1991) was developed at TU-Delft in late nineteen eighties for the simulation of the reaction process and of the formation of the microstructure in hydrating Portland cement. HYMOSTRUC (acronym for HYdration MOrphology and STRUCture) attempts to take into account some of the most important aspects of kinetics affecting the hydration rate and the development of microstructure. In this model the degree of hydration is simulated as a function of the particle size distribution, the chemical composition of the cement, the water to cement ratio and the reaction temperature. The cement particles are modelled as digitised spheres randomly distributed in a 3D body and the hydrating cement grains are simulated as growing spheres (Breugel, 1991; Koenders, 1997). As cement hydrates the cement grains gradually dissolve and a porous shell of hydration products is formed around the grain. This results in the swelling of the particles. The hydrates around the cement grains first cause the formation of small isolated clusters. Bigger clusters are formed when small cement particles become embedded in the outer shell of other particles. These bigger clusters provoke the swelling of these particles. Figure 3.10 below gives an idea about the core of the model.

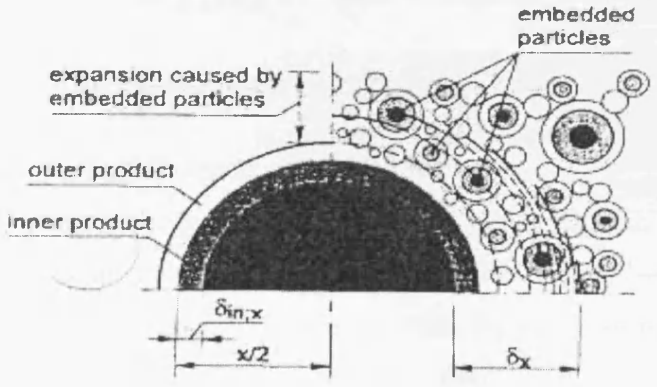

Figure 3.10: Formation of interparticle contacts as simulated in HYMOSTRUC (Breugel, 1991).

Figure 3.10 shows schematically the interaction mechanisms for the expanding particles. On contact with water an arbitrary cement particle x starts to dissolve under

the formation of reaction products. These products are formed partly inside and partly outside the original surface of the particle. In this way cement particles undergo an outward expansion, thus making contact with neighbouring particles. At a certain time interval, the degree of hydration of this central particle x is α_x and the depth of penetration of the reaction front is δ_{in}. Further hydration of this particle is accompanied with further expansion and embedding of neighbouring particles. The embedding of particles causes an extra expansion, and as a consequence the embedding of more particles.

It has to be mentioned that the HYMOSTRUC model was developed on the basis from the work by Pommersheim, which was described earlier. HYMOSTRUC is a numerical model, and as a numerical model it is based on an algorithm that simulates the interaction between hydrating cement particles. To reduce the number of calculations the model divides the sample into cells (Figure 3.11), the size and number of which depends upon the particle size distribution and the water to cement ratio.

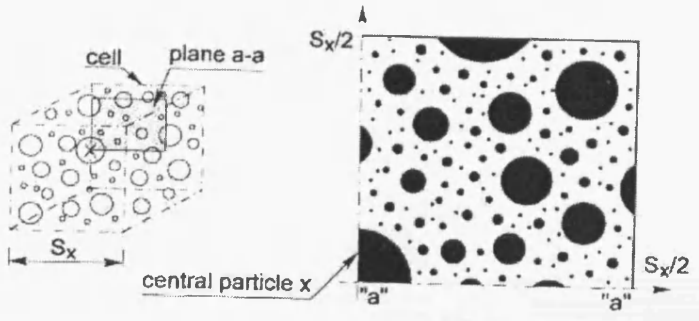

Figure 3.11: The cell concept in the HYMOSTRUC model (Breugel, 1995).

A cell is defined as a cubic space with sides having size S_x in which the central particle has a diameter of x μm. The side size S_x further depends on the water to cement ratio of the paste and the particle size distribution of the cement. The amount of the cement found in a fictitious cell with a certain thickness, surrounding a central particle x, will also depend on the water to cement ratio and the particle size distribution of the cement. This amount of cement plays an important role in the formation of interparticle contacts during hydration.

It could be argued that a large amount of detail is lost through the division of the paste into cells. However, this amount of detail cannot be considered of great importance since the outputs of the model are plots of temperature and degree of hydration as a function of time rather than a simulated microstructure. The developed hydration algorithm is applied iteratively to each cell. Unlike other numerical models, HYMOSTRUC keeps a track of the elapsed time. Hydration occurs in each time increment, but just before the next cycle of hydration will take place the reaction rate equations (in other words the algorithm) are re-adjusted according to the variables taken into account in the model.

HYMOSTRUC model is summarised in the flowchart shown in Figure 3.12. The input consists of cement composition, particle size distribution, w/c ratio and four different independent variables (K_0, δ_{tr}, β_1, β_2). K_0 is the basic hydration rate constant, δ_{tr} is the thickness of CSH around the cement at which the reaction changes over from being phase-boundary controlled to diffusion controlled, and β_1, β_2 are scaling factors used to refine the output of the model.

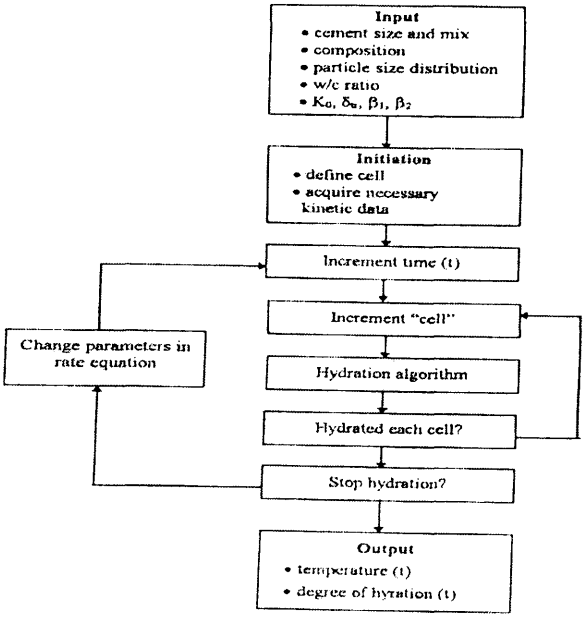

Figure 3.12: HYMOSTRUC basic flowchart (Jennings *et al.*, 1996).

3.4 Conclusions

Several models are nowadays capable of defining a reasonably detailed picture of the microstructure of the cement-based materials. Models dealing with the quantities of various phases are available and with the use of powerful computers can be used to formulate analogue and digital representations of the physical distribution of phases in the microstructure. The microstructure of the cement-based materials is dynamic. In other words it undergoes changes with time. These changes are triggered by chemical reactions within the matrix, loading, change of curing temperature and drying. Some major examples of models dealing with the microstructure of the cement-based materials have been discussed and most of them focus on the microstructure at the micron level.

Chapter 4: Some Aspects of Hydration and Volume Changes of Cement-Based Materials

4.1 Introduction

Cement, in the general sense of the word, can be described as a material with adhesive and cohesive properties which make it capable of bonding mineral fragments into a compact whole. A large variety of cementing materials are embraced in this definition. The cements of interest in the making of concrete have the property of setting and hardening under water by virtue of a chemical reaction. Such cements are termed *hydraulic cements*. Hydraulic cements consist mainly of silicates and aluminates of lime, and can be classified broadly as natural cements, Portland cements and high-alumina cements.

On contact with water Portland cement particles start to dissolve and react with water leading to the formation of hydration products. Hydration products form a complex gel. This colloidal and micro-porous system has a huge internal surface and therefore reacts strongly with water. The reaction of cement with water is accompanied with liberation of heat and chemical and physical binding of water.

In this section the chemistry of cement will be briefly examined, as well as some of the mechanisms associated with the cement hydration. This will be the basis of further analysis towards the understanding of the volume changes that the cementitious materials undergo. Different types of shrinkage will be examined, as well as different types of concrete. Special attention will be given to the development of the autogenous shrinkage strains and their possible triggering factors.

4.2 Cement chemistry

The process of manufacture of cement consists of grinding the raw materials, mixing them intimately in certain proportions and burning in a large rotary kiln at a temperature of up to about 1450°C when the material sinters and partially fuses into

balls known as clinker. The clinker is cooled and ground to a fine powder, with some gypsum added, and the resulting product is the commercial Portland cement (Neville, 1995). The raw materials used in the manufacture of Portland cement consist mainly of lime, silica, alumina and iron oxide. These compounds interact with one another in the kiln to form a series of more complex products and apart from a small residue of unused lime which has not had sufficient time to react, a state of chemical equilibrium is reached. Four compounds are usually regarded as the major constituents of cements. These compounds are the tricalcium silicate, the dicalcium silicate, the tricalcium aluminate and the tetracalcium aluminoferrite. Table 4.1 below summarises these constituents together with their abbreviated symbols.

Table 4.1: Main chemical compounds of Portland cement.

Compound	Oxide Composition	Chemical Abbreviation
Tricalcium Silicate	$3CaO.SiO_2$	C_3S
Dicalcium Silicate	$2CaO.SiO_2$	C_2S
Tricalcium Silicate	$3CaO.Al_2O_3$	C_3A
Tetracalcium Aluminoferrite	$4CaO.Al_2O_3.Fe_2O_3$	C_4AF

In reality, the silicates are not pure compounds in cement, but contain minor oxides in solid solution. These oxides have significant effects on the atomic arrangements, crystal form and hydraulic properties of the silicates. Furthermore, in addition to the main chemical compounds listed in Table 4.1, there exist minor compounds, such as MgO, TiO_2, Mn_2O_3, K_2O and Na_2O and they usually occupy not more than a few per cent of the mass of cement. Two of the minor compounds are of particular interest, namely the oxides of sodium (Na_2O) and potassium (K_2O), known as the alkalis. They have been found to react with some of the aggregates giving products that cause disintegration of the concrete and have also been observed to affect the rate of gain of strength of cement (Neville, 1995).

4.3 Cement hydration

The presence of water is the factor which triggers the chemical reactions which in turn help the Portland cement to become a bonding agent. The silicates and aluminates listed above react with the water and produce a firm and hard mass, the hydrated cement paste, which is going to be examined in the following sections. Le Chatelier was the first to observe, more than 100 years ago, that the products of hydration of cement are chemically the same as the products of hydration of the individual compounds under similar conditions. This was later confirmed in the literature taking however into account the fact that the products of reaction may influence one another or may themselves interact with the other compounds of the system (Neville, 1995). The physical behaviour of the cement during hydration is governed by the two main cementitious compounds contained in it, namely the two calcium silicates (Table 4.1).

The hydrated cement bonds firmly to unreacted cement, but the exact way in which this process takes place is not certain. One possibility is that the newly produced hydrate forms an envelope which grows from within by the action of water that has penetrated the surrounding film of hydrate. Alternatively, the formed envelope is passed through by the dissolved silicates that precipitate as an outer layer. A third option is for the colloidal solution to be precipitated through the mass after a condition of saturation has been reached, the hydration further continues within the structure.

Whatever the mode of precipitation of the products of hydration, the rate of hydration decreases continuously, so that even after a long time there remains an appreciable amount of unhydrated cement. Extensive research and microscopic observations of the hydrated cement paste have not proved the existence of any channelling of the water into the grains of cement to hydrate selectively the more reactive compounds, such as C_3S, which may lie in the centre of the particle (Neville, 1995).

It has to be mentioned that the cement paste not only gains strength as the hydration proceeds but also becomes warm, particularly during the setting and early hardening period. In other words the reactions associated with the cement hydration are exothermic, and the heat release with respect to time is shown in Figure 4.1.

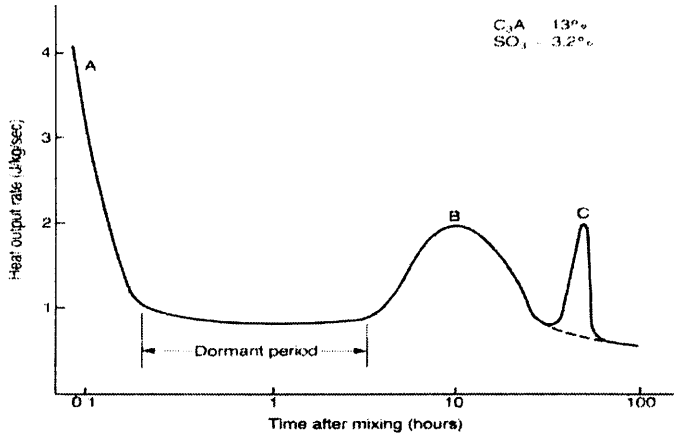

Figure 4.1: Typical rate of heat output from Portland cement during hydration at constant temperatures (Illston, 1996).

4.4 Volume changes

During and after the hardening period, concrete which is regarded as a homogeneous material is subjected to volume changes. From the structural point of view this dimensional instability is of vital importance. In homogeneous materials, shrinkage deformations are partly or wholly restrained and a state of eigenstresses is achieved as a result of the humidity distribution. High tensile stresses are induced in the dry outer zones, which, if excessive, result in crack formation (Wittmann, 2001). According to Wittmann, under usual climatic conditions the tensile strength of the material is quickly reached. Then follows the softening in the highly stressed zones, and finally cracks form. It is useful to mention, that a part of these deformations is irreversible.

Changes in temperature, moisture content (which is expressed as relative humidity) and applied load are the main factors affecting the volume changes in concrete. Concrete may also be subjected to potentially destructive forces due to chemical attack, which may lead to disintegration problems, e.g. sulphate attack, alkali silica reaction, corrosion etc. Currently, there is no theory that can describe sufficiently well the concrete volume change mechanisms. Any theories developed on the basis of shrinkage measurements are necessarily unrealistic (Wittmann, 2001). Real shrinkage mechanisms are formulated only on the basis of a very complicated analysis and so far most of the shrinkage models are either purely theoretical or, in the best case, a first approximation.

Concrete can undergo either contraction due to moisture loss, such a phenomenon is termed "shrinkage" or "swelling" due to gain of moisture. Wittmann subdivides shrinkage mechanisms into real and apparent. Among the real mechanisms are physical and chemical reactions that lead directly to volume change. In usual conditions the observed deformations are strongly affected by crack formation, local creep deformations and even by geometry.

4.4.1 Shrinkage classification

4.4.1.1 Chemical shrinkage

When cement and water react and form hydration products, they occupy about 7% less volume than cement and water separately. This phenomenon – otherwise known as *"Le Chatelier"* contraction - is called chemical shrinkage. This volume change is strongly dependent on the degree of hydration. The hydration products form a spatial network in which the cement particles are fixed in a certain position. Bazant and Wittmann believe that the formation of such as spatial network is able to generate pressure within the matrix and hence may cause moderate swelling of the system (Bazant and Wittmann, 1982). Other researchers attributed this possible early expansion to the formation of ettringite (Tezuka, 1986).

The volume reduction caused by chemical shrinkage is almost completely transferred into the empty pores. Together with the water-filled pores the latter form the porous network in the hydrating paste. Narrow pores will accommodate water, which gradually in turn will dry out into wider pores. As hydration proceeds, the relative humidity in the system eventually drops. This drop is followed with the capillary tension in the pore water. The tensile stresses developed are equilibrated by compressive stresses in the solid skeleton of the hydration products. The compressive stresses are accompanied by deformations of the matrix. Deformations can be either elastic or time-dependent (Persson, 1999). It has been realised some time ago that the volume change as observed on drying concrete specimens is the complex response of the composite material to time-dependent state of eigenstresses within the matrix.

On the basis of Japan Concrete Institute (JCI) classification of shrinkage terminology, chemical shrinkage is defined as the phenomenon in which the absolute volume of hydration products is less than the total volume of unhydrated cement and water before hydration. The chemical shrinkage can be calculated by using the following formula:

$$S_{hy} = \frac{(V_c + V_W) - V_{hy}}{V_{ci} + V_{Wi}} \times 100 \qquad (4.1)$$

where S_{hy} represents the chemical shrinkage ratio (%), V_c the volume of hydrated cement, V_W the volume of reacted water, V_{hy} the volume of hydration products, V_{ci} the volume of cement before mixing and V_{Wi} the volume of water before mixing.

The notation used in the above equation is shown in Figure 4.2.

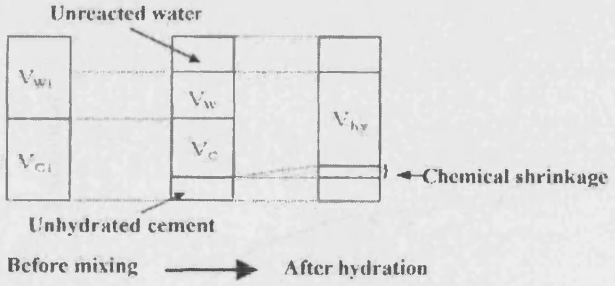

Figure 4.2: Notation in the equation for the chemical shrinkage (Japan Concrete Institute, 2001).

It is useful to mention that the CaO present in the cementitious material produces $Ca(OH)_2$, during hydration of cement, which acts as a source of alkalinity

Cement + Water

$2C_3S + 6H \rightarrow C_3S_2H_3 + 3Ca(OH)_2$

(C-S-H) + [CH]

(i.e. cement gel + $Ca(OH)_2$)

This alkalinity is gradually destroyed by CO_2 in the form of carbonation (Bazant and Wittmann, 1982).

4.4.1.2 Autogenous shrinkage

The expression autogenous shrinkage was first introduced in the literature in mid-nineteen thirties and positively defined in early nineteen forties as a macroscopic volume change caused by the hydration of cement. Generally in the literature there are about 8 different expressions to describe the phenomenon of autogenous shrinkage. The more precise definition – currently – is given by the Japan Concrete Institute stating that autogenous shrinkage is the phenomenon of macroscopic volume reduction of cement paste, mortar and concrete triggered by chemical shrinkage. It has to be noted that the latter definition is strictly applicable to concretes with normal workability. The autogenous shrinkage is considered to be at least one order smaller than the chemical shrinkage. In High Performance Concrete (HPC) autogenous shrinkage increases as the w/c – and w/b – decreases (Tazawa and Miyazawa, 1995). The relation between autogenous shrinkage and chemical shrinkage is shown in Figure 4.3.

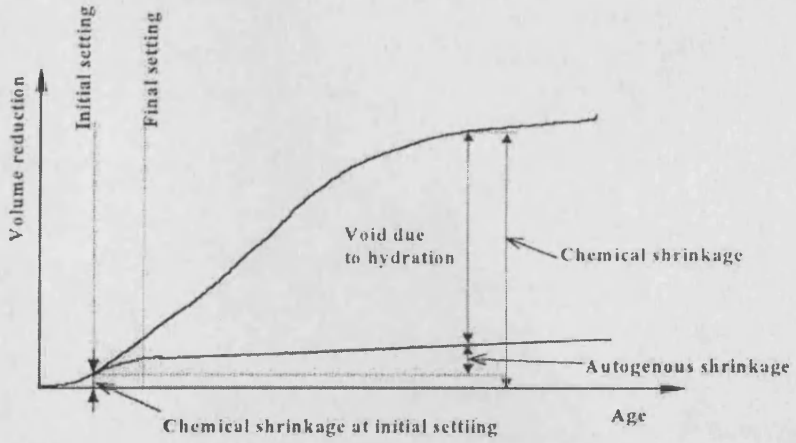

Figure 4.3: Relation between autogenous and chemical shrinkage (Japan Concrete Institute, 2001).

The relation between autogenous and chemical shrinkage of cement paste without evaporation and any external source of water is described by the following equation:

$$S_{hy} = S_P + S_{as} + \Delta S_{hy} \tag{4.2}$$

where S_{hy} represents the chemical shrinkage ratio (%), S_P represents the ratio of the volume of voids created by hydration to the volume of hardened cement paste (%), S_{as}

represents the autogenous shrinkage ratio (%) and ΔS_{hy} is the chemical shrinkage ratio at the time of initial setting. It has to be mentioned that in equation (4.2), right and left sides are not explicitly equal to each other. This is because the initial volume for the calculating chemical shrinkage (S_{hy}) is specified as the volume of the mixture at the end of mixing and on the contrary that for autogenous shrinkage (S_{as}) is specified as the volume at the initial setting.

Another important parameter is that the volume changes in horizontal and vertical direction differ when the effect of gravity cannot be neglected. The relation between autogenous and chemical shrinkage in horizontal and vertical directions, is shown in Figures 4.4 and 4.5.

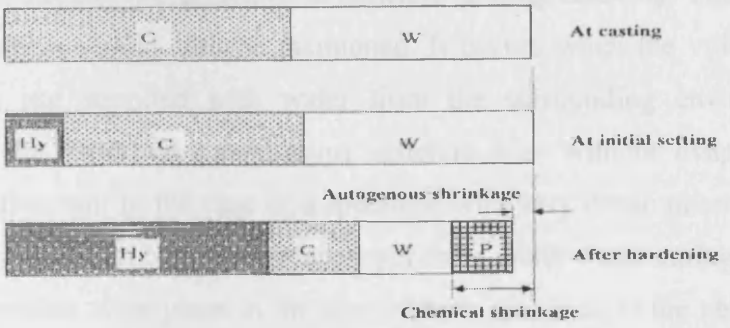

Figure 4.4: Relation between chemical and autogenous shrinkage in horizontal direction (Tazawa, 1999).

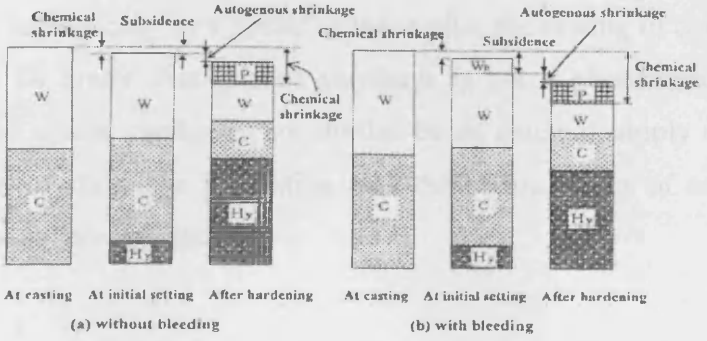

Figure 4.5: Relation between chemical and autogenous shrinkage in vertical direction (Tazawa, 1999).

In the above figures W represents the unhydrated water, W_B is the bleeding water, C represents the unhydrated cement, the hydration products are noted as H_y and P

represents the voids generated by hydration. With the term subsidence is defined the vertical length change in cementitious materials before initial setting, which is caused by bleeding, chemical and autogenous shrinkage (Tazawa, 1999). In the cases where the skeleton of hydration products has not been formed, such as in fresh concrete, cement particles are rearranged by the effect of gravity as chemical and autogenous shrinkage proceed, then macroscopic shrinkage occurs in vertical direction. Therefore, subsidence of concrete is caused not only by the difference in specific gravities of the solid particles, which leads to bleeding, but also by chemical and autogenous shrinkage.

After setting, a rigid framework of cement hydrates is formed and autogenous volume change takes place in a three-dimensional manner. When autogenous shrinkage is restrained, self-stresses are generated in concrete causing cracking. The phenomenon of self-desiccation should also be mentioned. It occurs when the voids created by hydration are not supplied with water from the surrounding environment, and consequently the hardened cementitious material dries without evaporation. It is useful to mention that in the case of a specimen with very dense microstructure, the water can penetrate into only the surface layer even under water curing therefore the phenomenon which takes place in the core of such specimen is the above described self-desiccation.

Autogenous shrinkage, which is linked directly to cement hydration, starts to develop uniformly and isotropically in a matter of hours after the casting of concrete – almost always before 24 hours. Autogenous shrinkage is not a phenomenon that can be prevented if the coarse capillaries are refilled by an external supply of water. More about this type of shrinkage in relation with the various types of concrete will be discussed in the following sections.

4.4.1.2.1 Factors affecting autogenous shrinkage

Autogenous shrinkage is affected by various different factors such as the type of cement, type of mineral admixtures and the water to cement ratio (*w/c*).

Type of Cement

The type of cement used in the mix is a very important parameter regarding the development of autogenous shrinkage strains. Figure 4.6 illustrates the variation of autogenous volume changes with the type of cement used.

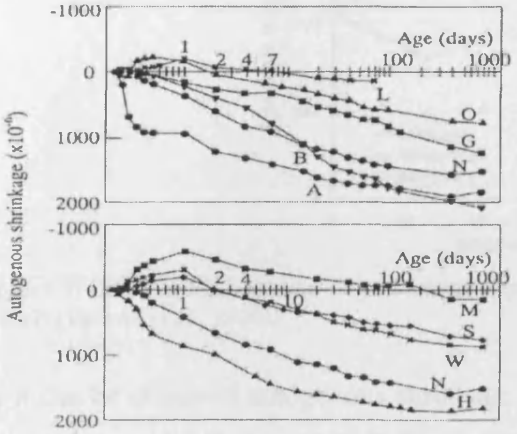

Type of cement	Mineral Compound (%)			
	C_3S	C_2S	C_3A	C_4AF
N	51.5	22.9	8.9	8.8
M	42.9	35.9	3.2	11.9
H	62.8	11.8	8.0	8.5
S	61.0	16.9	1.7	14.6
W	61.1	16.5	12.1	0.6
O	57.6	20.5	2.2	13.7
L	22.9	58.8	2.5	9.4

Figure 4.6: Autogenous shrinkage variation with different cement type used (w/c=0.3) (Tazawa, 1999).

It has to be mentioned that the dependence of shrinkage upon the type of cement is not the case for the drying shrinkage. Tazawa suggested that the autogenous shrinkage of cement paste can be described by the following equation.

$$\varepsilon_p(t) = a\alpha_{C_3S}(t)\cdot(C_3S\%) + b\alpha_{C_2S}(t)\cdot(C_2S\%) + c\alpha_{C_3A}(t)\cdot(C_3A\%) + d\alpha_{C_4AF}(t)\cdot(C_4AF\%) + e(Blaine) + f \quad (4.3)$$

where $\varepsilon_p(t)$ represents the autogenous shrinkage of cement paste ($x10^{-6}$), $\alpha_i(t)$ is the degree of hydration of compound i (%), (Blaine) is the blaine fineness of cement (cm^2/g) and a,b,c,d,e and f are constants. These constants can be determined from regression analysis using experimental data. It has been proved that the coefficients c and d, which correspond to C_3A and C_4AF, are much larger than those corresponding to C_2S and C_3S by one or two orders. Therefore the above equation suggests that autogenous shrinkage greatly depends on the contents and degree of hydration of C_3A and C_4AF (Tazawa, 1999).

Mineral admixtures

The addition of mineral admixtures to the matrix has significant effect on the development of autogenous shrinkage strains. The effect of blast furnace slag on the autogenous shrinkage of cement paste has been examined by Tazawa (Figure 4.7).

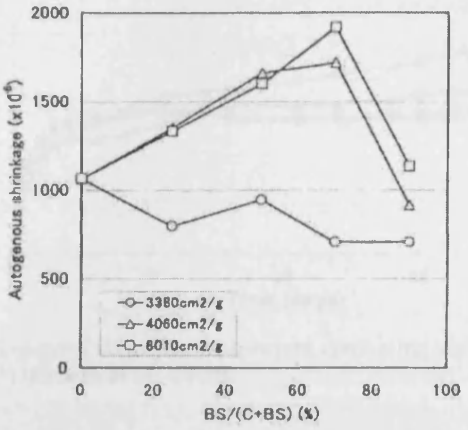

Figure 4.7: Effect of blast furnace slag on autogenous shrinkage of cement paste (water to binder ratio of 0.40) (Tazawa *et al.*, 2000).

As it can be observed autogenous shrinkage is slightly decreased by addition of blast furnace slag with low Blaine fineness. Inclusion of blast furnace slag with high Blaine fineness leads to an increase of the developed autogenous shrinkage strains, especially at large replacement ratios (Tazawa *et al.*, 2000). Extensive research has proven that the inclusion of silica fume in the matrix causes an increase in the autogenous shrinkage. As it was explained in previous Chapter the inclusion of silica fume has been reported to refine the pore size distribution in the concrete matrix. This refinement of pores increases the capillary tension, the suction potential and therefore the autogenous shrinkage. Another aspect that has to be remembered is the pozzolanic action of silica fume, which as shown in Chapter 2 – equation (2.2) during the secondary reaction of hydrating cement paste eliminates the surplus of calcium hydroxide. An indication of the increase of autogenous shrinkage with silica fume is given by Figure 4.8.

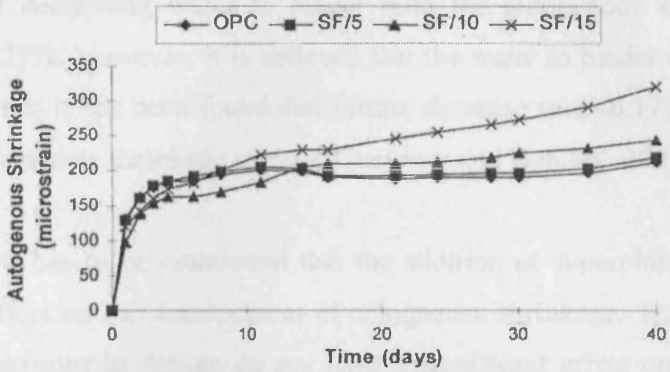

Figure 4.8: Variation of autogenous shrinkage of concrete containing different amounts of silica fume (water to binder ratio is 0.23) (Brooks *et al.*, 1999).

The increase in autogenous shrinkage by the addition of silica fume has been noticed by many researchers (Tazawa *et al.*, 1995; Brooks *et al.*, 1999; Cheyrezy and Behloul, 2001; Zhang *et al.*, 2003).

Water to cement ratio

The water content and therefore the water to cement (*w/c*) ratio is an important parameter regarding the development of the autogenous shrinkage strains. Literature reports that by decreasing *w/c* the autogenous shrinkage increases (Figure 4.9).

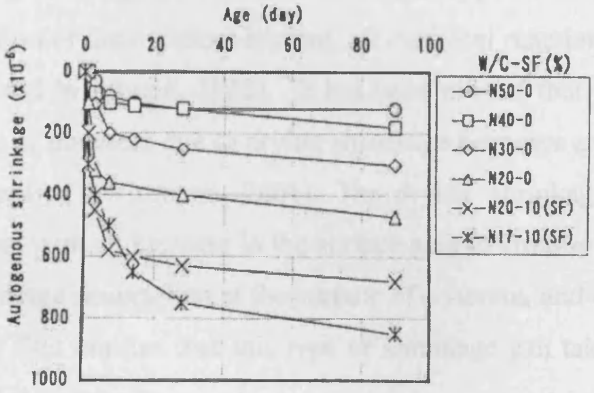

Figure 4.9: Effect of water to cement ratio on the development of autogenous shrinkage strains (Tazawa *et al*, 2000).

As it can be observed there is a big increase in the autogenous shrinkage strains as the w/c decreases. Furthermore, autogenous shrinkage of concretes with lower w/c increases more rapidly at early ages than those with higher *w/c*. It has to be mentioned that the concept of increasing autogenous shrinkage strains as the *w/c* decreases can be also extended to decreasing water to binder ratio (*w/b*). As it can be shown in

Figure 4.9, for decreasing water to binder ratio the autogenous shrinkage strains increase about 25%. However, it is believed that the water to binder ratio of 0.17 is a critical point since it has been found that further decrease ($w/b<0.17$) causes a steady decrease in autogenous shrinkage as well (Cheyrezy and Behloul, 2001).

In conclusion, it has to be mentioned that the addition of superplasticisers (SP) has only a slight effect on the development of autogenous shrinkage. The different types of SP and differences in dosage do not have a significant effect on the autogenous shrinkage (Tazawa *et al*, 2000). Some slight reductions in autogenous shrinkage may be due to the small effect superplasticisers have on the rate of hydration.

4.4.1.3 Drying shrinkage

Drying shrinkage is defined as the time-dependent deformation due to evaporation of internal water in hardening concrete at constant temperature and relative humidity. Drying shrinkage occurs without the application of any loading. According to Wittmann, drying shrinkage not only takes place in zones of drying sample – which are under high tensile stress (Wittmann, 2001) – but it also is supposed to be the only possible hygral length change of concrete. Since this type of shrinkage is strongly related to the variation of the moisture content, all chemical reactions can therefore be neglected (Bazant and Wittmann, 1982). It has been proved that the damage to the composite structure of concrete due to drying shrinkage becomes anisotropic when an external load is applied (Wittmann, 2001). The drying shrinkage of cementitious composites increases with an increase in the surface area to volume ratio (Aitcin *et al.*, 1997). Drying shrinkage occurs first at the surface of concrete, and only at the surface exposed to the air. This implies that this type of shrinkage can take place on all the exposed surfaces of the concrete.

The driving force for the drying shrinkage is the evaporation of the water from the capillary network in the concrete, which is exposed to air with a relative humidity lower than that within the capillary pores. Researchers still disagree about the fundamental mechanism responsible for drying shrinkage (Aitcin, 1999). These mechanisms include the capillary tension, the surface absorption and the interlayer water removal.

It has to be mentioned that the causes of drying shrinkage are the same as the causes of autogenous shrinkage because it is the same physical phenomenon that is developing within the concrete. However, there are some major differences between these two types of shrinkage:

- Drying shrinkage develops causing a mass loss to the concrete, unlike autogenous shrinkage.
- Drying shrinkage progresses from drying surface to the core of the element – causing what we are going to call later, differential drying shrinkage – while autogenous shrinkage develops isotropically.
- Drying shrinkage causes relative humidity gradients while autogenous shrinkage does not.

4.5 Hardened Cement Paste (HCP)

Fresh cement paste is a plastic network of cement particles in water. Once the paste has set its apparent volume remains approximately constant. Cement paste is a multiphase composite material. It consists of a plastic network of hydrated cement particles, unhydrated cement, pores and water.

4.5.1 Structure of the hydrated cement paste

There are two kinds of pores in the cement paste. The residue of water filled spaces in the fresh paste is the capillary pores and the pores in the gel itself, which are termed gel pores. Capillary pores are one or two orders of magnitude larger than the gel pores (Neville, 1995).

The significance of these pores is going to be examined later. Although, there are various phases that can be identified in the cement paste only two dominate in the volumetric proportions, namely the calcium silicate hydrate (C-S-H) and the calcium hydroxide or Portlandite ($Ca(OH)_2$ or CH). These two phases consist more than 85% of the total volume of the matrix.

4.5.1.1 Calcium Silicate Hydrate – CSH

Calcium silicate hydrate is the most important ingredient of the cement paste and occupies 50 – 60% of total matrix volume. C-S-H form the major binding phase for all the cement based materials, governing their mechanical properties. Their structure varies from poorly crystalline fibres to a reticular or crumbled sheet-like network. For ordinary Portland cement the lime to silica ratio varies between 1.5 and 2.0 whereas the quantity of water, that is the water bound in the crystal structure, varies even more. Calcium silicates do not hydrate in the solid state but the anhydrous silicates probably first pass into solution and then react to form less soluble hydrated silicates which separate out of the supersaturated solution (Neville, 1995). Le Chatelier was actually the first to predict such a hydration mechanism in 1881.

The most important feature of C-S-H structure is its colloidal nature and the extremely high surface area, estimated to be between 100 and 700 m^2/mg. That is about a thousand times greater than the cement particles from which it was formed. However, some information has been gained on the nanostructure of C-S-H in recent years primarily by the use of trimethilsilylation (TMS) and solid state nuclear magnetic resonance (NMR) spectroscopy. The structure of C-S-H has not been verified and explained sufficiently yet. There are some models (Powers 1958; Brunauer 1962) that try to explain the C-S-H structure but are based on the assumptions that the material is stratified and its strength is mainly due to van der Waals forces. Later on, it was suggested that due to the colloidal dimensions of the C-S-H crystals they would be better examined with electron optical microscopy. The results of those examinations suggest that the C-S-H resemble natural minerals such as Tobermorite and Jennite with many imperfections and irregularities, such that it becomes nearly amorphous (Jennings, 2000).

4.5.1.2 Calcium Hydroxide – $Ca(OH)_2$

Calcium hydroxide crystals or Portlandites occupy 20-25% of the total cement paste volume, and appear to grow in regions initially occupied by water. In contrast to the calcium silicate hydrate, this constituent has a definite stoichiometry ($Ca(OH)_2$). The CH crystals form hexagonal prisms (in ideal conditions) and in general they do not

affect the strength of the matrix. As hydration proceeds the CH crystals become massive in quantity and of unidentified shape. Actual crystal sizes vary from a few μm to several hundreds of μm, and depend on temperature, hydration time, available space and impurities present in the system (Lea, 1970). Transmission Electron Microscope (TEM) studies revealed that a small proportion of calcium hydroxide in cement pastes, especially in the case of low water to cement ratio pastes, is cryptocrystalline and intimately mixed with the C-S-H. The large crystals and the small surface area make the calcium hydroxides a limiting contributor to the strength of hardened cement paste. Nevertheless, the calcium hydroxide crystals provide the hardened cement paste matrix with some additional stiffness. In fact, at the scale of μm, the cement paste matrix can be considered as a composite material of C-S-H gel with stiff calcium hydroxide crystals as inclusions. Finally it has to be mentioned that the high solubility of calcium hydroxide affects adversely the performance of the matrix since it makes it vulnerable to oxide environment (chemical attack).

4.5.1.3 Calcium Sulphates, Aluminates and Ferrites

Calcium sulphates together with aluminates and ferrites occupy 15% of the cement paste volume, and they do not affect seriously the macroscopic mechanical performance of the matrix. However, some of these compounds become very important in the case of calcium leaching. In particular the trisulphate hydrate, widely known as ettringite, which forms needle shaped prismatic crystals. The tendency of ettrignite to accumulate in the aggregate-cement paste interface makes it a very significant compound especially for mortars and concretes. In fact, ettrignite together with the calcium hydroxide crystals dominate the interface properties (Neubauer *et al.*, 1996).

4.5.1.4 Unhydrated Cement Grains – Clinker

Unhydrated cement grains may be present in the cement paste even for a long time after the hydration of cement. Their quantity depends on the cement particle size and on the degree of hydration. During the hydration process, initially the small particles

dissolve first whereas the larger particles shrink. Due to the limited space between the particles, the hydration products tend to crystalise very close to the clinker grains and appear as coating to them. Therefore, further hydration results in the creation of a dense product with morphology very similar to the initial clinker. This implies that since the hydration products occupy more space than the cement they are made of, complete hydration cannot take place if the water to cement ratio is below a certain level. It has been proved experimentally that a w/c of 0.38 is sufficient to allow full hydration to occur (Aitcin, 2000).

4.5.2 Pores in hardened cement paste

It is widely accepted that the hardened cement paste (hcp) consists of several different types of pores which can affect its mechanical behaviour. These types of pores are described as thoroughly as possible below because of their importance to autogenous shrinkage.

4.5.2.1 Interlayer pores

The voids between the various layers in the C-S-H have extremely small dimensions and therefore they do not affect the strength and the permeability of the cement paste. This kind of pores, commonly termed as gel pores, can hold water due to hydrogen bonds, and its removal can contribute to drying shrinkage and creep. It is useful to mention that the interlayer space within C-S-H phase is assumed to be a part of the solid phase of hcp. The gel pores occupy about 28% of the total volume of gel. The actual value of the interlayer pores is characteristic for a given cement but is largely independent of the water to cement ratio of the mix and of the progress of hydration. Consequently, as the total volume of gel increases with the progress of hydration, the total volume of gel pores also increases (Neville, 1995).

4.5.2.2 Capillary pores

The total volume of the mixture of cement and water does not alter after hydration, whereas the bulk density of the hydration products is lower than the density of the

cement. The voids that are filled neither with cement nor with the hydration products are termed capillary pores. Because the hydration products occupy more than twice the volume of the original solid phase alone, the volume of the capillary pore system is reduced with the progress of hydration.

Capillary pores, otherwise termed mesopores, represent the porosity of the cement paste. The volume and the size of such pores are dependent on the initial distance/space between the unhydrated cement grains, the w/c and the degree of hydration. The rate of hydration is of no importance whereas the type of cement used is important since it affects the degree of hydration. It has been reported in the literature that for water to cement ratios at about 0.38, the volume of the gel is not sufficient to fill all the space available to it and therefore some capillary pores will be left even after the process of hydration has been finished (Neville, 1995). The diameter of such pores in well-hydrated cement pastes with relatively low *w/c* varies between 10 – 50nm. In pastes with high w/c and which are at first stages of hydration process the size of the capillary pores is about 3 – 5 μm.

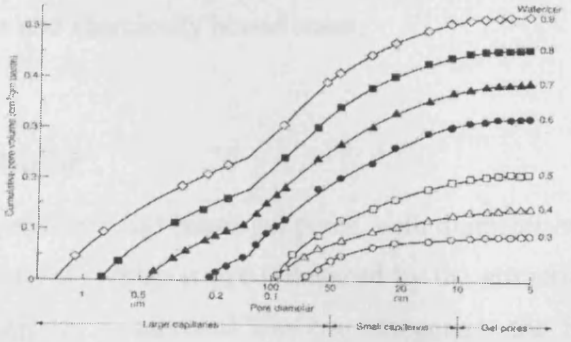

Figure 4.10: Pore size distribution in 28 day old hydrated cement paste (Illston, 1996)

It has to be mentioned that what is of vital importance and affects the properties of concrete is the distribution of pores and not the whole of the porosity. Capillary pores with sizes well over 50nm influence the strength and the permeability of concrete. Pores with sizes below 50nm are of major importance when the drying shrinkage and creep are concerned.

4.5.2.3 Air pores

In contrast to capillary pores, air pores have a specific (spherical) shape. These voids are trapped in the matrix during mixing and have a diameter of about 3μm. Actually, they form the upper limit of capillary pores and they widely termed macropores. Such pores may even be entrained in the mix as well, in order to enhance its performance. In such case their size is much larger (50 – 200μm). Macropores are considerably larger than capillary pores and they strongly affect the mechanical properties of the concrete matrix.

4.5.3 Water in the hardened cement paste

As has already been mentioned both solids and pores exist in the cement paste in various forms. The same happens with water. The large surface areas in the matrix give hardened cement paste (hcp) a considerable affinity for water and make its overall dimensions water sensitive. This behaviour can be explained by considering the ways in which water is contained in the paste. In a hydrating water/cement system the water is present in roughly four different forms, namely capillary water, adsorbed water, interlayer water and chemically bound water.

4.5.3.1 Capillary water

This is located in the capillary and larger gel pores, with diameter over 50Å (5nm). It is considered as bulk water, which is not influenced by the attractive forces of solid surfaces. Capillary water is subdivided into two categories: the free water, which exists in voids larger than about 50nm and its removal, does not correspond to any volume change; and water that is subjected to capillary tension forces and exists in pores smaller than 50nm and its removal at normal temperatures and humidity may result in some shrinkage.

4.5.3.2 Adsorbed water

This is the water that is close to the solid surfaces, and under the influence of surface attractive forces. Several molecular layers (about five) of water can be held together,

forming a thick layer of about 13nm. A huge amount of this kind of water can be lost on drying to 30% relative humidity (RH) and it is the main contributing factor to drying shrinkage.

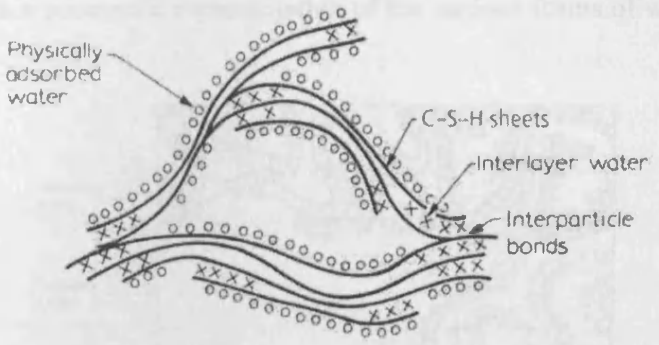

Figure 4.11: Schematic representation of adsorbed water in the hydrating cement paste (Neville, 1995).

4.5.3.3 Interlayer water

This is the single molecular layer of water that exists in C-S-H pores narrower than 2.6nm. Such water is strongly held by hydrogen bonds and its removal is very difficult and only at elevated temperatures and/or RH less than 10%. But its removal results in considerable shrinkage.

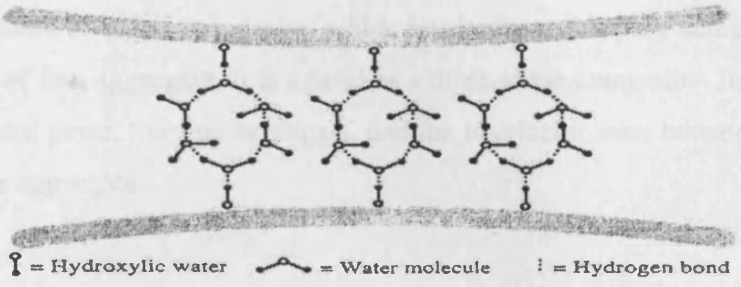

Figure 4.12: C-S-H interlayer water structure (Basile and Beaudoin, 2000).

4.5.3.4 Chemically bonded water

At complete hydration of cement, an amount of water of about 25% of the weight of the anhydrous cement is chemically bound to the cement (Breugel, 2000). This is the water combined with cement in the hydration reactions. In this form, which actually includes water molecules which are most tightly adhered to the surfaces of the

reaction products, it is considered to be an inherent part of the solid matter. It is not lost during drying but is only expelled when heating to high temperatures in excess of 1000°C which decomposes the paste.

Figure 4.13 gives a schematic representation of the various forms of water present the cement paste.

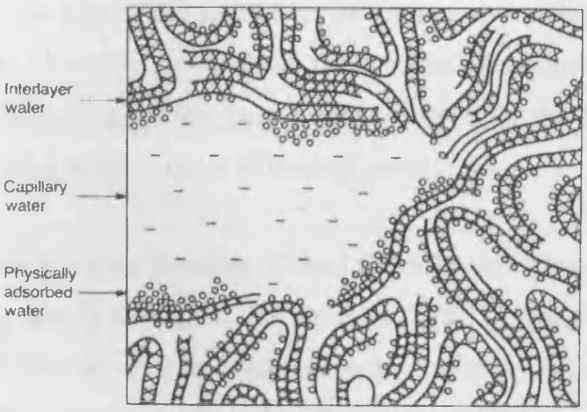

Figure 4.13: Schematic representation of the various types of water present in the hardened cement paste (Illston, 1996).

4.6 Mortar

Mortar is a cement-based composite, which results from the pure cement paste with the addition of fine aggregate. It is treated as a three-phase composite. Its three phases are: the cement paste, the fine aggregate, and the interfacial zone between the cement paste and the aggregate.

4.6.1 Interfacial transition zone (ITZ)

The stiffness of the cement-based composites is weakened by the existence of several interfaces in their matrix. The most important of these interfaces is the cement-aggregate interface, which is widely known as interfacial transition zone (ITZ). The microstructure of cement paste in the vicinity of an aggregate in mortar – and concrete – differs significantly from the microstructure of cement paste far away from aggregates. The ITZ can explain a series of phenomena, such as the following:

i. Mortar and concrete has a brittle behaviour in tension, whereas it is extremely strong in compression.
ii. Although the different constituents of mortar and concrete (cement paste, aggregate) have a linear elastic behaviour mortar and concrete do not.
iii. Hydrated cement paste has higher strength than mortar and concrete, for the same w/c, cement content and age. The strength of mortar and concrete decreases as the size of the aggregates incorporated into the mix increases.
iv. Permeability of mortar and concrete is one order of magnitude larger than that of the corresponding cement paste. That seems to be the case even when the aggregates used in the mix are extremely small.

The main characteristic of the structure of the ITZ is the existence of higher w/c ratio near the aggregates than in the regions distant from them. This higher w/c ratio results in the formation of oriented crystals – vertical to the surface of aggregate – with larger dimensions than the crystals in the rest of the paste and hence in the formation of pores.

Another reason for the weak nature of the ITZ is the presence of microcracks, whose density depends on various factors such as w/c ratio, cement content, the aggregate grading, curing conditions, relative humidity etc. ITZ is very sensitive to microcracking due to tensile forces triggered by various deformations between aggregates and cement paste, such as shrinkage and swelling. So, it is apparent that microcracks are present in mortars and concrete well before the application of any loading. Drying shrinkage, permanent and impact loading are factors that increase the number and the size of microcracks.

4.6.2 Cement paste and mortar associated volume changes

Earlier we have described the various types of water present in the cement paste. The loss of this water results in a net contraction, which is widely known as drying shrinkage.

The shrinkage of the C-S-H matrix, which consequently controls the shrinkage of the cement-based materials, is determined by the re-arrangement of the water in the nanometer scale gel pores, as relative humidity is reduced. A part of the drying shrinkage that cement paste undergoes is reversible upon rewetting. Conversely, some of the deformation is permanent, termed irreversible or irrecoverable shrinkage. The mechanisms responsible for the reversible drying shrinkage are well developed, whereas those controlling irreversible drying shrinkage are still unclear, although it has been observed that total and irreversible drying shrinkage increase with surface area and pore volume, when the degree of hydration and w/c ratio are held constant (Juenger and Jennings, 2002).

Several factors influence the degree of drying shrinkage, including the w/c ratio and age. Both these, as we have already seen affect the capillary porosity, which in turn strongly influences the drying shrinkage. The presence of C-S-H is also another key aspect. C-S-H is highly porous and therefore will shrink upon drying. It is very possible that drying shrinkage is affected not only by the amount of C-S-H present, but by its microstructure as well.

4.7 Conventional concrete

4.7.1 Structure of concrete

Concrete is a very complex and heterogeneous composite in terms of its microstructure, and even today the mechanisms that relate the latter to the corresponding properties have not been yet identified. Nevertheless a good understanding of the properties of the concrete matrix will help us to clearly identify the factors that affect its principal properties such as strength, creep and shrinkage.

Aggregates of various sizes and shapes, which are bonded together with the hardened cement paste consist the major phase of the concrete matrix. A microscopic examination of the matrix reveals its complexity. First of all is identified a third phase, the interfacial transition zone (ITZ), which represents the surface between the large aggregates and the cement paste having a thickness of 10-50 μm. As it was explained

in an earlier section on mortar, the ITZ is a very weak region, in comparison with the other concrete phases, and has a strong influence on the mechanical properties of the matrix. Second, each of the three phases in the concrete matrix consists of several other phases. For instance the aggregates consist of minerals, micro-cracks and voids whereas the cement paste and the ITZ consist of various solids, pores and micro-cracks. Furthermore, it has to be mentioned that the structure of concrete changes continuously with time, humidity of the surrounding environment and temperature. A thorough analysis of the different phases of concrete and how they affect shrinkage was done in a previous section (Section 4.4).

4.7.2 Time-dependent properties of concrete

Early age deterioration of concrete is a persistent problem that arises from complex volume changes such as autogenous shrinkage, drying shrinkage and thermal deformation. These volume changes cause tensile stresses in the material when the strength is relatively low. There is a competition in the microstructure of the material between the development of tensile stresses and the development of strength that evolves with time. This competition can be relatively hazardous for the material since it is responsible for premature cracking.

In terms of shrinkage the only forms that we meet in normal concrete are the drying and autogenous shrinkage. From a practical point of view drying shrinkage is the only type of shrinkage that develops significantly in ordinary concrete. As a result of disequilibrium in the relative humidity between concrete and its environment, concrete loses water when exposed to an environment whose relative humidity is lower than that existing in its capillary network. This loss of water leads concrete to shrink. Actually, when talking about conventional concrete the term shrinkage is used synonymously for the drying shrinkage. The water movement within concrete is more complex than other porous media because a very wide range of pore structures are present in the cement paste, pore structures that change continuously with time. For concrete members exposed to environmental conditions, water movement occurs by moisture diffusion in concrete. Thus moisture content in concrete varies in both space and time, and hence the moisture distribution of a cross section of concrete is non-

uniform. This non-uniform moisture distribution causes what is termed the differential drying shrinkage. From this type of drying shrinkage, tensile stresses develop on the exposed surfaces of concrete members and may result in crack formation. Up to now there is only a small amount of the research focused on this particular field due to the complexity of the moisture diffusion process in concrete. The only available model used to examine the differential shrinkage was a model proposed by Bazant and was described in Chapter 2 – Section 2.3.1.1, which is based on the moisture diffusion. However, in the last few years an attempt was made to produce a model for differential shrinkage using the analytical results of moisture distribution. Kim and Lee (1998), using a regression analysis managed to make a prediction for the differential drying shrinkage. Their results are in good agreement with the tests results, revealing that the internal drying shrinkage strain varies significantly according to the depth from drying surface. Furthermore, the stresses induced by this differential drying shrinkage may cause surface cracks. Moreover, they proposed that for the analysis of this particular type of shrinkage the creep of concrete has to be taken into consideration.

In the literature there are numerous papers describing the shrinkage mechanisms in concrete. Some of these are based on shrinkage measurements and some are derived from direct observations or calculations of the interaction between water and cement surfaces. According to Wittmann, shrinkage mechanisms can be subdivided into real and apparent (Wittmann, 1982). Physical and chemical reactions that lead to volume change are considered as real mechanisms, whereas mechanical interactions, such as crack formations and local creep deformations, are at the origin of apparent mechanisms. Wittmann also proposed that real mechanisms have to be taken into serious consideration in order to understand the effect of the chemical composition of the pore solution on shrinkage. Sufficient knowledge of the real shrinkage mechanisms will lead to ways of minimising it. As has already been mentioned shrinkage causes damage to the composite structure of concrete. This damage becomes anisotropic with the application of an external load (Wittmann, 2001). Test results have revealed that stress-free shrinkage of concrete is considerably higher than restrained shrinkage.

Autogenous shrinkage of concrete has been defined as decrease in volume due to hydration of cement, not due to other causes such as evaporation, temperature change and external loading. For conventional concrete, autogenous shrinkage is so little compared to the other deformations that it has been ignored. This kind of shrinkage starts to dominate the volume changes of concrete only when the w/c ratio becomes relatively small, in contrast to the drying shrinkage. Such a phenomenon will be considered later in the sections on high strength/high performance concretes (Sections 4.8.1 and 4.9.2).

4.8 High strength concrete

The term high strength is used to describe concretes, which with the aid of specific admixtures exhibit a significant increase in their compressive strength (up to 80 MPa). Such admixtures are the silica fume (or microsilica), the fly ash, the granulated ground blast-furnace slag (ggbs) and water reduction agents such as superplasticisers. In the current study we are going to concentrate only on high strength concretes made with microsilica and superplasticisers.

4.8.1 Shrinkage of high strength concrete

As it has already been mentioned the only type of shrinkage that practically exists in conventional concrete is the drying shrinkage. Autogenous shrinkage is quite small for normal concrete and therefore is neglected. However, with the reduction of the w/c and the water to binder ratio (i.e. in the case of high strength concrete) autogenous shrinkage increases and with addition of silica fume in particular becomes larger. Furthermore it has to be mentioned that in high strength concrete thermal stresses due to hydration heat of cementitious materials develop simultaneously with the autogenous shrinkage strains. High strength concrete having water to binder ratio of 0.30 or less and a replacement ratio of microsilica not less than 10% generates a value of autogenous shrinkage in the order of 200 – 400x10^{-6}. This value is about two to three times larger than that of the autogenous shrinkage of normal concrete. Experiments revealed that the relative humidity in the centre of a high strength

concrete specimen decreases to about 80% a week after placement as shown in Figure 4.14.

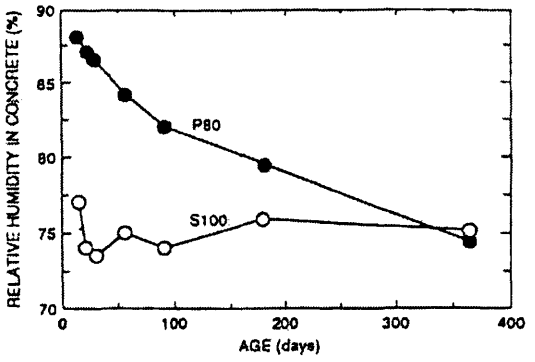

Figure 4.14: Relative Humidity in high strength concrete with (S) or without (P) silica fume (Tazawa, 1999).

This phenomenon of self-desiccation is pronounced in high strength concrete, because the relatively small amount of water used for mixing is rapidly consumed by early age hydration of cement. Actually that is the main reason of the large amount of autogenous shrinkage in this type of concrete.

Previous research conducted in this particular field revealed that autogenous shrinkage is influenced by water to binder ratio and dosage of microsilica (Brooks *et al.*, 1999). Other factors such as cement type and fineness, mineral composition of cement, inclusion of chemical admixtures and aggregate* content have been identified to have an effect on autogenous shrinkage. It had been shown that the greater part of total shrinkage of high strength concrete is contributed by autogenous shrinkage especially as the w/b decreases and the content of microsilica increases. Furthermore, in some model tests where high strength concrete was used it was reported that autogenous shrinkage might be responsible for self-stress generation and cracking (Paillere *et al.*, 1989). Extensive experimentations revealed that at early ages large tensile self-stresses were caused by restrained autogenous shrinkage. Moreover, the self-stress generation in early ages is strongly influenced by autogenous shrinkage and any concurrently occurring thermal strain. In such case the autogenous shrinkage

* Inclusion of aggregate leads to a reduction in autogenous shrinkage, as in the case of drying shrinkage.

strain must be superimposed on thermal strain in order to get the total strain of concrete (Tazawa and Miyazawa, 1996; Igarashi *et al.*, 2000).

There is experimental evidence in support of a relationship between the autogenous shrinkage and drying shrinkage. Both these two types of shrinkage of concretes with relatively low w/c ratio are found to be nearly the same. In other words, the shrinkage that has been regarded as the result of drying actually occurs independently of drying. Meanwhile, the reduction of weight indicates that drying is not responsible for the shrinkage of such concretes with low *w/c* (Tazawa and Miyazawa, 1995). Figure 4.15 shows the relation between autogenous and drying shrinkage as the *w/c* decreases and the amount of microsilica incorporated into the mix increases. Superplasticisers slightly affect (by reducing) the value of autogenous shrinkage and this might be due to the effect of these chemical admixtures on the hydration of concrete.

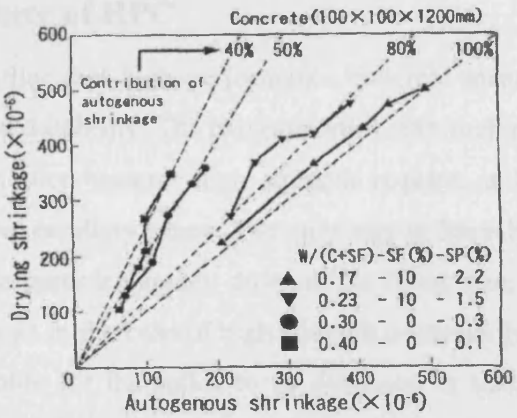

Figure 4.15: Relation between *w/c* and contribution of autogenous shrinkage (Tazawa and Miyazawa, 1995).

An interesting point regarding the autogenous shrinkage is the size effect, which cannot be neglected in both water-cured specimens and sealed specimens. This phenomenon is probably strongly related to the complexity of the discontinuous capillary water and the processes in the microstructure of the high strength concrete matrix (Tazawa and Miyazawa, 1995). Thus there is a lack of consistency between the values obtained in a number of different experiments. This is one of the problems that will be examined in this thesis for CARDIFRC®.

4.9 High performance concrete (HPC)

The term high performance concrete was introduced in order to replace a former name, which was high strength concrete. Unlike the latter, high performance concrete (HPC), besides the high strength, has also improved durability, which is a result of the extremely dense microstructure of such concretes. The huge reduction in total porosity – and more importantly – in pore sizes has resulted in considerable improvements in mechanical properties with remarkable strength values. With respect to strength, it should be noted that the meaning of the term "high strength" has changed significantly over the years. A value of 40 N/mm^2 in 1960's was considered as high strength concrete. This value increased in 50 N/mm^2 in early 1980's and a decade later the strength values were pushed up to 70 N/mm^2. Today, the high strength concrete is 100 N/mm^2, and even higher.

4.9.1 Microstructure of HPC

It was mentioned earlier that high performance concrete means concrete with high strength and improved durability. The two properties, although not necessarily related, are linked to one another because high strength requires a low volume of pores, especially of the larger capillary pores. The only way to have low volume of pores is for the mix to contain particles graded down to the finest size. This is achieved with the use of microsilica as in the case of high strength concrete. However, the mix must be sufficiently workable for the solids to be dispersed in such a manner that dense packing is achieved, which requires deflocculation of cement particles and is achieved with the addition of superplasticisers into the mix. The effect of microsilica and superplasticisers in the mix has been thoroughly examined in Chapter 2.

It is clear that high performance concrete is very dense and its microstructure contains a minimal volume of capillary pores. These pores become segmented upon curing. At the same time a significant proportion of the cement particles remain unhydrated even when the specimens are cured in water. This is due to the fact that water cannot penetrate into the matrix. These unhydrated cement particles can be viewed as extremely fine aggregates, which are well bonded to the products of hydration (Neville, 1995).

4.9.2 Shrinkage of HPC

As has already been mentioned, in high performance concretes the w/b ratio is kept as low as possible. This results in an increase in autogenous shrinkage, whereas the drying shrinkage is minimised. Although for high w/b the latter is easy to be measured in the case of HPC the very early development of autogenous shrinkage during the early stages of hydration makes the measurement of drying shrinkage very difficult. The autogenous shrinkage, which is linked directly to cement hydration, starts to develop uniformly and isotropically in a matter of hours after the casting of concrete (mainly before 24 hours), whereas drying shrinkage starts to develop more slowly (it can take up to several days) at the exposed surface of the hardened concrete (Aitcin, 1999).

The addition of silica fume together with the reduction in the w/b causes a significant drop in the relative humidity during hydration. It has to be mentioned that the pozzolanic activity of the silica fume becomes predominant two weeks after mixing despite the very low relative humidity. As a consequence of self-desiccation, the cement paste undergoes shrinkage. Since the Young Modulus of the aggregates is higher than that of the cement paste, the autogenous shrinkage causes the formation of the tensile stresses in the matrix and in bulk deformation of the concrete itself (Lura *et al.*, 2001). Both these phenomena cause micro and macrocracking of the concrete matrix. Experiments on the effect of curing temperature on the autogenous shrinkage revealed that the variation of temperature does not cause large differences in the total amount of deformation. Higher temperatures did not lead to larger deformations but they caused faster shrinkage and faster development of self-induced stresses (Lura *et al.*, 2001). The effect of the superplasticisers on the autogenous shrinkage of HPC has not been thoroughly examined in the literature. There are some indications that the use of more effective superplasticisers will lead to a reduction of the initial autogenous shrinkage (in the first three days) (Tazawa and Miyazawa, 1995). However, such results are dependent on the w/c and the cement type used, and cannot be considered as a significant approach to the study of superplasticiser effect. Furthermore, as it was explained in a previous section of the current Chapter it is strongly believed that the superplasticisers do not have a dominant role in the development of autogenous shrinkage strains.

In the case of Ultra High Performance Concretes (UHPCs – compressive strengths reaching 200MPa) the phenomenon of shrinkage is much more complex. Extensive experimental work has revealed that the shrinkage of such concretes is followed by more intense shrinkage occurring before and during setting (Cheyrezy and Behloul, 2001). This shrinkage was found to be non-isotropic and corresponds to settlement in the mould. From the same set of results it was observed that shrinkage (linear and volumetric) remains non-isotropic at the early ages of the hardened concretes and furthermore, seems to be affected the geometry of the sample. This fact was observed in the case of conventional concretes also. Another very interesting point regarding the autogenous shrinkage of UHPCs is that they do not follow the trend observed in common HPCs, where the autogenous shrinkage increased as the *w/b* decreased. For UHPCs made with *w/b* less than 0.17, the last statement cannot be extended. It was observed that below that limit the autogenous shrinkage steadily decreased. This is probably due to the fact that the reduction of hydration products prevail all the other phenomena involved. At this point it has to be mentioned that for such concretes the autogenous shrinkage is a long lasting phenomenon – it was found that it was still in progress even after six months – whereas drying shrinkage (if any) could hardly be detected after ten months. Finally, post-setting heat treatment (at 90°) was observed to lead to complete elimination of any later shrinkage.

4.9.3 Microcracking

A factor that has to be taken into serious consideration when studying volume changes is the occurrence of microcracking. Past research in this field has revealed that pastes with w/c ratio between 0.3 and 0.4 have shown microcracks after 30 days (Setter and Roy, 1978). Microcracking, provoked by endogenous and drying shrinkage, was also observed by Sadouki and Wittmann (Sadouki and Wittmann, 2000). The lower the water to binder ratio the more susceptible were the pastes to microcracking. It has to be mentioned that this phenomenon is negligible in the normal concrete due to the relatively high *w/c* ratio. The presence of microcracking requires that strains and tensile stresses are present prior to the formation of the crack. The hardening binding cement matrix with low *w/c* ratio – such as in high performance concrete – is generally subjected to strong self-desiccation inducing internal drying. This self-

desiccation has been mentioned as the triggering factor for the formation of microcracks. The latter will result in expansion of the system resulting in that way in the reduction of shrinkage strains. Figure 4.16 indicates clearly how the microcracking affects the matrix leading to a reduction of autogenous shrinkage.

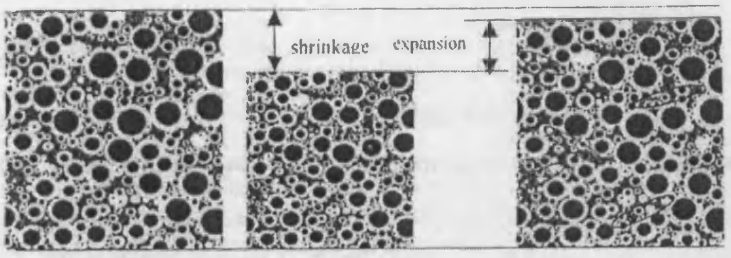

Figure 4.16: Effect of microcracking on the volume changes of hardening cement pastes. Middle: autogenous shrinkage. Right: swelling due to microcracking (Breugel, 2000).

It has to be mentioned that endogenous shrinkage plays a major role with respect to crack formation in high performance concrete. The microcracked matrix in high performance concrete was found to be statistically isotropic (Sadouki and Wittmann, 2000).

4.10 Fibre reinforced concrete

According to ACI, fibre reinforced concrete (FRC) is that kind of concrete made of hydraulic cements containing aggregate of various sizes and amounts and discontinuous discrete fibres (ACI Committee 544, May 1982). The fibres used have to be not more than 50mm and 500μm in length and diameter respectively. Furthermore, the volume fraction of fibres used must not exceed 2% of total volume of mix. A typical water to cement ratio used in FRC mixes is in the range of 0.35.

4.10.1 Durability

Fibre Reinforced Concrete is generally a very durable material regardless of the type of fibre used. Steel fibres used these days are mainly brass coated in order to avoid the corrosion problems of the past. Generally, steel fibres are well protected in uncracked concrete where the high alkalinity provides a passive layer on the fibre surface. But even in the past where non-stainless steel fibres were used serious corrosion needed

many years to occur. In the case of cracked concrete, fibres (if not corrosion protected) may corrode very rapidly in the presence of chlorides. More aspects regarding the properties and the development of the fibre reinforced concrete have been examined in Chapter 2.

4.10.2 Shrinkage of FRC

Information published in the literature regarding this particular area show that steel fibres generally tend to produce a slight reduction in the shrinkage of concrete compared to that of plain concrete. It was found that the presence of fibres exercises a clear restraint to free shrinkage up to 20% (Johnston, 1980). The restraint was found to increase with increasing fibre volume and a reduction of 40% in total shrinkage was achieved. Other researchers concluded that the reduction in shrinkage of steel fibre reinforced concrete was a function of exposure age, volume fraction of fibres and the aspect ratio of fibres incorporated into the mix (Chern and Young, 1990). It was also observed that the shrinkage-time curves for steel fibre reinforced concrete were similar to the corresponding for plain concrete. This could be an indication that the non-linear diffusion theory of concrete can be applied to steel fibre reinforced concrete in order to predict long term shrinkage values. However, in the case of high strength concrete the behavior of steel fibres is not yet clear.

4.11 High performance fibre reinforced concrete (HPFRC)

The production of a cement-based material having high tensile and compressive strengths, remarkable energy absorption capacity and which will be homogeneous and isotropic (almost similar to cast iron) is no longer a utopia any more. The incessant research in the field of FRC has led to the production of HPFRC, which shows a combination of amazing properties compared to other cementitious composites.

4.11.1 Microstructure of HPFRC

Microsilica besides being perfect microfiller between the cement particles and having a very good pozzolanic behavior reduces the rate of internal liquid migration by blocking capillary channels between cement grains. This results in a paste with

enhanced degree of internal cohesion. In other words, the produced paste exhibits increased resistance to bleeding, a property which enables the use of such material in severe wet environment. Furthermore, the blocked capillary channels lead to the reduction of the diffusion of the chloride ions through the binder. This implies that high performance paste is much more durable than ordinary cement paste.

The use of a highly reactive pozzolanic material such as microsilica in comparison with the cement and the addition of superplasticiser leave no doubt about the compressive strength of HPC. The strength of these materials can reach the value 270 MPa, ranging between 130 MPa to 270 MPa, depending upon the type of aggregate used. However, high performance pastes are very brittle -- the higher the compressive strength the higher the brittleness. Nevertheless, it is only the binder phase, which is brittle. Addition of a suitable aggregate to the binder phase leads to a reduction in brittleness and to a much more ductile composite material with reduced shrinkage. The ductility and therefore the toughness of the composite are further increased by the incorporation of fibres. Both aggregates and fibres have a dual effect on the high performance concrete matrix. First of all, they reduce the brittleness and convert a rather brittle material to a ductile one and secondly they reduce the tendency of the matrix to crack. Standard proportions of aggregates and fibres do not exist. The composition of such mixes is optimized in order to suit particular applications.

It can be said in general that in high performance cements the strain hardening response is achieved at relatively low volume fractions of fibre (4-6% by volume). This is believed to be the result of the very dense microstructure of high performance matrix, which enables better mechanical anchorage of the fibres to the matrix (Figure 4.17), since the contact area between the fibres and the surrounding matrix has been enhanced.

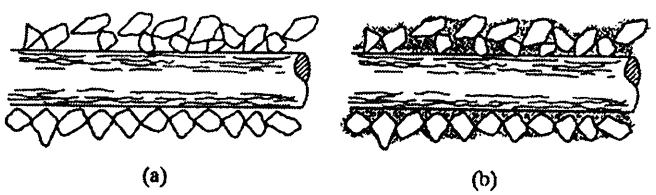

Figure 4.17: Fibres embedded in (a) cement paste, (b) dense high performance paste (Karihaloo, 1995).

The effect of the incorporation of fibres in the matrix as well as the microstructural mechanisms associated with the addition of superplasticisers and microsilica in the cement paste have been extensively discussed in Chapter 2.

4.11.2 Shrinkage of HPFRCC

The following points can be observed in the literature regarding the shrinkage of high performance fibre reinforced concrete.

- Autogenous shrinkage in HPC lead to rapid cracking even in the absence of any evaporation. This phenomenon is probably linked with the intense excessive self-desiccation of such concretes. The incorporation of fibres into the high performance matrix lengthens the time before the occurrence of cracking – decreasing that way the shrinkage – and moreover provides a reliable crack arresting mechanism (Paillere *et al.*, 1989)
- Incorporation of fibres into the mix introduces an additional group of large pores. The interfacial zone between the fibres and the cement probably causes this group of pores. The latter is believed to reduce the capillary pressure in the cement paste, thus reducing the shrinkage cracking (Wang *et al.*, 2001).
- In the case of UHPCs incorporation of a small volume fraction of fibres into the mix (~2% by volume) causes a slight decrease in the autogenous shrinkage in the order of 10 – 20% (Cheyrezy and Behloul, 2001).
- The clumping pressure induced by shrinkage, which is acting on the aggregates and the fibres was found to be a function of time (Stang, 1996).

4.11.3 Shrinkage mechanisms

Deformations associated with a decrease of the relative humidity in the pore system have been discussed intensively in the past. Some of the major proposed shrinkage mechanisms are illustrated below. These mechanisms are the basis for the majority of the existing models regarding the volume changes of hardening cement pastes.

4.11.3.1 Changes in surface tension

A solid colloidal particle with radius r will experience a compressive stress P, as a result of the presence of surface tension γ_s, ($P = \frac{2\gamma_s}{r}$). Absorption of a water layer will change the surface tension by an amount $\Delta\gamma$. According to Gibbs the change in the surface tension is related to the change in the vapour pressure of the absorbed water (Breugel, 2000). For a change in vapour pressure from h_1 to h_2, Gibbs formed the following equation:

$$\Delta\gamma = RT \int_{h_1}^{h_2} \frac{w_a}{V_s} d(\ln h) \equiv RT \int_{h_1}^{h_2} \frac{w_a}{V_s} \frac{dh}{h} \tag{4.3}$$

where R is the universal gas constant, T is the temperature in Kelvin, w_a is the amount of water absorbed at the solid particles, V_s the volume of the absorbent and h the relative vapour pressure. Based on that principle, Powers derived the following equation, which describes the volume change in a solid particle:

$$\frac{\Delta V}{V} = \frac{2}{3} K \frac{RT}{M} \int_{h_1}^{h_2} \frac{w_a}{V_s} d(\ln h) \equiv \frac{2}{3} K \frac{RT}{M} \int_{h_1}^{h_2} \frac{w_a}{V_s} \frac{dh}{h} \tag{4.4}$$

where K is a coefficient that describes the compressibility of the solid particle and M is the molar mass of the absorbent, i.e. the water.

4.11.3.2 Variation of capillary depression

The mechanism of the variation of the capillary depression is deduced by the Kelvin and Laplace laws.

$$p_v - p_c = \frac{2\sigma}{r}\cos\theta \qquad \text{Laplace Law} \tag{4.5}$$

$$p_c - p_v = \frac{RT}{Mv}\ln(h) \qquad \text{Kelvin Law} \tag{4.6}$$

where: σ = surface tension of the water/water vapour interface

θ = moistening angle (Figure 4.18)

p_c = pressure in water

p_v = pressure in water vapour (often assumed zero)

r = radius of the pore where there is a meniscus

v = specific volume of water

M = molar mass of water

R = ideal gas constant

T = temperature in Kelvin

h = relative humidity

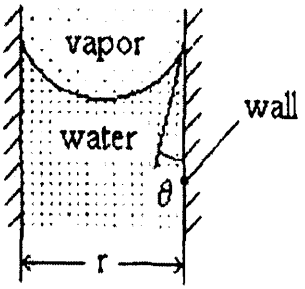

Figure 4.18: An unsaturated capillary (Hua *et al.*, 1995).

According to Kelvin and Laplace laws for a given unsaturated state, there is an access radius r_0 such that all capillaries with access radius larger than r_0 are filled with water and all other capillaries are empty. Such an access radius introduces a corresponding tension in the liquid phase, so the solid skeleton undergoes compression, whence the shrinkage (Hua *et al.*, 1995).

The only subject of discussion for this mechanism is the validity of the above laws and the existence of the meniscus surface tension at microscopic scale. Extensive research in the area of the colloidal science has revealed that the meniscus effects can be precisely evaluated by the above laws for a meniscus radius greater than 50 Å. This implies that these macroscopic laws are valid only for relative humidity greater than 80% (Hua *et al.*, 1995).

4.11.3.3 Variation of disjoining pressure

This mechanism concerns the interaction between two solid surfaces, very close together, in the presence of absorbed water molecules. The thickness of a layer of absorbed water – at a given temperature – depends on the relative humidity. This layer of absorbed water can no longer develop freely above a certain relative humidity simply because the distance between the two surfaces is too small. If the relative humidity increased again, the thickness of the absorbed water layer becomes larger and tends to separate the two solid surfaces. Therefore, the latter undergo a pressure called the "disjoining pressure". This pressure reaches its maximum value at saturated state, so when the system "moves" from the saturated state to unsaturated state,

shrinkage takes place since the disjoining pressure decreases and the two solid surfaces come closer together (Hua *et al.*, 1995; Breugel, 2000). Measurements of the disjoining pressure revealed that it remains practically constant at high relative humidity (80% - 100%). This implies that at such high levels of relative humidity the variation of the disjoining pressure does not cause much change between absorbed and unabsorbed water molecules.

The volume changes in the range of relative humidity up to 50% could be attributed to changes in the surface tension of the solid according to Bangham equation, whereas at relative humidity below 50% the disjoining pressure would be the dominant mechanism (Breugel, 2000). According to Hua (Hua *et al.*, 1995) the variation of capillary depression is the dominant mechanism for relative humidity between 80% up to saturation. On the other hand, at such high relative humidity levels the disjoining pressure mechanism was found not to generate substantial volume changes.

4.11.3.4 Drying process and self-desiccation

In order to be able to evaluate the endogenous and drying shrinkage strains the spatial moisture variations in the material must be known for any time. Drying of concrete is due to moisture migration and moisture loss. Actually, moisture flow in porous materials like concrete is a very complex process involving capillary suction, capillary condensation and subsequent evaporation, gas phase flow and surface diffusion (Quenard and Sallee, 1992). Mathematically, the drying process under isothermal conditions can be expressed by the following second order partial differential equation (Sadouki and Wittmann, 2000; Zijl *et al.*, 1998; Bazant, 1988):

$$\frac{\partial h}{\partial t} = \nabla \cdot \left(D(h, \tau) \nabla h \right) \tag{4.7}$$

where h is the moisture potential, τ is the age of the material, $D(h,\tau)$ is the moisture transfer coefficient. If the material is subjected to self-desiccation the term $q(\tau)$ representing the rate of moisture loss in the system has to be added on the right side of the above equation (Sadouki and Wittmann, 2000). The equation governing drying and self-desiccation is as follows:

$$\frac{\partial h}{\partial t} = \nabla \cdot (D(h,\tau)\nabla h) + q(\tau) \tag{4.8}$$

It has to be mentioned that both parameters $D(h,\tau)$ and $q(\tau)$ are strongly dependent on the composition of the cement-based material. In case the specimen is subjected to a given surrounding atmosphere with a relative humidity h_{ext}, then the moisture flux due to an exchange between the system and the environment can be expressed as follows:

$$\vec{q} = \beta \cdot (h_s - h_{ext}) \cdot \vec{\Gamma} \tag{4.9}$$

in which β is the hygral convection coefficient and h_s the humidity on the exposed surface Γ of the specimen. It is apparent that if the specimen is well sealed the moisture flux in the last equation is zero, i.e. the last equation becomes equal to zero. It has to be mentioned that in the approach discussed above, thermal effects are not taken into consideration. However, coupled heat and mass transfer can be simulated in a similar way (Sadouki and Wittmann, 2000).

4.12 Conclusions

To gain more knowledge of the relationship between the autogenous shrinkage of hardening concrete and the autogenous shrinkage of paste it is necessary to look at the material microstructure in more detail. The way the chemical compounds of cement react with water and one with another is a very important issue in this respect. The various types of shrinkage have been examined as well as their relationship. The study was mainly focused on the autogenous shrinkage as this is the main topic of the current thesis. The development of autogenous shrinkage strains for various concrete types has been examined and the effect of the addition of microsilica and fibres to the matrix has been addressed. Finally, a brief outline of the apparent shrinkage mechanisms has been given in order to give a better understanding of the triggering mechanisms behind the phenomenon of self-induced shrinkage.

Chapter 5: Modelling of Autogenous Shrinkage

5.1 Introduction

As has been discussed in the previous Chapters, during the hydration process of a low water to cement ratio cement paste a change of the original mix volume is observed. If the moisture exchange with the surrounding environment is prevented, the volume reduction of the hardening cement paste can only be the result of either chemical or physical processes that take place during hardening. Moreover, as has been outlined earlier, the volume reduction triggered by the chemical reactions between the cement and water gives rise to a pore system in the cement paste.

Summarising what has been discussed previously regarding the associated volume changes in cement based materials it can be said that autogenous shrinkage is defined as the external macroscopic dimensional reduction (volume or linear) of a cement-based system occurring under isothermal conditions without exchange of moisture with the surrounding environment (Tazawa *et al.*, 1995). Autogenous shrinkage is a phenomenon that is dominant in cement-based materials with a low water to cement ratio. The main driving force for such shrinkage is the cement hydration. In cement-based materials with water to cement ratio below 0.3, the amount of water can become so low during the ongoing hydration that the relative humidity in the pore system will drop below 100%. As a result such materials exhibit self-desiccation shrinkage. Furthermore, the presence of microsilica in the paste promotes the autogenous shrinkage strains since it leads to a very fine pore structure which increases capillary stresses (Bisshop, 2002). It has to be mentioned that the pozzolanic reaction of microsilica involves an amount of chemical shrinkage, but in case of cement-based materials with very low water to cement ratio (such as CARDIFRC®) the autogenous shrinkage mechanism is assumed to be the dominant shrinkage mechanism (under isothermal conditions) and therefore any other shrinkage strains are neglected (Tazawa *et al.*, 1995; Jensen and Hansen, 1996).

In this Chapter we will describe how the induced stresses from autogenous shrinkage can be modelled. The analysis will be focused on the mechanisms behind the

autogenous shrinkage. Analysis of the moisture state in the constantly changing pore system is the primary aim of this Chapter. We will then show how the restraint offered by the fibres to the free autogenous shrinkage of CARDIFRC® can be captured through the increasing stiffness of CARDIFRC® as the hydration proceeds.

5.2 Thermodynamic approach

There is a general agreement in the literature that the volume changes in the cement-based materials are the result of the reduction in the relative humidity. Based on this concept, several authors have developed models using thermodynamic principles in order to predict these volume changes.

The thermodynamic phenomena in a porous cement-based material have been discussed in depth by several authors (Koenders, 1997; Breugel, 1991; Bazant and Wittmann, 1982; Hua *et al.*, 1995). The basis of discussion is the Gibbs theory (1906) (Koenders, 1997), which deals with the equilibrium between the gas pressure in an arbitrary volume of a closed system and the product of the stress and area in the adsorption layer against the pore walls. Regarding the cement-based materials this theory can be applied for thermodynamic analysis of the moisture state in the changing pore space. In cement-based materials the equilibrium must be established between the volume and pressure in the empty pore space (gas pressure) and the surface tension in the adsorption layer at the total pore wall area.

5.2.1 Existing thermodynamic models

The Gibbs theory formed the basis for many researchers in order to develop models able to predict the microstructural deformation of cement-based materials in relation to the changes in the relative humidity. The models proposed described the swelling of an oven-dried material on exposure to water. The more fundamental models regarding the explanation of the mechanisms behind the swelling of the material are three, namely the Powers-Brunaur model, the Feldman-Sereda model and the Munich model (Koenders, 1997). In these three models the swelling mechanism is described as a function of the adsorption of the water molecules to the internal surface. The

main difference between them is the assumed driving force behind the phenomenon of the expansion of the dry microstructure.

In Powers-Brunaur model it is assumed that the presence of water molecules between the individual particles provokes the separation of the latter and consequently causes the swelling of the microstructure on exposure to water. However, the chemical bonds between these individual particles are assumed to limit the swelling of the microstructure (Koenders, 1997).

In Feldman-Sereda model, the swelling mechanism is not considered to be a result of single mechanism but a phenomenon that is triggered by several mechanisms. These are:

i. the reduction of free surface energy due to water molecule attraction
ii. the penetration of water molecules between layers
iii. the menisci effect due to capillary condensation
iv. the ongoing hydration effect

The changes in the free surface energy are considered to be responsible for the swelling of microstructure according to Munich model. This can be considered as a change of the surface tension in the adsorption layer at the pore wall area. It has been found that for values of relative humidity below 40% the relationship between the change of free surface energy and the swelling of microstructure is considered to be linear (Figure 5.1). For higher values of relative humidity this relationship becomes non-linear (Koenders, 1997).

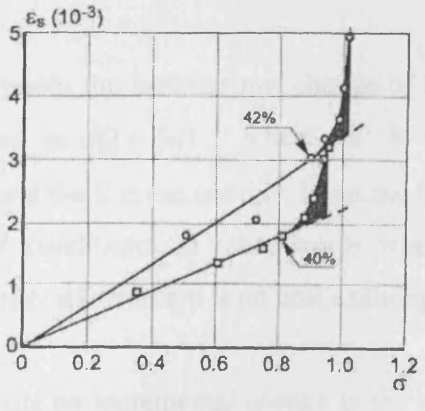

Figure 5.1: Swelling deformation versus changes of surface tension according to Munich model (Koenders, 1997).

For relative humidity range between 40 to 100% the swelling deformations can be attributed to what is known as disjoining pressure which has been discussed in Chapter 4. All three above mentioned thermodynamical models have proved to be adequate to describe the swelling of a dry microstructure exposed to a very humid environment. Therefore the basis of the theory as developed by Gibbs can be extended for the case of the cement-based materials. The model proposed in this chapter is based on the thermodynamic mechanisms and their associated microstructural changes. The main difference from the above-mentioned models is that the proposed model is going to be used in order to predict the autogenous shrinkage strain development and not the swelling of the microstructure.

5.2.2 Thermodynamic analysis of a pore system

The changes in the associated thermodynamics can be used to determine the volume changes in the hardening cement paste. A change in the degree of hydration will affect the thermodynamic equilibrium in a continuously changing pore volume. It becomes obvious that as the hydration proceeds the actual state of energy of the paste changes and a new state of equilibrium must be established. By using the first law of thermodynamics this can be described by the following equation:

$$dQ = dU + dW \tag{5.1}$$

where: dQ = heat produced during an infinitesimal change of a mechanical system
dU = internal energy in the system
dW = work carried out by the system

In the case of a closed system the infinitesimal change of the heat increment (dQ) is mathematically expressed as $dQ = SdT$, where dT is the absolute temperature increment of the system and the S is the entropy. From the last relationship it becomes clear that for isothermal conditions, in other words when the temperature of the system remains constant (i.e. dT=0) there is no heat exchange so that dQ=0.

In a hardening cement paste an incremental change in the hydration process affects a large number of parameters associated with the conservation of internal work. After

mixing, cement paste consists only of water-cement dispersion. At this early age, no skeleton has been formed by the hydrating cement grains since these are distributed randomly in the paste. Furthermore, at this early stage all the pores are considered to be full of water. At some stage of the hydration process the pores are partly filled with water. Air has now filled the empty pore volume. A thin layer of water molecules is adsorbed on the pore wall area and there exists a water/vapour interface between the adsorbed water and the air in the pore volume. It is clear that such a system can be considered as a three phase system – adsorbed water – interface layer – air. As the hardening proceeds the thickness of the adsorption layer changes. Gibbs theory gives a macroscopic definition of the adsorbed volume (Koenders, 1997).

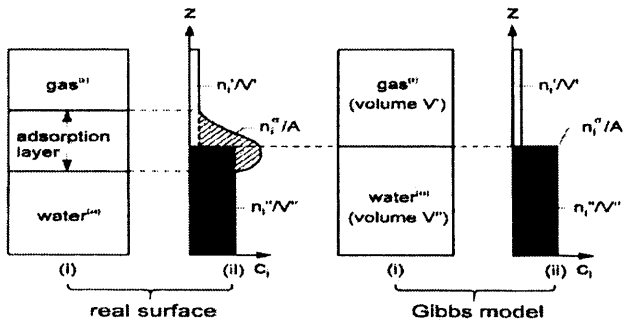

Figure 5.2: Representation of the three phases system. Left: Real Situation, Right: According to Gibbs Model (Koenders, 1997).

Since the thickness of the adsorption layer changes as the hardening proceeds it is useful to express this layer in weight fractions or moles. As we can see from Figure 5.2, in the real situation the thickness of the adsorption layer is finite, whereas in the Gibbs model it is initially taken as zero. The actual volume of the adsorption layer can be found with the help of the concentrations of the actual phases. By assuming that c_i is the concentration of component i in moles per unit volume, the actual number of moles is given by $n_i=c_iV_i$. For the number of moles in the empty pore volume in the cement paste we have the following equation:

$$n = n_\sigma + n_{liquid} + n_{gas} \tag{5.2}$$

where n = total number of moles in the system

n_σ = number of moles adsorbed to the pore wall area

n_{liquid} and n_{gas} = number of moles present in the water and air phases respectively

The thickness of the adsorption layer in turn can be calculated using the following relationship:

$$\Gamma = \frac{n_\sigma}{A_{por}(\alpha)} \tag{5.3}$$

where $A_{por}(\alpha)$ is the total pore wall area. Equation (5.3) shows that the thickness of the adsorption layer is also a function of the degree of hydration α.

In a hardening cement paste it can be assumed that there is no internal energy dissipation and therefore the internal energy of the system will be constant (i.e. dU=0). In other words all the energy is conserved during hardening. A more simplified formulation results by regarding the conservation of actual energy level in the system, and this concerns only the internal work done by the system which is also constant (i.e. dW=0).

Consider now the three-phase system, as described above. An infinitesimal change of the mechanical work dW in the pore system can be formulated as follows:

$$dW = d(p_g V_g) - d(\sigma A_{por}) = 0 \tag{5.4}$$

where: p_g = gas pressure in empty pores

V_g = volume of gas in empty pores

σ = surface tension (free surface energy)

A_{por} = the pore surface area that is subjected to the surface tension

By expanding equation (5.4) we get the following relationship:

$$dp_g V_g + p_g dV_g = d\sigma A_{por} + \sigma dA_{por} \tag{5.5}$$

For an incremental change, if we have V_g = constant, then $dV_g = 0$.

On the other hand, if A_{por} = constant, then $dA_{por} = 0$.

Due to these considerations, equation (5.5) yields:

$$dp_g V_g = d\sigma A_{por} \Rightarrow \frac{d\sigma}{dp_g} = \frac{V_g}{A_{por}} \tag{5.6}$$

Equation (5.6) describes the change of the surface tension in adsorption layer as a function of the gas pressure in the empty pore volume. The gas pressure is assumed to to follow the "ideal" gas law which states that:

$$\frac{p_g V_g}{T} = n_\sigma R \tag{5.7}$$

As it can be observed from the last equation the gas volume can be expressed as a function of the pressure that prevails in the gas. Note that R is the "ideal" gas constant and T is the absolute temperature of the system.

By combining equations (5.6) and (5.7), a new relationship is developed that connects the surface tension in the adsorption layer and gas pressure in the empty pore volume.

$$\frac{d\sigma}{dp_g} = \frac{RTn_\sigma}{p_g A_{por}(\alpha)} \tag{5.8}$$

Now by substituting equation (5.8) into equation (5.3), we have:

$$\Gamma = \frac{p_g}{RT}\frac{d\sigma}{dp_g} \quad \Rightarrow \quad \int d\sigma = RT \int_{p_g/p_0}^{p_g/p_0=1} \Gamma \frac{dp_g}{p_g}$$

Integration of the last equation leads to the basic formulation for the surface tension (Equation 5.9).

$$\sigma = RT \int_{p_g/p_0}^{p_g/p_0=1} \Gamma d\left[\ln(\frac{p_g}{p_0})\right] \tag{5.9}$$

Equation (5.9) is the basic equation that gives the surface tension. As can be seen the surface tension is a function of the relative humidity (p_g/p_0) present in the empty pore volume, and a change of this relative humidity will cause an increase in the surface tension (Koenders, 1997). Equation (5.9) can be used to establish iteratively the thermodynamic equilibrium. It has to be mentioned that the thickness of the adsorption layer Γ is also considered to be a function of this relative humidity (p_g/p_0) i.e. $\Gamma = \Gamma\left(\frac{p_g}{p_0}\right)$. In other words, a change in the relative pressure in the pore volume not only will cause changes in the surface tension but also to the thickness of the adsorption layer. Analytical solution of equation (5.9) is given in Appendix B.

5.3 Relative humidity and air (gas) pressure in the empty pore space

Immediately after setting, the microstructure of a hardening cement paste starts to develop. That is the point where the pore structure starts to develop too. Initially the relative humidity in the pore spaces is 100% and the pressure of the system is equal to the atmospheric pressure. As hydration proceeds water reacts with the anhydrous cement particles to form new hydration products. Due to this process parts of the pores remain filled with capillary water and parts of the pores become empty. It is clear that the relative humidity will drop below 100% and implicitly the pressure in the system will be less than the atmospheric. In the numerical model HYMOSTRUC (Chapter 2 – Section 2.3.2.3), which will be the basis of our modeling, the relative humidity in the pore space is described by the Kelvin equation (Breugel, 1991; Hedlund and Westman, 1999).

$$\ln(RH) = \ln\left(\frac{p_g}{p_0}\right) = \frac{-4\sigma}{RT\gamma_w\phi_{wat}} \tag{5.10}$$

The above equation describes the relative humidity of the system as a function of the actual surface tension σ and the widest pore diameter that is still completely filled with water, namely ϕ_{wat}. As hydration proceeds both the surface tension and the pore

diameter will change. Further progression of the hydration will cause a reduction of the capillary volume and hence a reduction of the pore diameter that is still filled with water. On the other hand such a reduction in the capillary volume leads to the increase of the surface tension. Note that γ_w represents the specific density of water in N/m^3.

The air (gas) pressure in the empty capillary pore space can be determined by using Boyle's law (Koenders, 1997). Therefore, the pressure component (p_g) in a gradually emptying pore space can be determined from:

$$p_g = \frac{RT}{V_w} \ln (RH) \tag{5.11}$$

Note that $RH = p_g/p_0$, where p_0 is the atmospheric pressure. In the literature we meet references stating that the relative humidity in the pore system of plain cement pastes generally varies between 80% and 100% (Jensen and Hansen, 1999; Jensen and Hansen, 2001). Powers however suggested that, that there exists a lower bound of 75% on the RH below which autogenous shrinkage can be assumed not to take place (Wittmann, 2001). Applying equation (5.11) within a relative humidity range of 75% and 100% the associated pressure in the empty pore space is found to range between -35 MPa and 0 MPa (Koenders, 1997). It is evident that such high values of reduced pressure in the pore system may lead to significant deformations of the microstructure. It is also clear that since the relative humidity is strongly affected by the degree of hydration, the pressure (and hence the corresponding deformations in the microstructure) in the empty pore space will also be strongly dependant upon the degree of hydration.

5.4 Dimensional changes in cement paste

As has been mentioned, as the hydration proceeds the relative humidity in the gradually emptying pore space will decrease. From a thermodynamic point of view, the relative humidity can be considered as the main parameter of the system. As it was shown above, equations (5.9) and (5.11), a change in the relative humidity of the system will result not only in a change of the air (gas) pressure in the empty pore

space (equation 5.11) but also in a change of the surface tension in the adsorption layer at the pore wall area (equation 5.9).

The surface tension can be considered as the driving force behind the mechanisms that cause the shrinkage of the microstructure. In the subsequent sections the constitutive equation proposed by Bangham, will be adopted in order to relate the microstructural deformation to the surface tension in the adsorption layer. Thus, the microstructural deformations of hardening cement-based materials can be also linked to the continuously decreasing relative humidity in the gradually emptying pore space. In other words, the adoption of the Bangham concept will allow us to relate the microstructural deformations to the phenomenon of self-desiccation, as the cementitious material dries out without any evaporation.

5.5 The modified Bangham concept

The reduction of the relative humidity in the pore space results in volume changes in hydrating cement paste (self-desiccation). Bangham first found that deformational changes of coal could be related linearly to the change in the effective surface tension ($\frac{\Delta L}{L} = \lambda \Delta \gamma$, where λ is a proportionality factor) (Koenders and Breugel, 1999; Day and Marsh, 1988). Wittmann has found that this approach is valid for hardened cement paste at low relative humidity. However, it was noticed that the Bangham equation was more of an empirical law – having a semi-phenomenological basis – and it should not considered as a physical law (Day and Marsh, 1988).

In the case of the hardening cement paste, the material properties and the state of the water change continuously as the degree of hydration increases. Therefore, the relationship between the external deformation and the change in the effective surface tension has to be incremental:

$$\frac{\partial \varepsilon_{\alpha}}{\partial \alpha} = \lambda \frac{\partial \sigma}{\partial \alpha} \tag{5.12}$$

Here $\partial\varepsilon_a$ is the strain increment that describes the microstructural deformation of the hardening paste – autogenous shrinkage due to self-desiccation - $\partial\sigma$ the surface tension increment and λ a proportionality factor. The latter is nothing but the compliance modulus of the cement paste and is strongly related to the degree of hydration. Bangham in his original study has proposed the following relationship in order to determine this proportionality factor (Koenders, 1997):

$$\lambda = \frac{\sum \cdot \rho}{3E} \tag{5.13}$$

where Σ is the pore wall area per unit weight, ρ is the density of the material and E the Young modulus. For hardening cement paste, these parameters cannot be considered as constants since they change as the hardening process takes place. It is clear that equation (5.13) has to be modified in order to take into account the volumetric changes in hardening cement paste. Hiller in his study proposed an equation that takes into account these volumetric changes (Koenders, 1997):

$$\lambda(\alpha) = \frac{\sum(\alpha) \cdot \rho_{pa}}{3E_{pa}(\alpha)} \tag{5.14}$$

where: $\sum(\alpha) = A_{por}(\alpha) - A_{wat}(\alpha)$ = (total pore wall area) – (pore wall area of water-filled pores) = pore wall area of the empty pores.

ρ_{pa} = Specific mass of the cement paste

$E_{pa}(\alpha)$ = Modulus of elasticity of the cement paste

α = degree of hydration

Having in mind that the specific mass of the cement paste is strongly dependant on the water to cement ratio the above relationship can be modified to give the following constitutive equation (Koenders, 1997):

$$\lambda(\alpha, RH, w/c) = Z \frac{\{A_{por}(\alpha) - A_{wat}(\alpha, RH)\} \cdot \rho_{pa}(w/c)}{E_p(\alpha)} \tag{5.15}$$

where Z is a constant. In the following sections, we will describe how the parameters of the above equation are determined. We will also exploit the evolution of the paste stiffness, mortar and CARDIFRC with hydration to account for the restraint offered to the free autogenous shrinkage of the CARDIFRC paste by fine aggregate and fibres.

5.6 Pore wall area of the empty pores

As has been explained in the previous chapter (Chapter 4 – Section 4.5.2) the pore structure of cement paste consists of two main types of pores namely the narrow interlayer or gel pores and the wider capillary pores. With the progress of hydration, and therefore as the degree of hydration increases, the pore volume of the system decreases at the cost of the larger pores. The smaller pore regions accumulate the remaining water for hydration, whereas the larger pores are emptied. The cumulative pore size distribution for the capillary pore water can be described mathematically using the following expression, developed by Breugel (1991) in his study:

$$V_{por} = \mathrm{a}\ln\left(\frac{\phi}{\phi_0}\right) \tag{5.16}$$

where V_{por} is the pore volume, ϕ the diameter of the capillary pore, ϕ_0 the minimum capillary pore diameter and "a" is the so-called pore structure constant. This constant can simply be found by dividing the pore volume V_{por} by the corresponding pore range $\ln(\phi/\phi_0)$. Extensive research in this field revealed that the pore structure constant strongly depends on the fineness of cement and ranges between 0.05 for coarse cement to 0.15 for fine cement (Koenders, 1997; Moukwa and Aitcin, 1988; Winslow, 1990).

Breugel (1991) in his study proposed a relationship that could give the capillary pore volume of all pores with diameter $\leq\phi$:

$$V_{\leq\phi} = \mathrm{aV}\ln\left(\frac{\phi}{\phi_0}\right) \tag{5.17}$$

where V is a volumetric unit. Note that the pore volume of pores having diameters smaller that 0.002 μm, i.e. the gel pores are not included in the pore volume calculated in the equation (5.17). Now, let us see how the pore wall area of the empty pores can be obtained from equation (5.17). By differentiating with respect to ϕ, we have:

$$dV_{\leq\phi} = \frac{aV}{\phi} d\phi \tag{5.18}$$

where the constant ϕ_0 has been consumed in volume V. By assuming that all pores have cylindrical shape, pore length l_ϕ and diameter ϕ (both in μm) the volume of the pores can be obtained using the following expression:

$$dV_\phi = \frac{\pi\phi^2}{4} dl_\phi \tag{5.19}$$

Combining equations (5.18) and (5.19) it follows that:

$$dl_\phi = \frac{4aV}{\pi\phi^3} d\phi \tag{5.20}$$

Now, the pore wall area ΔA_ϕ can be obtained by using the following expression:

$$dA_\phi = (\pi\phi) dl_\phi = \frac{4aV}{\phi^2} d\phi \tag{5.21}$$

A simple integration of equation (5.21) between the limits ϕ_0 and ϕ_{por} gives the total pore wall area A_{por}:

$$A_{por}(\alpha) = -4aV\left\{\phi_{por}^{-1}(\alpha) - \phi_0^{-1}\right\} \tag{5.22}$$

Equation (5.22) gives the total pore wall area as a function of the degree of hydration α. The units of the total pore wall area are μm^2 per unit volume V. Here $\phi_{por}(\alpha)$ is the maximum pore size (its calculation will be explained later) and ϕ_0 is the smallest capillary pore. $A_{por}(\alpha)$ is the first factor in equation (5.15).

In the same manner, and after a series of calculations involving differentiations and integrations, the wet pore wall area $A_{wat}(\alpha)$ is obtained:

$$A_{wat}(\alpha) = -4aV\left\{\phi_{wat}^{-1}(\alpha, RH) - \phi_0^{-1}\right\} \tag{5.23}$$

Therefore, the factor $\Sigma(\alpha)$ in equation (5.14) is simply calculated by subtracting equation (5.23) from (5.22):

$$\sum(\alpha) = A_{por}(\alpha) - A_{wat}(\alpha) = -4aV\left(\phi_{por}^{-1}(\alpha) - \phi_{wat}^{-1}(\alpha, RH)\right) \tag{5.24}$$

In the case where $\phi_{wat}(\alpha,RH)$ is equal to $\phi_{por}(\alpha)$, all the pores in the system are filled with water. For this particular situation, it is apparent that the relative humidity in the system is 100%. From equation (5.24) we have that $\Sigma(\alpha)$ is equal to zero and therefore by using relationships (5.14) and (5.12) it can be concluded that in such a case (RH = 100%) there will be no microstructural changes. As hydration proceeds, the relative humidity will drop, the pores will be gradually emptied, the surface tension will increase and eventually the microstructure will start to deform. This deformation is described by equation (5.12), with $\lambda(\alpha)$ given by equations (5.14) and (5.24).

5.7 Specific mass of plain cement paste

The proportionality factor λ defined by equation (5.15), depends on the specific mass of the cement paste, ρ_{pa}. Moreover, the deformation mechanism described in equation (5.12) is also dependant on the specific mass of the cement paste. The relationship giving the specific mass of the cement paste according to Koenders (1997) is as follows:

$$\rho_{pa} = \frac{\rho_{ce}(1+\omega_0)}{1+\rho_{ce}\omega_0} \tag{5.25}$$

where ρ_{pa} is the specific mass of the cement paste, ρ_{ce} is the specific mass of the cement and ω_0 is the water to cement ratio of the paste. Figure 5.3 shows the relationship between the specific mass of the paste and the water to cement ratio.

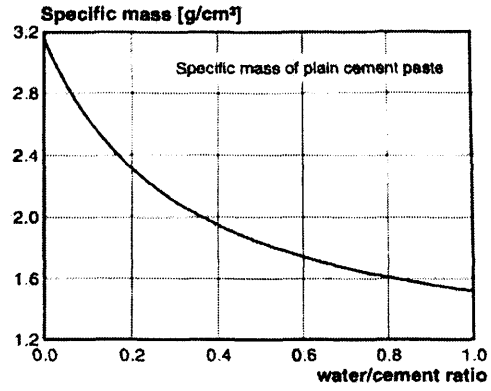

Figure 5.3: Specific mass of the cement paste against the water to cement ratio (Koenders, 1997).

5.8 Modulus of elasticity of hardening cement paste

A very significant parameter in the calculation of the deformations in the microstructure (equation 5.12) is the modulus of elasticity appearing in equation (5.15). The subject of modulus of elasticity has been also addressed briefly in a previous chapter (Chapter 2 – Section 2.2.5.1). As has been mentioned earlier such a mechanical property cannot be considered as a constant during hydration. The modulus of elasticity changes as the hydration evolves and the paste hardens. The modulus of elasticity has in some way to be modeled in order to take into account the changes in the elastic properties of the microstructure. In fact, the evolution of the stiffness of the CARDIFRC® with fibres can be exploited to calculate the restraint offered by the fibres to the free autogenous shrinkage of CARDIFRC® matrix without fibres.

A lot of work has been done regarding the evaluation of the elastic modulus of composite materials consisting of two or more distinct phases with quite different elastic properties (Nielsen, 1984; Phan-Thien and Huilgol, 1980; Phan-Thien and Karihaloo, 1994; Russel, 1972). Research has been also focused on the determination of the elastic properties of cement-based materials (Lange-Kornbak and Karihaloo, 1999; Nilsen and Monteiro, 1993; Tasdemir and Karihaloo, 2001; Ramesh *et al.*, 1996). Recently attention has been given to the evaluation of the modulus of elasticity of high performance concrete (Lange-Kornbak and Karihaloo, 1999; Zhou *et al.*, 1995; Ramesh *et al.*, 1996). One of the most common models for the prediction of the

modulus of elasticity is the Hobbs model, using the following expression (Tasdemir and Karihaloo, 2001).

$$E = E_p \left[\frac{(E_a - E_p)\cdot V_a + E_p + E_a}{(E_a + E_p)\cdot V_a + E_p + E_a} \right] \tag{5.26}$$

where E_p and E_a are the moduli of elasticity of the cement paste and aggregate, respectively. The volume fraction of the aggregate is denoted as V_a. From the above equation it was found that the modulus of elasticity increases significantly as the aggregate volume fraction increases. The experimental and model observations as well as the schematic representation of the Hobbs model are presented in Figure 5.4 below.

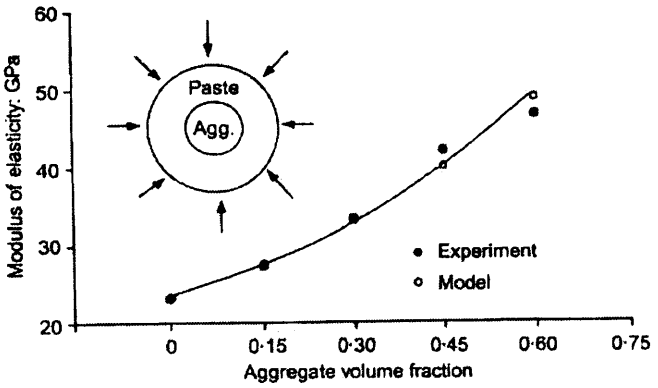

Figure 5.4: Modulus of elasticity of concrete against the aggregate volume fraction (Tasdemir and Karihaloo, 2001).

A model that can be of high interest in the case of CARDIFRC® is a model for plain concrete proposed by Nielsen (Lange-Kornbak and Karihaloo, 1999; Nielsen, 2001). The model used as basis a relationship, derived by Hill, between the average phase stresses and Young's modulus of the phases and is based on the assumption of a two-phase isotropic composite. The equation proposed by Nielsen is:

$$E = E_m \frac{n + \Theta + V\Theta(n-1)}{n + \Theta - V(n-1)} \tag{5.27}$$

where V is the volume fraction of the discrete phase, Θ is a geometry function accounting for the configuration of the discrete phase and n is the ratio of the modulus

of elasticity of the discrete phase to the modulus of elasticity of the continuous phase, E_m. Cement paste, mortar and CARDIFRC® can be considered as two phase cementitious composites with modulus of elasticity obtained by repeatedly using equation (5.27). In the following section we will show how equation (5.27) can be used in order to evaluate the modulus of elasticity of CARDIFRC®. For cement paste a distinction is made between water to cement ratios below and above $1.2\rho_w/\rho_c$, where the numerator represents the density of water and the denominator the density of unhydrated cement particles (i.e. $w/c \approx 0.375$). In the former range, the cement is considered as a collection of unhydrated cement particles with modulus of elasticity E_u embedded in a partially hydrated cement gel with $E_m = 24480*\alpha$ (MPa), where α is the relative degree of hydration (Lange-Kornbak and Karihaloo, 1999). This is of course a very restrictive assumption, the implications of which will be discussed later. The volume fraction of the unhydrated cement particles as well as the corresponding geometry function Θ are given by equations (5.28) and (5.29).

$$V = \frac{1 - 0.83\alpha\left(\frac{w}{c}\right)\left(\frac{\rho_c}{\rho_w}\right)}{1 + \left(\frac{w}{c}\right)\left(\frac{\rho_c}{\rho_w}\right)} \tag{5.28}$$

$$\Theta = \frac{1}{2}\left[\eta_u\sqrt{1-V}(1-n) + \sqrt{\eta_u^2(1-V)(1-n)^2 + 4n}\right] \tag{5.29}$$

where η_u is a shape factor of an unhydrated cement particle. For water to cement ratios greater than $1.2\rho_w/\rho_c$ (i.e. $w/c \approx 0.375$), the cement paste is regarded as a collection of capillary pores embedded in a solid (Lange-Kornbak and Karihaloo, 1999). In our case, this particular situation does not arise because the water to cement ratio for CARDIFRC® is less than 0.375. Note that for $w/c > 0.375$, Powers formula (Table 3.1) for unhydrated cement is applicable. It is unlikely that equations (5.26) and (5.27) will give accurate estimates of the modulus of elasticity until the mix has set. However, since equation (5.27) will not be used until 19 hours after casting when the mix has set, it is quite appropriate to use it in the present work.

5.9 Proposed model for the calculation of E of CARDIFRC®

CARDIFRC® is considered to be a two-phase material. The two phases are the mortar (cement paste + fine sand) and the steel fibres used. In order to evaluate the Young

Modulus, the concept explained in the previous section is going to be used. Equations (5.27), (5.28) and (5.29) will be modified in order to suit the CARDIFRC® case. The analysis will take place in three main stages starting from hydrating cement through mortar and concluding with CARDIFRC®.

Stage 1 – Hydrating Cement

For our study, the modulus of elasticity for normal Portland hydrating cement will be assumed to be A*α (MPa), where α represents the relative degree of hydration. The constant A (MPa) will be calibrated by matching the measured value of E of CARDIFRC with the model value in Chapter 7. It should be mentioned though that in the literature a value of A = 27200 MPa for ordinary Portland cement is often met. Thus for the cement paste, equation (5.27) can be written as:

$$E_{paste}(\alpha) = E_{hc}(\alpha)\frac{n_1 + \Theta + V\Theta(n_1 - 1)}{n_1 + \Theta - V(n_1 - 1)} \qquad (5.30)$$

In the above two-phase formula, the hydrating cement forms the continuous phase with the unhydrated cement particles as the discrete phase.

where $E_{paste}(\alpha)$= elastic modulus of the cement paste at a degree of hydration α

$E_{hc}(\alpha)$ = elastic modulus of the hydrating cement = A*α (MPa)

$n_1 = E_u / E_{hc}$

E_u = elastic modulus of unhydrated cement particles =A MPa

Θ = geometry function for unhydrated cement particles, given by equation (5.29) assuming η_u is unity ($\eta_u \approx 1$).

V = volume fraction of unhydrated cement particles, given by equation (5.28).

The value for the modulus of elasticity of the unhydrated cement particles (E_u) is assumed to be the same as the elastic modulus of the hydrating cement (E_{hc}) when full hydration takes place in the system, in other words when $\alpha=1$.

Stage 2 – Mortar

In this second stage equation (5.27) is modified so as to deal with mortar. It has to be mentioned that the information obtained from the above stage regarding the value of the elastic modulus of the cement paste is used here, connecting in that way the Young's Modulus evaluation with the degree of hydration. In this stage the hydrating cement paste forms the continuous phase and the fine aggregate (sand) the discrete phase.

$$E_{mor}(\alpha) = E_{paste}(\alpha)\frac{n_2 + \Theta_s + V_s\Theta_s(n_2 - 1)}{n_2 + \Theta_s - V_s(n_2 - 1)} \qquad (5.31)$$

where $E_{mor}(\alpha)$ = elastic modulus of the mortar

$E_{paste}(\alpha)$ = elastic modulus of cement paste, given by equation (5.30)–Stage 1

$n_2 = E_{sand} / E_{paste}$

Θ_s = geometry factor for sand which for nearly spherical quartz sand particles ≈ 1

V_s = volume fraction of quartz sand used

Concerning the modulus of elasticity of the sand used, as reported in the literature a value of three times larger than the E-value of the bulk cement paste can be assumed ($E_{sand}=3*E_{paste}$) (Neubauer *et al.*, 1996).

Stage 3 – CARDIFRC®

Having completed the first two stages of the procedure the E-value of the mortar has been evaluated. In the third stage the elasticity modulus of the CARDIFRC® will be obtained. As it has been discussed in Chapter 2 – Section 2.3.6, CARDIFRC® contains two different types of fibre. Therefore, the contribution of each type of fibre in the development of the total elasticity modulus of CARDIFRC® has to be examined. For that reason, the analysis in this third stage will be divided in two sub-stages. Each of these sub-stages will take into account the effect of one type of fibre.

stage 3i – effect of short fibres

Equation (5.27) still applies with the mortar as the continuous phase and the fibres as the discrete phase. Thus:

$$E_{ffs}(\alpha) = E_{mor}(\alpha)\frac{n_3 + \Theta_f + V_{ffs}\Theta_f(n_3 - 1)}{n_3 + \Theta_f - V_{ffs}(n_3 - 1)} \quad (5.32)$$

where $E_{ffs}(\alpha)$ = elastic modulus contributed by short fibres

$E_{mor}(\alpha)$ = elastic modulus of mortar, given by equation (5.31) – Stage 2

$n_3 = E_f / E_{mor}$

E_f = modulus of elasticity of the steel fibres ($E_f \approx 210{,}000$ MPa)

Θ_f = geometry factor for the needle-like fibres ≈ 1.2

V_{ffs}= volume fraction of short fibres used (5% and 4.5% for CARDIFRC® Mix I and Mix II, respectively).

stage 3ii – effect of long fibres

Equation (5.27) applies once more:

$$E_{ffl}(\alpha) = E_{mor}(\alpha)\frac{n_3 + \Theta_f + V_{ffl}\Theta_f(n_3 - 1)}{n_3 + \Theta_f - V_{ffl}(n_3 - 1)} \quad (5.33)$$

where $E_{ffl}(\alpha)$ = elastic modulus contributed by long fibres

$E_{mor}(\alpha)$ = elasticity modulus of mortar, given by equation (5.31) – Stage 2

$n_3 = E_f / E_{mor}$

E_f = modulus of elasticity of the steel fibres ($E_f \approx 210{,}000$ MPa)

Θ_f = geometry function for the needle-like fibres ≈ 1.2

V_{ffl}= volume fraction of long fibres used (1% and 1.5% for CARDIFRC® Mix I and Mix II, respectively).

The total value for the modulus of elasticity of CARDIFRC® can now be obtained simply by adding equations (5.32) and (5.33).Thus:

$$E_{CARDIFRC^{®}}(\alpha) = E_{ffs}(\alpha) + E_{ffl}(\alpha) \quad (5.34)$$

A flowchart of calculation procedure is presented in Chapter 7.

5.10 Alternative ways to obtain E-value of composite materials

Another approach to the evaluation of the modulus of elasticity of CARDIFRC® is the simple rule of mixtures. By applying the rule of mixtures to CARDIFRC® at any time during hydration, the following relationship is derived:

$$E_{\text{CARDIFRC}®}(\alpha) = E_{mor}(\alpha)V_{mor} + E_{steel}V_f$$

$$\therefore E_{\text{CARDIFRC}®}(\alpha) = E_{mor}(\alpha)(1-V_f) + E_{steel}V_f \qquad (5.35)$$

The components of equation (5.35) have the same meaning as described in previous stages. Note that the modulus of elasticity for the mortar is taken as it has been calculated above from stage 2.

The problem of modeling the elastic modulus of reinforced composite materials has been widely addressed in the literature (Phan-Thien and Huilgol, 1980; Phan-Thien and Karihaloo, 1994; Russel, 1972). Especially the proposed model by Russel (1972) could be of high interest in case of CARDIFRC® but due to the geometry and the volume fractions of the fibres used the Russel theory proved to be insufficient to predict accurately the Young Modulus of CARDIFRC®.

5.11 Overview of the proposed model

In cement-based materials during the hardening process the degree of hydration and the relative humidity of the system are two parameters that continuously change. The relative humidity in the gradually emptying pore space is an unknown parameter that has to be calculated from the actual moisture state in the hardening cement paste. Immediately after mixing, the relative humidity reaches its maximum value, 100%. As hydration proceeds this value will drop leading to self-desiccation. The thermodynamic equilibrium of the system requires an increase in the surface tension in the adsorption layer. This increase in the surface tension is associated with stresses that act from the interior of the hardening microstructure and provoke autogenous shrinkage. The constitutive relation that connects the autogenous shrinkage to the surface tension in adsorption layer is equation (5.12), noting that the pore wall area,

the specific mass of the paste and the modulus of elasticity of the paste change throughout the hardening process.

Thermodynamic equilibrium in the gradually emptying pore space can only be established iteratively. The reason for this is that all the associated equations are implicit functions and therefore no direct solution can be obtained. The following sections outline how the proposed model evolves up to the point of calculating the autogenous shrinkage strains. It has to be mentioned that the proposed model has been based on the modified HYMOSTRUC model developed by Koenders (1997).

5.11.1 Determination of total pore volume and capillary water volume

As has been mentioned above (equation 5.17) Breugel (1991) in his study proposed a relationship that gives the capillary pore volume of all pores with diameter $\leq\phi$. Using equation (5.17), we show how the total pore volume and the volume of capillary water can be expressed as functions of the degree of hydration α. The porosity at an arbitrary degree of hydration can be written as:

$$V_{por}(\alpha) = V_{cap}(\alpha) + V_{ch}(\alpha) \tag{5.36}$$

where $V_{cap}(\alpha)$ is the volume of capillary water as function of degree of hydration and $V_{ch}(\alpha)$ is the volume reduction caused by the chemical shrinkage. Breugel (1991) has also proposed a relationship to describe the amount of the capillary water left when a certain degree of hydration has been reached:

$$V_{cap}(\alpha) = V_w^0 - 0.4\alpha \frac{\rho_{ce}}{\rho_w + \rho_{ce}\omega_0} V \tag{5.37}$$

where V_w^0 is the initial water volume in the paste, ρ_{ce} is the specific mass of cement, ρ_w is the specific mass of water and ω_0 the water to cement ratio. The initial water volume V_w^0 is calculated by equation (5.38) (Breugel, 1991):

$$V_w^0 = \frac{\rho_{ce}\omega_0}{\rho_w + \rho_{ce}\omega_0} V \tag{5.38}$$

From equations (5.37) and (5.38) the following equation, giving the volume of the capillary water is obtained:

$$V_{cap}(\alpha) = (\omega_0 - 0.4\alpha)\frac{\rho_{ce}}{\rho_w + \rho_{ce}\omega_0} V \tag{5.39}$$

In order to determine the pore volume caused by chemical shrinkage it is assumed that this volume corresponds to about 25% of the volume of the chemically bound water. The chemically bound water in turn is estimated at 25% of the weight of the reacted cement (Breugel, 1991). Thus it follows that:

$$V_{ch}(\alpha) = 0.25 * 0.25 * \alpha \frac{\rho_{ce}}{\rho_w + \rho_{ce}\omega_0} V \tag{5.40}$$

Combining equations (5.36), (5.39) and (5.40) the relationship that gives the total pore volume is obtained (equation 5.41).

$$V_{por}(\alpha) = (\omega_0 - 0.3375\alpha)\frac{\rho_{ce}}{\rho_w + \rho_{ce}\omega_0} V \tag{5.41}$$

The maximum pore size $\phi_{por}(\alpha)$ (appearing in equation 5.22) is found by equating (5.41) and (5.17).

$$\phi_{por}(\alpha) = \phi_0 \exp\left(\frac{V_{por}(\alpha)}{a}\right) \tag{5.42}$$

Here it should be mentioned once again that the absolute minimum for the capillary pore size cannot exceed the maximum value for the gel pores (Table 5.1), i.e. $\phi_{min} = \phi_0 = 0.002$ μm.

Table 5.1: Classification of pores in cement paste (Koenders, 1997).

Type of Pore	Diameter (μm)	Description	Assumed Function
Air Voids	>10	Entrained Air	No transport medium
Capillary Pores	10 – 0.002	Meso-Macro Pores	Able to transport water or air
Gel Pores	< 0.002	Micro Pores	No transport medium

As has been illustrated in equation (5.41), the actual pore volume depends on the degree of hydration; therefore it changes throughout the hardening process. Apparently, the continuous formation of hydration products will lead to the reduction of the pore space. However, the ongoing chemical reactions between cement and water in the cement paste cause volumetric reduction, namely chemical shrinkage as discussed in Chapter 4 – Section 4.4.1.1. This volumetric reduction leads to the formation of new pore space. Now the reason of linking the pore volume, in equation (5.36), with the volume of capillary water and the volume reduction due to chemical shrinkage has been clarified. The volume of capillary water and the volume reduction due to the chemical shrinkage are the main contributors for the formation of the actual pore space. It has to be mentioned that changes in the total pore volume are accompanied by changes in the pore wall area, equation (5.22).

The pore wall area of the hardening cement paste is considered to be covered by a thin adsorption layer of water molecules, having thickness Γ given by equation (5.3). As mentioned before the thickness of the adsorption layer is a function of the relative humidity of the system. Any changes in the water volume in the system due to hydration will immediately affect the relative humidity and eventually the thickness of the adsorption layer. Figure 5.5 shows the state of water in the pore system.

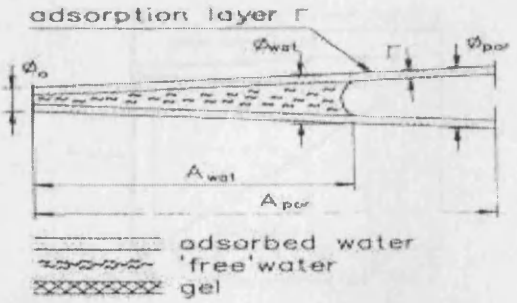

Figure 5.5: The state of the water in the pore system (Breugel, 1991).

5.11.2 Model implementation

The procedure starts with an input value for the degree of hydration. After this update the degree of hydration is a known parameter, therefore the total pore volume, the pore wall area and the total capillary volume can be found using equations (5.41), (5.22) and (5.39), respectively

$$V_{por}(\alpha) = (\omega_0 - 0.3375\alpha)\frac{\rho_{ce}}{\rho_w + \rho_{ce}\omega_0}V$$

From the pore size distribution and the total pore volume, the maximum pore diameter can be obtained using equation (5.42):

$$\phi_{por}(\alpha) = \phi_0 \exp\left(\frac{V_{por}(\alpha)}{\mathrm{a}}\right)$$

Since the maximum pore diameter (equation 5.42) and the minimum pore diameter (ϕ_0^*=0.002) are now known, the total pore wall area can be determined from equation (5.22):

$$A_{por}(\alpha) = -4\mathrm{aV}\left\{\phi_{\mathrm{por}}^{-1}(\alpha) - \phi_0^{-1}\right\}$$

Capillary water volume can be found by using equation (5.39)

$$V_{cap}(\alpha) = (\omega_0 - 0.4\alpha)\frac{\rho_{ce}}{\rho_w + \rho_{ce}\omega_0}V$$

From the above information, a clear idea of the state of the water as well as the pore volume in the pore system is obtained. Figure 5.6 shows schematically the pore size distribution in the system.

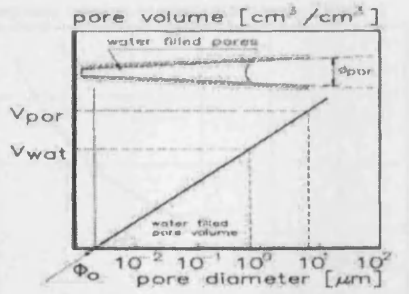

Figure 5.6: Pore size distribution in the system (Breugel, 1991).

In order to establish thermodynamic equilibrium in the system, an iterative procedure has to be initialized, beginning with the determination of the starting values for the relative humidity, the thickness of the adsorption layer and the surface tension in the adsorption layer. Assume initially that the relative humidity reaches its maximum value of 100% and consider the following chart (Figure 5.7).

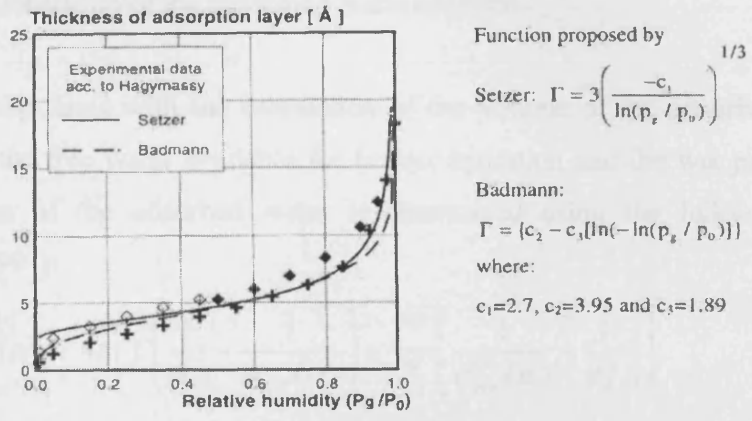

Figure 5.7: Thickness of the adsorption layer against RH and some proposed functions for Γ. Note that for RH = 100% the thickness of the adsorption layer reaches the maximum of 18Å (Koenders, 1997).

As can be observed on the chart, the maximum relative humidity is reached at the maximum value for the thickness of the adsorption layer. An indication of how the surface tension in adsorption layer changes along with alterations in the thickness of the adsorption layer is shown in Figure 5.8. The latter shows the results regarding the change in the surface tension of the model HYMOSTRUC, which has been discussed in Chapter 3 – Section 3.3.2.3.

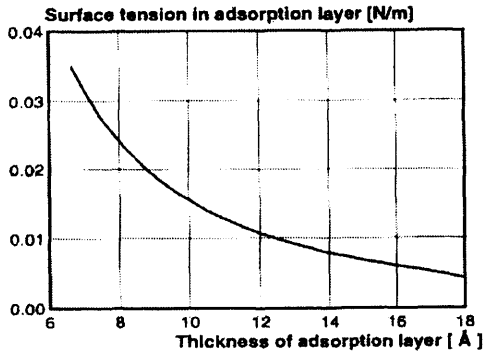

Figure 5.8: Surface tension vs. the thickness of the adsorption layer as calculated by HYMOSTRUC (Breugel, 1991; Koenders, 1997).

From Figure 5.8 it can be seen that the trend is asymptotic and very similar to the decay curve discussed in Chapter 3 – Section 3.3.1. As hydration proceeds, the surface tension in the adsorption layer increases. That is a very interesting point since the surface tension, which acts from the interior, may be considered as responsible for a certain deformation of the hardening microstructure.

The next step deals with the calculation of the volume of the adsorbed water, the volume of the free water available for further hydration and the wet pore wall area. The volume of the adsorbed water is determined using the following equation (Breugel, 1991):

$$V_{ad}(\alpha) = 4a\left(\Gamma\left(\frac{1}{\phi_0} - \frac{1}{\phi_{por}(\alpha)}\right) + \frac{\Gamma^2}{2}\left(\frac{1}{\phi^2_{por}(\alpha)} - \frac{1}{\phi_0^2}\right)\right) \tag{5.43}$$

Now, in order to find the volume of the remaining free water for further hydration, we just subtract the adsorbed water volume from the capillary water volume:

$$V_{free}(\alpha) = [\text{Equation 39}] - [\text{Equation 43}]$$

$$V_{free}(\alpha) = V_{cap}(\alpha) - V_{ad}(\alpha) \tag{5.44}$$

The diameter of the largest pore still completely filled with capillary water can now be found, since the volume of free water is known from equation (5.44), in the same manner as the maximum pore size (ϕ_{por}) was obtained in equation (5.42). Therefore:

$$\phi_{wat}(\alpha) = \phi_0 \exp\left(\frac{V_{free}(\alpha)}{a}\right) \tag{5.45}$$

The volume of the free water is strongly related to the thickness of the adsorption layer which is a function of the relative humidity. Thus the amount of the free water is related to the relative humidity and hence the value of ϕ_{wat} should be also defined as a function of the relative humidity, i.e.

$$\phi_{wat}(\alpha, RH) = \phi_0 \exp\left(\frac{V_{free}(\alpha)}{a}\right) \tag{5.45a}$$

At this point, all the parameters entering equation (5.23) are known and therefore the area of the pores completely filled with water can be determined from equation (5.23):

$$A_{wat}(\alpha) = -4a\left\{\phi_{wat}^{-1}(\alpha, RH) - \phi_0^{-1}\right\}$$

Now, using equation (5.10) a more accurate estimate of the relative humidity in the empty pore space can be calculated. For this calculation the diameter of the pores filled with water is needed, as well as the surface tension of the adsorbed area. The diameter of the pores completely filled with water has been calculated with the help of equation (5.45a). The value of surface tension used in this calculation is taken from Figure 5.7, assuming that the thickness of the adsorption layer for relative humidity of 100% is 18Å (Figure 5.7).

A change in the relative humidity is associated with change in the thickness of the adsorption layer, as illustrated in Figure 5.7. Using Setzer's approach the new value for the thickness of the adsorption layer can be found.

$$\Gamma = 3\left(\frac{-2.7}{\ln\left(p_g / p_0\right)}\right)^{1/3} \tag{5.46}$$

Now, using this new estimate for the thickness of the adsorption layer the actual surface tension in this layer can be found by solving equation (5.9).

$$\sigma = RT \int_{p_g/p_0}^{p_g/p_0=1} \Gamma d\left[\ln\left(\frac{p_g}{p_0}\right)\right]$$

Once the above calculations have been completed, the relative humidity in the empty pore space can be compared with the initial value of the relative humidity. If these two values are not equal, the thermodynamic equilibrium has not yet established and the procedure has to be repeated. The new values of the relative humidity, the thickness of adsorption layer and the surface tension are the initial values used in the next iteration. The iterations will continue until the thermodynamic equilibrium is established. When the thermodynamic equilibrium has been achieved, the next step in the calculation procedure will be the determination of the proportionality factor λ from equation (5.15).

$$\lambda(\alpha, RH, w/c) = Z\frac{(A_{por}(\alpha) - A_{wat}(\alpha, RH))\cdot \rho_{pa}(w/c)}{E_p(\alpha)}$$

Note that the modulus of elasticity and the specific mass of the cement paste are both calculated as described in preceding sections with the help of equations (5.30) and (5.25), respectively. Furthermore it has to be mentioned that the constant Z appearing in the above equation is set equal to 1/3, i.e. Z=1/3 (Koenders, 1997).

As the surface tension of the adsorption layer and the proportionality factor are now known, the increment of the deformation can be simply determined by using the modified Bangham concept (equation 5.12).

$$\Delta\varepsilon_s = \lambda\Delta\sigma \tag{5.47}$$

The total deformation of the microstructure has to be determined incrementally, the proportionality factor λ is not a constant (it depends on the degree of hydration and the relative humidity of the system). Consequently:

$$\varepsilon_s = \sum_{RH}\Delta\varepsilon_s \tag{5.48}$$

To calculate the corresponding deformation of CARDIFRC® matrix without fibres, the modulus of elasticity of mortar is used (equation (5.31)), whereas that of CARDIFRC® with fibres uses the equation (5.34). A flowchart of the iterative procedure will be given in Chapter 7.

5.11.3 Limitations of the model

At this point, we need to consider the limitations of the above-described procedure as applied to CARDIFRC®. These limitations have to do with the microstructural parameters.

First of all is the water to cement ratio. CARDIFRC® has very low water to cement ratio reaching values as low as 0.22 and 0.20. Such a low water to cement ratio has never been used in a numerical model dealing with the thermodynamic equilibrium of the pore space in the microstructure, and that is the reason why some well known numerical models such as NIST model proved inadequate to model the development of microstructure and the associated volume changes in CARDIFRC®. Another major issue is that the effect of microsilica is not taken into account directly anywhere in the calculations. There are two reasons for that. First of all the chemical reactions associated with the effect of microsilica in the system would make the process far more complex than it already is. So, instead of searching mathematical formulations to describe a very complex phenomenon such as the effect of microsilica, we can alter the maximum pore size diameter. In the literature there are reports relating the maximum pore diameter in a hardening cement paste and the percentage of silica fume that is included in the paste (Figure 5.9) (Koenders, 1991). There is also a relationship that helps towards the alteration of the pore diameters:

$$f(SF) = a_1 SF + 1 \tag{5.49}$$

where f(SF) is the correction factor which describes the reduction of the largest pore diameter in the paste due to the addition of microsilica, a_1 is a constant and SF is the amount of microsilica included in the paste, expressed as a percentage. Regarding the constant a_1 it was found to have a value of -0.028 and moreover it was found to be independent of the water to cement ratio. Therefore, this correction factor is applicable in a very wide range of water to cement ratios (0.2 to 0.5).

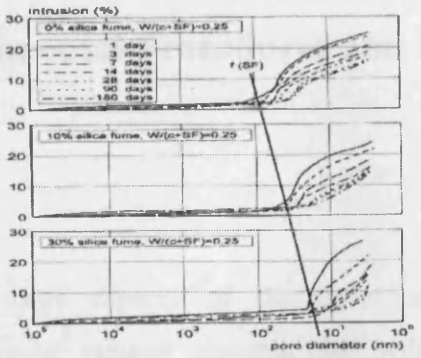

Figure 5.9: Pore size reduction for different percentages of microsilica used in the paste (after Feldman) (Koenders, 1997).

As can be observed from Figure 5.9, the maximum pore diameter becomes smaller as the percentage of microsilica used increases. The second reason for not taking into account the effect of microsilica directly has to do with the curing regime. The CARDIFRC® specimens, as will be discussed in the next Chapter, were wrapped after demoulding, which takes place 17 hours after casting. In other words, the typical curing regime for CARDIFRC® (7 days in a hot water at 90^0C) is not followed. Thus the specimens are cured under isothermal conditions, since they are wrapped, in a room having constant temperature of 20^0C. Therefore, since the specimens are not in a very hot environment during the first crucial hours of the hydration it can be assumed that the secondary reaction described in Chapter 2 – Section 2.2.2 (equation 2.2) will not take place, i.e. the chemical effect of the microsilica is ignored and it is only regarded as a microfiler and not as a pozzolan.

5.12 Conclusions

In this Chapter a model was proposed for determining the volume changes and especially autogenous shrinkage in cement based materials. Fundamental concepts have been discussed, such as the Bangham concept and the thermodynamic equilibrium in the microstructure of the cement based materials. A model based on the thermodynamic changes within the microstructure of CARDIFRC® has been developed. To capture the constraint offered by the fibres to the free autogenous shrinkage of CARDIFRC® matrix without fibres, the evolution of the stiffness of the various phases of CARDIFRC® with hydration was followed.

Chapter 6: Experimental Procedures and Results

6.1 Introduction

In previous Chapters some aspects of the development of HPFRCCs, the microstructural modelling of volume changes, the hydration and the associated volume changes in cement based materials have been discussed. The experimental program consists of control tests in order to obtain the mechanical properties of the material, as well as tests for the autogenous shrinkage measurement. The results of the experimental work are presented in the following sections.

6.2 Definition of mixes

The current study deals with the phenomenon of autogenous shrinkage and self-desiccation of CARDIFRC®. CARDIFRC® consists of two base mixes designated Mix I and Mix II and their composition has been presented in Table 2.1 – Chapter 2 – Section 2.3.6.

Each mix consists of Portland cement commercially available from Blue Circle, Elkem Refractory microsilica U983 Grade, fine sand*, superplasticiser commercially available from Adomast, water and two kinds of fibre – short having length 6mm and long having length 13mm – commercially available from Bekaert. In order for the mechanical properties of both mixes to be evaluated, some control tests were undertaken. Properties such as the compressive strength, tensile splitting strength and the Young's Modulus have been obtained. The test procedures and results will be analysed thoroughly in a later section.

* It has to be mentioned that in Mix I 2 grades of fine sand are used whereas in Mix II 3 grades are used.

6.3 Mix preparation

The mixes were prepared according to the most effective regime, determined from past experimentations. The procedure is described in the patent application GB 0109686.6. The first step in the mix procedure was to evaluate the mould volume, adding about 15% to take into account any waste. Then the constituents were scaled down to this desired volume and weighed.

Mix I

The coarsest and the finest of the ingredients, i.e. the 250-600 μm sand and the microsilica were placed into the mixer. Initially, they were mixed by hand and then by the mixer for at least two minutes. It has to be noted at this stage that special care has to be taken during mixing in order to avoid spillage of the powder from the mixer, since the latter operates at a speed that can cause the powder to spill.

After the first two minutes of mixing the remaining constituents were added one at a time followed by two minutes of mixing to ensure uniformity. The sequence of the ingredient addition was as follows: the 2nd coarsest (sand 9-300 μm) and then the 2nd finest (cement). All the ingredient additions were followed by more than 2 minutes of mixing. After the addition and mixing of the last grade of sand the next ingredient to be added are the steel fibres.

The short (6mm) fibres were added first while the long (13mm) ones were added afterwards. Both short and long fibres were added in four instalments i.e. 25% of the total quantity each time. It has to be mentioned that as the fibres were added into the mix, they were passing through a vibrating sieve. The reason was to separate the fibres, which were stuck together due to the electrostatic forces between them. Each instalment of fibres was followed by two minutes of mixing to ensure even distribution of the fibres in the mix. After the last instalment was added and mixed for the required time, water and superplasticiser were added. Two thirds of the measured volume of superplasticiser was added to the water volume. The liquid mixture in turn was poured into the dry mix in increments of 50%, 25%, 12.5% and 12.5%. This procedure had to be precise for the microstructure to become densely packed. Each

increment of the superplasticiser – water mixture was followed by two minutes of mixing.

Mix II

The mixing sequence is mainly the same for Mix II as for Mix I. The main differences between the two mixes are the 3rd grade of fine sand used in Mix II, the larger amount of long fibres used in Mix II and as a consequence of the last two the larger amount of superplasticiser incorporated in Mix II.

Again, the coarsest and the finest of the ingredients, i.e. the 1-2 mm sand and the microsilica were placed into. Initially, they were mixed by hand – in order to ensure better dispersion of particles - and then by the mixer for at least two minutes. The sequence remained the same as earlier, i.e.: the 2nd coarsest (sand 212 – 1000 μm), then the 2nd finest (cement) and the last grade of sand (9 – 300 μm). After the last instalment of the sand and the adequate mixing time the steel fibres added in the mix in exactly the same way as described for Mix I earlier. Once again it has to be mentioned that special care has to be taken when mixing the fibres so that the mix is very homogeneous and the fibres well distributed. After the last instalment of fibres was added and mixed for the required time, water and superplasticiser were added into the mix again exactly as described earlier for Mix I. It has to be mentioned that earlier research in that field revealed that the superplasticiser (SP) is active for about 15 minutes having as a starting point the last inclusion of SP and water in the mix. In other words the mixing of that last instalment and the casting have to be completed within 15 minutes in order the SP to be fully effective. This implies that casting has to be quick and precise. Another important factor for such a material is adequate vibration. Especially for this material an electric vibration table is used (the vibration is triggered by two electric motors), since the magnetic vibration table can affect the orientation of the fibres in the matrix.

After casting, the specimens are left for 24 hours to set and at about a day after casting they can be demoulded and placed in the tanks for curing. The curing regime that is used for CARDIFRC® is the 9 day hot curing (90°C).

6.4 Control tests

As mentioned earlier, some control tests have been conducted in order to evaluate the mechanical properties of CARDIFRC®. For this purpose compressive and tensile splitting strength tests have been done, as well as tests towards the evaluation of the Young's Modulus of the material.

For the purpose of these tests cubes and cylinders were prepared according to the specifications defined by the British Standards.

6.4.1 Compressive strength

Cubes from both Mix I and II were cast and cured as described earlier. After the curing the specimens were tested (Figure 6.1) in order to determine their compressive strength according to BS 1881-116 (1983). At this point it has to be mentioned that for both mixes some trial castings were done. It was found that the original superplasticiser (SP) to water (*sp/w*) ratios did not give sufficiently workable mixes and as a result the compaction and therefore the specimens did not fulfil the standards, i.e. specimens with large voids on their surface. It was apparent that the *sp/w* ratio had to be increased somewhat in order for the mixes to be more workable. For Mix I two trial *sp/w* ratios – from which only the one was selected to be the *sp/w* ratio for the whole of the experimental work - were used (0.18 and 0.21, instead of 0.15) whereas in Mix II *sp/w* ratio of 0.4 used instead of 0.37. In both cases the *sp/w* ratios were increased only by increasing the SP quantity and keeping the amount of water the same as for the base mixes (Table 2.1 – Chapter 2 – Section 2.3.6). Tables 6.1 and 6.2 illustrate the values achieved during the compressive tests.

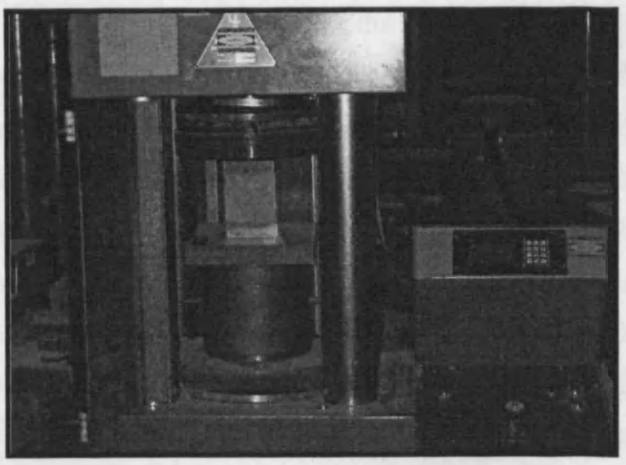

Figure 6.1: The machine used for the compressive strength tests.

Table 6.1: Compressive Strength results for Mix I – *sp/w* = 0.18

Cube Number	Weight (kg)	Fc (kN)	Compressive Strength (MPa)
1	2.68	1841	184.10
2	2.67	2076	207.60
3	2.71	1963	196.30
4	2.79	1915	191.50
5	2.70	1875	187.50
6	2.70	1946	194.60
		Mean f_{cu}	193.60
		COV	4.23

Table 6.2: Compressive Strength results for Mix I – *sp/w* = 0.21

Cube Number	Weight (kg)	Fc (kN)	Compressive Strength (MPa)
1	2.60	1843	184.30
2	2.59	1877	187.70
3	2.64	1774	177.40
4	2.61	1729	172.29
5	2.65	1774	177.40
6	2.67	1776	177.60
		Mean f_{cu}	179.45
		COV	3.00

In Tables 6.1 and 6.2 Fc is the applied compressive load.

As it can be seen in both cases the values for the compressive strength are quite high as expected. Nevertheless, in the case of *sp/w* ratio of 0.21 the values of the compressive strength are somewhat lower than the corresponding values for *sp/w* ratio of 0.18. The latter had a mean compressive strength of 193.60 MPa whereas the former only 179.45 MPa with the coefficient of variation (COV) being 4.23 and 3.00, respectively. This resulted in the selection of *sp/w* = 0.18 as the ratio to be used – as the most effective both in terms of strength and workability – in the rest of the experimental work regarding Mix I mixes. It has to be mentioned that in the case of mixes with *sp/w* equal to 0.21, after demoulding the specimens were dark gray in colour which is an indication that there is excessive amount of SP in the mix.

As mentioned earlier, in the case of CARDIFRC® Mix II the *sp/w* ratio increased slightly in order to make a more workable and easy to cast mix, since the provisional *sp/w* ratio of 0.37 was found to give a very stiff mix. Table 6.3 shows the values of the compressive strength for CARDIFRC® Mix II with *sp/w* of 0.40.

Table 6.3: Compressive Strength results for Mix II – *sp/w* = 0.40

Cube Number	Weight (kg)	Fc (kN)	Compressive Strength (MPa)
1	2.64	1914	191.40
2	2.70	2146	214.60
3	2.70	2068	206.80
4	2.68	2093	209.30
5	2.70	2187	218.70
6	2.67	2027	202.70
7	2.70	1956	195.60
8	2.64	2116	211.60
9	2.67	2113	211.30
10	2.70	2054	205.40
11	2.64	2138	213.80
12	2.69	2025	202.50
		Mean f_{cu}	206.98
		COV	3.85

The obtained values of the compressive strength are once more remarkably high. In some cubes the compressive strength has exceed the 212 MPa, resulting in a mean value of 206.98 MPa and a coefficient of variation of 3.85. It has to be mentioned that this value of compressive strength for Mix II is the highest value of f_{cu} ever obtained for this material. Previously the compressive strength values – for Mix II – of about 185 MPa had been achieved (Alaee, 2002).

6.4.2 Tensile splitting test

For the purpose of the tensile splitting tests, cylinders were cast and cured properly from both mixes I and II. The specimens prepared and tested according to the British Standards (BS 1881-117:1983). Again for Mix I there two *sp/w* (0.15 and 0.21) ratios whereas for Mix II only one (*sp/w* = 0.40). Figures 6.2 and 6.3 illustrate the jig used in the experiment according to the British Standards as well as the machine set-up in the laboratory.

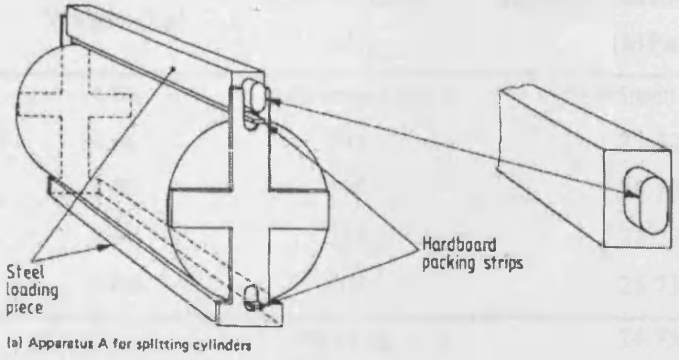

Figure 6.2: The jig used for the tensile splitting test (BS1881-117:1983).

Figure 6.3: The laboratory set-up for the tensile splitting test.

The following tables present the obtained values for the tensile splitting strength for mixes I and II.

Table 6.4: Tensile Splitting Strength results for Mix I – *sp/w* = 0.18

Cylinder Number	Weight (kg)	Applied Load (kN)	Indirect Tensile Strength (MPa)
1	4.20	889	28.31
2	4.22	784	24.97
3	4.22	855	27.23
4	4.21	1045	33.28
5	4.21	925	29.46
		Mean σ_{ct}	28.65
		COV	10.71

Table 6.5: Tensile Splitting Strength results for Mix I – *sp/w* = 0.21

Cylinder Number	Weight (kg)	Applied Load (kN)	Indirect Tensile Strength (MPa)
1	4.04	Specimen Lost	Specimen Lost
2	4.06	795	25.32
3	4.08	790	25.16
4	4.08	715	22.77
5	4.06	808	25.73
		Mean σ_{ct}	24.75
		COV	5.41

It has to be mentioned that during the tests, the bolts at the base of the jig, which is designed for normal strength concrete mainly, in one case failed due to shear. That is the reason for the indication "specimen lost" against cylinder 1 in Table 6.5. It is obvious that the material was very strong and the applied load very large and hence the steel loading piece at the top (Figure 6.2) at some point instead of being vertical, and therefore distributing the applied load uniformly along the cylinder, had a very small inclination, large enough though to cause shear failure of the bolts at the base, since the applied load was not vertical but at an angle.

Once more the results obtained for this test (as for the compressive test) are remarkable, with indirect tensile strength values reaching 33.28 and 25.73 MPa for mixes with *sp/w* 0.18 and 0.21, respectively. The COV for mixes with *sp/w* of 0.18 found to be 10.71 whereas in the case of mixes with *sp/w* of 0.21it was calculated to be 5.41. Again the highest values are observed in the mix with the lower *sp/w* ratio, as expected.

Table 6.6: Tensile Splitting Strength results for Mix II – SP/w = 0.40

Cylinder Number	Weight (kg)	Applied Load (kN)	Indirect Tensile Strength (MPa)
1	4.19	860	27.39
2	4.22	571	18.18
3	4.19	794	25.29
4	4.22	635	20.22
5	4.20	535	17.04
6	4.20	641	20.41
7	4.15	507	16.15
8	4.19	694	22.10
9	4.19	764	24.33
10	4.20	748	23.82
11	4.15	631	20.10
		Mean σ_{ct}	21.37
		COV	16.65

The indirect tensile values obtained for this mix are very high, reaching up to 27.39 MPa and having a mean value of 21.37 MPa and a coefficient of variation of 16.65.

6.4.3 Modulus of elasticity (E)

For the determination of the modulus of elasticity of the two mixes of CARDIFRC®, cylinders of each mix were tested according to BS 1881-121:1983. For Mix I, one cylinder with *sp/w* = 0.18 was tested. For Mix II, one cylinder with *sp/w* = 0.40 was tested. The specimens were taken from the same group of specimens that were tested for tensile splitting strength. The tests were performed in an AVERY-DENISON

Type 7152, Servo-Hydraulic Testing Machine, with a load capacity of 600 kN. The machine was fitted with a DARTEC 9600 Digital Feedback Controller. On each cylinder 2 strain gauges 30 mm long were glued, after a very careful surface preparation, for the measurement of the specimen strains. For comparison purposes LVDTs were also used in order to obtain a second value of the elastic modulus. The specimens were loaded up to the one third of their compressive strength (approximately 455 kN) and then unloaded. The value of 455 kN was calculated by transforming the average compressive load measured on CARDIFRC® cubes into a circular surface (100 mm diameter). The loading-unloading procedure was repeated two times. The load was applied in 50 kN load increments, starting at 5 kN. The modulus of elasticity for Mix I, *sp/w* = 0.18 is E = 47.79 GPa and for Mix II, *sp/w* = 0.40 is E = 49.63 GPa. The results were very satisfactory since both values were very close to the theoretical modulus of elasticity, according the Rule of Mixtures (50 GPa). The E-value of Mix II is slightly higher than Mix I, a result which was expected since Mix II contains coarser sand than Mix I.

Table 6.7: The mechanical properties of CARDIFRC® mixes as obtained from the control tests.

	Mix I		**Mix II**
	SP/w = 0.18	SP/w = 0.21	SP/w = 0.40
Splitting Strength (MPa)	28.65	24.75	21.37
Compressive Strength (MPa)	193.60	179.45	207
Young Modulus (GPa)	48	-	50

It is worth mentioning that the E-value obtained for Mix II (49.63 GPa) is the largest ever achieved on this particular material.

6.5 Shrinkage tests

The evaluation and classification of shrinkage in CARDIFRC® is the main purpose of the current study. For the shrinkage experiments the specimens were in the shape of prisms of dimensions 50x50x250mm. Both fibred and plain specimens are going to be prepared. The idea of this is not only to evaluate the shrinkage of the plain matrix but also to investigate the effect of the fibres on shrinkage. Furthermore, some larger

specimens have been prepared, beams having dimensions 100x100x500mm, and tested.

6.5.1 Shrinkage specimen preparation and testing

The beam specimen preparation for the shrinkage experiments in terms of mixing, casting and vibrating is the same as described in an earlier section for the mixing procedures. A very interesting point for the shrinkage specimens is the curing regime. It quickly became apparent that if the specimens were cured using the traditional curing regime used for CARDIFRC® specimen (i.e. 7 days at 90°C) the main dominating period, which is the first seven days after casting (Cheyrezy and Behloul, 2001), for the autogenous shrinkage is lost. In order to overcome this problem, the specimens, instead of hot curing immediately after demoulding, were wrapped using thin vinyl acetate sheets and stored in a temperature-controlled room at 20°C.

In the literature it is mentioned that for high performance fibre reinforced cementitious composites it can be assumed that for about the first 19 hours, having as a starting point the time just after casting, there is no shrinkage taking place since that is the time needed for the initial material setting and therefore any shrinkage can be ignored (Cheyrezy and Behloul, 2001). Hence, the material remained in the steel moulds for about 17 hours in order for it to harden sufficiently well for handling the specimens. The moulds have been well greased before casting. When the placement of the material in the moulds had finished, a clean piece of glass was placed above the moulds so as to protect the specimens as well as to prevent any moisture loss to the environment. Moisture exchange with the surrounding environment could lead to drying shrinkage microcracking. Finally a wet piece of cloth was placed above the glass and around the moulds in order to ensure a very humid environment for the material for the first hours until initial setting. It has to be stressed that we are ignoring any autogenous shrinkage which develops within these 19 hours.

About 17 hours after casting the specimens were demoulded and the acoustic vibrating wire gauges were attached on the sides. Each beam carries two of these gauges, which are carefully placed on the sides of the beam so that they are exactly

opposite each other. The gauge is constructed so that a wire is held taut between two mounting blocks that are welded to the structural member with the help of very strong adhesive agent. The gauges have been calibrated first before attaching to the specimen. Calibration procedure includes the tension of the wire at specific frequency with the help of a frequency meter apparatus. Changes in length of the beam alter the distance between the two mounting blocks and thereby the tension of the wire. An electromagnet is used to pluck the wire and measure the frequency of vibration. Strain is then calculated from the equation shown below by applying calibration factors to the frequency measurement.

$$\mu\varepsilon = (F_1^2 - F_2^2) \times GF$$

where F_1^2 is the initial or datum frequency reading, F_2^2 is a subsequent measured frequency and GF is the appropriate gauge factor for the gauge used. For the gauges used in the current study, Figure 6.4, the applied gauge factor was 3.025×10^{-3}.

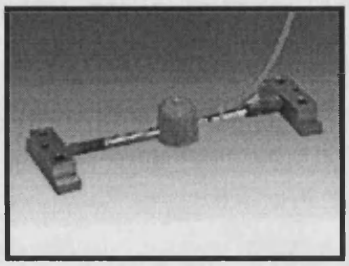

Figure 6.4: Surface-mount acoustic vibrating wire gauge (www.gage-technique.demon.co.uk).

After attaching the gauges, the beams were carefully wrapped, taking care not to cause any damage to the gauges, since this will affect the readings later on. The specimens were wrapped with vinyl acetate sheets and secured with aluminium adhesive tape, ensuring that way the adiabatic conditions needed for the test, as well as preventing any moisture exchange with the surrounding environment (Figure 6.5). If one wanted to conduct a test under isothermal conditions it would be necessary to monitor the temperature of the interior of the specimen continuously and to adjust the surrounding temperature accordingly. After wrapping the specimens and insulating them properly, they were connected to the data logger (Figure 6.6).

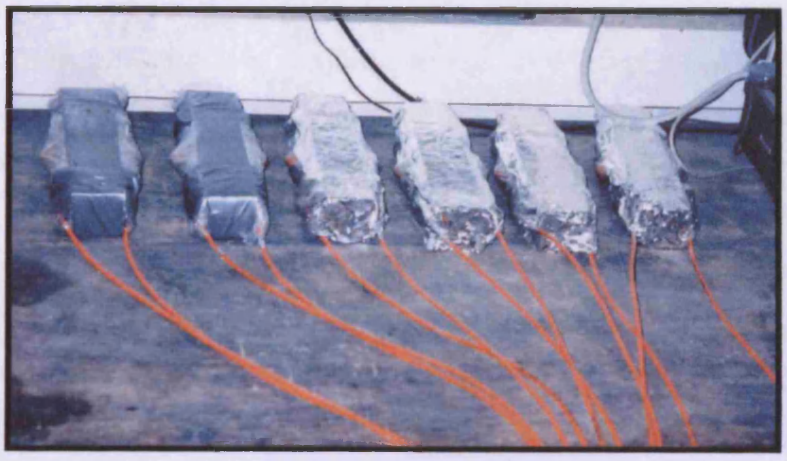

Figure 6.5: Small prisms wrapped and insulated.

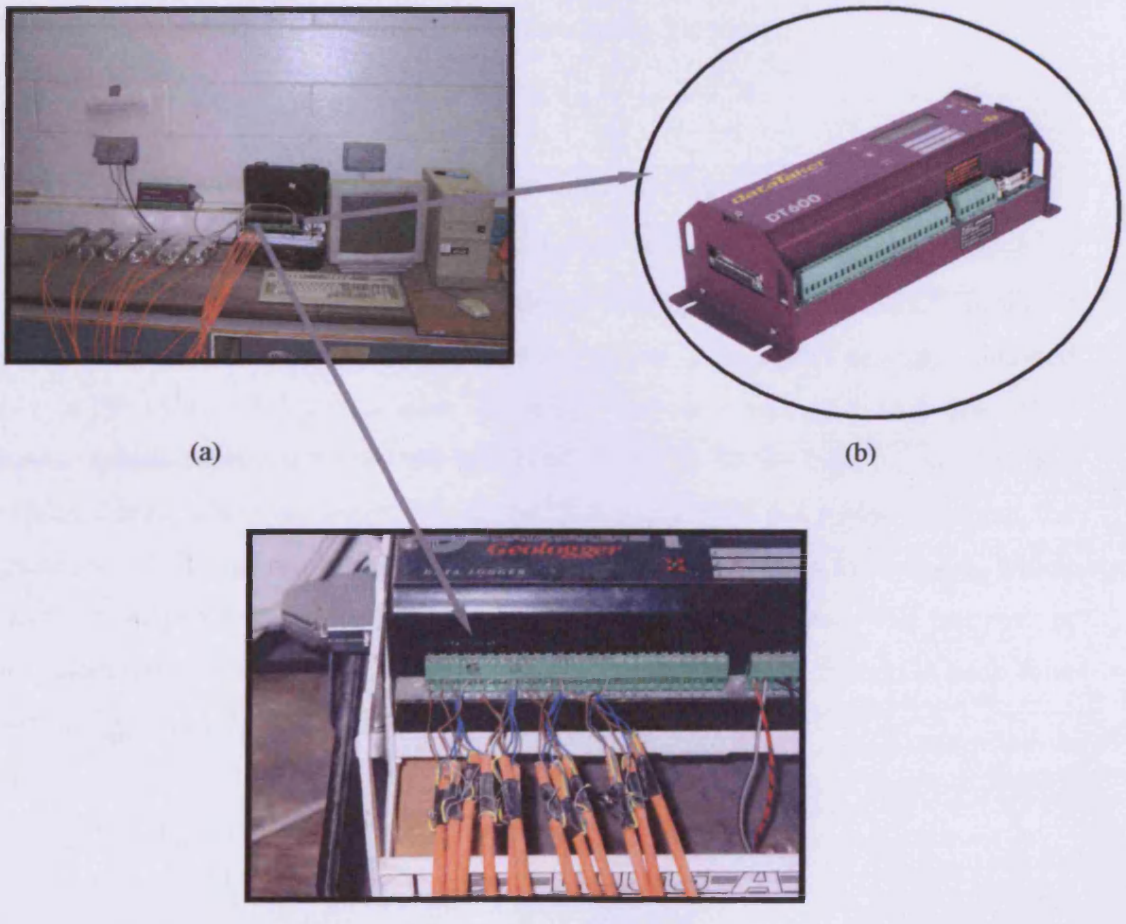

(a) (b)

(c)

Figure 6.6: (a) Autogenous shrinkage specimens connected to the data logger. (b) Detail of the data logger used (datataker.com). (c) Detail of the connection point between gauges and datataker.

The data logger used for the experiments is a *data-Taker DT600* range of general purpose, battery powered data acquisition and data logging system which can conveniently and securely store data in computer memory and/or removable memory cards. The accuracy of the measurements is fairly high. Computer software allows the acquisition of the results as well as the monitoring of the data collection throughout the testing period. The first seven days the logger was set to take readings every 15 minutes. The time step was increased to 2 hours between the seventh day and the twentieth day. From the twentieth day until the end of the measuring period the time step for taking readings from the specimens was further increased to 12 hours. The selection of small time step between the readings in the first seven days was due to the fact that the first week regarded as very crucial concerning the development of the autogenous shrinkage strains in the matrix, an assumption which has been verified by the measurements, as will be clear in the following sections. On the other hand, after day 20 the development of autogenous strains seems to have stabilised sufficiently for the time step between the readings to be substantially increased.

6.5.2 Shrinkage results for the large specimens

The larger specimens were discarded in favour of smaller specimens because no reliable conclusions regarding the autogenous shrinkage of CARDIFRC® could be drawn, in view of the very large scatter in the results. This scatter has been obtained only in the mixes with fibres since the mixes without fibres gave very consistent results. Tables 6.8 and 6.9 show the measured strains for all the large beams with and without fibres, respectively. It has to be mentioned that the tables illustrate the autogenous shrinkage strains obtained at various time intervals up to 90 hours, which was the time point where the tests on the large beams were halted. The last row in each table represents the coefficient of variation for the results at the end of each time interval. Figures 6.7 and 6.8 show results for the large beams.

Table 6.8: Summary of results for large beams with fibres at the end of various time intervals.

	Time Intervals (hours)								
	10	**20**	**30**	**40**	**50**	**60**	**70**	**80**	**90**
Beam 1	70.59	112.33	144.07	172.86	200.73	226.62	251.49	272.65	293.75
Beam 2	139.12	195.04	236.09	270.35	302.88	333.53	361.07	384.93	408.03
Beam 3	77.95	132.37	172.58	208.45	242.78	274.17	303.30	327.52	351.17
Beam 4	63.75	101.41	130.03	155.97	181.07	204.36	226.73	245.75	264.71
Beam 5	84.28	143.18	186.73	225.62	262.84	296.91	328.53	354.84	380.55
Beam 6	153.53	215.35	260.78	298.72	334.77	368.74	399.30	425.79	451.44
Mean	98.20	149.95	188.38	221.99	254.18	284.05	311.74	335.25	358.28
COV	35.49	27.81	24.84	22.67	21.11	20.08	19.12	18.48	17.88

Table 6.9: Summary of results for large beams without fibres at the end of various time intervals.

	Time Intervals (hours)								
	10	**20**	**30**	**40**	**50**	**60**	**70**	**80**	**90**
Beam 1	72.82	135.71	183.05	223.23	259.31	290.77	318.26	342.26	364.37
Beam 2	72.73	135.53	182.81	222.93	258.97	290.38	317.84	341.80	363.88
Beam 3	66.94	128.93	178.16	219.25	256.45	289.47	316.68	341.88	364.29
Beam 4	68.93	132.80	183.55	225.91	264.28	298.35	326.42	352.44	375.57
Beam 5	72.90	135.85	183.29	223.46	259.59	291.08	318.60	346.62	364.75
Beam 6	67.11	129.26	178.61	219.80	257.10	290.20	317.48	342.75	365.21
Mean	70.24	133.01	181.57	222.43	259.28	291.71	319.21	343.96	366.34
COV	3.77	2.22	1.25	1.02	0.97	1.03	1.03	1.11	1.13

The spread of the results for beams with fibres is very large, since even at the end of the first 10 hours the COV is relatively high for such set of data. It is apparent that no serious consideration can be given to such results. These tests were therefore discontinued after 90 hours. On the other hand as expected the specimens without fibres gave very consistent results with small differences. This is verified also by the fairly small COV between the results for the whole of the experimental process.

Figures 6.7 and 6.8 present graphically the results for large beams with and without fibres, respectively. On the scale of Figure 6.8 the six beam results are nearly indistinguishable.

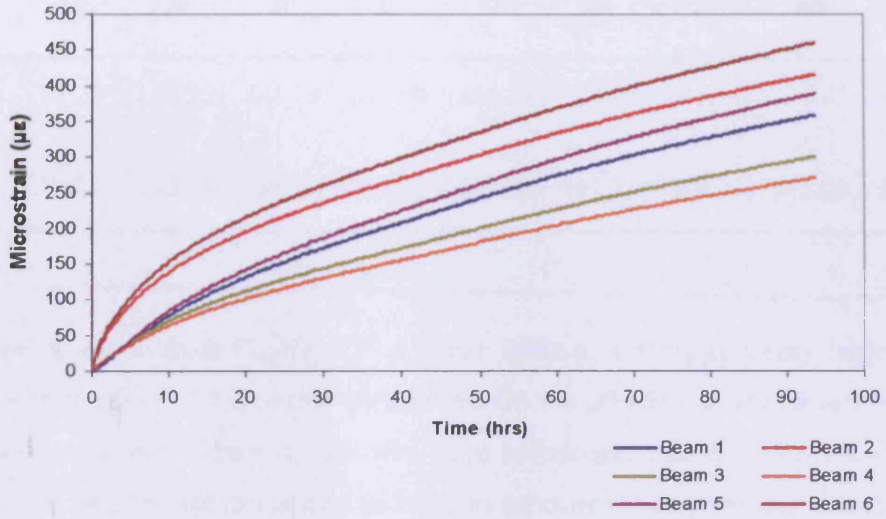

Figure 6.7: Autogenous shrinkage strain variation with time for CARDIFRC® Mix I.

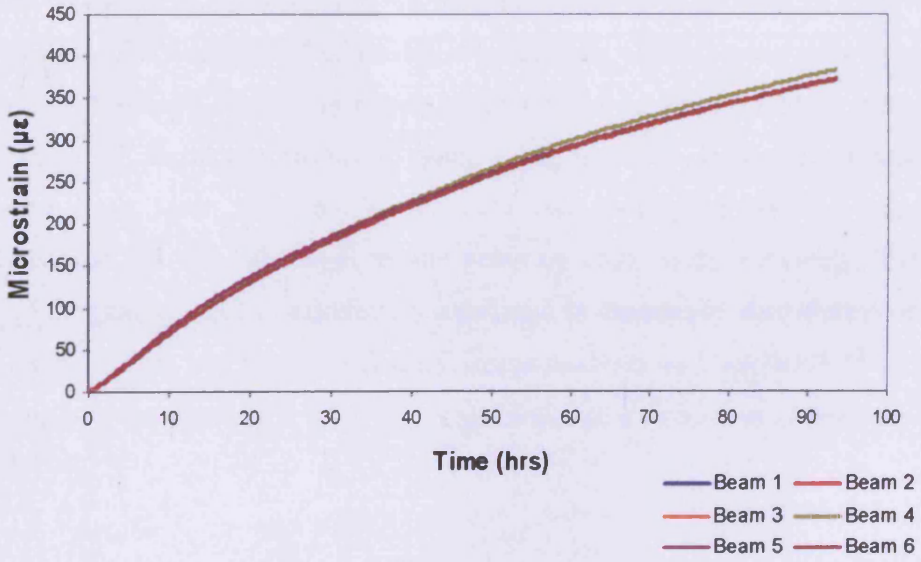

Figure 6.8: Autogenous shrinkage strains variation with time for CARDIFRC® Mix I without fibres.

Table 6.10 shows the average strain values obtained for the six beams in each case at the end of several time intervals.

Table 6.10: Average autogenous shrinkage strains at the end of various time intervals; values are expressed as microstrains (με) (F: mix with fibres; NF: mix without fibres).

	Time Intervals (hours)								
	10	**20**	**30**	**40**	**50**	**60**	**70**	**80**	**90**
F	98.20	149.95	188.38	221.99	254.18	284.05	311.74	335.25	358.28
NF	70.24	133.01	181.57	222.43	259.28	291.71	319.21	343.96	366.34

As can be observed from Figures 6.7, 6.8 and Table 6.10 there is a very large spread of results in the case of the beams with fibres. On the other hand, the results obtained for the beams without fibres do not give large scatter and this is confirmed from the relatively small standard deviation, taking into account the large amount of data. By taking into consideration the average values from all six beams of each case we have noticed another interesting point regarding the large beams. The average values reveal no effect on the shrinkage strains by the addition of fibres in the mix. In other words, the inclusion of fibres instead of having a restraining effect on the development of autogenous shrinkage strains, as expected, proved to be insufficient to restrain the development of shrinkage strains in such a big member. However, it has to be mentioned once again that this is the case only when the average values are considered and not the individual results given by each beam separately. The large spread of the results can be undoubtedly attributed in the uneven distribution of fibres in the matrix. This has been verified by image analysis on CARDIFRC® strips cut from large beams (Nicolaides, 2004). Figure 6.9 shows a typical result from the image analysis.

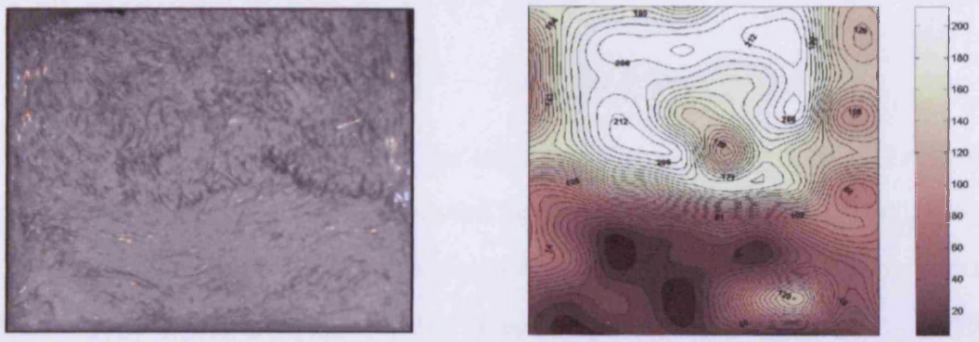

(a) (b)

Figure 6.9: (a) Strip cut from CARDIFRC® 100x100x500mm beam. (b) Contour plot showing the fibre distribution in the strip shown in (a) (Nicolaides, 2004).

In Figure 6.9(b), dark colour indicates low fibre concentration whereas light colour is used to show high fibre concentrations. As can be observed from the results of image analysis the distribution of fibres in the specimen is fairly uneven. Very low fibre concentration at the bottom of the strip, whereas a large number of fibres is present at the top. Another distinctive case of uneven fibre distribution in the matrix of large beams is shown in Figure 6.10.

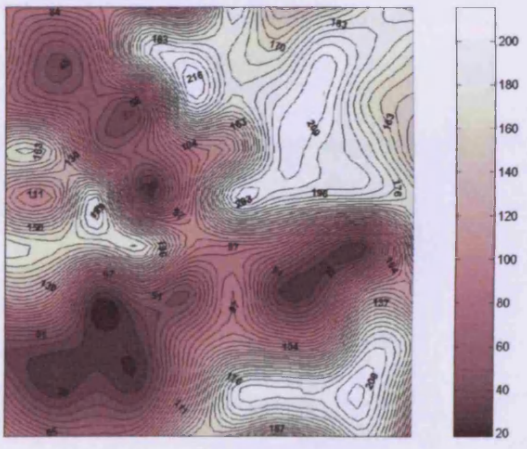

Figure 6.10: Contour plot showing the fibre distribution for the 100x100x500mm beam (Nicolaides, 2004).

In the case shown in Figure 6.10 once again the fibre distribution is clearly uneven. Large amounts of fibres are concentrated in right top and bottom corners, whereas the

core of the cut section as well as the left top and bottom corners have a relatively small number of fibres.

Two possible reasons were identified for this phenomenon. First, the specimens were excessively large to be well compacted so that the fibres could not distribute uniformly in the matrix. That also explains the fact that CARDIFRC® is a material intended only for use as strips of relatively small dimensions, suitable for retrofitting, and not large members. The second possible reason for the uneven distribution of fibres in the matrix had to do with the vibration frequency used, which was initially set at 97 Hz. This frequency proved to be too high and as a result the vibration was excessively powerful and caused segregation of the fibres in the mix, leading to situations like the ones shown in Figures 6.9 and 6.10. For this reason, the experimental work was focused on the small prisms and no further experiments were conducted with large beams. Furthermore, the vibration frequency adopted for the casting of the remaining prisms was 50 Hz. However, it has to be mentioned that the uneven distribution of fibres is not the case in all large beams containing steel fibres. It has been found that some of these large beams have relatively good fibre distribution (Figure 6.11) but since a number of beams of this geometry exhibit this phenomenon of inconsistent fibre dispersion they could not be adopted as the preferred geometry for the experimental purposes.

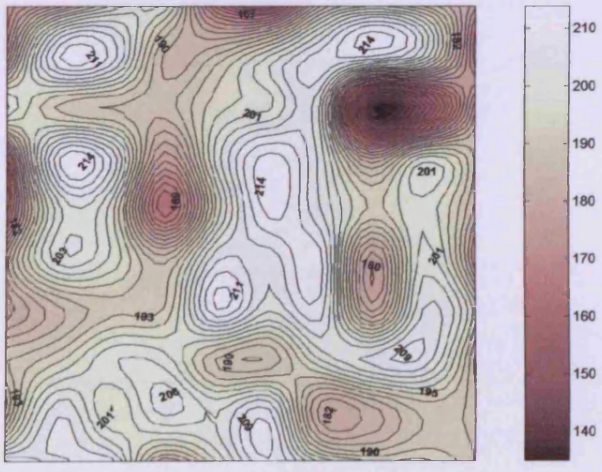

Figure 6.11: Contour plot showing the fibre distribution for the 100x100x500mm beam. Note the very good fibre distribution in the matrix (Nicolaides, 2004).

6.5.3 Shrinkage results for the small specimens

In this section the results from the experiments on small specimens for the determination of the autogenous shrinkage strains will be presented. For the presentation of the experimental results, a distinction is made between the time divisions. As has been outlined earlier, both mixes with and without fibres have been prepared. Twelve prisms having dimensions 50x50x250mm have been made for each type of mix. The graphs illustrated in the following sections are the average values of the twelve prisms for both mixes. Figures showing each beam separately are presented in Appendix D. From the experimental set-up, the development of the autogenous shrinkage strains is automatically registered as a function of time.

0-24 Hours

Figure 6.12 shows the development of average autogenous shrinkage in the first 24 hours. Table 6.11 presents the average results and standard deviations obtained at the end of several time intervals up to 24 hours. The starting point (0 hr) for the measurements is taken the 19th hour after casting. As it has been mentioned earlier 19 hours are needed in order for the material to set and therefore it is assumed that no shrinkage takes place during this period of time. In Figure 6.11 and elsewhere, SF and SNF are used to designate small prisms with and without fibres, respectively.

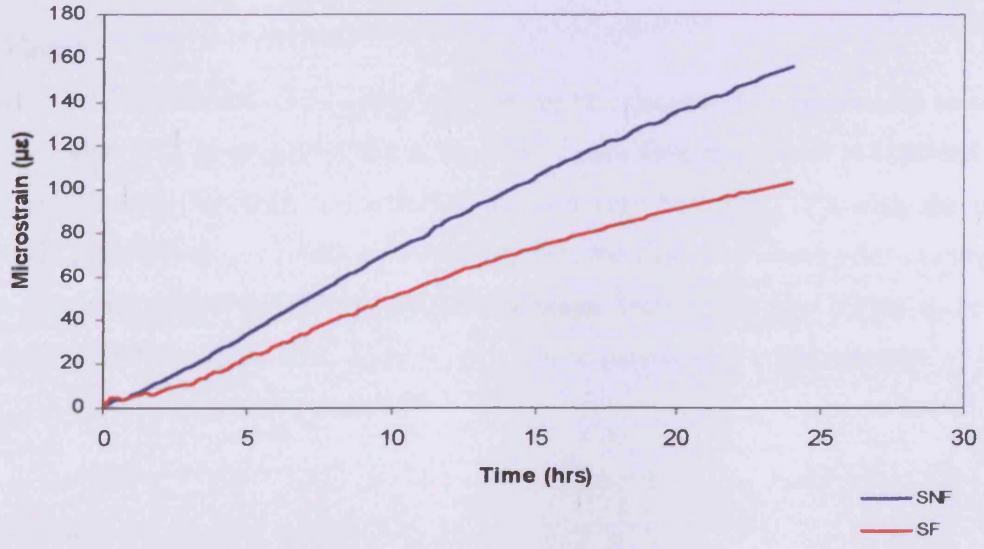

Figure 6.12: Autogenous shrinkage strain variation with time for mixes with and without fibres (0-24 hours).

Table 6.11: Average autogenous shrinkage strain (με) values (with COV) for mixes with and without fibres at the end of each time interval.

	Time Intervals (hours)					
	4	**8**	**12**	**16**	**20**	**24**
SF	14.81	37.52	57.45	73.94	87.60	99.42
COV	21.00	14.01	12.03	10.73	10.26	9.29
SNF	20.99	49.94	77.66	101.88	124.42	143.82
COV	3.70	2.43	2.26	2.34	2.69	2.37

It has to be mentioned that both types of mix have nearly the same constituents expect for the fibres. It becomes quickly clear that the presence of fibres reduces the autogenous shrinkage strains as expected. The mixes without fibres exhibit a rapid development of autogenous shrinkage strains. This increase in shrinkage strains takes place at a higher rate than for the mixes containing fibres. The strains for mixes with and without fibres, at the end of the first twenty-four hours are about 99 and 144 με, respectively. It clear already from the first hours that the inclusion of fibres in the matrix has a restraining effect on the development of the autogenous shrinkage strains. The omission of fibres from the matrix results in a 45% increase in the measured shrinkage strains after 24 hours.

0-7 days

Figure 6.13 shows how the average autogenous shrinkage strains develop up to seven days. Table 6.12 gives the results at the end of each time interval. It is expected that the autogenous shrinkage keeps increasing at a very high rate, following the trend seen in Figure 6.12. As it was mentioned earlier, the first seven days after casting are the dominant period for the autogenous shrinkage. During this time period there is a major autogenous strain development, as it will be presented in a later section.

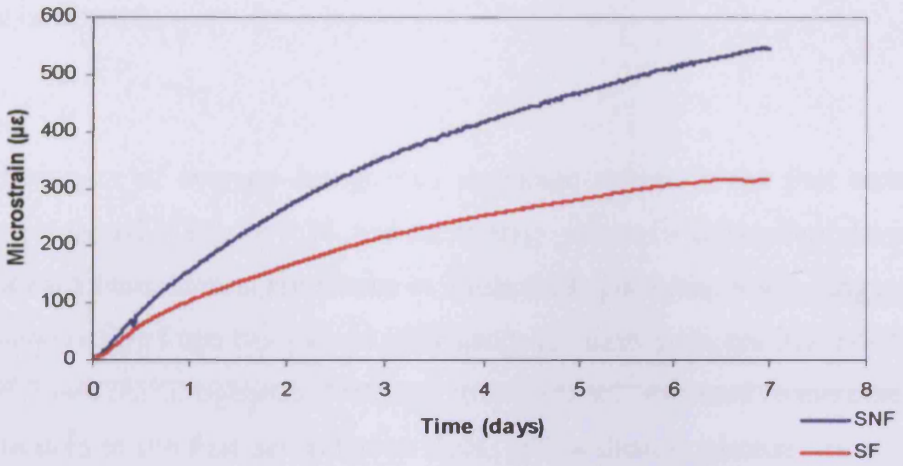

Figure 6.13: Autogenous shrinkage strain variation with time for mixes with and without fibres (0-7 days).

Table 6.12: Average autogenous shrinkage strain (με) values (with COV) for mixes with and without fibres at the end of each time interval.

	Time Intervals (days)						
	1	2	3	4	5	6	7
SF	99.42	160.17	212.09	250.11	278.94	305.03	328.34
COV	9.29	7.66	6.81	5.86	5.59	5.04	4.91
SNF	143.82	248.52	329.91	391.19	442.31	485.23	521.63
COV	2.37	2.09	2.04	2.07	1.94	1.92	1.89

It can be observed from Figure 6.13 that the autogenous shrinkage strains development continues at high rates, especially for the mixes without fibres. Mixes containing fibres exhibit a significant decrease in the values of autogenous strains. The difference between the measured values for mixes with and without fibres further increases. The strain values on the seventh day are about 328 and 521 με for the mixes with and without fibres, respectively. The difference between the maximum values reaches 59%, whereas in the first twenty-four hours it was only 45%. It is clear that in the first seven days a large amount of autogenous deformation takes place in the plain

matrix, whereas in the case of fibred mixes this deformation is restrained by the existence of fibres.

0-30 days

The development of average autogenous shrinkage strains in the first month after casting is presented in Figure 6.14, and the average values (with standard deviation) at the end of each time interval are shown in Table 6.13. The main dominating period for the autogenous shrinkage has passed after about ten days from casting. For that time up to one month the autogenous shrinkage strains are still expected to increase but at a lower rate than in the first seven to ten days, with a distinct plateau being observed especially in the mixes containing fibres.

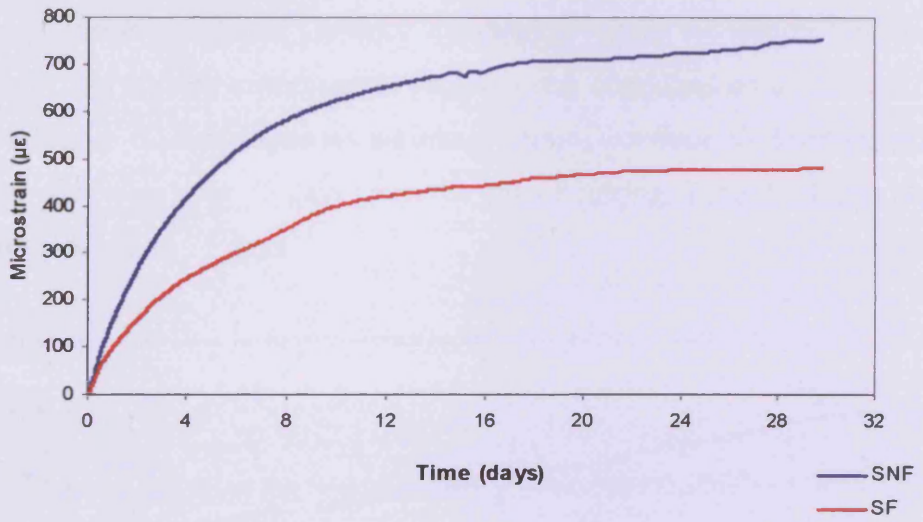

Figure 6.14: Autogenous shrinkage strain variation with time for mixes with and without fibres (0-30 days).

Table 6.13: Average autogenous shrinkage strain (με) values (with COV) for mixes with and without fibres at the end of each time interval.

	Time Intervals (days)					
	5	**10**	**15**	**20**	**25**	**30**
SF	278.94	404.78	447.03	496.89	483.23	479.53
COV	3.98	2.87	2.61	2.20	2.21	1.97
SNF	442.31	589.16	644.60	678.22	693.82	754.25
COV	195	1.87	2.15	2.11	2.17	2.32

From Figure 6.14 it can be observed that the rate of increase of autogenous shrinkage strains is smaller after the tenth day. This confirms our earlier observations which are also mentioned in literature; the main dominating period for the autogenous shrinkage is the first ten days after casting. The shrinkage strains reached in the first month of measurements are about 754 and 480 με for mixes without and with fibres, respectively. At this stage, the reduction of the autogenous shrinkage strains by fibres seems to decrease the actual difference between the measured values at the end of 30 days to around 57%, whereas on the seventh day that difference had reached in excess of 59% (Figure 6.13).

More than 30 days

As has already been observed, when the first crucial ten days have passed the autogenous shrinkage strains continue developing within the matrix but at a much slower rate. The current experimental program was continued up to 75 days. As it is shown in Figure 6.15, autogenous shrinkage strains continue to develop, albeit at a very slow rate, even after 75 days from the day of casting. Table 6.14 also shows the recorded values up to 75 days.

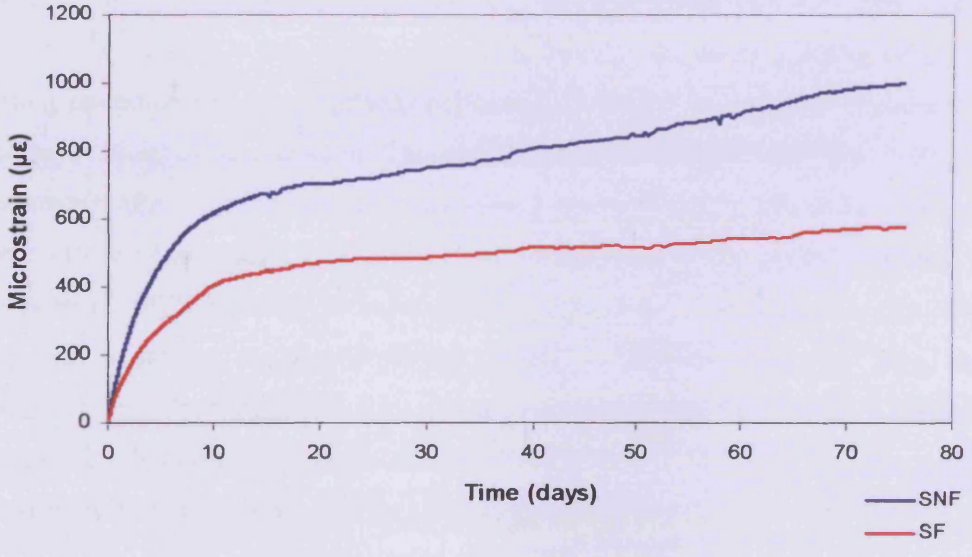

Figure 6.15: Autogenous shrinkage strain variation with time for mixes with and without fibres (up to 75 days).

Table 6.14: Average autogenous shrinkage strain (με) values (with COV) for mixes with and without fibres at the end of each time interval.

	Time Intervals (days)						
	10	**20**	**30**	**40**	**50**	**60**	**75**
SF	404.78	496.89	479.53	515.69	518.57	540.73	577.00
COV	3.98	2.87	2.61	2.20	2.21	1.97	1.66
SNF	589.16	678.22	754.25	775.53	842.41	903.01	1000.24
COV	1.87	2.11	2.32	1.63	1.58	1.62	1.45

As it can be seen autogenous volumetric changes still take place even at the end of 75 days. However, it is clear that the values in both mixes, with and without fibres, nearly reach a plateau. The rate of strain development is slower compared to the early stages. The strains are expected to continue increasing. The most probable reason for this phenomenon is the relatively coarse type of the cement used (Blaine fineness 290-420 m^2/kg), which results in a slow hydration process. Such phenomena of long lasting hydration and slow autogenous volume deformations have been also reported in the literature (Cheyrezy and Behloul, 2001; Koenders, 1997; Koenders and Breugel, 1999; Tazawa and Miyazawa, 1995). The recorded values for the shrinkage strains at the end of 75 days for mixes with and without fibres are 577 and 1000 με, respectively. Another key issue which may help in the understanding of this long lasting phenomenon of autogenous shrinkage is that the material, as explained in an earlier section of the current Chapter, has not undergone any hot curing. The specimens after demoulding and attachment of the acoustic vibrating wire gauges were insulated and placed in a room with controlled environment (constant room temperature of 20°C). The fact that no hot curing has taken place possibly leads to chemical reactions, triggered during hydration period, to be a long lasting phenomenon. Therefore both the primary and secondary reactions, explained in Chapter 2 – Section 2.2.2, need a long period of time to complete and that might be the reason for having some residual self-induced volume changes even after 75 days.

The effect of fibres on the reduction of autogenous shrinkage strains is pronounced. The exclusion of fibres results in an excessive 74% increase in the self-induced

shrinkage strains. As can be observed the autogenous shrinkage causes large strains in the hardening matrix. It might have been thought that restraining such excessive shrinkage strains may cause the formation of tensile stresses and consequently development of microcracking. That might be the case for ordinary concretes but not for CARDIFRC®. No visible cracking has been observed on the specimens after the end of the experimental period. That is not surprising since CARDIFRC® contains a relatively large amount of small fibres, which act as crack arresting mechanism. Table 6.15 summarises recorded autogenous shrinkage strains at the end of each time interval.

Table 6.15: The recorded strain values (with standard deviation) at the end of each time interval for mixes with and without fibres.

	Autogenous shrinkage strains mixes with fibres (με)	**Autogenous shrinkage strains mixes without fibres (με)**
0-24 hours	99.42 (9.25)	143.82 (1.92)
0-7 days	328.34 (16.11)	521.63 (9.86)
Up to 30 days	479.53 (12.50)	754.25 (17.50)
Up to 75 days	577.00 (9.55)	1000.24 (14.47)

6.6 Possible sources of errors in experimental work

In the preceding sections of the current Chapter the experimental set-up and the test results have been described. In order to draw the best possible and reliable conclusions from these results, we have to take into account possible sources of error during shrinkage experiments. First of all the vibration of the material during compaction of the specimens has to be precise so as to eliminate the formation of any air voids (Chapter 4 – Section 4.5.2.3) within the matrix. Another very important issue is the good insulation of the material from the surrounding environment for the first 17 hours. This is vital because we want the material to harden only by consuming the water added during mixing and not by using an external water source like the humidity available in the environment.

A very critical point in the experimental procedure is the demoulding of specimens after 17 hours. Once the specimens have been demoulded, they have to be placed

aside and covered with a vinyl acetate blanket, consisting of three or four vinyl acetate sheets. This will prevent the moisture exchange between the specimens and the surrounding environment while the strain gauges are being attached. Special care has to be taken during demoulding and generally throughout the gauge attachment period, especially of the specimens without fibres. The reason for this is the fact that the plain CARDIFRC® matrix is very brittle and jerks may induce microcracks, which in turn will affect the subsequent strain readings.

Care has also got to be exercised during the attachment of the gauges. First of all, the gauges, as mentioned earlier, have to be exactly opposite each other on the sides of the specimens. Any other positioning of the gauges will affect the readings. The adhesive used is very strong and hardens rapidly. The process has to be quick and precise. Using a lot of adhesive to glue the mounting blocks of the gauge on the surface of the specimen may affect the readings, since the bond between the blocks and the specimen will be very strong and therefore the gauge might have problems picking the volume changes of the material. On the other hand, inadequate amount of glue will result in poor bonding and eventually in the failure of the bond between the mounting blocks and the specimen. This happened in a couple of instances which had to be repeated.

The wrapping of the specimen has to be done carefully, taking care not to damage the gauges or their calibration. Placement of the wrapped specimens is also very important. The specimens have to be placed in a room with controlled environment. Furthermore, they have to be kept away from any sources of vibration since even any small movement of the specimens will cause inconsistencies in the recorded data. It has to be borne in mind that the gauges used are acoustic vibration wire gauges and any movement or noise can affect their readings. It should be mentioned however that despite the efforts made to seal the specimens some contact with the surrounding environment may have occurred resulting in some drying shrinkage. This may explain why the measured autogenous shrinkage is very large and continued to be recorded throughout the testing period.

6.7 Size effect in autogenous shrinkage strain

As has been discussed in Section 6.5.2 of the current Chapter the large beams without fibres gave very consistent results regarding the development of the autogenous shrinkage strains (Table 6.9 – Figure 6.8). The values at 90 hours for the large beams are comparable with those of small beams over this time interval, as can be seen in Table 6.16 and Figure 6.16. Note that the values presented in Table 6.16 are the mean values (and COV) observed from all the beams tested of each size up to 90th hour.

Table 6.16: Autogenous shrinkage strains (με) at various time intervals up to 90 hours for large and small beams (LNF: large beams without fibres; SNF: small beams without fibres).

	Time Intervals (hours)								
	10	**20**	**30**	**40**	**50**	**60**	**70**	**80**	**90**
LNF	70.24	133.01	181.57	222.43	259.28	291.71	319.21	343.96	366.34
COV	3.77	2.22	1.25	1.02	0.97	1.03	1.03	1.11	1.13
SNF	63.82	124.42	171.38	214.94	254.25	290.59	321.72	349.74	374.44
COV	1.33	1.34	1.35	1.36	1.37	1.38	1.39	1.39	1.40

A quick perusal of Table 6.16 and Figure 6.16 leads to the conclusion that there is practically no difference between the measured strain values for large and small specimens without fibres.

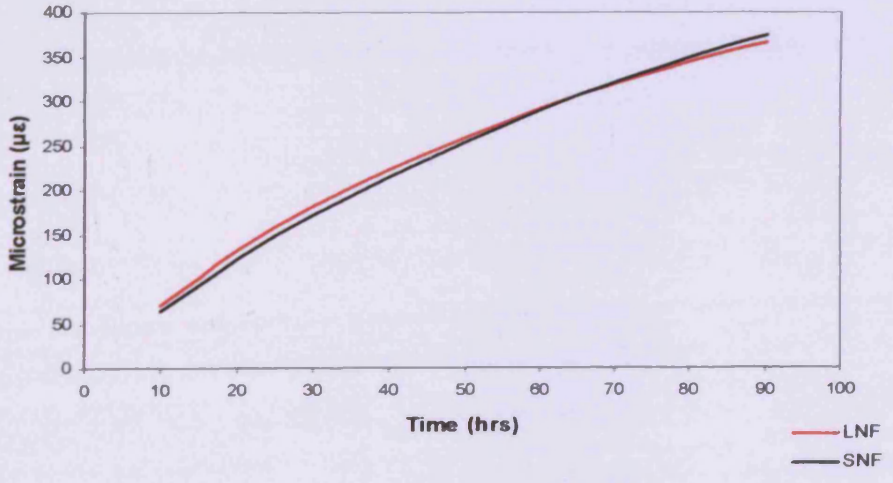

Figure 6.16: Autogenous shrinkage strain variation up to 90 hours for large and small beams without fibres.

This shows that there is no size effect in the development of the autogenous shrinkage strains in plain CARDIFRC® matrix. Although the larger beams (100x100x500mm) are two times bigger than the small prisms (50x50x250mm) their behaviour as far as the self-induced volume changes are concerned is found to be nearly identical. In other words, in the case of specimens without fibres the size of the member does not seem to play a key role in the development of autogenous shrinkage strains. This would also mean that autogenous shrinkage is a bulk phenomenon and that no shrinkage cracking has taken place because cracking is a surface phenomenon which necessarily would have produced a size effect.

6.8 Conclusions

Experimental results have been presented in this section. Autogenous shrinkage is found to be a long-lasting phenomenon for this kind of material, a phenomenon that could last up to 75 days and even more. This property of long-lasting hydration can be mainly attributed to the fairly coarse nature of the cement used, as well as to the fact that no hot curing had taken place and therefore the hydration reactions need a lot of time to occur. Because of the delayed hydration the rate of gain of the stiffness for this material is also slow. The first ten days proved to be the dominating period for the development of the autogenous shrinkage strains since during this time period the strains develop at very high rates, whereas after the tenth day the development of self-induced strains started progressively to stabilise. Fibres are found to have a significant restraining effect on the autogenous shrinkage of CARDIFRC® matrix. No size effect was found in the shrinkage strains of CARDIFRC® specimens without fibres.

Chapter 7: Model Predictions and Comparison

7.1 Introduction

In this Chapter, we will use the models developed in Chapter 5 for the evolution of autogenous shrinkage and the stiffness of paste, mortar and CARDIFRC® as hydration proceeds and compare the model predictions with the autogenous strain measurements reported in Chapter 6. We show in particular that the reduction in the autogenous shrinkage in plain CARDIFRC® mixes brought about by the addition of fibres can be explained by the restraint provided by the fibres to free autogenous shrinkage and that this restraint can be adequately captured by the increase in the stiffness of CARDIFRC® with fibres as the hydration progresses.

7.2 Evolution of the E of CARDIFRC® matrix and CARDIFRC® with hydration

The proposed model for the evaluation of the modulus of elasticity for the CARDIFRC® has been discussed in Chapter 5 – Section 5.9. The model evaluates the modulus of elasticity with respect to the changes in the degree of hydration, since these two parameters are strongly interconnected. As the hardening proceeds and the degree of hydration increases, the material becomes stiffer and therefore the Young modulus increases. The evaluation of the evolution of the elastic modulus with degree of hydration is of high importance in the prediction of the autogenous shrinkage strains. As has been described in Chapter 5 – Sections 5.4, 5.5 and 5.11, in order to predict the autogenous shrinkage strains we have to relate the microstructural volume changes taking place in the material with the surface tension of the adsorption layer. For this purpose the modified Bangham concept (Chapter 5 – Section 5.5) was used as the basis of the thermodynamic model proposed in Chapter 5 – Section 5.11. As equation (5.12) shows, the change in the external deformation of a hardening cement paste is proportional to the change in the effective surface tension. The proportionality factor that relates these two quantities is given by equation (5.15). This proportionality factor depends on the Young Modulus of the matrix examined. Such a property is not constant during the hardening of the material and therefore has to be

evaluated in order to model accurately the volumetric changes of hardening cement-based materials.

Therefore, it is important to know how the elastic modulus of the matrix evolves with increasing degree of hydration so that to use this information for the prediction of the autogenous shrinkage strains according to the model described in Chapter 5 – Section 5.11. Figure 7.1 shows the flowchart for the calculation of the E of the paste, matrix and finally CARDIFRC® with fibres, based on the multi-stage procedure described in Chapter 5.

E-Value Calculation Model

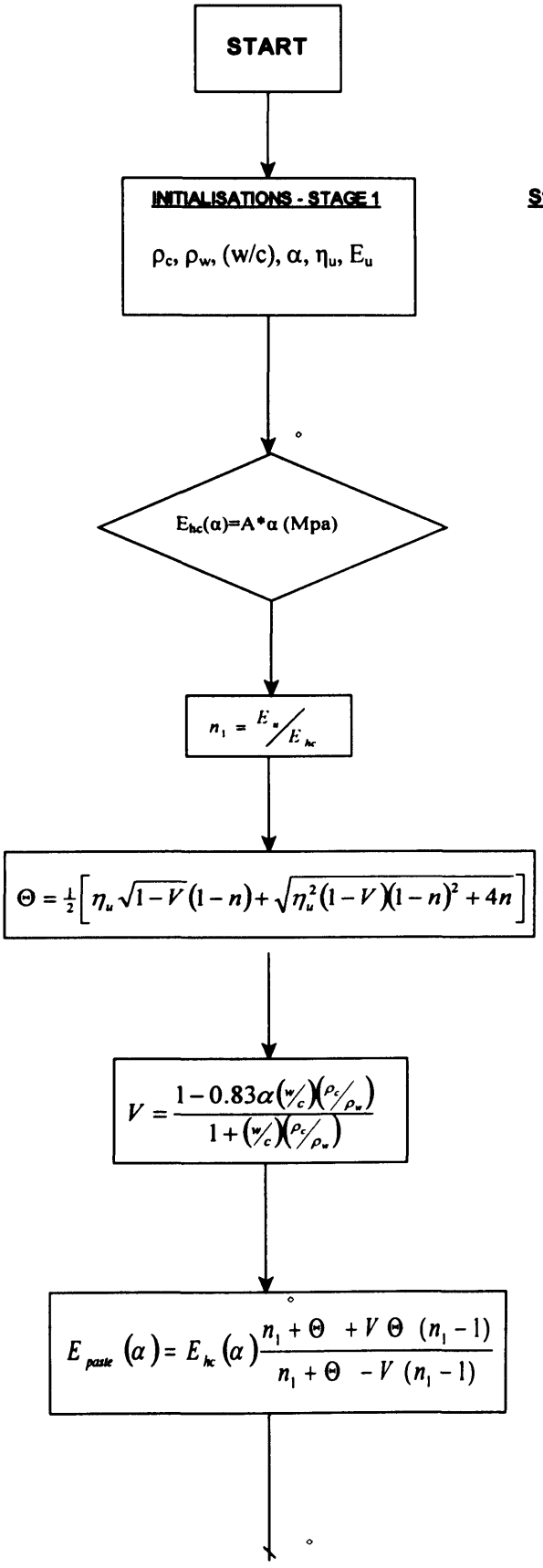

Stage 1 - Cement Paste

(eq. 5.29)

(eq. 5.28)

(eq. 5.30)

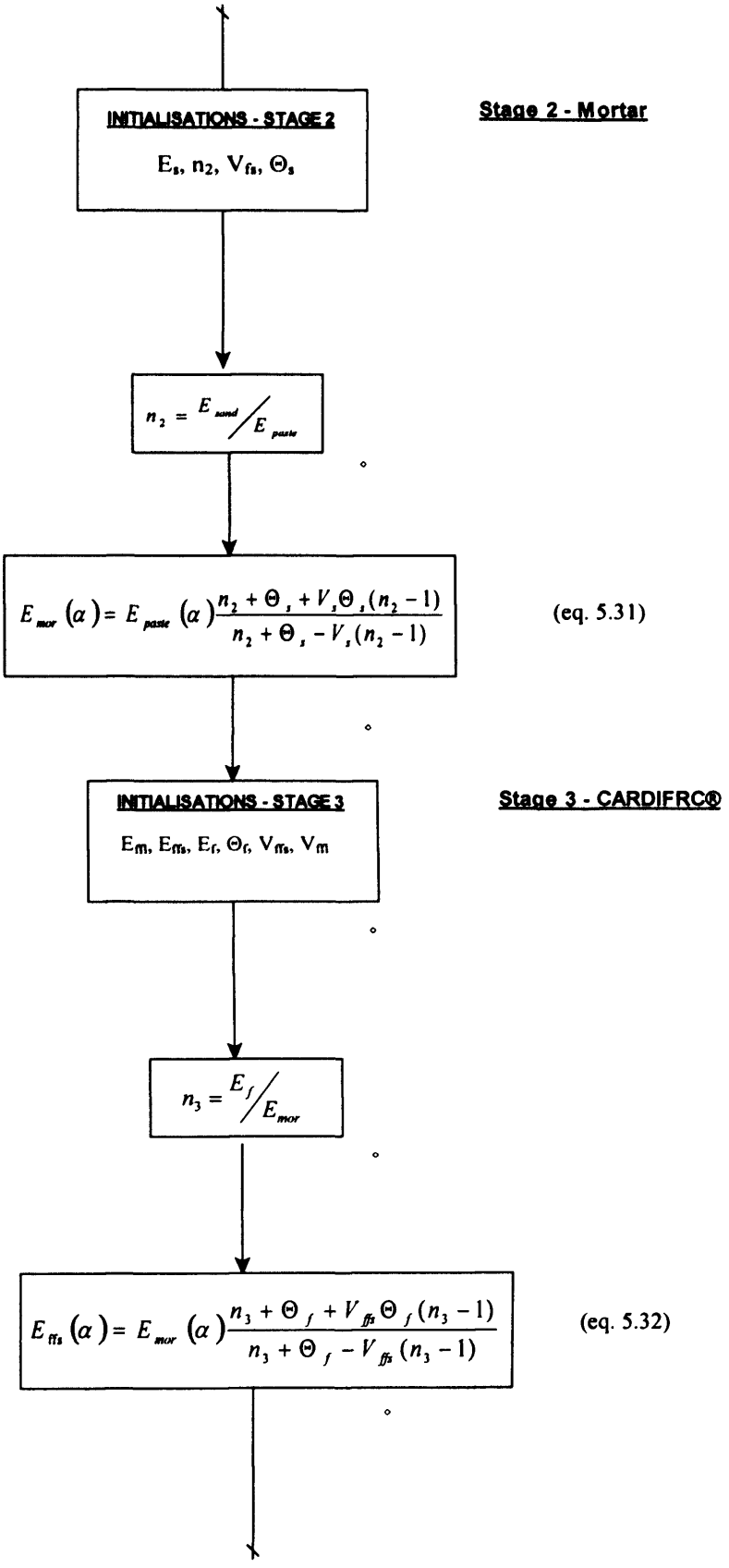

Stage 2 - Mortar

(eq. 5.31)

Stage 3 - CARDIFRC®

(eq. 5.32)

$$E_{ffl}(\alpha) = E_{mor}(\alpha)\frac{n_3 + \Theta_f + V_{ffl}\Theta_f(n_3 - 1)}{n_3 + \Theta_f - V_{ffl}(n_3 - 1)} \quad \text{(eq. 5.33)}$$

$$E_{CARDIFRC}{}^{®}(\alpha) = E_{ffs}(\alpha) + E_{ffl}(\alpha) \quad \text{(eq. 5.34)}$$

Figure 7.1: Flowchart showing the calculation procedure for the evaluation of E-value.

Figure 7.2 shows how the modulus of elasticity increases as the paste becomes stiffer by continued hydration and by the addition first of fine sand and afterwards of the steel fibres for an arbitrarily chosen value of A = 24480 MPa of the unhydrated cement (see Chapter 5), characteristic of coarse grained OPC.

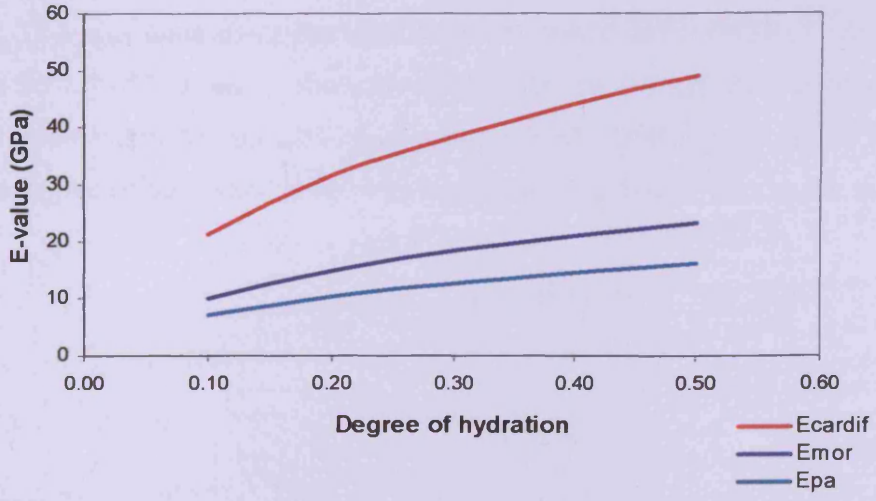

Figure 7.2: The modulus of elasticity variation with degree of hydration ($E_{cardifrc}$: CARDIFRC® E-value; E_{mor}: Mortar E-value; E_{pa}: Cement paste E-value).

The fine quartz sand does not seem to add significantly to the stiffness of the cement paste, but the contribution from the fibres is very significant. Note that there is no point in continuing the calculations beyond α=0.5 because of the very low water to cement ratio used in CARDIFRC® which is not sufficient to hydrate all the cement used. This will be confirmed below when we relate degree of hydration to the time since mixing.

The maximum obtained E-value for the CARDIFRC® with the model is 49.07 GPa which is somewhat higher than the actual value achieved in the laboratory (Table 6.7). This may suggest that α has not even reached 0.5 in the test specimens at the age of testing. Table 7.1 illustrates the results for the elastic modulus of cement paste, mortar and CARDIFRC® at specific degrees of hydration. We shall adjust this value below.

Table 7.1: Elastic modulus values (GPa) at specific degrees of hydration for cement paste, mortar and CARDIFRC®.

	Degree of hydration				
	0.1	**0.2**	**0.3**	**0.4**	**0.5**
E_{pa}	6.96	10.38	12.70	14.57	16.23
E_{mor}	9.99	14.90	18.23	20.90	23.29
$E_{CARDIFRC®}$	21.22	31.54	38.52	44.10	49.07

In order to be able to compare the predicted value of the E of CARDIFRC® with the measured value, it is necessary first to relate the degree of hydration to the time since mixing. This was done using the microstructural model HYMOSTRUC described in Section 3.3.2.3 of Chapter 3 (Koenders, 2004). This simulation was performed on the paste with the characteristics and constituents of CARDIFRC® paste. Table 7.2 shows how the degree of hydration varies with time during the first 24 hours after mixing.

Table 7.2: Variation of degree of hydration with time (Koenders, 2004).

Time (Hours)	α	Time (Hours)	α
3.00	0.028	13.67	0.142
3.33	0.036	14.00	0.143
3.67	0.043	14.33	0.145
4.00	0.049	14.67	0.147
4.33	0.055	15.00	0.149
4.67	0.061	15.33	0.150
5.00	0.066	15.67	0.152
5.33	0.071	16.00	0.153
5.67	0.075	16.33	0.155
6.00	0.080	16.67	0.156
6.33	0.084	17.00	0.158
6.67	0.088	17.33	0.159
7.00	0.091	17.67	0.161
7.33	0.095	18.00	0.162
7.67	0.098	18.33	0.164
8.00	0.101	18.67	0.165
8.33	0.104	19.00	0.166
8.67	0.107	19.33	0.168
9.00	0.110	19.67	0.169
9.33	0.113	20.00	0.170
9.67	0.116	20.33	0.171
10.00	0.118	20.67	0.173
10.33	0.121	21.00	0.174
10.67	0.123	21.33	0.175
11.00	0.125	21.67	0.176
11.33	0.127	22.00	0.177
11.67	0.130	22.33	0.178
12.00	0.132	22.67	0.179
12.33	0.134	23.00	0.181
12.67	0.136	23.33	0.182
13.00	0.138	23.67	0.183
13.33	0.140	24.00	0.184

These results are plotted on Figure 7.3. They are best represented by the equation (7.1), obtained using the inbuilt facility of EXCEL.

$$\alpha = 0.075 \ln(t) - 0.0546 \tag{7.1}$$

where α is the degree of hydration and t is the time in hours (t>1 hour).

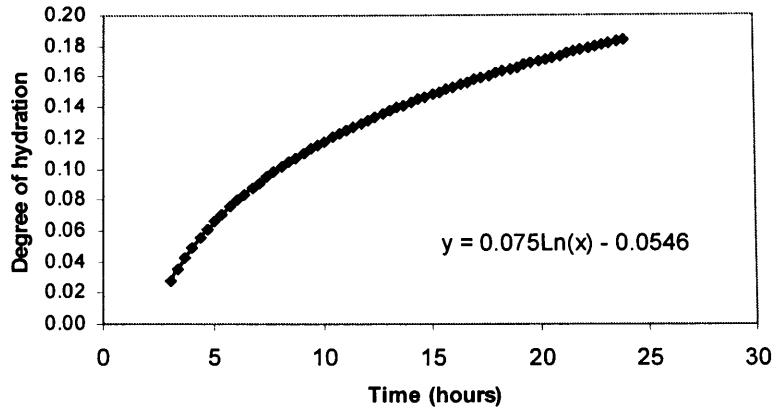

Figure 7.3: Variation of degree of hydration with time and the equation between them.

Although this equation is only valid up to 24 hours, we have used it to forecast the degree of hydration beyond 24 hours in the knowledge that the rate of hydration is already showing signs of decreasing. This is shown in Figure 7.4 where the degree of hydration has been projected up to 1800 hours (75 days) after mixing.

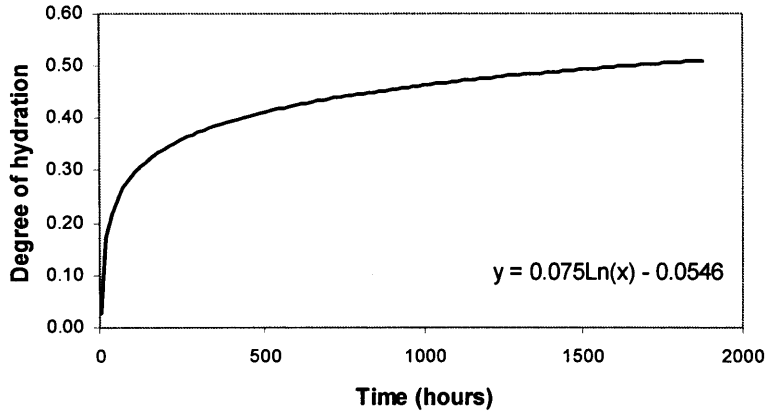

Figure 7.4: Forecast of the evolution of degree of hydration with time up to 1800 hours using equation (7.1).

It is seen that in the view of the very low water to binder ratio in CARDIFRC® only about 50% of the binder is hydrated after 75 days. This is supported by visual observations during compressive and indirect tensile testing during which a lot of loose unhydrated material dropped out of the specimens.

Equation (7.1) is now used to plot the evolution of the elastic modulus of paste, mortar and CARDIFRC® with time, corresponding to Figure 7.2 where the evolution with degree of hydration is shown.

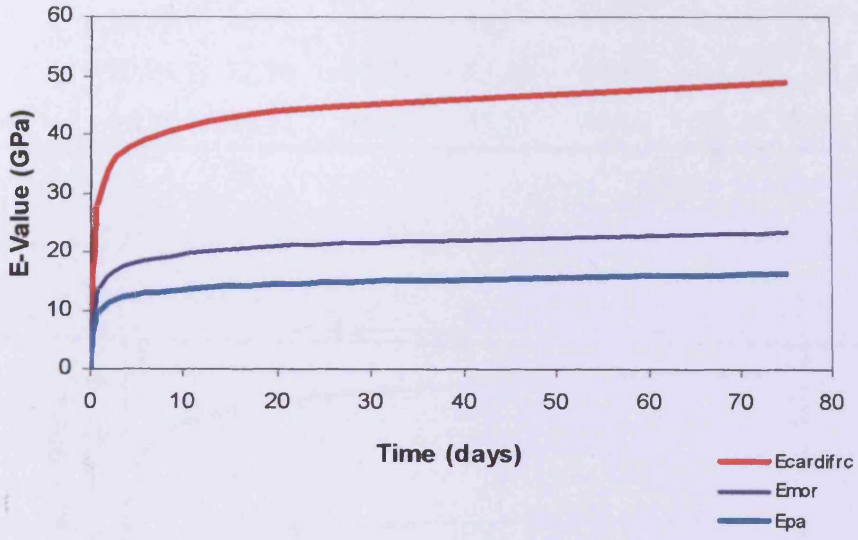

Figure 7.5: The modulus of elasticity variation with time ($E_{cardifrc}$: CARDIFRC® E-value; E_{mor}: Mortar E-value; E_{pa}: Cement paste E-value).

As the specimens for the measurement of E-value of CARDIFRC® were tested in the laboratory after 25 days (600 hours) (Table 6.7), as can been seen from Figure 7.5 the model predicts that the elastic modulus of CARDIFRC® is about 45 GPa at this time whereas the measured value is 48 GPa (Table 6.7). The specimens tested in the laboratory had undergone 9-day hot curing and had been left in ambient conditions for a further 16 days (total 25 days). That may explain the slightly higher measured value than the model prediction at that age (600 hours). Nevertheless, we shall use the measured value of 48 GPa at 600 hours in order to calibrate the model, i.e. to fix the arbitrarily chosen value of A (24480 MPa). This was done by trial and error. The resulting value of A is 25920 MPa.

Table 7.3 summarises the model predictions at the end of various time intervals for the calibrated value of A. The evolution of E of paste, mortar and CARDIFRC with age are shown in Figure 7.6.

Table 7.3: Elastic modulus values (GPa) at specific time intervals for cement paste, mortar and CARDIFRC®.

	Time Intervals (days)							
	10	**20**	**25**	**30**	**40**	**50**	**60**	**75**
E_{pa}	14.59	15.58	15.88	16.11	16.50	16.79	17.03	17.18
E_{mor}	20.94	22.36	22.79	23.12	23.67	24.09	24.43	24.66
$E_{CARDIFRC®}$	44.18	47.13	48.02	48.71	49.86	50.74	51.45	51.91

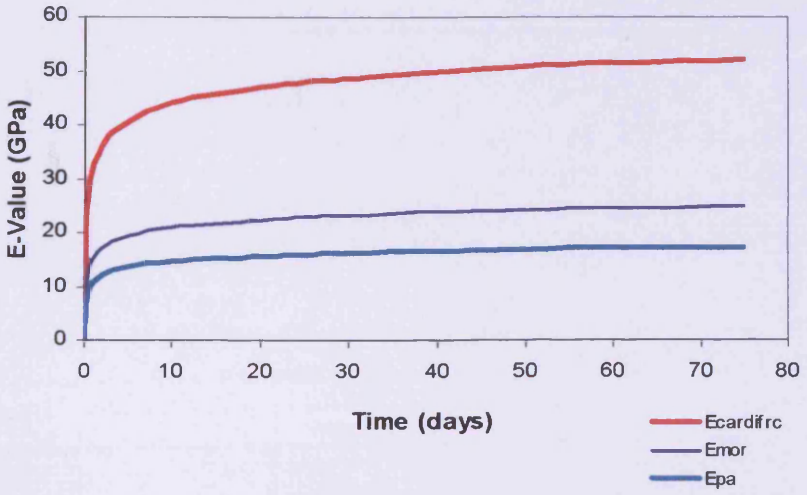

Figure 7.6: The modulus of elasticity variation with time for A=25920 MPa ($E_{cardifrc}$: CARDIFRC® E-value; E_{mor}: Mortar E-value; E_{pa}: Cement paste E-value).

As can be seen in Table 7.3 the model after the calibration for A gives a very good prediction for the elastic modulus. Note that the measured value of E of CARDIFRC® is 48 GPa at 25 days and the model has been calibrated to exactly the same value at 25 days. A very interesting point regarding the evolution of modulus of elasticity as the hydration proceeds is the ratio between the predicted values for CARDIFRC® and mortar. The ratio of $E_{CARDIFRC®}$ to E_{mor} is almost constant and equals to 2.10 throughout the whole hydration process. In other words, in both cases the material gains stiffness at the same rate but in the case of CARDIFRC® the values are much higher as a result of the incorporation of steel fibres in the mix. By looking back at the autogenous shrinkage results (Chapter 6), it was found that the ratio of measured strains for the mixes without fibres to those measured for mixes with fibres is also

almost constant during the measurement time and equal to 1.70. The variation and evolution of stiffness in CARDIFRC®, with and without fibres, can therefore shed some light on the expected difference in the measured autogenous shrinkage strains of mixes with and without fibres.

7.3 Experimental shrinkage data versus model predictions

Having calibrated the model, we are now in a position to predict the autogenous shrinkage strains in CARDIFRC® with and without fibres. This will follow the procedure outlined in the flowchart on Figure 7.7.

Autogenous Shrinkage Strains Prediction Model

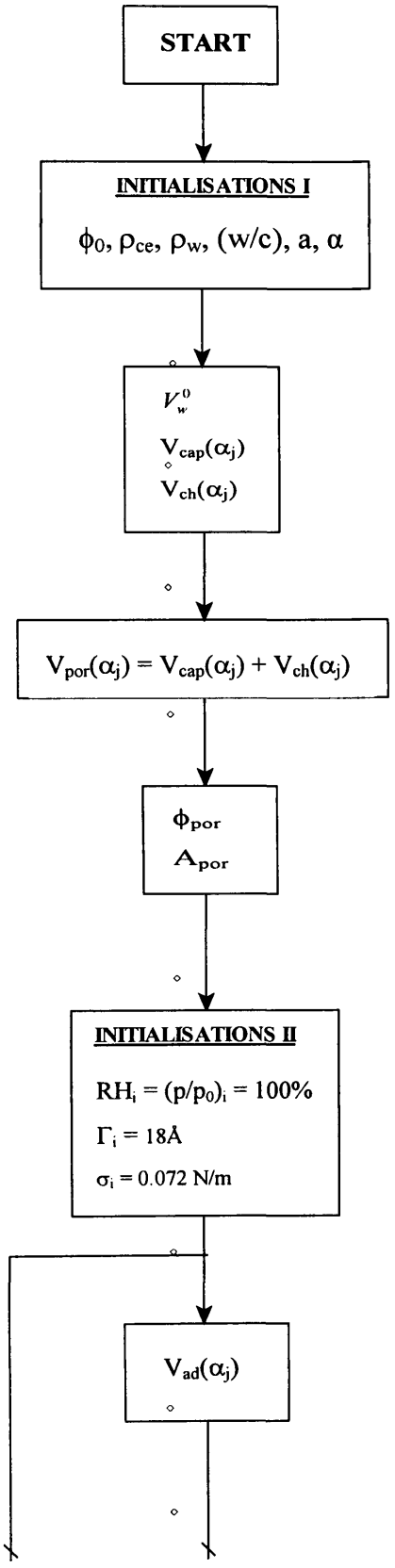

(eq. 5.38)

(eq. 5.37)

(eq. 5.40)

(eq. 5.42)

(eq. 5.22)

(eq. 5.43)

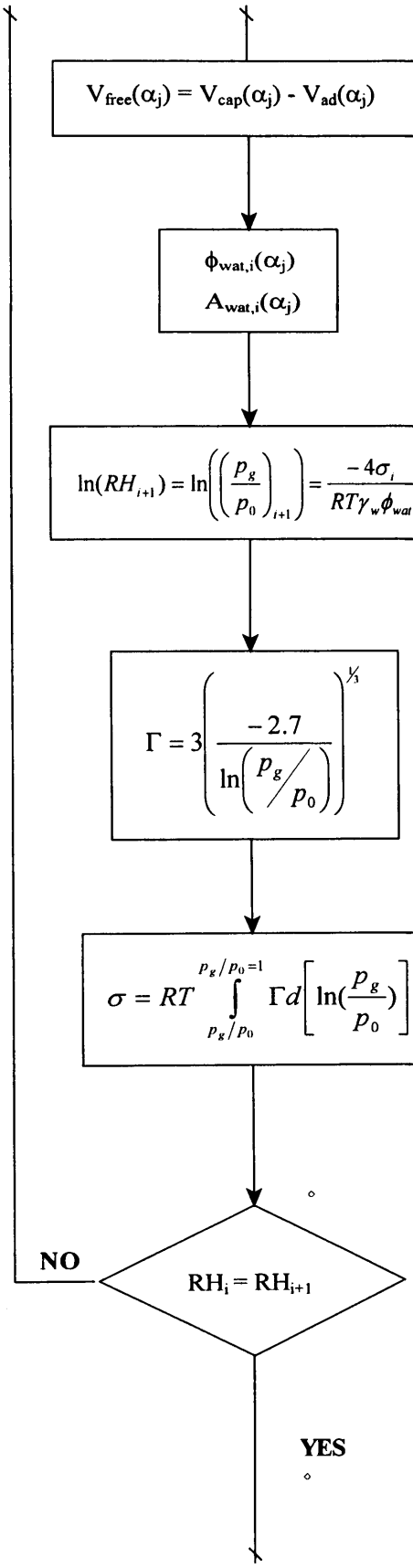

(eq. 5.45(a))

(eq. 5.23)

(eq. 5.10)

(eq. 5.46)

(eq. 5.9)

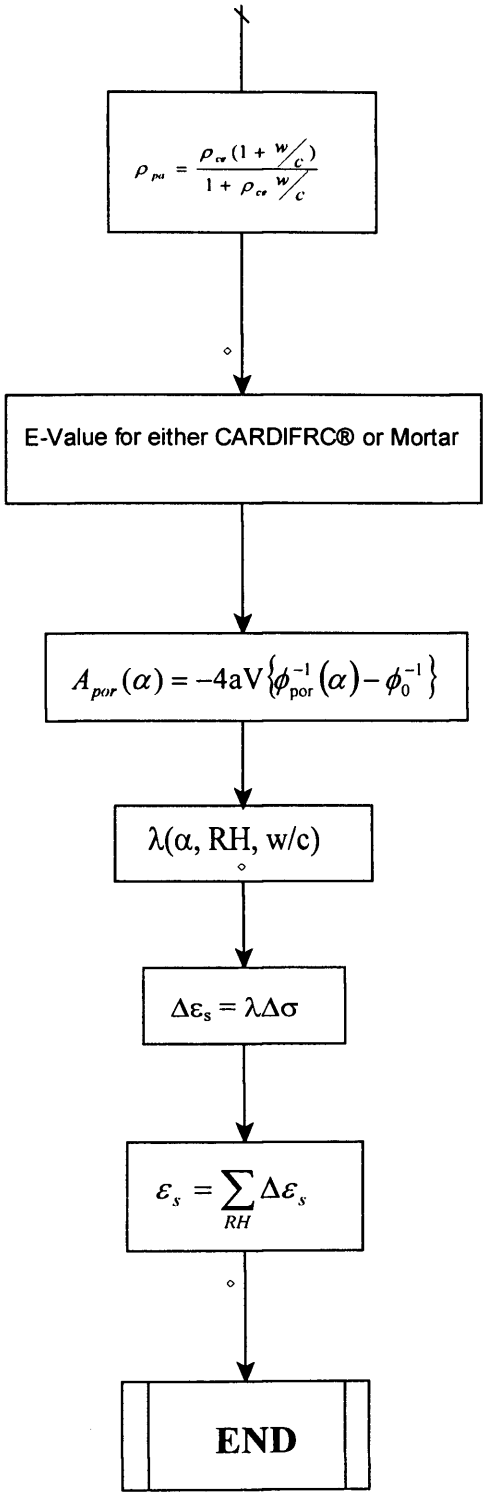

(eq. 5.25)

either (eq. 5.34) or (eq. 5.31)

(eq. 5.22)

(eq. 5.15)

(eq. 5.47)

(eq. 5.48)

Figure 7.7: Flowchart for the used model for the prediction of the autogenous shrinkage strains.

Before presenting the shrinkage strains it is useful to get an idea of how the available water is consumed during hydration and how the capillary pore size distribution and other relevant quantities change during hydration. We will show these results up to the degree of hydration of 50%, which, as we have seen above corresponds roughly to an age of 75 days during which the autogenous shrinkage measurements were taken. Table 7.4 presents the variation of the water volumes with degree of hydration. Figure 7.8 illustrates graphically the variation of water volume with degree of hydration.

Table 7.4: Variation of water free water volume, capillary water volume and pore water volume (values are in m^3; V_{free}: volume of free water for hydration; V_{cap}: volume of capillary water; V_{por}: volume of water in pores).

α	V_{free}	V_{cap}	V_{por}
0.1	0.15	0.34	0.35
0.2	0.12	0.26	0.29
0.3	0.08	0.19	0.22
0.4	0.04	0.11	0.16
0.5	0.00	0.05	0.11

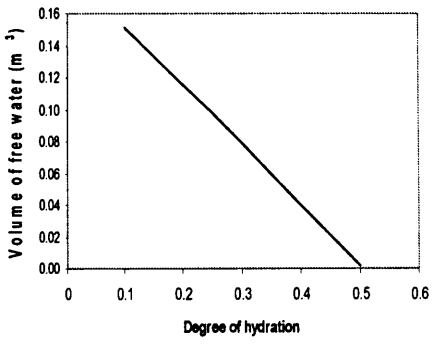

(a)

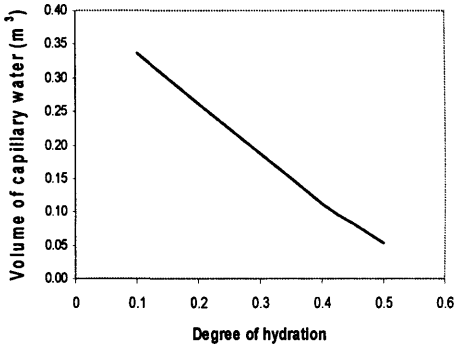

(b)

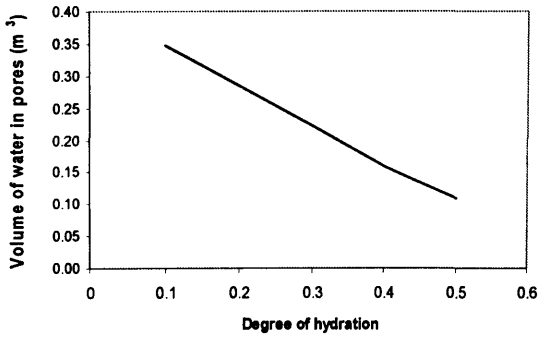

(c)

Figure 7.8: Variation of water volume with degree of hydration; (a) volume of free water for hydration; (b) volume of capillary water and (c) volume of water in pores.

In Figure 5.5 (Section 5.11.1) the state of the water in the pore system has been presented. It is expected that as the volume of the free water for hydration is reduced the volume of the adsorbed water will reduce leading to a reduction of the thickness of the adsorption layer and the maximum pore diameter. Consequently the surface tension of the adsorption layer increases. These assumptions have been verified by the model as illustrated in Table 7.5 Figures 7.9 and 7.10.

Table 7.5: Variation of volume of adsorbed water (V_{ad}), maximum pore diameter ϕ_{por}, thickness of the adsorption layer (Γ) and surface tension (σ) with degree of hydration.

α	V_{ad} (m^3)	ϕ_{por} (nm)	Γ (Å)	σ (N/m)
0.1	0.19	5.48	9.15	0.02
0.2	0.15	4.33	7.22	0.03
0.3	0.11	3.39	5.64	0.05
0.4	0.07	2.60	4.34	0.08
0.5	0.04	1.96	3.46	0.13

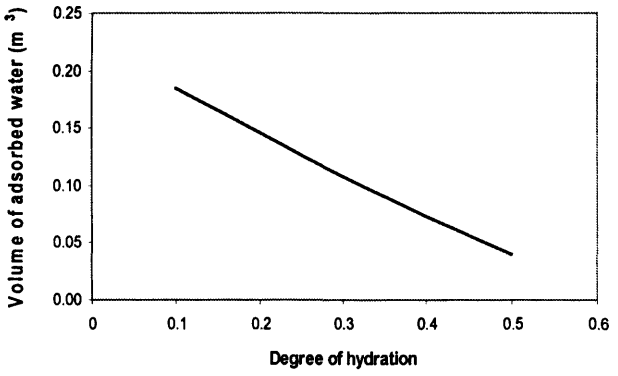

(a)

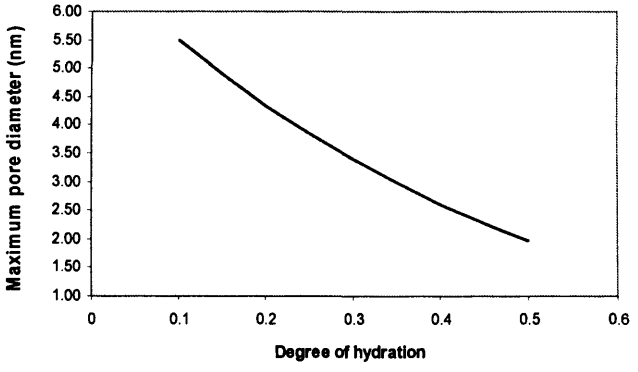

(b)

Figure 7.9: (a) variation of volume of adsorbed water with degree of hydration; (b) variation of maximum pore diameter with degree of hydration.

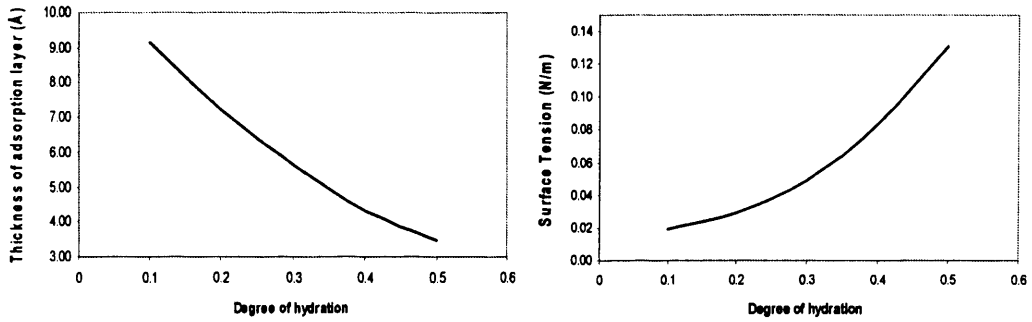

(a) (b)

Figure 7.10: (a) variation of thickness of the adsorption layer with degree of hydration; (b) variation of surface tension of the adsorption layer with degree of hydration.

As observed from Figure 7.10 as the thickness of the adsorption layer decreases with increasing degree of hydration the surface tension increases. As discussed in Chapter 5, the surface tension is considered to be the force that acts inside the microstructure and assumed to be responsible for the deformation of the hardening paste. The variation of surface tension with the thickness of the adsorption layer is shown in Figure 7.11.

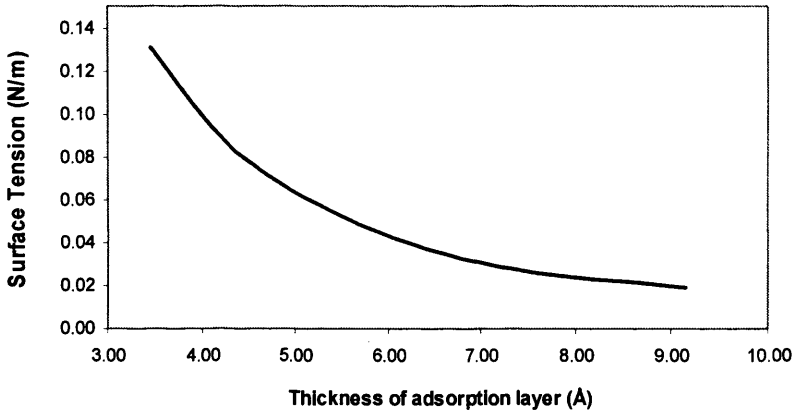

Figure 7.11: Variation of surface tension with thickness of the adsorption layer.

From Figure 7.11 is seen that the surface tension in the adsorption layer increases from 0.02 N/m to 0.13 N/m while the thickness of the adsorption layer drops from 9Å

to 3.5 Å. That was expected to occur and the results obtained are very comparable to results mentioned in literature for similar pastes (Section 5.11.2 – Figure 5.8).

In the light of what has been discussed up to now, Figure 7.12 illustrates a typical comparison between the average experimental data and those predicted by the proposed model. In Figure 7.12 and elsewhere Model-NF and Model-F are used to designate the model predictions for mixes without and with fibres, respectively.

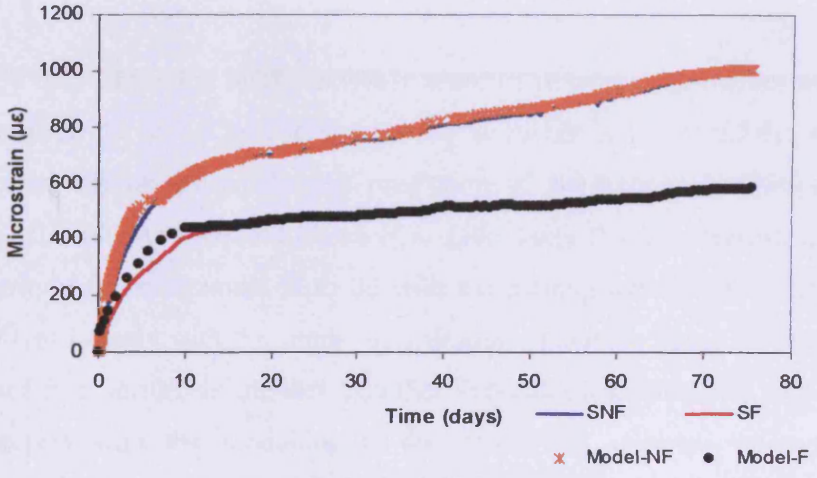

Figure 7.12: Experimental and model results for mixes with and without fibres.

As it can be observed for both mixes with and without fibres the model predictions are in good agreement with the experimental results. As observed from Figure 7.12 the model slightly overestimates the measured values for mixes without fibres whereas it gives a very good fitting with the measured values from mixes with fibres. The predicted values are roughly 3% larger than the measured values for mixes without fibres whereas this difference between predicted and measured values drops approximately below 2% for mixes with fibres. Table 7.6 presents the results for both model and experiments at various time intervals.

Table 7.6: Experimental and model results at various times (F: mixes with fibres; NF: mixes without fibres).

		Experimental Values (με)	Model Values (με)
At 10 days	**F**	405	439
	NF	589	619
At 35 days	**F**	497	494
	NF	749	783
At 75 days	**F**	577	585
	NF	1000	1004

This slight overestimation by the model in terms of shrinkage prediction indicates that the model is on the safe side. Therefore, as far as design is concerned the model offers a very good approximation for the prediction of autogenous shrinkage strains in CARDIFRC® with and without fibres. It is quite likely that the overestimation in the initial period of measurement is to do with the assumption that the stiffness of the paste evolves linearly with the degree of hydration. It is more likely that this evolution takes place in a non-linear manner. Another important issue that has to be addressed in connection with the modelling is the dense and complex microstructure of CARDIFRC®. As it has been pointed out in Chapter 4, the modelling of cement-based materials and especially of those with very low water to cement ratio is a very difficult task. The ultra fine dimensions of the materials used as well as a number of reactions taking place make such modelling extremely complex. The actual state of the microstructure during hardening is very difficult to be modelled, and what the majority of the models, as well as the proposed model, offer is a very good approximation of the hardening process in the matrix making of course a number of assumptions, which have been discussed thoroughly in Chapter 5 – Section 5.11.3.

It is useful to point out once again the long extent of the hardening period , in excess of 75 days. The simulations revealed that the maximum degree of hydration that can be achieved in this particular material is about 0.5. That was to be expected. The water content of the mix is very low whereas the content of the reacting materials (cement and microsilica) as well as the chemically inert materials (extra fine sand and

fibres) is very high. Therefore, the water present in the mix is insufficient for complete hydration to take place. Moreover, as we discussed earlier, the shrinkage test specimens had not undergone hot curing and as a result the hydration process proved to be a long-lasting phenomenon. Despite the simplifications made in the proposed model, the predictions are reasonably close to the measured autogenous shrinkage strains (Table 7.7).

Table 7.7 summarises the results from the experiments and the model predictions for both mixes with and without fibres. Note that the experimental values shown in the table are the mean values (and standard deviations) of the twelve beams tested in each case. The individual beam results are compared in Appendix D.

Table 7.7: Summary of experimental and modelling results at various time intervals, values are in με, (F: mixes with fibres; NF: mixes without fibres).

	Time Intervals (days)						
	10	**20**	**30**	**40**	**50**	**60**	**75**
NF							
Experimental	589.16	678.22	754.25	775.53	842.41	903.01	1000.24
COV	1.87	2.11	2.32	1.63	1.58	1.62	1.45
Model	619.23	710.91	763.23	821.91	865.66	931.61	1004.50
F							
Experimental	404.78	496.89	479.53	515.69	518.57	540.73	577.00
COV	3.98	2.87	2.61	2.20	2.21	1.97	1.66
Model	439.24	466.73	481.53	515.23	518.37	542.89	585.45

7.4 Comparison of CARDIFRC® with similar HPFRCCs

In this section we will make a comparison between the results obtained in the current experimental study on CARDIFRC® and the results available in the literature for other high performance fibre reinforced cementitious composites regarding the development of autogenous shrinkage strains in them.

7.4.1 CARDIFRC® and *Ductal®*

As described in Chapter 2 – Section 2.3.4, Reactive Powder Concrete (RPC) was one of the first HPFRCCs with extremely dense microstructure and enhanced mechanical

properties developed over the last two decades. The dramatic reduction in total porosity and primarily in pore sizes has resulted in considerable improvements in mechanical properties and durability. Nowadays, an improved version of RPC is marketed under the trade name *Ductal*®. Table 7.8 compares the compressive strength and elastic modulus values for CARDIFRC® and *Ductal*®.

Table 7.8: Compressive strength and Young Modulus values for CARDIFRC® and *Ductal*®.

	CARDIFRC®	***Ductal*®**
Compressive Strength (MPa)	194 – 207	190 – 240
Young Modulus (GPa)	48 – 50	45 - 56

Cheyrezy and Behloul (2001) performed autogenous shrinkage tests on various *Ductal*® mixes with and without fibres having water to cement ratios between 0.26 and 0.19. Table 7.9 shows the detailed composition of two different *Ductal*® mixes to be discussed below. Furthermore, the CARDIFRC® Mix I composition is reproduced from Chapter 2 for comparison purposes.

Table 7.9: Composition (kg/m^3) of two different *Ductal*® mixes and CARDIFRC® Mix I (Note that in Mix I two different types of sand are used as shown in Chapter 2 - Table 2.1).

	***Ductal*®**		**CARDIFRC®**	
	1	**2**	**Mix I**	
Cement	687	693	855	
Microsilica	223	225	214	
Ground Quartz	206	208	-	
Sand	983	991	940	
Superplasticiser	14.5	14.4	34	
Steel Fibres	152	151	6 mm 390	13 mm 78
Water	179	159	188	
w/c	0.26	0.23	0.22	
w/b	0.20	0.17	0.18	
sp/w	0.08	0.09	0.18	

A quick look at the above table shows that the amount of cement as well as the amount of superplasticiser used are larger in CARDIFRC® than in *Ductal*®. The total mass of fibres used in CARDIFRC is three times larger than that used in the *Ductal*® mixes.

Figure 7.13 shows the autogenous and drying shrinkage test results on the *Ductal*® mixes presented in Table 7.8.

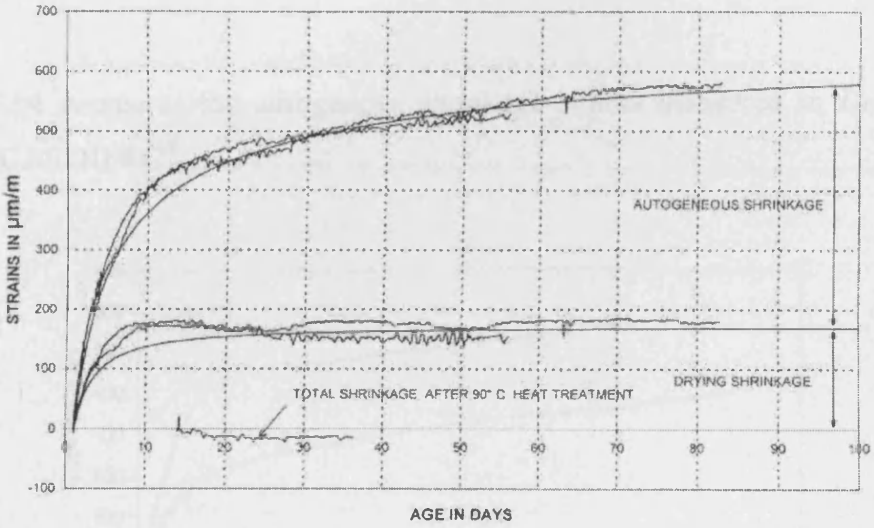

Figure 7.13: Autogenous and drying shrinkage for *Ductal*® mixes 1 and 2 (Cheyrezy and Behloul, 2001).

As shown in Figure 7.13, mixes 1 and 2 exhibit very similar behaviour, and the measured autogenous shrinkage strains are practically identical for both mixes. The development of autogenous shrinkage strains is quite intense in the first ten days but starts to stabilize thereafter. That was also the case for CARDIFRC® Mix I as have seen earlier (Figure 6.15). Note that the total shrinkage of hot-cured Ductal specimens was found to be negative. In other words, hot-cured *Ductal*® specimens proved to exhibit swelling and not shrinkage. Table 7.10 summarizes the results for *Ductal*® and CARDIFRC® at various time intervals.

Table 7.10: Summary of results for autogenous shrinkage strains (με) at the end of various time intervals for *Ductal*® and CARDIFRC®.

	Time Intervals (days)						
	10	**30**	**50**	**60**	**75**	**80**	**90**
***Ductal*®**	200	280	330	350	370	380	400
CARDIFRC®	405	479	518	540	577	-	-

Figure 7.14 compares the autogenous shrinkage strains measured in *Ductal*® with those of CARDIFRC®.

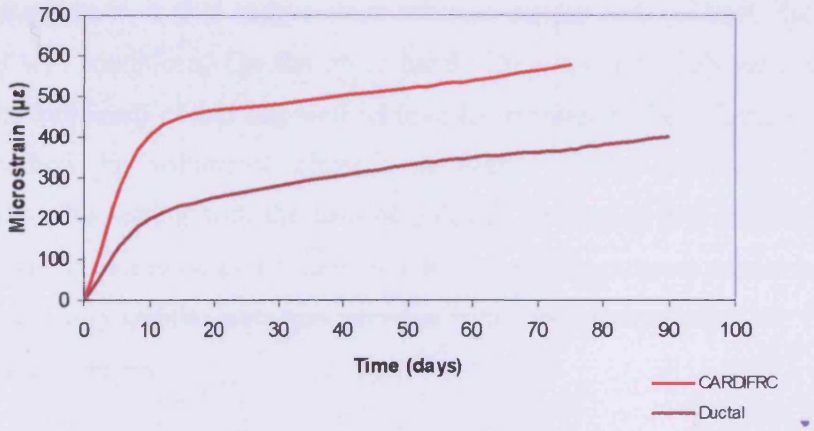

Figure 7.14: Comparison between the autogenous shrinkage strain values for *Ductal*® and CARDIFRC®.

As can be observed from both Table 7.10 and Figure 7.14, CARDIFRC® exhibits considerably larger autogenous shrinkage. The values obtained in the current study, up to 75 hours, are found to be almost 1.5 times larger than the corresponding values measured by Cheyrezy and Behloul (2001). The trend however seems to be the same in both cases, since as discussed earlier the first ten days proved to be very crucial regarding the development of autogenous shrinkage strains, whereas this rate of strain gain is found to decrease significantly afterwards.

This large difference may be attributed to the fact that in Ductal® mixes a substantial amount of ground quartz has been used. Quartz inclusions are points of stress

concentration and therefore the interfacial zone between quartz and paste is a zone of high stress concentration and consequently microcracks can be induced. These microcracks can lead to the reduction of the shrinkage since they act to restrict any volume changes. However, the authors have given no indication of whether or no any microcracking was observed in the specimens. It is interesting to note that the difference between the strains in Ductal® and CARDIFRC® reduces substantially if the drying shrinkage strains are added to the reported autogenous shrinkage strains in Ductal® (see Figure 7.13). The large difference in Figure 7.14 between the autogenous shrinkage strains in Ductal® and CARDIFRC® also seems to subject that a certain proportion of the strains measured in CARDIFRC® are of the drying shrinkage type, as mentioned earlier in Section 6.6. Another reason for the observed differences may be the different testing methods used. In the case of CARDIFRC® ,as described in Chapter 6, the wrapping of specimens immediately after demoulding and direct connection to a data logger were selected as the best solution for attaining isothermal test conditions. On the other hand, Cheyrezy and Behloul (2001) have selected the immersed rubber bag method in order to measure the volumetric changes. In this method the volumetric changes on pastes can be measured during and immediately after setting with the help of a device consisting of a small rubber bag whose volume is measured by immersion in a constant temperature container of water. However, it is very questionable how accurate is this transformation of the volumetric strains to linear strains.

It has to be mentioned that regarding the mixes without any fibres, Cheyrezy and Behloul (2001) found that the inclusion of fibres in the mix can lead to small reduction in the development of autogenous shrinkage strains. This reduction was found to be only 10% to 20%. In case of CARDIFRC® mixes this reduction was found to be significantly large, in the range of 40% to 50% (Figure 6.15).

7.4.2 Comparison with other models

As has been outlined in the previous Chapters, the modelling of the continuously hardening microstructure of cement-based materials is a very difficult and complex procedure, necessitating a relatively large number of assumptions. Some of the

existing microstructural models have been discussed in Chapter 3. Models such as the Powers model, Jennings-Johnson model and the HYMOSTRUC model are pure microstructural models, which predict and simulate the formed microstructure in incessant hardening cement-based materials. However, such models do not predict the development of shrinkage at all. On the other hand, models such as the NIST model, the modified HYMOSTRUC and the empirical model proposed by Tazawa and Miyazawa predict shrinkage strains. It has to be mentioned that NIST model predicts chemical shrinkage, whereas the other two predict autogenous shrinkage.

In Chapter 3 one of models discussed was due to Powers (Section 3.3.1.7). Powers proposed some equations for the evaluation of the various pore volumes in the microstructure. These formulae are listed in Table 3.1. It would be interesting to compare the results for the capillary pore volume, the unhydrated cement pore volume and the total pore volume obtained by using Powers equations with the corresponding values calculated by the proposed model. Table 7.11 presents the formulae used in order to estimate the pore volumes.

Table 7.11: Summary of the formulae used by Powers and current model to estimate the various pore volumes in the microstructure.

	Powers Model	**Proposed Model**	
Capillary pores	$\frac{(w_0/c)-0.36\alpha}{(w_0/c)+0.32}$	$V_{cap}(\alpha)=(\frac{w}{c}-0.4\alpha)\frac{\rho_{ce}}{\rho_w+\rho_{ce}\omega_0}V$	eq. (5.39)
Unhydrated cement	$\frac{0.32(1-\alpha)}{(w_0/c)+0.32}$	$V=\frac{1-0.83\,\alpha\,(w/c)(\rho_c/\rho_w)}{1+(w/c)(\rho_c/\rho_w)}$	eq. (5.28)
Total pores	$\frac{(w_0/c)-0.17\alpha}{(w_0/c)+0.32}$	$V_{por}(\alpha)=(\frac{w}{c}-0.3375\alpha)\frac{\rho_{ce}}{\rho_w+\rho_{ce}\omega_0}V$	eq. (5.41)

By using the Powers equations for different degrees of hydration and for water to cement ratio of 0.22, we will compare the results obtained from these formulae to the results obtained using the proposed model. Table 7.12 summarises the results.

Table 7.12: Summary of results for different pore volumes at different degree of hydration intervals for both Powers model and current model.

α	Capillary pore volume		Unhydrated cement volume		Total pore volume	
	Powers	**Current**	**Powers**	**Current**	**Powers**	**Current**
0.1	0.34	0.34	0.53	0.55	0.38	0.35
0.2	0.27	0.26	0.47	0.52	0.34	0.29
0.3	0.21	0.19	0.41	0.49	0.31	0.22
0.4	0.14	0.11	0.36	0.45	0.28	0.16
0.5	0.07	0.05	0.30	0.42	0.25	0.11

As can be seen from Table 7.12, although the results obtained by using the Powers formulae seem to be fairly close to those obtained from the current model, they actually diverge as the degree of hydration increases. Since we are dealing with very small quantities even a very small difference could be very significant regarding the pore status of the microstructure. This divergence between the Powers model and proposed model can be attributed to the fact that the Powers model cannot account for very small water to cement ratios. Eventually, as the hydration proceeds less and less water is available in the microstructure of CARDIFRC®. In fact, for very small degrees of hydration where enough water for hydration is available, the values given by Powers model are in fairly good agreement with the values obtained from the current model. However, as an increase in the degree of hydration implies less and less water being available for hydration, the Powers model is unable to cope. Figure 7.15 illustrates the difference in the values obtained using Powers formulae and the proposed model.

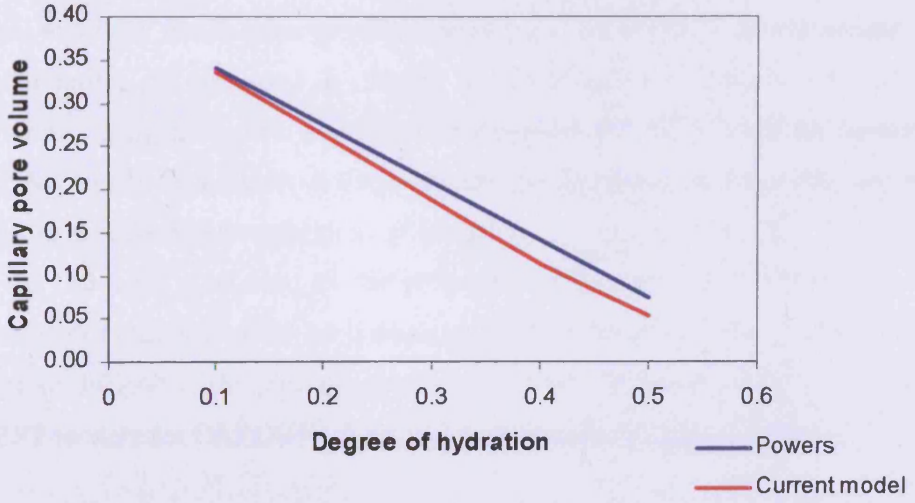

(a)

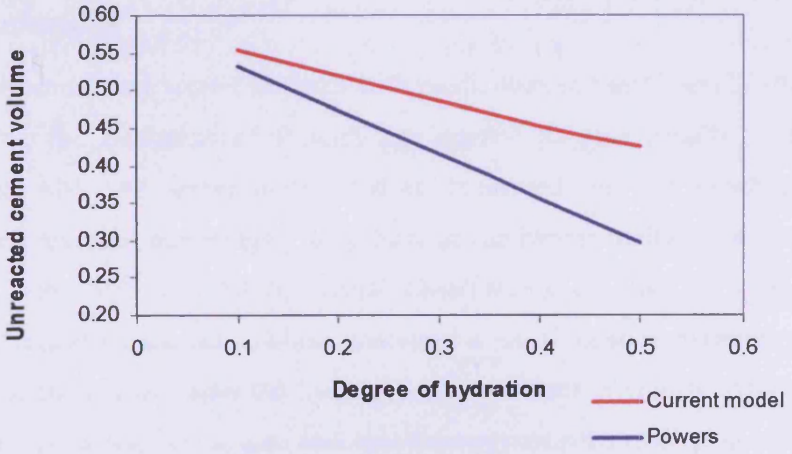

(b)

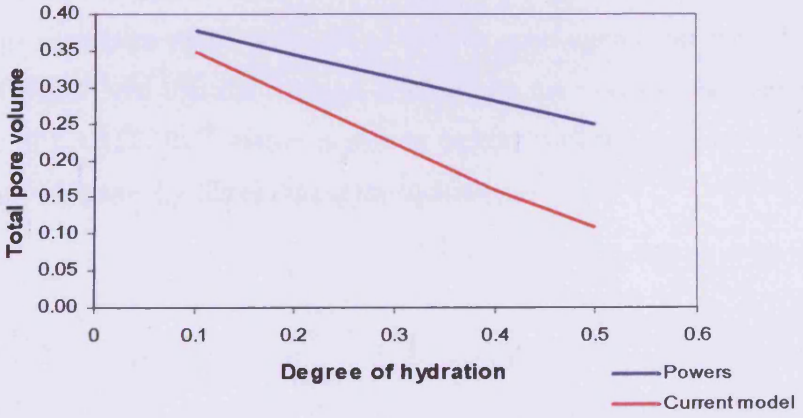

(c)

Figure 7.15: Variation of pore volumes with degree of hydration using Powers formulae and current model. (a) capillary pore volume; (b) unhydrated cement pore volume; (c) total pore volume.

Regarding the NIST model (Bentz, 1991) it has been found that the model cannot simulate relatively dense microstructures with very low water to cement and/or water to binder ratios. As discussed in Chapter 3 – Section 3.3.2.1, the NIST model is a pixel model using a specific algorithm to represent the microstructure particles as pixels. By trying to simulate a very densely packed microstructure the algorithm, during the process of representation of particles as pixels, fails to complete the task, since the 100-pixel cube used by the program to represent the microstructure is not large enough to accommodate such dense packing of particles. The problem becomes even more difficult if the particle dispersion is also taken into account. Attempts to use NIST models for CARDIFRC® proved unsuccessful for these reasons.

7.5 Conclusions

The experimental data were compared with predictions in this Chapter. The model for determining the evolution of E with age proved to give results in fairly good agreement with the experimental values measured in the laboratory. Model simulations revealed that roughly only 50% of the binder hydrates in CARDIFRC®. This has been also verified by visual observations of cracked specimens from compressive and tensile tests, which contained a lot of loose unhydrated material. In case of hot-cured specimens the hydration of the binder is significantly accelerated, whereas in specimens left to cure at ambient temperature the hydration of the binder is found to be a very long-lasting phenomenon. Model results showed that in order for about 50% of the binder to hydrate, roughly 75 days are needed. The predicted autogenous shrinkage strains were found to be in good agreement with the measured strains. It was shown that the restraint provided by the fibres to the free autogenous shrinkage of CARDIFRC® matrix is able to capture well the increase in the stiffness of the matrix induced by fibres during the hydration.

Chapter 8: Conclusions and Recommendations

8.1 Conclusions

From the model for autogenous shrinkage, the experimental work and the simulations described in Chapters 5, 6 and 7, respectively, the following major conclusions can be drawn.

- The surface tension in the adsorption layer is the internal driving force that acts inside the microstructure and leads to autogenous shrinkage.

- The thermodynamic approach to the modelling of autogenous shrinkage based on the concept of thermodynamic equilibrium being reached at each and every stage of hydration gives reasonably accurate predictions of the development of autogenous shrinkage strains in CARDIFRC®. However for this accurate prediction, it is equally important to model accurately the evolution of the stiffness of the CARDIFRC mixes with and without fibres.

- The effect of silica fume was not included in the model because the test specimens of CARDIFRC® had not undergone any hot curing which is the normal curing regime for this material. The reason for not using hot curing was the desire not to miss the first 7 days of hardening which, by all accounts, is the dominant period for the development of autogenous shrinkage strains. The results of this study are therefore more likely to represent the performance of CARDIFRC® which has been cured for 28 days at ambient temperature. They are likely to overestimate the autogenous shrinkage strains that would develop in CARDIFRC® cured at 90°C for 7 days.

- The elastic modulus of cement paste, mortar and CARDIFRC® was modelled by regarding each as a two-phase material whose stiffness evolves with time as the paste hardens. The stiffness of the binder was assumed to evolve linearly during hardening, with the constant of proportionality calibrated in such a way that the predicted value of the Young modulus of CARDIFRC® matched exactly its measured value at the age of testing.

- The experimental results revealed that in large members made with CARDIFRC® the even distribution of fibres is very difficult to achieve. This was confirmed both by image analysis of cut sections from large CARDIFRC® members and from the autogenous shrinkage tests. The recorded strain values for these members had a very large scatter, thus preventing any firm conclusion to be drawn concerning the size effect in the autogenous shrinkage of CARDIFRC® with fibres. The uneven distribution of fibres was a result of the very high frequency used during compaction of the specimens. The frequency of compaction was reduced during the preparation of the remaining specimens used in this study.

- As expected, the first seven to ten days form the dominating period for the development of the autogenous shrinkage strains in CARDIFRC®. In both mixes with and without fibres during this period 60% to 70% of the final autogenous shrinkage strain had already been recorded.

- The autogenous shrinkage proved to be a long lasting phenomenon in CARDIFRC®. Shrinkage strains in both mixes with and without fibres were found to continue to develop even after 75 days from casting, albeit at a much slower rate than in the initial 7 –10 day period.

- This continued development of autogenous shrinkage in CARDIFRC® can be attributed to many reasons. Among these are the cement fineness (in coarser cements the hydration takes longer) and the lack of hot curing of the specimens, as a result of which chemical reactions are delayed in such a material containing a large proportion of silica fume.

- Despite the steps taken to ensure that the specimens were properly sealed, it is likely that there was some exchange of moisture between the specimens and the surroundings resulting in some drying shrinkage.

- The lack of hot curing not only results in slowed chemical reactions in the hardening microstructure but also causes a substantial reduction in the rate of gain

of the stiffness. As a result, the restraint provided by the fine aggregate and fibres to the free autogenous shrinkage of the paste is also reduced, so that CARDIFRC® mixes with and without fibres both exhibit very high autogenous shrinkage strains.

- That is not to say that the inclusion of fibres in the mix does not reduce the autogenous shrinkage strains very considerably. Tests showed that the fibres reduce the strains in the CARDIFRC® mortar by at least 40%. The restraint provided by the fibres to the free autogenous shrinkage of CARDIFRC® matrix is shown to be well captured by the increase in the stiffness of the mortar induced by fibres during hydration.

- Model simulations revealed that only about 50% of the binder hydrates in CARDIFRC®. This has been also verified by visual observations of cracked specimens from compressive and tensile tests, which contained a lot of loose unhydrated material.

- There is no size effect in the autogenous shrinkage of CARDIFRC® mortar. This means that autogenous shrinkage is a purely bulk phenomenon in this material. The absence of size effect confirms that no surface phenomena are involved, such as microcracking. In fact, despite the large autogenous shrinkage strains recorded in CARDIFRC® mortar there was no evidence of microcracking in any of the test specimens even after 75 days. It is quite likely that the much smaller strains recorded on another HPFRCC, namely Ductal, are a result of the release of strains through microcracking.

- The thermodynamic model showed that Powers formulae for the evolution of porosity and pore sizes are only applicable during the very early stages of hydration of CARDIFRC® when there is enough water available. As the hydration proceeds and less and less water is left the predictions of Powers model become less reliable. This only confirms that Powers model is applicable when there is enough water available for the complete hydration of cement, which requires a water to cement ratio of 0.375.

8.2 Recommendations for future work

For further development in the understanding of the processes in the hardening matrix of cement-based materials as well as for the further development of a more accurate model the following needs to be done in the future.

- Investigate the effect of cement fineness on the autogenous shrinkage of CARDIFRC®.

- Investigate the effect of different fibre and sand contents on the autogenous shrinkage of CARDIFRC®. This can be simply done by examining CARDIFRC® Mix II since in the current work only Mix I was considered.

- Examine large size specimens in order to investigate any size effect on autogenous shrinkage of mixes with fibres.

- Analyse more closely the possibility of any microcracking in the Interfacial Transition Zone as well as in the microstructure in general. Existence of micro-cracks will lead to reduction in autogenous shrinkage.

- Examine the possible effect of the cement particle sizes on the pore size distribution in the microstructure.

- Investigate more fully the effect of the hydration of all the mineral compounds on the predictions of the thermodynamic model.

- Develop a model that will take into consideration the pozzolanic reaction of silica fume, as well as being able to deal with the very dense microstructures and the very small water to cement ratios. In other words, improve NIST-type model.

- Examine the effect of hot curing on the autogenous shrinkage strains of CARDIFRC®.

List of References

ACI Committee 544, "State-of-the-art Report on fiber reinforced concrete", Report ACI 1R-82, Concrete International: Design and Construction, May 1982.

Aitcin P.C. "Autogenous Shrinkage Measurement", *Proc. of the International Workshop organised by JCI*, Edited by Ei-ichi Tazawa, E & FN Spon 1999, pp. 257-268.

Aitcin P.C. "Cements of Yesterday and Today – Concrete of Tomorrow", *Cement & Concrete Research*, No. 30, 2000, pp. 325-344.

Aitcin P.C., Neville A.M. and Acker P., "Integrated view of shrinkage deformation", *Concrete International*, No. 19, 1997, pp. 35-45.

Alaee F. "Retrofitting of concrete structures using high performance fibre reinforced cementitious composite (HPFRCC)", *PhD Thesis*, Cardiff University, 2002.

Bache H.H. "Compact reinforced composite. Basic principles", *CBL Report No. 41, Aalborg Portland*, Cement-og Betonlaboratoriet, 1987.

Bache H.H. "Densified cement ultra-fine particle-based materials", *CBL Report No.40*, pp. 35, Aalborg Portland, Denmark, 1981.

Balaguru P.N. and Kendzulak J. "Flexural behaviour of slurry infiltrated fibre concrete (SIFCON) made by using condensed silica fume", *In Fly Ash, Silica Fume, Slag and natural Pozzolans in Concrete, SP-91, ACI*, Detroit, 1986, pp. 1215-1229.

Balaguru P.N. and Shah S.P. "Fibre-reinforced cement composites", McGraw-Hill, New York, 1992.

Basile T.T. and Beaudoin J.J., "Basic Creep of Hardened Cement Paste – A Re-Examination of the Role of Water", *Cement & Concrete Research*, No. 30, 2000, pp. 1465-1475.

Bazant Z.P. and Wittmann F.H., "Creep and shrinkage in concrete structures", John Wiley & Sons, First Edition, 1982.

Bazant Z.P., "Mathematical modelling of creep and shrinkage of concrete", John Wiley & Sons, 1988.

Benson S. "CARDIFRC® - Development and Constitutive Behaviour", *PhD Thesis*, Cardiff University, Cardiff School of Engineering, 2003.

Benson S.D.P. "Retrofitting damaged reinforced concrete flexural members with HPFRCC", *MEng Thesis*, Cardiff University, 1999.

Bentz D.P. "CEMHYD3D: A three-dimensional cement hydration and microstructure development modelling package – Version 2.0", *National Institute of Standards and Technology Internal Report No 6485*, Building and Fire Research Laboratory – NIST, 2000.

Bentz D.P. and Garboczi E.J. "Percolation of phases in a three dimensional cement paste microstructural model", *Cement & Concrete Research*, No. 21, 1991, pp. 325-344.

Bisshop J., "Drying shrinkage microcracking in cement based materials", *PhD Thesis*, Delft University Press, 2002.

Breugel K. van "Numerical modelling of volume changes at early ages – potential, pitfalls and challenges" *Shrinkage of Concrete, Proc. Of Int. RILEM Workshop*, edited by Baroghel-Bouny V. and Aitcin P.C., PRO17, RILEM Publications S.A.R.L., 2000, pp.271-286.

Breugel K. van "Simulation of hydration and formation of structure in hardening cement based materials", *PhD Thesis*, Delft University Press, 1991.

Breugel K. van, "Numerical simulation of hydration and microstructural development in hardening cement based materials. Theory (I) and Applications (II)", *Cement and Concrete Research*, (I) Vol. 25, No. 2, pp. 319-331, (II) Vol. 25, No. 3, 1995, pp. 522-530.

Brooks J.J., Cabrera J.G. and Megat Johari M.A., "Factors Affecting the Autogenous Shrinkage of Silica Fume High Strength Concrete", *Proc. of the International Workshop organised by JCI*, Edited by Ei-ichi Tazawa, E & FN Spon 1999, pp. 195-202.

Brown P.W., Pommersheim J. and Frohnsdorff G. "A kinetic model for the hydration of tricalcium silicate", *Cement and Concrete Research*, Vol. 15, 1985, pp. 35-41.

BS 5400: "Steel, concrete and composite bridges: Part 4: code of practice for design of concrete bridges", *British Standards Institution*, London, 1990.

BS:1881: part 116: 1983. "Testing Concrete: Method for determination of compressive strength of concrete cubes", *British Standards Institution*, 1983.

BS:1881: part 117: 1983. "Testing Concrete: Method for determination of tensile splitting test", *British Standards Institution*, 1983.

BS:1881: part 121: 1983. "Testing Concrete: Method for determination of static modulus of elasticity in compression", *British Standards Institution*, 1983.

CEB – FIP, Model Code '90 - Model Code for concrete structures, Paris, 1990.

Chern J.C. and Young C.H., "Study of Factors Influencing Drying Shrinkage of Steel Fiber Reinforced Concrete", *ACI Materials Journal*, No. 87, 1990, pp. 123-129.

Cheyrezy M. and Behloul M., "Creep and Shrinkage of Ultra-High Performance Concrete, Proc. of the 6th Int. Conf. on Creep", *Shrinkage and Durability Mechanics of Concrete and other Quasi-Brittle Materials*, edited by Ulm F.J., Bazant Z.P. and Wittmann F.H., Elsevier, 2001, pp. 527-538.

Day R.L. and Marsh B.K., "Measurement of Porosity in blended cement pastes", *Cement and Concrete Research*, Vol. 18, 1988, pp. 63-73.

Dugat J, Roux N. and Bernier G. "Mechanical properties of reactive powder concretes (RPC)", *Materials and Structures*, Vol. 29, 1996, pp. 133-240.

Garboczi E.J. and Bentz D.P. "Computer based models of the microstructure and properties of cement based materials", *In 9th International Congress on the Chemistry of Cement*, New Delhi, India, Vol. I, 1992, pp. 3-15.

Gardner N. J. and Zhao J. W. "Creep and Shrinkage revisited", *ACI Materials Journal*, Vol. 90, Issue3, 1993.

Gopalaratnam V.S and Shah S.P. "Properties of steel fibre reinforced concrete subjected to impact loading", *Journal of The American Concrete Institute*, Vol. 83, No. 1, 1986, pp. 117-126.

Hedlund H. and Westman G., "Evaluation and comparison of sealed and non-sealed shrinkage deformation measurements of concrete", *Proc. of the International Workshop on Autogenous Shrinkage of Concrete organised by JCI*, Edited by Ei-ichi Tazawa, E & FN Spon 1999, pp. 123-134.

Horii H., Hasegawa A. and Nishino F. "Process zone model an influencing factors in fracture of concrete", *In Shah S.P. and Swartz S.E. (editors) Fracture of Concrete and Rocks*, New York: Springer Verlag, 1989, pp. 205-219.

Hoy C.W. and Bartos P.J.M. "Interaction and packing of fibers: Effects on the mixing process", *In High Performance Fiber Reinforced Cement Composites (HPFRCC3)*, Reinhardt H.W. and Naaman A.E. (editors), RILEM Publishers, 1999, pp. 181-191.

http://www.concrete.elkem.com/ - Elkem Materials web site

http://datataker.com/ - Powerful Data Logger and Flexible Data Acquisition & Data Logging Systems

http://www.gage-technique.demon.co.uk/ - Gage Technique for Vibrating Wire Strain Gages

Hua C., Acker P. and Ehrlacher A., "Analysis and models of the autogenous shrinkage of hardening cement paste", *Cement and Concrete Research*, Vol. 25, No. 7, 1995, pp. 1457-1468.

Igarashi S., Bentur A. and Kovler K., "Autogenous Shrinkage and Induced Restraining Stresses in High Strength Concretes", *Cement & Concrete Research*, No. 30, 2000, pp. 1701-1707.

Illston J.M., "Construction Materials: Their Nature and Behavior", Second Edition, E & FN Spon, ISBN 0-419-15470-1, 1996.

Japan Concrete Institute (JCI), "Technical Committee on Autogenous Shrinkage of concrete", August 2001, pp. 1-7.

Jennings H.M. "A model for the microstructure of calcium silicate hydrate in cement paste", *Cement and Concrete Research*, No. 30, Vol. 1, 2000, pp. 101-116.

Jennings H.M. Hsieh J., Srinivasan R., Jaiswal S., Garci M., Sohn D., Hinners C., Heppner S. and Neubauer C. "Modelling and materials science of cement based materials – Part I: An Overview", *The Modelling of Microstructure and Its Potential for Studying Transport Properties and Durability*, edited by Jennings H.M., Kluwer Academic Publishers, 1996, pp. 29-61.

Jensen O.M. and Hansen P.F., "Autogenous deformation and change of the relative humidity in silica fume modified cement paste", *ACI Materials Journal*, Vol. 93, No. 6, 1996, pp. 539-543.

Jensen O.M. and Hansen P.F., "Autogenous Shrinkage and RH change in perspective", *Cement and Concrete Research*, Vol. 31, 2001, pp. 1859-1865.

Jensen O.M. and Hansen P.F., "Influence of temperature on autogenous deformation and relative humidity change in hardening cement paste", *Cement and Concrete Research*, Vol. 29, 1999, pp. 567-575.

Johnston C.D. "Properties of Steel Fibre Reinforced Mortar and Concrete", *Proceedings of Symposium on Fibrous Concrete (CI80)*, Edited by The Concrete Society, The Construction Press Ltd, 1980, pp. 29-47.

Juenger M.C.G. and Jennings H.M., "Examining the Relationship Between the Microstructure of Calcium Silicate Hydrate and Drying Shrinkage of Cement Pastes", *Cement & Concrete Research*, No. 32, 2002, pp. 289-296.

Karihaloo B.L. "Fracture Mechanics & Structural Concrete", Longman Scientific & Technical, ISBN 0-582-21582-X, 1995.

Karihaloo B.L. and de Vriese K.M.B. "Short-fibre reinforced reactive powder concrete", *Concrete Communication Conference*, BCA, 1999, pp. 67-77.

Karihaloo B.L. and Lange-Kornbak D. "Optimisation techniques for the design of high performance fibre-reinforced concrete", *Structural and Multidisciplinary Optimisation*, 21, 2001, pp. 32-39.

Karihaloo B.L. and Wang J. "Mechanics of fibre-reinforced cementitious composites", *Computers & Structures*, 76, 2000, pp. 19-34.

Karihaloo B.L., Alaee F.J. and Benson S.D.P. "A new technique for retrofitting damaged concrete structures", *Concrete Communication Conference*, 2001, pp. 293-304.

Karihaloo B.L., Alaee F.J. and Benson S.D.P. "A new technique for retrofitting damaged concrete structures", *Proceeding of the Institution of Civil Engineers, Building & Structures*, 152(4), 2002, pp. 309-318.

Karihaloo B.L., Benson S.D.P, Didiuk P.M., Fraser S.A., Hamill N. and Jenkins T.A. "Retrofitting damaged RC beams with high-performance fibre-reinforced concrete", *Proc Concrete Communication Conf*, British Cement Association, 2000, pp. 153-164.

Karihaloo B.L., Wang J. and Grzybowski M. "Doubly periodic arrays of bridged cracks and short fibre-reinforced cementitious composites", *Journal of the mechanics and physics of solids*, 44(10), 1996, pp. 1565-1586.

Kim J.K. and Lee C.S., "Prediction of Differential Drying Shrinkage in Concrete", *Cement & Concrete Research*, No. 28, 1998, pp. 985-994.

Koenders E.A.B. and Breugel Van, K. "Modelling dimensional changes in low water/cement ratio pastes", *Autogenous Shrinkage of Concrete*, edited by Ei-ichi Tazawa, E & FN Spon, London, ISBN:0419238905, 1999, pp. 289-298.

Koenders E.A.B., "Simulation of volume changes in hardening cement based materials", *PhD Thesis*, Delft University Press, 1997.

Koenders E.A.B., *Personal communication*, 2004

Lange-Kornbak D. and Karihaloo B.L. "Tension softening of fibre-reinforced cementitious composites", *Cement and Concrete Composites*, 19, 1997, pp. 315-328.

Lange-Kornbak D. and Karihaloo B.L., "Role of microstructural parameters in the properties of plain concrete", *Concrete Science and Engineering*, Vol. 1, 1999, 238-252.

Lankard D.R. and Newell, J.K. "Preparation of highly reinforced steel fibre reinforced concrete composites", *ACI Special Publication, SP-81, American Concrete Institute*, Detroit, 1984, pp. 286-306.

Lea F.M. "The Chemistry of Cement and Concrete", Edward Arnold Ltd, 3rd edition, ISBN 7131-2277-3, 1970.

Lewis J.A and Kriven W.M. "Microstructure property relationships in Macro-Defect-Free Cement", MRS *Bulletin*, 1993, pp. 72-77.

Li V.C. "A simplified micromechanical model of compressive strength of fibre reinforced cementitious composites", *Cement and Concrete Composites*, 14, 1992b, pp. 131-141.

Li V.C. "From micromechanics to structural engineering- the design of cementitious composites for civil engineering applications", *JSCE Journal of Structural Mechanics and Earthquake Engineering*, 10(2), 1993, pp. 37-48.

Li V.C., Wang Y. and Backer S. "A micromechanical model of tension softening and bridging toughening of short random fibre reinforced brittle matrix composites", *Journal of the Mechanics and physics of Solids*, 39(5), 1991, pp. 607-625.

Lura P., Breugel K. van and Maruyama I., "Effect of Curing Temperature and the Type of Cement on Early-Age Shrinkage of High Performance Concrete", *Cement & Concrete Research*, No. 31, 2001, pp. 1867-1872.

Mobasher B., Stang H. and Shah S.P. "Microcracking in fibre reinforced concrete", *Cement and Concrete Research*, 20, 1990, pp. 665-676.

Morin V., Cohen Tenoudji F., Feylessoufi A. and Richard P. "Superplasticizer effects on setting and structuration mechanisms of ultrahigh-performance concrete", *Cement and concrete Research*, 31, 2001, pp. 63-71.

Moukwa M. and Aitcin P.C., "The effect of drying on cement pastes pore structure as determined by mercury porosimetry", *Cement and Concrete Research*, Vol. 18, 1988, pp. 745-752.

Naaman A.E. "SIFCON: tailored properties for structural performance, in High Performance Fibre Reinforced Cement composites", *Proceedings of the International RILEM/ACI Workshop*, Reinhardt H.W. and Naaman A.E. (editors), Mains, Germany, 1991, pp. 18-38.

Naaman A.E., Reinhardt H.W. and Fritz C. "Reinforced concrete beams using SIFCON as a matrix", *Darmstadter Massivbau Report*, Germany, 1990, 85 pages.

Naaman, A.E. and Shah S.P. "Pull-out mechanism in steel fibre reinforced concrete", *ASCE Journal of the Structural Division*, 102(ST8), 1976, pp. 1537-1548.

Neubauer C.M., Jennings H.M. and Garboczi E.J., "A three-phase model of the elastic and shrinkage properties of mortart", *Advanced Cement Based Materials*, No. 4, 1996, pp. 6-20.

Neville A.M., "Properties of Concrete", 4th Edition", Longman Group Ltd., ISBN 0-582-23070-5, 1995.

Nielsen L.F. "Elasticity and damping of porous materials and impregnated materials", Journal *of the American Ceramic Society*, Vol. 67, No. 2, 1984, pp. 93-98.

Nielsen L.F. "Numerical analysis of composite materials", *Materialenyt 1:2001, Danish Society of Materials Testing and Research*, 2001, pp. 1-24.

Nielsen L.F. "Stiffness of fibre composite", *Report TR-264*, Technical University of Denmark, 1992.

Nikolaides D. "Fracture and Fatigue of CARDIFRC® ", *PhD Thesis*, Cardiff University, Cardiff School of Engineering, 2004.

Nilsen A.U. and Monteiro P.J.M., "Concrete: A three phase material", *Cement and Concrete Research*, Vol. 23, 1993, pp.147-151.

Ortiz M. "Microcrack coalescence and macroscopic crack growth initiation in brittle solids", *International Journal of Solids and Structures*, 24, 1988, pp. 231-250.

Paillere A.M., Buil M. and Serrano J.J., "Effect of Fiber Addition on the Autogenous Shrinkage of Silica Fume Concrete", *ACI Materials Journal*, No. 86, 1989, pp. 139-144.

Person B., "Creep and shrinkage of young or mature HPC", *Proc. 5th Int. Symp. On Utilization of high strength/high performance concrete*, Sandefjord, June 1999. pp. 1272-1281

Phan-Thien N. and Huilgol R.R., "A micromechanic theory of chopped-fibre-reinforced materials", *Fibre Science and Technology*, Vol. 13, 1980, pp. 423-433.

Phan-Thien N. and Karihaloo B.L., "Materials with negative Poisson's ratio: A qualitative microstructural model", *Journal of Applied Mechanics*, Vol. 61, 1994, pp. 1001-1004.

Quenard D. and Sallee H., "Water vapour absorption and transfer in cement based materials: a network simulation", *Materials and Structures*, No. 25, 1992, pp. 515-524.

Ramesh G., Sotelino E.D. and Chen W.F. "Effect of transition zone on elastic moduli of concrete materials", *Cement and Concrete Research*, Vol.46, No. 4, 1996, pp. 611-622

Reinhardt H.W. "Fibres and cement, a useful co-operation: Introductory note, High Performance Fibre Reinforced Cement Composites", *Proceedings of the International RILEM/ACI Workshop*, Reinhardt H.W. and Naaman A.E. (editors), Mains, Germany, 1991.

Richard P. and Cheyrezy M.H. "Composition of reactive powder concretes", *Cement and Concrete Research*, 25(7), 1995, pp.1501-1511.

Richard P. and Cheyrezy M.H. "Reactive powder concretes with high ductility and 200-800MPa compressive strength", *ACI Spring Convention*, San Francisco, USA, 1994.

RILEM Committee TC 107, Subcommittee 1 "Creep and shrinkage prediction model for analysis of concrete structures: Model B3", *Materials & Structures*, 28, 1995.

Russel W.B. and Acrivos A., "On the effective moduli of composite materials: Slender rigid inclusions at dilute concentrations", *Journal of Applied Mathematics and Physics*, Vol. 23, 1972, pp. 434-464.

Sadouki H. and Wittmann F.H., "Shrinkage and internal damage induced by drying and endogenous shrinkage", *Shrinkage of Concrete, Proc. Of Int. RILEM Workshop*, edited by Baroghel-Bouny V. and Aitcin P.C., PRO17, RILEM Publications S.A.R.L., 2000, pp.299-314.

Sakata K. and Shimomura T. "Recent Progress in Research on and Code Evaluation of Concrete Creep and Shrinkage in Japan", *Journal of Advanced Concrete Technology*, Vol. 2, No. 2, 2004, pp. 133-140.

Setter N. and Roy D.M., "Mechanical features of chemical shrinkage of cement paste", *Cement & Concrete Research*, Vol. 8, No. 5, 1978, pp. 623-634.

Shah S.P, Peled A., Aldea C.M. and Akkaya Y. "Scope of high performance fibre reinforced cement composites", *In Third International Workshop on high Performance Fibre Reinforced Cement composites (HPFRCC3)*, Reinhardt H.W. and Naaman A.E. (editors), Mains, Germany, 1999, pp. 113-129.

Shah S.P. and Young J.F. "Current research at the NSF Science and Technology Centre for Advanced Cement-Based Materials", *American Ceramic Society Bulletin*, 1990, pp. 1319-1331.

Shannag M.J. and Hansen W. "Tensile properties of fibre-reinforced very high strength DSP mortar", *Magazine of Concrete Research*, 52(2), 2000, pp. 101-108.

Stang H., "Significance of Shrinkage Induced Clamping Pressure in Fiber Matrix Bonding in Cementitious Composite Materials", *Advanced Cement Based Materials*, No. 4, 1996, pp. 106-115.

Stroud K.A. and Booth D.J. "Engineering Mathematics", Palgrave Macmillan, Fifth Edition, London, ISBN 0-33-91939-4, 2001.

Sullivan A.P. "The effect of hydrothermal curing at 90°C and the use of 12 mm steel fibres on reactive powder concrete", *MSc Thesis*, Cardiff University, 1999.

Tasdemir M.A. and Karihaloo B.L., "Effect of aggregate volume fraction on the fracture parameters of concrete: a mesomechanical approach", *Magazine of Concrete Research*, Vol. 53, No. 6, 2001, pp. 405-415.

Tazawa E. "Autogenous shrinkage of concrete", *Proceedings of the International Workshop organised by JCI*, edited by Tazawa E., E & FN Spon, ISBN 0-419-23890-5, 1999.

Tazawa E. and Miyazawa S. and Kasai T., "Chemical shrinkage and autogenous shrinkage of hydrating cement paste", *Cement & Concrete Research*, Vol. 25, No. 2, 1995, pp. 288-292.

Tazawa E. and Miyazawa S., "Experimental Study on Mechanism of Autogenous Shrinkage of Concrete", *Cement & Concrete Research*, Vol. 25, No. 2, 1995, pp. 1633-1638.

Tazawa E. and Miyazawa S., "Influence of Autogenous Shrinkage on Cracking in High Strength Concrete", *4th International Symposium of High Strength/High Performance concrete*, Paris 1996.

Tazawa E., Sato R., Sakai E. and Miyazawa S., "Work of JCI Committee on Autogenous Shrinkage", *Shrinkage of Concrete, Proc. Of Int. RILEM Workshop*, edited by Baroghel-Bouny V. and Aitcin P.C., PRO17, RILEM Publications S.A.R.L., 2000, pp. 21-40.

Tezuka Y "Hydration Characteristics and Properties of Mixtures of Cement and High Content of Calcium", *Proc. 8th Int. Congress on Chemistry of Cement*, Rio de Janeiro, Vol. II (1986), pp.323-329.

Tjiptobroto P. and Hansen W. "Tensile strain hardening and multiple cracking in high-performance cement-based composites containing discontinuous fibres", *ACI Materials Journal*, 90(1), 1993, pp. 16-25.

Wang J. and Karihaloo B.L. "Material instability in the tensile response of short-fibre-reinforced quasi-brittle composites", *Archives of Mechanics*, 52, 2000, pp. 839-855.

Wang K., Shah S.P. and Phuaksuk P., "Plastic Shrinkage Cracking in Concrete Materials – Influence of Fly Ash and Fibers", *ACI Materials Journal*, No. 98, 2001, pp. 458-464.

Winslow D.L., "The pore structure of paste in concrete", *Cement and Concrete Research*, Vol. 20, 1990, pp. 227-235.

Wittman F.H., "Creep and Shrinkage Mechanisms, in: Creep and Shrinkage in Concrete Structures", Edited by Bazant and Wittmann, John Wiley & Son Ltd., 1982, pp. 129-161.

Wittmann F.H., "Mechanisms and mechanics of shrinkage, Symposium Keynote Lecture", Proc. of the 6th Int. Conf. on Creep", *Shrinkage and Durability Mechanics of Concrete and other Quasi-Brittle Materials*, edited by Ulm F.J., Bazant Z.P. and Wittmann F.H., Elsevier, 2001, pp. 3-12.

Wittmann F.H., "Mechanisms and mechanics of shrinkage, Symposium Keynote Lecture", Proc. of the 6th Int. Conf. on Creep", *Shrinkage and Durability Mechanics of Concrete and other Quasi-Brittle Materials*, edited by Ulm F.J., Bazant Z.P. and Wittmann F.H., Elsevier, 2001, pp. 3-12.

Zanni H., Cheyrezy M., Maret V., Philipot S. and Nieto P. "Investigation of hydration and pozzolanic reaction in reactive powder concrete (RPC) using ^{29}Si NMR", *Cement and Concrete Research*, 26(1), 1996, pp. 93-100.

Zhang M.H., Tam C.T. and Leow M.P., "Effect of water to cementitious materials ratio and silica fume on the autogenous shrinkage of concrete", *Cement & Concrete Research*, Vol. 33, 2003, pp. 1687-1694.

Zhou F.P., Lydon F.D. and Barr B.I.G. "Effect of coarse aggregate on elastic modulus and compressive strength of high performance concrete", Cement and Concrete Research, Vol. 25, No. 1, 1995, pp. 177-186.

Zijl van G.P.A.G., de Brost R. and Rots J.G., "FE analysis of the interaction between moisture migration, creep, shrinkage and cracking", *Computational Modelling of Concrete Structures*, editors de Brost, Bicanic, Mang & Meschke, Balkema, Rotterdam, 1998, pp 505-511.

Appendix A – Product Information Sheets

Blue Circle Portland Cements (CEM I 42,5 52,5)

Properties

a) Grey colour.

b) Consistent strength meeting all the conformity criteria in BS EN 197-1.

c) Compatible with admixtures such as air-entraining agents and workability aids, with cement replacement materials such as fly ash and ground granulated blastfurnace slag and with pigments. Trial mixes are recommended to determine the optimum mix proportions.

Typical properties		
Surface area	(m^2/kg)	290 to 420
Setting time - initial	(minutes)	80 to 200
BS EN 196-1 Mortar- compressive strength 2 day 7 day 28 day	 (N/mm^2) (N/mm^2) (N/mm^2)	 25 to 35 40 to 50 54 to 64
Apparant particle density	(kg/m^3)	3080 to 3180
Bulk density	(kg/m^3) Aerated Settled	 1000 to 1300 1300 to 1450
Colour	Y value	27.5 to 37.5
Sulfate	SO_3 (%)	2.5 to 3.5
Chloride	Cl (%)	Less than 0.06
Alkali	Eq Na_2O (%)	0.4 to 0.75
Tricalcium Silicate	C_3S (%)	45.0 to 60.0
Dicalcium Silicate	C_2S (%)	15.0 to 25.0
Tricalcium Aluminate	C_3A (%)	7.0 to 12.0
Tetracalcium Aluminoferrite	C_4AF (%)	6.0 to 10.0
Portland cements are predominantly compounds of calcium silicate and calcium aluminate with a small proportion of gypsum. They are produced by buring or sintering, at a temperature in excess of 1400°C, a finely ground mixture of raw materials which contain predominantly calcium carbonate, aluminium oxide, silica and iron oxide. The cooled clinker formed is ground under controlled conditions with the addition of typically 5% gypsum.		

Elkem

Material Safety Data Sheet

MH501.GBR

1. Identification of the Substance and Company

Product name:	***Elkem Microsilica ®***
Address/Phone No.:	**Elkem ASA,** **Materials** P.O.Box 8126 Vaagsbygd N-4602 Kristiansand S., Norway Telephone: + 47 38 01 75 00 Telefax: + 47 38 01 49 70
Contact person:	Tore Danielssen
Emergency Phone No.:	Not applicable

2. Composition/Information on Ingredients

Synonyms:	*Microsilica, Silica powder, Amorphous silica,* Silicon dioxide powder, condensed SiO_2-fume, Silica fume.
CAS No :	69012-64-2
EINECS No.:	273-761-1
HAZARDOUS INGREDIENT(S):	None
Symbol:	None
R and S Phrases:	None

Constituents (analysis):	Weight%
Silicon dioxide (SiO_2) amorphous	85-98
Iron oxide (Fe_2O_3)	max.3.0
Aluminium oxide (Al_2O_3)	max.1.5
Calcium oxide (CaO)	max.0.7
Magnesium oxide (MgO)	max.2.0
Sodium oxide (Na_2O)	max.1.0
Potassium oxide (K_2O)	max.3.0
Carbon (C)	max.3.0

ADOMAST

ADOMAST BUILDING CHEMICALS Ltd

DATA SHEET

ADOFLOW EXTRA

Super Plasticiser for Concrete and Mortar

Description

A liquid plasticiser and water reducing agent which imparts extremely high workability when added to a concrete mix or a cementitious grout. Being a highly effective deflocculating agent it disperses cement paste into its primary particles significantly increasing the flow characteristics of the paste.

Benefits

- Enables concrete to achieve high compaction with minimal or no vibration or tamping.
- Increases flow characteristics of concrete to assist with difficult pours.
- Permits significant reduction in water content of normal workability concrete with consequent reduction in water/cement ratio to produce higher early and ultimate strengths.

Addition

The optimum addition rate of ADOFLOW EXTRA is best determined after preliminary trials with the actual concrete under consideration. As a guide for carrying out trials an addition rate of 0.5 litres to 1.5 litres per 100 kilos Portland cement is recommended. Where high early and ultimate strength concrete is required, necessitating a steep reduction in water/cement ratio, the addition rate of ADOFLOW EXTRA may be increased up to 2.0 litres per 100 kilos Portland cement.

Mixing

ADOFLOW EXTRA is best added during the mixing cycle preferably at the same time as the water. Alternatively it may be added to a normal concrete mix just prior to the pour allowing for a further mixing cycle of at least 2 minutes.

Typical Comparisons

The following data is typical of what can be expected when comparing a concrete mix with the inclusion of ADOFLOW EXTRA to a control mix.

High Workability Self Compacting Concrete

- Aggregate/Cement Ratio 5.2:1
- W/C Ratio - Control Mix 0.58
- W/C Ratio - Test Mix 0.58

ADOFLOW EXTRA - Test Mix 1.0 litre per 100 kg OPC

- Slump - Control Mix 50 mm
- Slump - Test Mix Collapse

Compressive Strength - Test Mix:

- 7 days: 102 % of control
- 28 days: 103 % of control

High Early & Ultimate Strength Concrete

- Aggregate/Cement Ratio 5.2:1
- W/C Ratio - Control Mix 0.58
- W/C Ratio - Test Mix 0.47

ADOFLOW EXTRA - Test Mix 1.25 litre per 100 kg OPC

- Slump - Control Mix 50 mm
- Slump - Test Mix 50 mm

Compressive Strength - Test Mix

- 1 day: 180 % of control
- 7 days: 144 % of control
- 28 days: 135 % of control

Storage & Shelf Life

Store at temperatures above freezing but not above 28° C in dry condition and under cover. Should freezing occur, completely thaw material and then mix thoroughly before use. In these circumstances shelf life is indefinite.

Specification Clause

ADOFLOW EXTRA manufactured by ADOMAST Building Chemicals Ltd shall be added to the concrete mix in accordance with the manufacturers recommendation

Health & Safety

ADOFLOW EXTRA is non-hazardous in normal use. If splashes should affect the eyes bathe immediately with copious quantities of clean water and then immediately seek medical advice. Reference should be made to the separate Health and Safety literature

ABCD 394 ISSUE: 4
ISSUED: JAN 1997

Lea Road Trading Estate, Lea Road
Waltham Abbey, Essex EN9 1AE

01992 710684 phone
01992 712813 fax

ABC

Appendix B – Analytical solution for surface tension equation

Appendix B – Analytical solution for surface tension equation

This section provides the analytical solution for the equation giving the surface tension in adsorption layer, equation (5.9).

$$\sigma = RT \int_{p_g/p_0}^{p_g/p_0=1} \Gamma d\left[\ln(\frac{p_g}{p_0})\right]$$

$$\Gamma = 3C_1^{1/3}\left[\frac{1}{-\ln\left(\frac{p_g}{p_0}\right)}\right]^{1/3}$$

Let $\frac{p_g}{p_0} = x$ and $C = 3C_1^{1/3}$

$$\therefore \Gamma = C\left[\frac{1}{-\ln(x)}\right]^{1/3}$$

therefore the equation for the surface tension yields :

$$\sigma = C\int_x^1 \frac{1}{(-\ln(x))^{1/3}} d(\ln x)$$

Now let $-y = \ln x$, the last equation transforms to :

$$\sigma = C\int_{-\ln(x)}^{0} \frac{-dy}{y^{1/3}} = -C\int_{-\ln(x)}^{0} \frac{dy}{y^{1/3}} = C\int_0^{-\ln(x)} \frac{dy}{y^{1/3}} = \frac{3}{2}C\left[y^{2/3}\right]_0^{-\ln(x)} = \frac{3}{2}C[-\ln(x)]^{2/3}$$

$$\therefore \sigma = \frac{3}{2}C\left[-\ln\left(\frac{p_g}{p_0}\right)\right]^{2/3}$$

Appendix C – Model spreadsheets

Appendix C – Model spreadsheets

Appendix C1 – E-value model spreadsheets at various values of degree of hydration

For α=0.1

Stage 1 - Cement Paste

INITIALISATIONS				RESULTS			
Definition	**Symbol**	**Value**	**Units**	**Definition**	**Symbol**	**Value**	**Units**
Degree of hydration	Dh	0.1	-				
E-value of hydrating cement	Ehc	2720	MPa	E-value of the paste	Epa	7.741357	GPa
E-value of unhydrated cement particles	Eu	27200	MPa				
Ratio of moduli of elasticity	n1	10	-				
Shape factor for unhydrated cement particles	η	1	-				
Volume of unhydrated cement particles	V	0.554209	m^3				
Geometry function for unhydrated cement	Θ	1.357484	-				

Stage 2 - Mortar

INITIALISATIONS

Definition	Symbol	Value	Units
E-value for the sand	Es	23224.07	MPa
Ratio of moduli of elasticity	n2	3	-
Total mass of sand used in 1 m^3 of mix	m	940	kg
Density of sand used	d	2632	kg/m^3
Volume fraction of sand for 1 m^3 of mix	Vfs	0.357143	-
Geometry function for fine sand	Θs	1	-

RESULTS

Definition	Symbol	Value	Units
E-value for the mortar	Emor	11.10716	GPa

Stage 3 - CARDIFRC®

INITIALISATIONS

Definition	Symbol	Value	Units
Volume fraction of 6mm fibres	Vffs	0.045	-
Volume fraction of 13mm fibres	Vffl	0.015	-
E-value for the steel fibres	Ef	210000	MPa
Ratio of moduli of elasticity	n3	18.90672	-
Geometry function for fine sand	Θf	1.2	-

RESULTS

Definition	Symbol	Value	Units
E-value of the matrix for 6mm fibres	Ef6	12127.34	MPa
E-value of the matrix for 13mm fibres	Ef13	11438.01	MPa
E-value of CARDIFRC®	$E_{CARDIFRC}$	23.56536	GPa

For α=0.2

Stage 1 - Cement Paste

INITIALISATIONS				RESULTS			
Definition	**Symbol**	**Value**	**Units**	**Definition**	**Symbol**	**Value**	**Units**
Degree of hydration	Dh	0.2	-				
E-value of hydrating cement	Ehc	5184	MPa	E-value of the paste	Epa	10.99676	GPa
E-value of unhydrated cement particles	Eu	25920	MPa				
Ratio of moduli of elasticity	n1	5	-				
Shape factor for unhydrated cement particles	η	1	-				
Volume of unhydrated cement particles	V	0.520044	m^3				
Geometry function for unhydrated cement	Θ	1.244979	-				

Stage 2 - Mortar

INITIALISATIONS

Definition	Symbol	Value	Units
E-value for the sand	Es	32990.29	MPa
Ratio of moduli of elasticity	n2	3	-
Total mass of sand used in 1 m^3 of mix	m	940	kg
Density of sand used	d	2632	kg/m^3
Volume fraction of sand for 1 m^3 of mix	Vfs	0.357143	-
Geometry function for fine sand	Θs	1	-

RESULTS

Definition	Symbol	Value	Units
E-value for the mortar	Emor	15.77796	GPa

Stage 3 - CARDIFRC®

INITIALISATIONS

Definition	Symbol	Value	Units
Volume fraction of 6mm fibres	Vffs	0.045	-
Volume fraction of 13mm fibres	Vffl	0.015	-
E-value for the steel fibres	Ef	210000	MPa
Ratio of moduli of elasticity	n3	13.3097	-
Geometry function for fine sand	Θf	1.2	-

RESULTS

Definition	Symbol	Value	Units
E-value of the matrix for 6mm fibres	Ef6	17155.74	MPa
E-value of the matrix for 13mm fibres	Ef13	16225.38	MPa
E-value of CARDIFRC®	$E_{CARDIFRC}$	33.38113	GPa

For α=0.3

Stage 1 - Cement Paste

INITIALISATIONS				RESULTS			
Definition	**Symbol**	**Value**	**Units**	**Definition**	**Symbol**	**Value**	**Units**
Degree of hydration	Dh	0.3	-				
E-value of hydrating cement	Ehc	7776	MPa	E-value of the paste	Epa	13.45489	GPa
E-value of unhydrated cement particles	Eu	25920	MPa				
Ratio of moduli of elasticity	n1	3.333333	-				
Shape factor for unhydrated cement particles	η	1	-				
Volume of unhydrated cement particles	V	0.485879	m^3				
Geometry function for unhydrated cement	Θ	1.171734	-				

Stage 2 - Mortar

INITIALISATIONS

Definition	Symbol	Value	Units
E-value for the sand	Es	40364.68	MPa
Ratio of moduli of elasticity	n2	3	-
Total mass of sand used in 1 m^3 of mix	m	940	kg
Density of sand used	d	2632	kg/m^3
Volume fraction of sand for 1 m^3 of mix	Vfs	0.357143	-
Geometry function for fine sand	Θs	1	-

RESULTS

Definition	Symbol	Value	Units
E-value for the mortar	Emor	19.30485	GPa

Stage 3 - CARDIFRC®

INITIALISATIONS

Definition	Symbol	Value	Units
Volume fraction of 6mm fibres	Vffs	0.045	-
Volume fraction of 13mm fibres	Vffl	0.015	-
E-value for the steel fibres	Ef	210000	MPa
Ratio of moduli of elasticity	n3	10.8781	-
Geometry function for fine sand	Θf	1.2	-

RESULTS

Definition	Symbol	Value	Units
E-value of the matrix for 6mm fibres	Ef6	20927.63	MPa
E-value of the matrix for 13mm fibres	Ef13	19832.34	MPa
E-value of CARDIFRC®	ECARDIFRC	40.75997	GPa

For α=0.4

Stage 1 - Cement Paste

INITIALISATIONS				RESULTS			
Definition	**Symbol**	**Value**	**Units**	**Definition**	**Symbol**	**Value**	**Units**
Degree of hydration	Dh	0.4	-				
E-value of hydrating cement	Ehc	10368	MPa	E-value of the paste	Epa	15.42983	GPa
E-value of unhydrated cement particles	Eu	25920	MPa				
Ratio of moduli of elasticity	n1	2.5	-				
Shape factor for unhydrated cement particles	η	1	-				
Volume of unhydrated cement particles	V	0.451714	m^3				
Geometry function for unhydrated cement	Θ	1.120484	-				

Stage 2 - Mortar

INITIALISATIONS

Definition	Symbol	Value	Units
E-value for the sand	Es	46289.48	MPa
Ratio of moduli of elasticity	n2	3	-
Total mass of sand used in 1 m^3 of mix	m	940	kg
Density of sand used	d	2632	kg/m^3
Volume fraction of sand for 1 m^3 of mix	Vfs	0.357143	-
Geometry function for fine sand	Θs	1	-

RESULTS

Definition	Symbol	Value	Units
E-value for the mortar	Emor	22.13844	GPa

Stage 3 - CARDIFRC®

INITIALISATIONS

Definition	Symbol	Value	Units
Volume fraction of 6mm fibres	Vffs	0.045	-
Volume fraction of 13mm fibres	Vffl	0.015	-
E-value for the steel fibres	Ef	210000	MPa
Ratio of moduli of elasticity	n3	9.485761	-
Geometry function for fine sand	Θf	1.2	-

RESULTS

Definition	Symbol	Value	Units
E-value of the matrix for 6mm fibres	Ef6	23943.42	MPa
E-value of the matrix for 13mm fibres	Ef13	22725.6	MPa
E-value of CARDIFRC®	$E_{CARDIFRC}$	46.66902	GPa

For α=0.5

Stage 1 - Cement Paste

INITIALISATIONS				RESULTS			
Definition	**Symbol**	**Value**	**Units**	**Definition**	**Symbol**	**Value**	**Units**
Degree of hydration	Dh	0.5	-				
E-value of hydrating cement	Ehc	12960	MPa	E-value of the paste	Epa	17.18902	GPa
E-value of unhydrated cement particles	Eu	25920	MPa				
Ratio of moduli of elasticity	n1	2	-				
Shape factor for unhydrated cement particles	η	1	-				
Volume of unhydrated cement particles	V	0.417549	m^3				
Geometry function for unhydrated cement	Θ	1.083199	-				

Stage 2 - Mortar

INITIALISATIONS

Definition	Symbol	Value	Units
E-value for the sand	Es	51567.06	MPa
Ratio of moduli of elasticity	n2	3	-
Total mass of sand used in 1 m^3 of mix	m	940	kg
Density of sand used	d	2632	kg/m^3
Volume fraction of sand for 1 m^3 of mix	Vfs	0.357143	-
Geometry function for fine sand	Θs	1	-

RESULTS

Definition	Symbol	Value	Units
E-value for the mortar	Emor	24.66251	GPa

Stage 3 - CARDIFRC®

INITIALISATIONS

Definition	Symbol	Value	Units
Volume fraction of 6mm fibres	Vffs	0.045	-
Volume fraction of 13mm fibres	Vffl	0.015	-
E-value for the steel fibres	Ef	210000	MPa
Ratio of moduli of elasticity	n3	8.514949	-
Geometry function for fine sand	Θf	1.2	-

RESULTS

Definition	Symbol	Value	Units
E-value of the matrix for 6mm fibres	Ef6	26619.3	MPa
E-value of the matrix for 13mm fibres	Ef13	25299.46	MPa
E-value of CARDIFRC®	$E_{CARDIFRC}$	51.91876	GPa

Appendix C2 – Shrinkage model spreadsheets at various values of degree of hydration for CARDIFRC® matrix

For α=0.1

INITIALISATIONS

Definition	Symbol	Value	Units	Definition	Symbol	Value	Units
Degree of Hydration	dh	0.1	-	Specific density of water	gw	10000	N/m^3
Specific mass of cement	pc	3180	kg/m^3	Constant Z	Z	0.3333333	-
Specific mass of water	pw	1000	kg/m^3	E-value for CARDIFRC	Emor	1.06E+10	Pa
Water to cement ratio	w0	0.22	-	Pore Structure Constant	a	0.15	-
Total Volume of mix	V	1	m^3	Min diameter for capillary pores	ph0	2.00E-09	m
Specific Mass of plain cement paste	ppa	5.5375393	kg/m^3	Initial Relative Humidity	RHi	0.9091148	-
Ideal Gas Constant	R	49	m/K	Thickness of the adsorption layer	Gi	9.15E-10	m
Temperature	T	293	K	Surface Tension	STi	0.0187663	N/m

RESULTS

Definition	Symbol	Value	Units
Volume of available water	Vw	0.4116263	m^3
Volume of capillary water	Vcap	0.3367851	m^3
Volume of chemically bound water	Vch	0.0116939	m^3
Volume of water in pores	Vpor	0.3484791	m^3
Maximum pore diameter	phpor	2.042E-08	m
Total pore wall area	Apor	8647185.2	m^2
Volume of the adsorbed water	Vad	0.1853681	m^3

Definition	Symbol	Value	Units
Volume of remaining free water	Vfree	0.151417	m^3
Largest pore diameter filled	ph_wat	5.488E-09	m
Area of filled pores	Awat	6.09E+06	m^2
Logarithm of new RH value	ln_RHj	0.0952744	-
New RH value	RHj	0.9091234	-
New Thick of adsorption layer	Gj	9.146E-10	m
New surface tension value	STj	0.0187675	N/m
Proportionality factor l	λ	0.0004455	-
Shrinkage Strain	ε	55.21	$\mu\varepsilon$

For α=0.2

INITIALISATIONS

Definition	Symbol	Value	Units	Definition	Symbol	Value	Units
Degree of Hydration	dh	0.2	-	Specific density of water	gw	10000	N/m^3
Specific mass of cement	pc	3180	kg/m^3	Constant Z	Z	0.3333333	-
Specific mass of water	pw	1000	kg/m^3	E-value for CARDIFRC	Emor	1.58E+10	Pa
Water to cement ratio	w0	0.22	-	Pore Structure Constant	a	0.15	-
Total Volume of mix	V	1	m^3	Min diameter for capillary pores	ph0	2.00E-09	m
Specific Mass of plain cement paste	ppa	5.5375393	kg/m^3	Initial Relative Humidity	RHi	0.8238514	-
Ideal Gas Constant	R	49	m/K	Thickness of the adsorption layer	Gi	7.22E-10	m
Temperature	T	293	K	Surface Tension	STi	0.0301239	N/m

RESULTS

Definition	Symbol	Value	Units
Volume of available water	Vw	0.4116263	m^3
Volume of capillary water	Vcap	0.261944	m^3
Volume of chemically bound water	Vch	0.0233879	m^3
Volume of water in pores	Vpor	0.2853318	m^3
Maximum pore diameter	phpor	1.34E-08	m
Total pore wall area	Apor	83182404	m^2
Volume of the adsorbed water	Vad	0.1460363	m^3

Definition	Symbol	Value	Units
Volume of remaining free water	Vfree	0.1159077	m^3
Largest pore diameter filled	ph_wat	4.331E-09	m
Area of filled pores	Awat	5.26E+07	m^2
Logarithm of new RH value	ln_RHj	-0.1937718	-
New RH value	RHj	0.8238459	-
New Thick of adsorption layer	Gj	7.219E-10	m
New surface tension value	STj	0.0301246	N/m
Proportionality factor l	λ	0.0035747	-
Shrinkage Strain	ε	245.45	$\mu\varepsilon$

For α=0.3

INITIALISATIONS

Definition	Symbol	Value	Units	Definition	Symbol	Value	Units
Degree of Hydration	dh	0.3	-	Specific density of water	gw	10000	N/m^3
Specific mass of cement	pc	3180	kg/m^3	Constant Z	Z	0.3333333	-
Specific mass of water	pw	1000	kg/m^3	E-value for CARDIFRC	Emor	1.93E+10	Pa
Water to cement ratio	w0	0.22	-	Pore Structure Constant	a	0.15	-
Total Volume of mix	V	1	m^3	Min diameter for capillary pores	ph0	2.00E-09	m
Specific Mass of plain cement paste	ppa	5.5375393	kg/m^3	Initial Relative Humidity	RHi	0.6664754	-
Ideal Gas Constant	R	49	m/K	Thickness of the adsorption layer	Gi	5.64E-10	m
Temperature	T	293	K	Surface Tension	STi	0.0493062	N/m

RESULTS

Definition	Symbol	Value	Units
Volume of available water	Vw	0.4116263	m^3
Volume of capillary water	Vcap	0.1871028	m^3
Volume of chemically bound water	Vch	0.0350818	m^3
Volume of water in pores	Vpor	0.2221846	m^3
Maximum pore diameter	phpor	8.797E-09	m
Total pore wall area	Apor	144674223	m^2
Volume of the adsorbed water	Vad	0.1081484	m^3

Definition	Symbol	Value	Units
Volume of remaining free water	Vfree	0.0789544	m^3
Largest pore diameter filled	ph_wat	3.386E-09	m
Area of filled pores	Awat	7.66E+07	m^2
Logarithm of new RH value	ln_RHj	0.4057619	-
New RH value	RHj	0.6664689	-
New Thick of adsorption layer	Gj	5.643E-10	m
New surface tension value	STj	0.049307	N/m
Proportionality factor l	λ	0.006506	-
Shrinkage Strain	ε	521.23	$\mu\varepsilon$

For α=0.4

INITIALISATIONS

Definition	Symbol	Value	Units	Definition	Symbol	Value	Units
Degree of Hydration	dh	0.4	-	Specific density of water	gw	10000	N/m^3
Specific mass of cement	pc	3180	kg/m^3	Constant Z	Z	0.3333333	-
Specific mass of water	pw	1000	kg/m^3	E-value for CARDIFRC	Emor	2.21E+10	Pa
Water to cement ratio	w0	0.22	-	Pore Structure Constant	a	0.15	-
Total Volume of mix	V	1	m^3	Min diameter for capillary pores	ph0	2.00E-09	m
Specific Mass of plain cement paste	ppa	5.5375393	kg/m^3	Initial Relative Humidity	RHi	0.4099718	-
Ideal Gas Constant	R	49	m/K	Thickness of the adsorption layer	Gi	4.34E-10	m
Temperature	T	293	K	Surface Tension	STi	0.0833418	N/m

RESULTS

Definition	Symbol	Value	Units
Volume of available water	Vw	0.4116263	m^3
Volume of capillary water	Vcap	0.1122617	m^3
Volume of chemically bound water	Vch	0.0467757	m^3
Volume of water in pores	Vpor	0.1590374	m^3
Maximum pore diameter	phpor	5.774E-09	m
Total pore wall area	Apor	158741962	m^2
Volume of the adsorbed water	Vad	0.0726734	m^3

Definition	Symbol	Value	Units
Volume of remaining free water	Vfree	0.0395883	m^3
Largest pore diameter filled	ph_wat	2.604E-09	m
Area of filled pores	Awat	5.63E+07	m^2
Logarithm of new RH value	ln_RHj	-0.8916803	-
New RH value	RHj	0.4099663	-
New Thick of adsorption layer	Gj	4.34E-10	m
New surface tension value	STj	0.0833426	N/m
Proportionality factor l	λ	0.0085384	-
Shrinkage Strain	ε	707.33	$\mu\varepsilon$

For α=0.5

INITIALISATIONS

Definition	Symbol	Value	Units	Definition	Symbol	Value	Units
Degree of Hydration	dh	0.5	-	Specific density of water	gw	10000	N/m^3
Specific mass of cement	pc	3180	kg/m^3	Constant Z	Z	0.3333333	-
Specific mass of water	pw	1000	kg/m^3	E-value for CARDIFRC	Emor	2.47E+10	Pa
Water to cement ratio	w0	0.22	-	Pore Structure Constant	a	0.15	-
Total Volume of mix	V	1	m^3	Min diameter for capillary pores	ph0	2.00E-09	m
Specific Mass of plain cement paste	ppa	5.5375393	kg/m^3	Initial Relative Humidity	RHi	0.1232901	-
Ideal Gas Constant	R	49	m/K	Thickness of the adsorption layer	Gi	3.27E-10	m
Temperature	T	293	K	Surface Tension	STi	0.1472099	N/m

RESULTS

Definition	Symbol	Value	Units
Volume of available water	Vw	0.4116263	m^3
Volume of capillary water	Vcap	0.0374206	m^3
Volume of chemically bound water	Vch	0.0584696	m^3
Volume of water in pores	Vpor	0.0958902	m^3
Maximum pore diameter	phpor	3.79E-09	m
Total pore wall area	Apor	52140480	m^2
Volume of the adsorbed water	Vad	0.040502	m^3

Definition	Symbol	Value	Units
Volume of remaining free water	Vfree	-0.0030814	m^3
Largest pore diameter filled	ph_wat	1.959E-09	m
Area of filled pores	Awat	-2.29E+06	m^2
Logarithm of new RH value	ln_RHj	-2.093268	-
New RH value	RHj	0.1232836	-
New Thick of adsorption layer	Gj	3.266E-10	m
New surface tension value	STj	0.1472124	N/m
Proportionality factor l	λ	0.0040739	-
Shrinkage Strain	ε	1004.50	$\mu\varepsilon$

Appendix C3 – Shrinkage model spreadsheets at various values of degree of hydration for CARDIFRC®

For α=0.1

INITIALISATIONS

Definition	Symbol	Value	Units	Definition	Symbol	Value	Units
Degree of Hydration	dh	0.1	-	Specific density of water	gw	10000	N/m^3
Specific mass of cement	pc	3180	kg/m^3	Constant Z	Z	0.3333333	-
Specific mass of water	pw	1000	kg/m^3	E-value for CARDIFRC	Ecard	2.25E+10	Pa
Water to cement ratio	w0	0.22	-	Pore Structure Constant	a	0.15	-
Total Volume of mix	V	1	m^3	Min diameter for capillary pores	ph0	2.00E-09	m
Specific Mass of plain cement paste	ppa	5.5375393	kg/m^3	Initial Relative Humidity	RHi	0.9091148	-
Ideal Gas Constant	R	49	m/K	Thickness of the adsorption layer	Gi	9.15E-10	m
Temperature	T	293	K	Surface Tension	STi	0.0187663	N/m

RESULTS

Definition	Symbol	Value	Units
Volume of available water	Vw	0.4116263	m^3
Volume of capillary water	Vcap	0.3367851	m^3
Volume of chemically bound water	Vch	0.0116939	m^3
Volume of water in pores	Vpor	0.3484791	m^3
Maximum pore diameter	phpor	2.042E-08	m
Total pore wall area	Apor	289013542	m^2
Volume of the adsorbed water	Vad	0.1853681	m^3

Definition	Symbol	Value	Units
Volume of remaining free water	Vfree	0.151417	m^3
Largest pore diameter filled	ph_wat	5.488E-09	m
Area of filled pores	Awat	2.04E+08	m^2
Logarithm of new RH value	ln_RHj	0.0952744	-
New RH value	RHj	0.9091234	-
New Thick of adsorption layer	Gj	9.146E-10	m
New surface tension value	STj	0.0187675	N/m
Proportionality factor l	λ	0.0070152	-
Shrinkage Strain	ε	86.99	$\mu\varepsilon$

For α=0.2

INITIALISATIONS

Definition	Symbol	Value	Units	Definition	Symbol	Value	Units
Degree of Hydration	dh	0.2	-	Specific density of water	gw	10000	N/m^3
Specific mass of cement	pc	3180	kg/m^3	Constant Z	Z	0.3333333	-
Specific mass of water	pw	1000	kg/m^3	E-value for CARDIFRC	Ecard	3.34E+10	Pa
Water to cement ratio	w0	0.22	-	Pore Structure Constant	a	0.15	-
Total Volume of mix	V	1	m^3	Min diameter for capillary pores	ph0	2.00E-09	m
Specific Mass of plain cement paste	ppa	5.5375393	kg/m^3	Initial Relative Humidity	RHi	0.8238514	-
Ideal Gas Constant	R	49	m/K	Thickness of the adsorption layer	Gi	7.22E-10	m
Temperature	T	293	K	Surface Tension	STi	0.0301239	N/m

RESULTS

Definition	Symbol	Value	Units
Volume of available water	Vw	0.4116263	m^3
Volume of capillary water	Vcap	0.261944	m^3
Volume of chemically bound water	Vch	0.0233879	m^3
Volume of water in pores	Vpor	0.2853318	m^3
Maximum pore diameter	phpor	1.34E-08	m
Total pore wall area	Apor	105032334	m^2
Volume of the adsorbed water	Vad	0.1460363	m^3

Definition	Symbol	Value	Units
Volume of remaining free water	Vfree	0.1159077	m^3
Largest pore diameter filled	ph_wat	4.331E-09	m
Area of filled pores	Awat	6.64E+07	m^2
Logarithm of new RH value	ln_RHj	-0.1937718	-
New RH value	RHj	0.8238459	-
New Thick of adsorption layer	Gj	7.219E-10	m
New surface tension value	STj	0.0301246	N/m
Proportionality factor l	λ	0.0021335	-
Shrinkage Strain	ε	146.77	$\mu\varepsilon$

For α=0.3

INITIALISATIONS

Definition	Symbol	Value	Units	Definition	Symbol	Value	Units
Degree of Hydration	dh	0.3	-	Specific density of water	gw	10000	N/m^3
Specific mass of cement	pc	3180	kg/m^3	Constant Z	Z	0.3333333	-
Specific mass of water	pw	1000	kg/m^3	E-value for CARDIFRC	Ecard	4.08E+10	Pa
Water to cement ratio	w0	0.22	-	Pore Structure Constant	a	0.15	-
Total Volume of mix	V	1	m^3	Min diameter for capillary pores	ph0	2.00E-09	m
Specific Mass of plain cement paste	ppa	5.5375393	kg/m^3	Initial Relative Humidity	RHi	0.6664754	-
Ideal Gas Constant	R	49	m/K	Thickness of the adsorption layer	Gi	5.64E-10	m
Temperature	T	293	K	Surface Tension	STi	0.0493062	N/m

RESULTS

Definition	Symbol	Value	Units
Volume of available water	Vw	0.4116263	m^3
Volume of capillary water	Vcap	0.1871028	m^3
Volume of chemically bound water	Vch	0.0350818	m^3
Volume of water in pores	Vpor	0.2221846	m^3
Maximum pore diameter	phpor	8.797E-09	m
Total pore wall area	Apor	182083818	m^2
Volume of the adsorbed water	Vad	0.1081484	m^3

Definition	Symbol	Value	Units
Volume of remaining free water	Vfree	0.0789544	m^3
Largest pore diameter filled	ph_wat	3.386E-09	m
Area of filled pores	Awat	9.64E+07	m^2
Logarithm of new RH value	ln_RHj	-0.4057619	-
New RH value	RHj	0.6664689	-
New Thick of adsorption layer	Gj	5.643E-10	m
New surface tension value	STj	0.049307	N/m
Proportionality factor I	λ	0.0038782	-
Shrinkage Strain	ε	310.63	$\mu\varepsilon$

For α=0.4

INITIALISATIONS

Definition	Symbol	Value	Units	Definition	Symbol	Value	Units
Degree of Hydration	dh	0.4	-	Specific density of water	gw	10000	N/m^3
Specific mass of cement	pc	3180	kg/m^3	Constant Z	Z	0.3333333	-
Specific mass of water	pw	1000	kg/m^3	E-value for CARDIFRC	Ecard	4.67E+10	Pa
Water to cement ratio	w0	0.22	-	Pore Structure Constant	a	0.15	-
Total Volume of mix	V	1	m^3	Min diameter for capillary pores	ph0	2.00E-09	m
Specific Mass of plain cement paste	ppa	5.5375393	kg/m^3	Initial Relative Humidity	RHi	0.4099718	-
Ideal Gas Constant	R	49	m/K	Thickness of the adsorption layer	Gi	4.34E-10	m
Temperature	T	293	K	Surface Tension	STi	0.0833418	N/m

RESULTS

Definition	Symbol	Value	Units
Volume of available water	Vw	0.4116263	m^3
Volume of capillary water	Vcap	0.1122617	m^3
Volume of chemically bound water	Vch	0.0467757	m^3
Volume of water in pores	Vpor	0.1590374	m^3
Maximum pore diameter	phpor	5.774E-09	m
Total pore wall area	Apor	216364804	m^2
Volume of the adsorbed water	Vad	0.0726734	m^3

Definition	Symbol	Value	Units
Volume of remaining free water	Vfree	0.0395883	m^3
Largest pore diameter filled	ph_wat	2.604E-09	m
Area of filled pores	Awat	7.68E+07	m^2
Logarithm of new RH value	ln_RHj	-0.8916803	-
New RH value	RHj	0.4099663	-
New Thick of adsorption layer	Gj	4.34E-10	m
New surface tension value	STj	0.0833426	N/m
Proportionality factor l	λ	0.0055206	-
Shrinkage Strain	ε	457.35	$\mu\varepsilon$

For α=0.5

INITIALISATIONS

Definition	Symbol	Value	Units	Definition	Symbol	Value	Units
Degree of Hydration	dh	0.5	-	Specific density of water	gw	10000	N/m^3
Specific mass of cement	pc	3180	kg/m^3	Constant Z	Z	0.3333333	-
Specific mass of water	pw	1000	kg/m^3	E-value for CARDIFRC	Ecard	5.19E+10	Pa
Water to cement ratio	w0	0.22	-	Pore Structure Constant	a	0.15	-
Total Volume of mix	V	1	m^3	Min diameter for capillary pores	ph0	2.00E-09	m
Specific Mass of plain cement paste	ppa	5.5375393	kg/m^3	Initial Relative Humidity	RHi	0.1232901	-
Ideal Gas Constant	R	49	m/K	Thickness of the adsorption layer	Gi	3.27E-10	m
Temperature	T	293	K	Surface Tension	STi	0.1472099	N/m

RESULTS

Definition	Symbol	Value	Units
Volume of available water	Vw	0.4116263	m^3
Volume of capillary water	Vcap	0.0374206	m^3
Volume of chemically bound water	Vch	0.0584696	m^3
Volume of water in pores	Vpor	0.0958902	m^3
Maximum pore diameter	phpor	3.79E-09	m
Total pore wall area	Apor	63974196	m^2
Volume of the adsorbed water	Vad	0.040502	m^3

Definition	Symbol	Value	Units
Volume of remaining free water	Vfree	-0.0030814	m^3
Largest pore diameter filled	ph_wat	1.959E-09	m
Area of filled pores	Awat	-2.81E+06	m^2
Logarithm of new RH value	ln_RHj	-2.093268	-
New RH value	RHj	0.1232836	-
New Thick of adsorption layer	Gj	3.266E-10	m
New surface tension value	STj	0.1472124	N/m
Proportionality factor l	λ	0.0023744	-
Shrinkage Strain	ε	585.45	$\mu\varepsilon$

Appendix D – Autogenous shrinkage results for the small specimens

Appendix D – Autogenous shrinkage results for the small specimens

Tables D1, D2 and D3 show indicative results at several time intervals from the small prisms having dimensions 50x50x250mm. The values shown are in με and correspond to the prisms without fibres.

Table D1: Summary of autogenous shrinkage strain (με) results at specific time intervals up to 24 hours for small prisms without fibres.

	Time Intervals (hours)					
	4	**8**	**12**	**16**	**20**	**24**
Beam 1	21.61	51.17	79.42	104.02	126.56	146.70
Beam 2	22.63	53.10	82.53	108.63	131.98	153.32
Beam 3	19.05	48.19	76.46	101.66	123.65	145.04
Beam 4	20.74	49.12	76.23	99.83	121.46	140.78
Beam 5	21.06	49.89	77.42	101.40	123.37	143.00
Beam 6	21.31	50.46	78.30	102.55	124.76	144.60
Beam 7	20.64	48.91	75.91	99.41	120.95	140.18
Beam 8	20.83	49.38	76.64	100.37	122.10	141.51
Beam 9	20.91	49.59	76.99	100.84	122.70	142.22
Beam 10	20.79	49.23	76.38	100.02	121.67	141.00
Beam 11	21.06	49.97	77.58	101.62	123.66	143.34
Beam 12	21.19	50.25	78.01	102.19	130.21	144.14
Mean	20.99	49.94	77.66	101.88	124.42	143.82
COV	3.70	2.43	2.26	2.34	2.69	2.37

Table D2: Summary of autogenous shrinkage strain (με) results at specific time intervals for small prisms without fibres.

	Time Intervals (days)								
	1	**2**	**3**	**4**	**5**	**6**	**7**	**8**	**9**
Beam 1	146.70	253.77	337.03	399.72	452.38	496.44	533.98	562.46	585.41
Beam 2	153.32	261.32	345.62	410.05	460.88	505.21	543.06	571.78	594.92
Beam 3	145.04	252.68	336.46	398.95	450.84	494.43	529.51	555.35	576.84
Beam 4	140.78	243.44	323.23	383.27	433.69	475.86	511.78	539.03	560.98
Beam 5	143.00	247.31	328.39	389.43	440.68	483.56	520.09	547.79	570.12
Beam 6	144.60	250.00	331.90	393.51	445.24	488.49	525.33	553.27	575.78
Beam 7	140.18	242.31	321.63	381.28	431.34	473.19	508.83	535.85	557.62
Beam 8	141.51	244.57	324.55	384.68	435.12	477.27	513.16	540.36	562.27
Beam 9	142.22	245.90	326.44	387.02	437.87	480.38	516.59	544.05	566.16
Beam 10	141.00	243.65	323.31	383.19	433.43	475.41	511.14	538.23	560.05
Beam 11	143.34	247.95	329.27	390.48	441.89	484.90	521.53	549.32	571.72
Beam 12	144.14	249.35	331.13	392.70	444.41	487.67	524.53	552.48	575.01
Mean	143.82	248.52	329.91	391.19	442.31	485.23	521.63	549.16	571.41
COV	2.37	2.09	2.04	2.07	1.94	1.92	1.89	1.87	1.86

Table D3: Summary of autogenous shrinkage strain (με) results at specific time intervals for small prisms without fibres.

	Time Intervals (days)						
	10	**20**	**30**	**40**	**50**	**60**	**75**
Beam 1	603.98	693.77	777.81	797.79	868.94	932.43	1000.90
Beam 2	613.63	697.72	763.95	770.21	826.77	882.95	993.35
Beam 3	593.93	707.22	782.29	797.20	856.29	914.89	1031.61
Beam 4	578.45	664.56	746.15	763.90	831.80	892.36	988.52
Beam 5	587.89	675.49	758.00	776.58	845.70	907.36	1005.29
Beam 6	593.70	681.97	764.86	783.77	853.32	915.34	1013.77
Beam 7	574.94	660.26	741.33	758.59	825.73	885.57	980.49
Beam 8	579.71	665.54	746.90	764.39	831.84	891.92	987.16
Beam 9	583.77	670.49	752.42	770.46	838.74	899.61	996.20
Beam 10	577.41	662.87	713.22	761.29	828.44	888.25	983.04
Beam 11	589.55	677.41	744.00	778.82	848.16	910.02	1008.27
Beam 12	592.94	681.35	760.09	783.39	853.16	915.41	1014.30
Mean	589.16	678.22	754.25	775.53	842.41	903.01	1000.24
COV	1.87	2.11	2.32	1.63	1.58	1.62	1.45

Tables D4, D5 and D6 show indicative results at several time intervals from the small prisms having dimensions 50x50x250mm. The values shown are in με and correspond to the prisms with fibres.

Table D4: Summary of autogenous shrinkage strain (με) results at specific time intervals up to 24 hours for small prisms with fibres.

	Time Intervals (hours)					
	4	**8**	**12**	**16**	**20**	**24**
Beam 1	17.13	41.13	62.02	79.01	93.27	105.06
Beam 2	11.09	31.14	49.03	64.06	76.61	88.09
Beam 3	17.80	42.79	64.52	82.20	97.03	109.29
Beam 4	17.39	42.11	63.62	81.11	95.78	107.90
Beam 5	11.19	31.48	49.56	64.75	77.42	89.00
Beam 6	17.52	42.11	63.49	80.88	95.47	107.53
Beam 7	11.03	31.03	48.85	63.81	76.30	87.81
Beam 8	11.22	31.55	49.67	64.89	77.60	89.20
Beam 9	17.13	41.16	62.06	79.05	93.31	105.09
Beam 10	11.16	31.40	49.44	65.58	77.22	88.77
Beam 11	17.58	42.25	63.71	81.15	95.80	107.89
Beam 12	17.51	42.07	63.43	80.81	95.38	107.43
Mean	14.81	37.52	57.45	73.94	87.60	99.42
COV	21.00	14.01	12.03	10.73	10.26	9.29

Table D5: Summary of autogenous shrinkage strain (με) results at specific time intervals for small prisms with fibres.

	Time Intervals (days)								
	1	**2**	**3**	**4**	**5**	**6**	**7**	**8**	**9**
Beam 1	105.06	167.14	219.92	257.45	286.56	312.02	335.59	362.09	389.17
Beam 2	88.09	145.17	194.48	232.34	260.15	286.62	309.15	336.75	363.90
Beam 3	109.29	173.77	228.53	267.41	297.56	323.91	348.29	375.68	403.65
Beam 4	107.90	171.70	225.85	264.31	294.13	320.18	344.28	371.37	399.02
Beam 5	89.00	146.54	196.16	234.18	262.06	288.59	311.13	338.72	365.84
Beam 6	107.53	170.96	224.80	263.04	292.68	318.58	342.54	369.46	396.94
Beam 7	87.81	144.39	193.26	230.70	258.15	284.26	306.46	333.61	360.29
Beam 8	89.20	146.87	196.60	234.71	262.67	289.25	311.85	339.51	366.69
Beam 9	105.09	167.05	219.64	256.97	285.91	311.19	334.57	360.83	387.65
Beam 10	88.77	146.16	195.64	233.55	261.36	287.81	310.29	337.80	364.84
Beam 11	107.89	171.54	225.57	263.94	293.69	319.68	343.72	370.74	398.33
Beam 12	107.43	170.80	224.59	262.79	292.40	318.27	342.21	369.10	396.56
Mean	99.42	160.17	212.09	250.11	278.94	305.03	328.34	355.47	382.74
COV	9.29	7.66	6.81	5.86	5.59	5.04	4.91	4.47	4.22

Table D6: Summary of autogenous shrinkage strain (με) results at specific time intervals for small prisms with fibres.

	Time Intervals (days)						
	10	**20**	**30**	**40**	**50**	**60**	**75**
Beam 1	410.87	474.76	481.25	515.91	518.83	539.87	574.38
Beam 2	386.16	457.28	466.49	504.67	507.49	531.20	577.51
Beam 3	426.05	491.93	498.78	534.30	537.31	558.96	594.43
Beam 4	421.16	486.28	492.99	528.16	531.13	552.52	585.58
Beam 5	388.03	458.80	467.91	505.82	508.61	532.09	569.11
Beam 6	418.95	483.68	490.31	525.29	528.24	549.51	584.34
Beam 7	382.12	451.74	460.61	497.98	500.72	523.80	560.18
Beam 8	388.93	459.89	469.04	507.03	509.83	533.37	570.48
Beam 9	409.12	472.24	478.56	512.81	515.69	536.41	570.36
Beam 10	386.96	457.53	466.60	504.41	507.19	530.60	567.50
Beam 11	420.42	485.38	492.05	527.15	530.11	551.45	586.42
Beam 12	418.55	483.21	489.82	524.78	527.73	548.97	583.76
Mean	404.78	496.89	479.53	515.69	518.57	540.73	577.00
COV	3.98	2.87	2.61	2.20	2.21	1.97	1.66

Figures D1 and D2 present the results obtained in the laboratory for the small prisms tested.

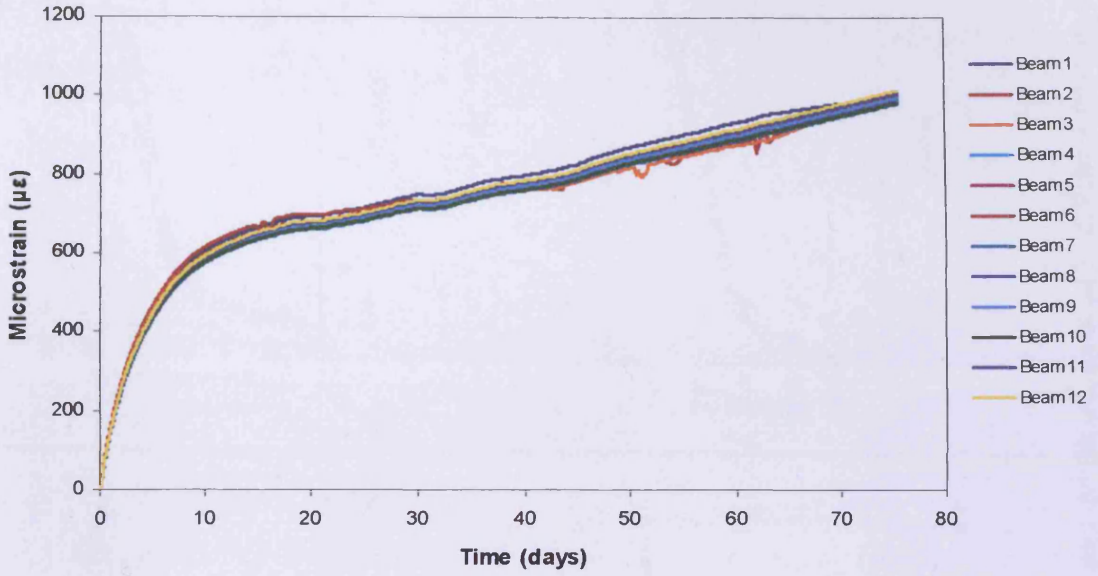

Figure D1: Autogenous shrinkage strain variation with time for all the beams without fibres.

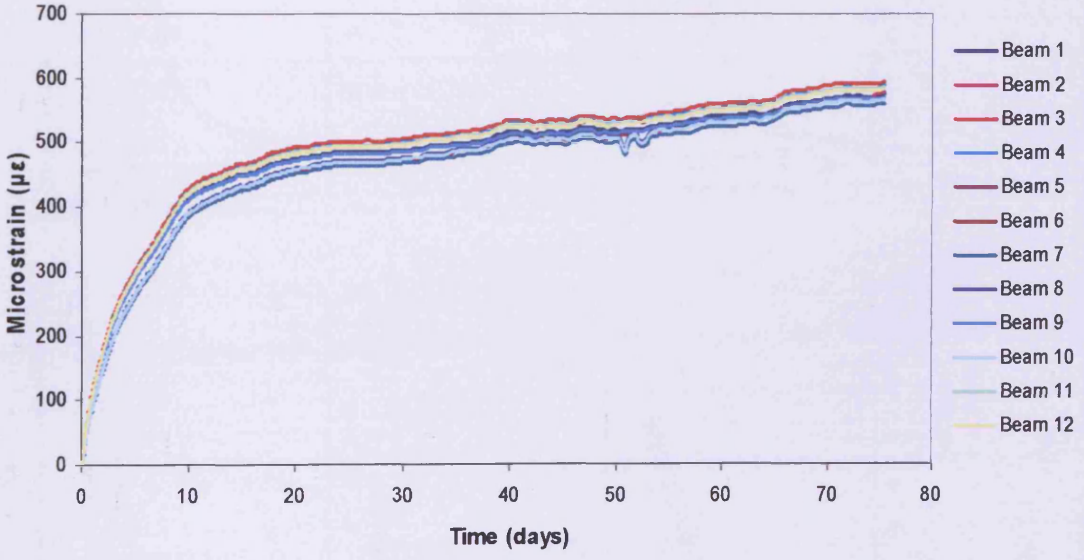

Figure D2: Autogenous shrinkage strain variation with time for all the beams with fibres.

Figures D3, D4, D5 and D6 show the comparison between each of the beams tested with the model.

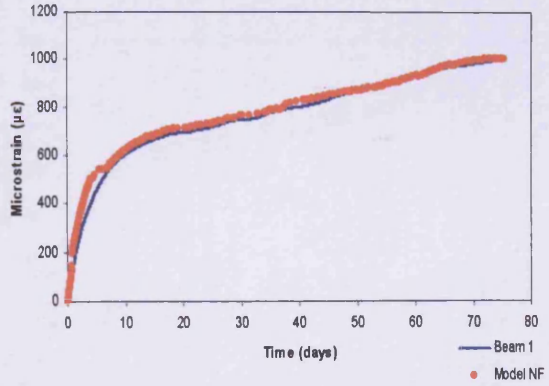

(a)

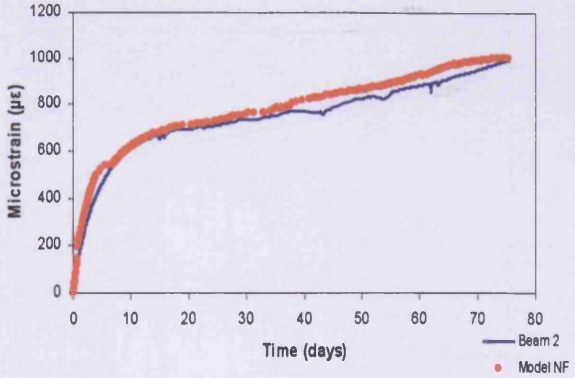

(b)

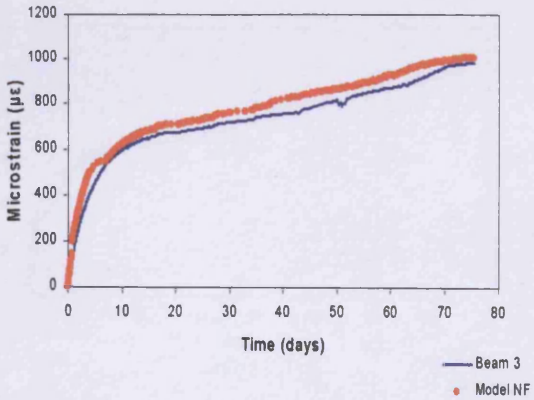

(c)

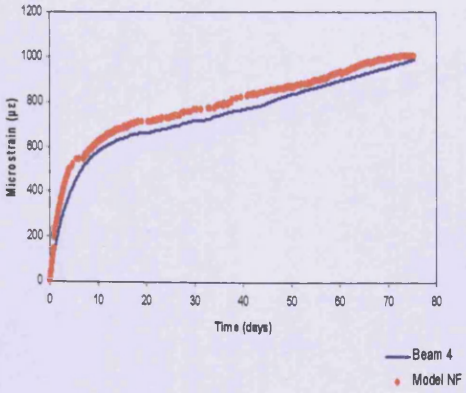

(d)

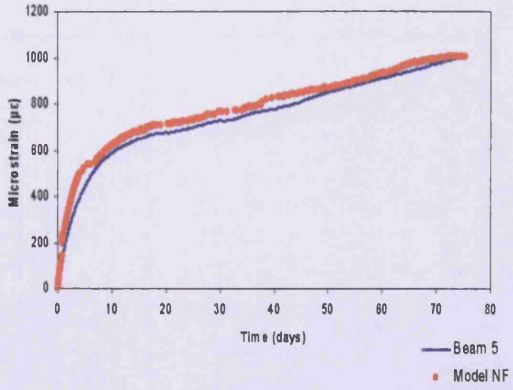

(e)

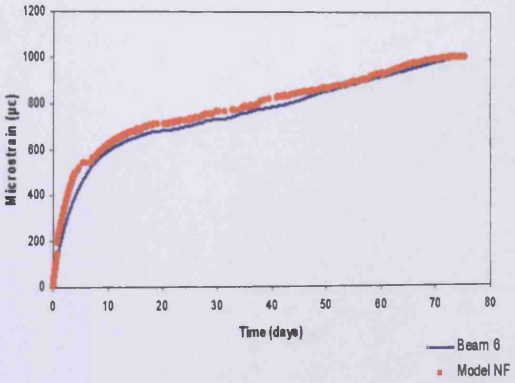

(f)

Figure D3: Autogenous shrinkage strain results of beams without fibres compared to the model, (a) Beam 1, (b) Beam 2, (c) Beam 3, (d) Beam 4, (e) Beam 5 and (f) Beam 6.

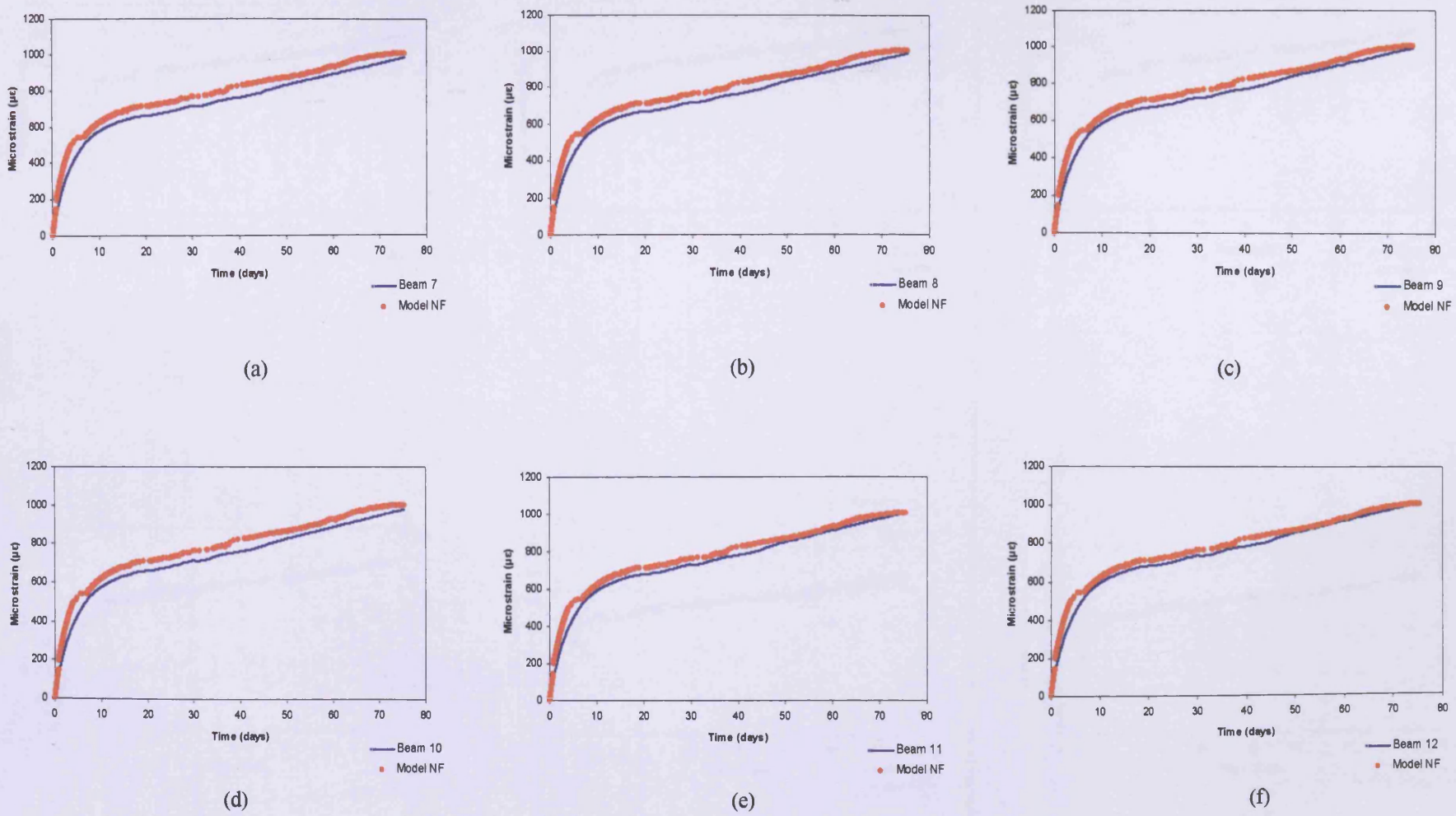

Figure D4: Autogenous shrinkage strain results of beams without fibres compared to the model, (a) Beam 7, (b) Beam 8, (c) Beam 9, (d) Beam 10, (e) Beam 11 and (f) Beam 12.

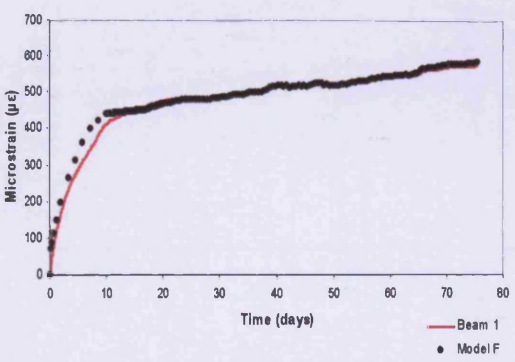

(a)

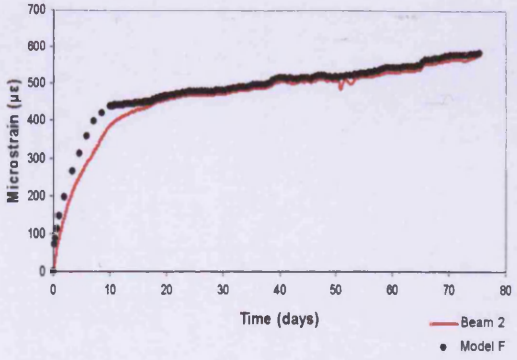

(b)

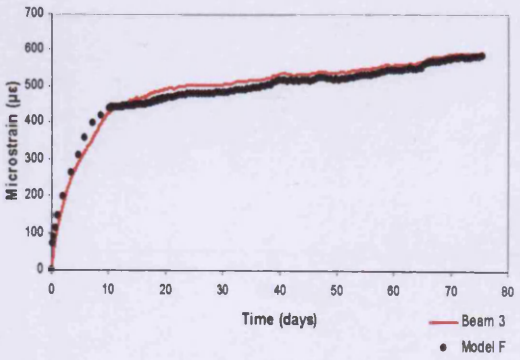

(c)

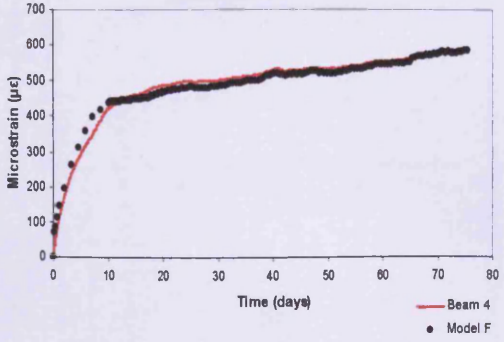

(d)

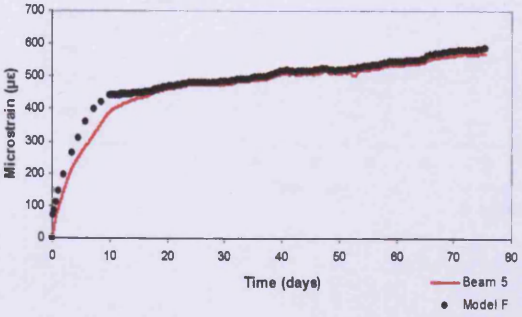

(e)

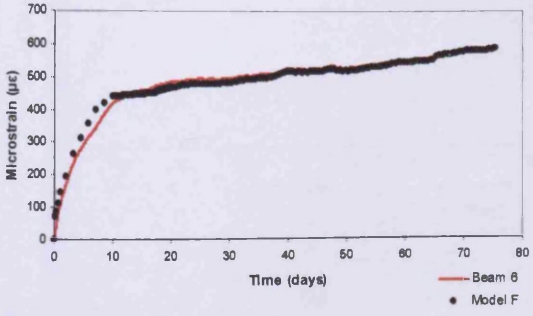

(f)

Figure D5: Autogenous shrinkage strain results of beams with fibres compared to the model, (a) Beam 1, (b) Beam 2, (c) Beam 3, (d) Beam 4, (e) Beam 5 and (f) Beam 6.

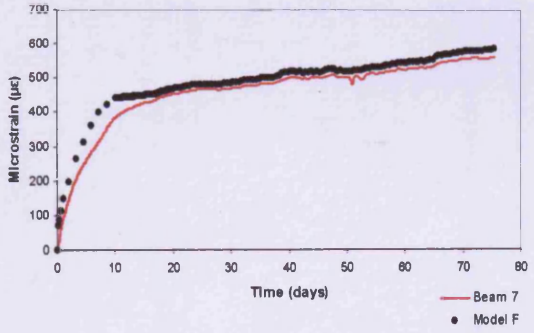

(a)

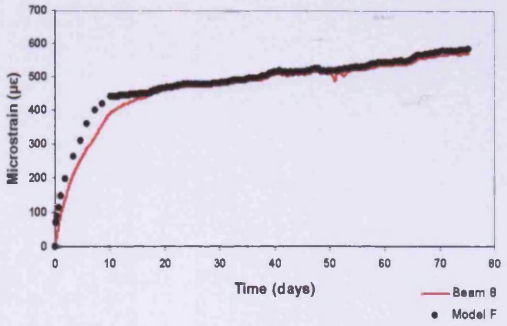

(b)

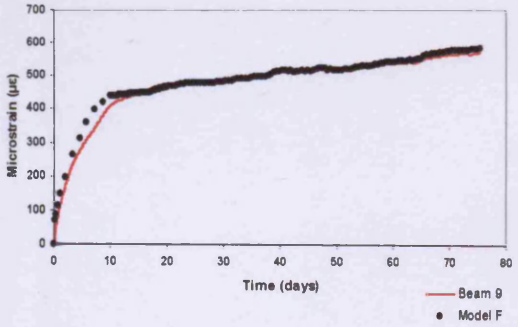

(c)

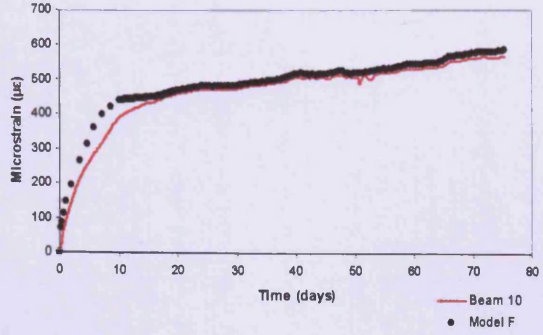

(d)

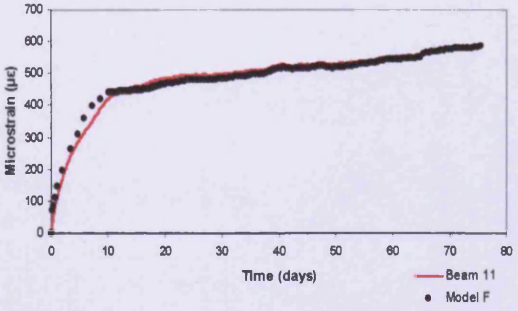

(e)

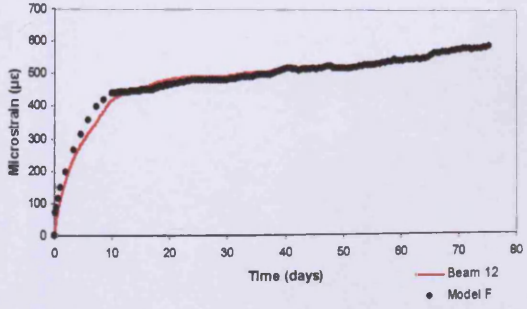

(f)

Figure D6: Autogenous shrinkage strain results of beams with fibres compared to the model, (a) Beam 7, (b) Beam 8, (c) Beam 9, (d) Beam 10, (e) Beam 11 and (f) Beam 12.